ENHANCING THE OPEN-CIRCUIT VOLTAGE OF DYE-SENSITIZED SOLAR CELLS: COADSORBENTS AND ALTERNATIVE REDOX COUPLES

THÈSE N^{O} 4066 (2008)

PRÉSENTÉE LE 25 AVRIL 2008
À LA FACULTÉ DES SCIENCES DE BASE
LABORATOIRE DE PHOTONIQUE ET INTERFACES
PROGRAMME DOCTORAL EN CHIMIE ET GÉNIE CHIMIQUE

ÉCOLE POLYTECHNIQUE FÉDÉRALE DE LAUSANNE

POUR L'OBTENTION DU GRADE DE DOCTEUR ÈS SCIENCES

PAR

Zhipan ZHANG

M.Sc. in chemistry, Tsinghua University, Beijing, Chine
et de nationalité chinoise

acceptée sur proposition du jury:

Prof. P. Vogel, président du jury
Prof. M. Grätzel, directeur de thèse
Prof. G. Boschloo, rapporteur
Dr S. Dai, rapporteur
Prof. X. Hu, rapporteur

ÉCOLE POLYTECHNIQUE
FÉDÉRALE DE LAUSANNE
Suisse
2008

Abstract

In Feburary 2008, the oil price easily exceeded $ 100 per barrel due to the weak US dollar and the imbalance between the increasing demands and deficient supplies. People are paying more and more attention to seek for alternative energy sources that would suffice the modern society in the following high-oil-price era. The work in this thesis is associated with some fundamental research in one of the solutions to the energy shortage, photovoltaics. Particularly, the dye-sensitized solar cell was taken as the system where the effects of coadsorbents and alternative couples to the classic iodide/iodine redox were studied and rationalized.

The first chapter was a general introduction to the photovoltaics and dye-sensitized solar cells, such as the operating principles and the characteristics of the dye cell.

In Chapter 2, we specified all the experimental issues, including the chemicals, materials, film preparation, characterization techniques and data analysis. A short part was also dedicated to the basics of the photovoltaics.

We studied the electronic effect of the scattering particles in our devices in Chapter 3. These particles were of 400 nm in diameter and always put on top of the nanotransparent layer to increase the light harvesting of the devices. It was found that the particles gave a small dark current but under illumination, they made a significant contribution to the total photocurrent. Photovoltage and photocurrent transient decay measurements performed under bias illumination showed that the density of electronic states of the light scattering layer was two times smaller than that of a transparent nanoparticle layer.

From Chapter 4 to Chapter 7, we systematically studied the function of the coadsorbents in our Application of an ω-guannidino carboxylic acid was found to increase the open-circuit voltage of the device by 50 mV. Coadsorbents with similar structures were then employed with an amphiphilic ruthenium sensitizer, Z-907, to scrutinize this effect. The voltage shift was interpreted as the effect of a negative shift in conduction band and a decrease in the back electron transfer of photoinjected electrons in TiO_2 to the triiodide species in the electrolyte, the former being the main reason for the large photovoltage increase. The specificity in the structure of the coadsorbents and its implication were also discussed.

In Chapters 8 and 9, we studied the possibility to use some one-electron transfer couples as the replacement of the iodide-based electrolyte. Mainly, 2,2,6,6-Tetramethyl-1-piperidinyloxy (TEMPO), phenoxazine derivatives and tetrathiafulvalene were selected as the candidates and their device performances were evaluated by electrochemical, photochemical and phototransient measurements. The redox potentials of these couples were 100 to 400 mV more positive than that of I^- / I_3^- couple, mitigating the potential mismatch between the Nernst potential of the dye cation and that of the redox mediator. TEMPO/$TEMPO^+$ based devices showed the best conversion efficiency of more than 5 % under AM 1.5 illumination at 100 $mWcm^{-2}$, a new record at this light intensity for non-iodine and non-pseudohologen electrolytes. On the other hand, the fast recapture of electrons in TiO_2 by the oxidized species of the couple was accounted for the lower observed increase in V_{oc} of the devices with these electrolytes than the simple shift in the redox potentials.

We drew some final conclusions in Chapter 10 together with our outlooks in the future research and development of coadsorbents and electrolytes for dye-sensitized solar cells.

Key words: Dye-sensitized solar cells, light scattering particles, coadsorbent, alternative redox TEMPO, MEEP, TTF.

Résumé

En Février 2008, le prix du baril de pétrole a facilement dépassé les $ 100, à cause d'un dollar US faible et d'un déséquilibre entre demandes croissantes et approvisionnements insuffisants. On prête de plus en plus attention à la recherche de sources d'énergie alternatives qui permettrait à la société moderne de se fournir en énergie dans l'ère imminente du pétrole cher. Le travail de cette thèse est associé à la recherche fondamentale pour développer une des solutions au manque d'énergie, le photovoltaïque. En particulier, les cellules photovoltaïques à colorant ont été utilisées comme système où les effets des coadsorbents et des couples redox alternatifs au couple classique iode/iodure ont été étudiés et rationalisés.

Le premier chapitre a été une introduction générale au photovoltaïque et aux piles solaires à colorant, avec les principes de fonctionnement et les caractéristiques d'une cellule à colorant. En Chapitre 2, nous avons indiqué tous les paramètres expérimentaux, y compris les produits chimiques, les matériaux, la préparation de film, les techniques de caractérisation et l'analyse de données. Une courte partie a également été consacrée aux bases du photovoltaïque. Nous avons étudié l'effet électronique des particules diffusantes dans nos dispositifs en Chapitre 3. Ces particules possèdent un diamètre de 400 nm et ont toujours été déposées sur la couche nanotransparente pour augmenter l'absorption lumineuse des dispositifs. On a constaté que ces particules ont contribué à un faible courant dans l'obscurité mais sous illumination, ils ont apporté une contribution significative au photocourant total. Les mesures de décroissance du photopotentiel réalisées sous illumination polarisée montrent que la densité des états électroniques de la couche dispersante est deux fois plus faible que celle d'une couche transparente de nanoparticules.

Du Chapitre 4 au Chapitre 7, nous avons étudié de manière systématique l'influence des dans nos dispositifs. L'application d'un acide carboxylique de ω-guannidine s'est avérée utile pour augmenter la tension de circuit ouvert du dispositif de 50 mV. Des coadsorbents ayant une structure similaire ont été alors employés avec le colorant amphiphile de ruthénium Z-907, pour étudier cet La variation de tension a été interprétée comme étant l'effet combiné d'un déplacement négatif de la bande de conduction et d'une diminution du taux de recombinaison des électrons photoinjectés

TiO_2 vers l’ion iodure de l'électrolyte, le premier étant la raison principale de l’augmentation importante du photovoltage. La spécificité dans la structure des coadsorbents et son implication ont également été discutées. En Chapitres 8 et 9, nous avons étudié la possibilité d’employer quelques couples redox monoélectroniques pour remplacer le couple iode/iodure de l'électrolyte. Principalement, le 2,2,6,6-Tetramethyl-1-piperidinyloxy (TEMPO), et des dérivés de phenoxazine et tetrathiafulvalene ont été sélectionnés et les performances de leurs dispositifs ont été évaluées par des mesures électrochimiques, photochimiques et phototransient. Les potentiels redox de ces couples de 100 à 400 mV plus positifs que celui du couple I^-/I_3^-, atténuant la différence de potentiel entre le potentiel de Nernst du cation du colorant et celui du médiateur redox. Les dispositifs basés sur le couple $TEMPO/TEMPO^+$ ont démontré la meilleure efficacité de conversion, plus de 5 %, sous une illumination de type AM 1.5 (100 $mWcm^{-2}$). Ceci constitue un nouveau record à cette intensité lumineuse pour des électrolytes non-iodés et de non-pseudohalogenés. Dans le même temps, la recombinaison rapide des électrons dans TiO_2 par l’espèce oxydée du couple a expliqué la moindre augmentation du V_{oc} de ces dispositifs utilisant ces électrolytes que la simple variation des potentiels redox.

Le Chapitre 10 donne les conclusions de ce travail et des perspectives envisageables pour le développement des coadsorbants et des électrolytes pour cellules solaires à colorant.

Mots clés: Cellules photovoltaïques à colorant, particules de dispersion de la lumière, coadsorbent, couples redox alternatifs, TEMPO, MEEP, TTF.

Table of Contents

1. Introduction

As the world is becoming more advanced in technology and economy, more energy is being consumed to keep up with the development and the demand on energy boomed over the past years. In 2005, the annual world primary energy consumption increased by 2.7% to 441 exajoules and is estimated to augment steeply to 762 exajoules by the year of 2030.[1] Presently, the energy economy is still highly dependent on three forms of fossil fuels - oil, natural gases and coal with percentages of 36.4%, 23.5% and 27.8%, respectively.[2] However, the world will shortly come to an end of fossil fuels as the world's primary energy resource. With a daily consumption of 82.5 million barrels, oil might run out in around 40 years at current reserves-to-production (R/P) ratio. A better synopsis is for natural gases that can last for about 60 years and coal, being the most abundant, for 150 years.[1] Meanwhile, the increasing awareness that the unpleasant environmental pollution arising from the combustion of these feedstocks necessitates urgent promotion of alternatives in renewable energy sources to cover the substantial deficit left by fossil fuels.

Of all the available technologies producing renewable energy, photovoltaic energy is a hot topic in current research. One simple reason is that the Earth receives 1.2 x 10^{17} W insolation or 3 x 10^{24} Joule energy per year from the Sun and this means covering only 0.13% of the Earth’s surface with solar cells with an efficiency of 10% would satisfy our present needs.[3] Apart from the abundance of potentially exploitable solar energy, photovoltaic cells also have other competitive advantages such as little need for maintenance, off-grid operation and silence, which are ideal for usage in remote sites or mobile applications.

The chapter will shortly review the discovery, development and state-to-art photovoltaic technologies. The history, structure and operating mechanism of dye-sensitized solar cell (DSC) is then discussed in details. Finally, the objective of this work will be elaborated at the end of this chapter.

1.1 Photovoltaics - A recent story

Mankind has exploited solar power since the ancient time. As early as in the 7th century B.C., magnifying glass was already used to concentrate sun’s rays to make fires. Later on, Roman people built the famous bathhouses (in the first to fourth centuries A.D) with large south-facing windows to employ the sun’s warmth. They named these sunspaces *heliocamini* (sun furnaces).[4] However, it was only until in the 19th century that the photovoltaic effect was discovered. In 1839, Edmund Becquerel, a French experimental physicist of nineteen years old, noticed the generation of an electric current while experimenting with a silver coated platinum electrode placed in the electrolyte.[5] In 1873, Willoughby Smith discovered the photoconductivity of selenium when testing flaws in the trans-Atlantic telegraph cables. He noted the conductivity of selenium bar immediately “increased from 15 to 100 percent according to the intensity of light” [6],[7] Three years later, William Grylls Adams and his student, Richard Evans Day, made the first solar cell by contacting a sample of selenium with two heated platinum contacts and proved selenium produced a “photoelectric” effect, rather than a mere thermal electricity effect, when exposed to light.[8] In 1883, Charles Fritts, an American inventor, described the details of the first large area solar cells from selenium wafers.[9] However, since the selenium cells converted far less than 1% of all incident sunlight into electric power and deteriorated very rapid when exposed to strong light, these pioneers in photoelectricity failed to build the solar devices that they had hoped to.

In 1901, Max Planck explained the spectral distribution of solar spectrum by his famous Planck's law.[10] Four years later, Albert Einstein published a simple description of “light quanta” (later called “photons” as suggested by Gilbert Lewis in 1926) and showed how they could be used to explain the photoelectric effect, [11] which won him the Nobel Prize in 1921. This is the theoretical basis for all photovoltaic devices and in common semiconductors, photons excite electrons out of the valence band and into the higher-energy conduction band, where they are collected and transported to the outer circuit.

In parallel, discoveries were also made in the material part. In 1904, Wilhelm Hallwachs made a semiconductor-junction solar cell from copper and copper oxide, a prototype of thin-film Schottky barrier devices. This barrier layer at the semiconductor-metal interface was confirmed by Goldmann and Brodsky in 1914 [12] and later studied in more details by Walter Schottky, Neville Mott and others in the 1930s.[13],[14] In 1918, Jan Czochralski, a Polish scientist, developed a way to measure crystallization rate of metals [15] and the Czochralski method was later adapted by Bell Labs to grow single crystals of suitable semiconductors in the 1950s. In 1932, Audubert and Stora discovered the photovoltaic effect in cadmium sulfide (CdS), opening up a way to II-VI solar cells.[16]

With the development of silicon electronics, the 1950s witnessed the breakthrough in photovoltaic devices. Fuller, a Bell chemist, intuitively had a nice idea of making near-surface *p-n* junctions by a boron trichloride treatment of *n* type silicon wafers,[17] which greatly favored charge separation of the device, and with these substrates, Chapin got near 6% conversion efficiency - 50 times more efficient than the selenium cells in 1930s.[18] In the following years, *p-n* junctions with CdS, GaAs, InP and CdTe were studied for a higher efficiency, stimulated by theoretical calculations. However, the cost of the photoelectricity was so high (several hundred $ per Watt) that the newly born technique became a privilege only to space applications at that time. After taking several technical measures, a team led by Dr. Berman at Solar Power Corporation cut the cost of single crystal module down to 10 - 20 $ per Watt in the early 1970s.[19]

The energy crisis in 1970s greatly stimulated the interest and funding for research in alternative sources of energy, including photovoltaics. It was during this period that the *second generation* solar cells were developed, such as polycrystalline and amorphous silicon, thin-film deposits of silicon, CdTe, $CuInSe_2$, (CIS) and $Cu(In,Ga)Se_2$ (CIGS), as well as multijuntion cell technology. These devices were initially designed to be high-efficiency but later turned out to be of the advantages in the mass of material and production cost compared to single crystalline silicon devices.

In the 1990s, new concepts of solar cells were conceived and realized. These technologies mainly include dye-sensitized solar cells, polymer solar cells, and nanocrystalline solar cells, all of which are now known as *third generation* photovoltaics since they are very different from the previous semiconductor devices as they do not rely on a traditional *p-n* heterojunction to separate photogenerated charge carriers. Instead, they form a ‘bulky’ junction where charge separation takes place. Because of the low-cost materials and easy fabrication, these technologies are expected to take a significant share in the fast growing photovoltaic areas.

With the advent of the new millennium, photovoltaics experienced an unprecedented golden developing period. In 2000, the global yearly solar cell production was 300 MW, while this sharply increased to about 2000 MW in 2005 [20] and was predicted to rise in an even more rapid rate. [21] Thus, with the large scale practical applications and still ongoing technological advances, a new era in photovoltaics could be foreseen.

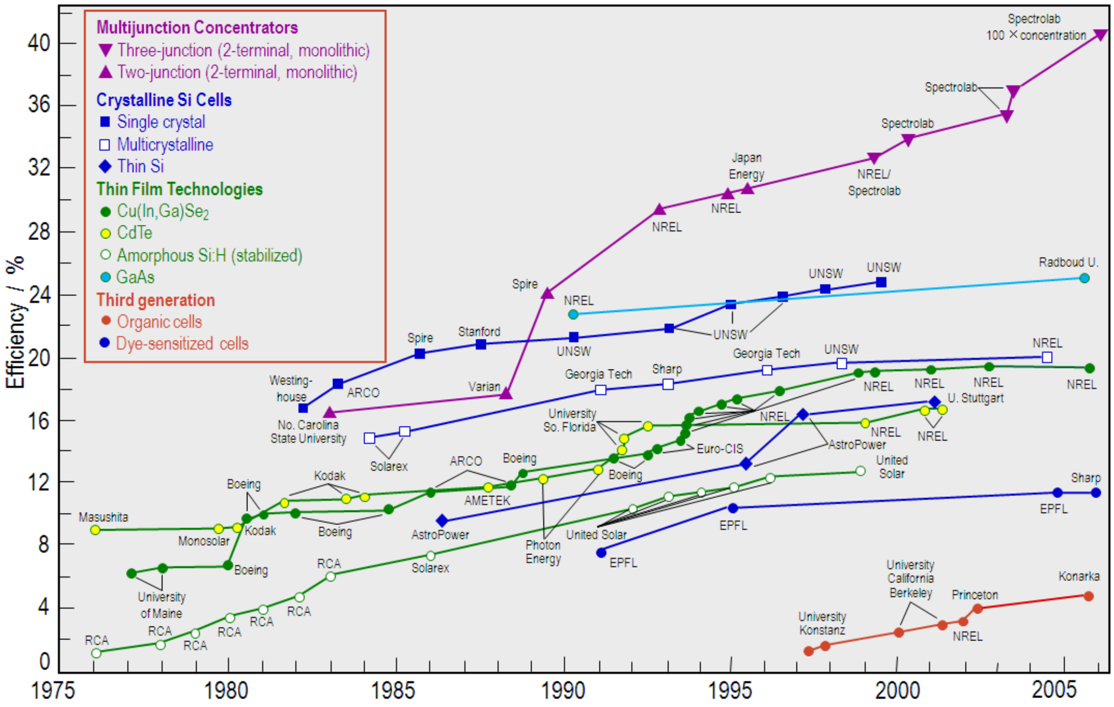

Figure 1.1 Thirty years evolution in conversion efficiencies of different photovoltaic technologies.[22]

1.2 Dye-sensitized Solar cells

1.2.1 A history with photography

In 1837, almost at the same time when Becquerel found the photovoltaic effect, Louis Daguerre made the first “daguerreotype” photographic image onto a mirror-polished surface of silver bearing a coating of silver halide particles, which is now considered as the beginning of photography. The silver halides used in photography have band gaps ranging from 2.7 to 3.2 eV, and are therefore not photoactive for wavelengths longer than 460 nm, lacking the sensitivity to the mid-visible spectral and red light. An improvement was made in 1873 by a German photochemist, Vogel, via the dye sensitization of silver halide emulsions, leading to an extended photoresponse into the red and even infrared regions and the first panchromatic film rendering a realistic black and white picture.[23] In 1887, Moser intuitively observed the first case of dye-sensitized semiconductor electrode when using the dye erythrosin on silver halide electrodes.[24] However, it was not until 1960s that people clearly understood the operating mechanism is the electron injection from a photo-excited state of the dye molecules into the conduction band of the n-type semiconductor substrates, following the work of

Namba and Hishiki,[25] Tributsch and Gerischer et al.[26]-[28] on zinc oxide. Those prototype dye-sensitized cells were characterized with poor dye anchorage (mostly physisorbed) on semiconductor surface and low conversion efficiencies restricted by the limited, weak light absorption (in the order of 1 to 2%) of the dye monolayer on the planar surface. Thicker dye layers increased the resistance of the system without adding to the current generation,[29] which disappointed Gerischer and led him not to “follow the idea of constructing a photocell based on this effect…with earlier experiments”.[30] Incremental improvements were then achieved both in the chemisorption of sensitizers,[31]-[33] electrolyte redox chemistry and the judicious selection of photoelectrode materials.[30], [33]-[39] Most semiconductors such as CdS, CdSe, GaP and Si underwent serious photocorrosion or even normal corrosion in the dark, thus a stable, wide band-gap semiconductor, TiO_2, became the material of choice, following the successful demonstration of direct photolysis of water with TiO_2.[40], [41] To solve the absorption dilemma, the concept of using dispersed particles to provide a sufficient interface emerged first,[42] then photoelectrodes with high surface roughness were employed to generate multiple reflections at a rough surface, permitting the capture of most of the incident light by a monolayer of a dye with a high molar extinction coefficient .[43],[44] All these improvements finally led to the announcement in 1991 of the sensitized nanocrystalline photovoltaic device with a conversion efficiency at that time of 7.1 -7.9 % under solar illumination and 12% in diffuse daylight.[45] With the discovery of the N3 sensitizer and the later panchromatic “black dye”, the power to electricity conversion efficiency was pushed well over 10%.[46],[47] An interesting modification to this classic system was replacing the electrolyte with a solid hole conductor, yielding an all-solid state dye-sensitized device.[48],[49] Recent achievements of long-time stability under accelerated experiments with non-volatile liquid and quasi-solid molten salt (ionic liquid) electrolyte greatly promoted the practical application of this third generation photovoltaic technology and put it currently right at the start of commercialization stage.[50]-[53]

1.2.2 Basic principles of dye-sensitized solar cells

1.2.2.1 A concept of ‘excitonic’ solar cell

Conventional photovoltaic cells are built on *p-n* junctions of silicon and other inorganic semiconductors. Figure 1.2a depicts the energy band diagram of a *p-n* junction after thermal equilibration of positive and negative charge carriers. Due to the concentration difference between the *p* and the *n* type semiconductor, holes move to the *n* region and electrons to *p* region. The uncompensated charges induced by the diffusion generate a built-in electric field at the junction and impair further percolation of charge carriers since the orientation of the electric field is contrary to the direction of the carrier diffusion. At equilibrium, no net charge diffusion occurs and a depletion region is formed, which is also referred to as a space charge layer. In the case of illumination as shown in Figure 1.2b, absorption of photons with an energy higher than a threshold, the band gap, results in generation of excitons which interact via columbic forces. Considering that excitons will recombine after a certain time with emission of photons or phonons (heat), therefore only those created in or close to the space charge layer can be separated by the built-in electric field and contribute to the photocurrent. Since both electrons and holes coexist in the same chemical phase, these cells are called minority carriers devices and their efficiencies are highly dependent on the ability of photogenerated minority carriers (for example, electrons in a *p*-type material) to be collected out of devices before recombining with the majority carriers (holes, in this case).[54]

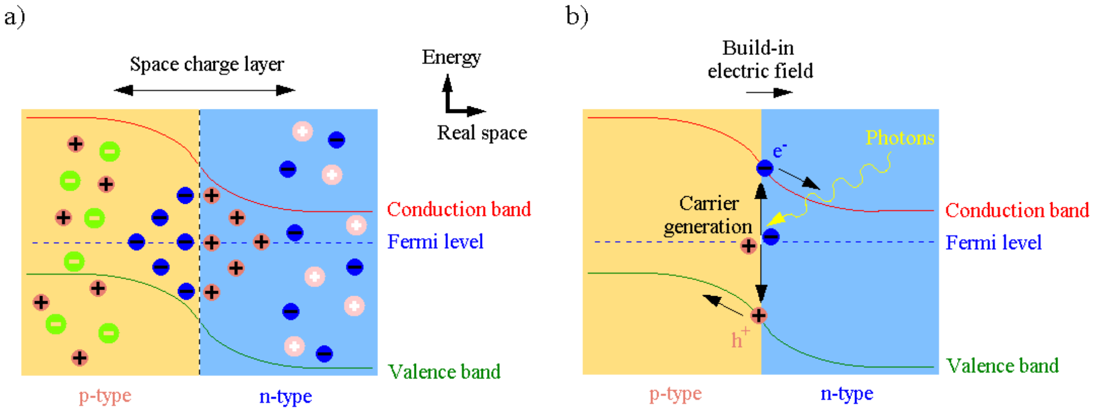

Figure 1.2 a) Energy band diagram of a conventional *p*-*n* junction solar cell in the case of short circuit condition; b) Charge separation under illuminations.

On the contrary, with an electron-conducting phase (*n*-type semiconductor) and a hole conducting phase (redox species or hole conductors) forming a “bulky” heterojunction, DSCs are majority carrier devices where electrons and holes are separated in two chemical phases. Upon illumination, the surface anchored dyes are sensitized to the exited state (S^*) by light absorption. This mode of carrier generation is also shared in organic, bulk junction solar cells where a light-absorbing organic polymer works as the sensitizer and a derivatized fullerene as the electron accepter. These devices are classified by Gregg as “excitonic solar cells”, referring to the generation of a molecular excited-state or Frenkel exciton as the first step of a photovoltaic event.[55][56] In most other “excitonic” solar cells, photogenerated excitons have to diffuse a few nm to the interface before dissociating to an electron-hole pair. While in DSCs, the excitons are generated right at the interface and they dissociate readily to create an electron-hole pair, with electrons subsequently injected into the conduction band of the semiconductor while the holes, at least initially, remain on the sensitizers.[56] The dye ground state (S^0) is then regenerated by electron donation from the redox system to the oxidized state of the sensitizer (S^+). The recuperation of redox system is realized by transporting holes to the counter electrode either in a diffusion or hopping mechanism (depending on the transporting mediator). The whole process is finally completed by electron migration via the outer circuit and the device generates electric power from light without penalty of any permanent chemical transformation.[57]

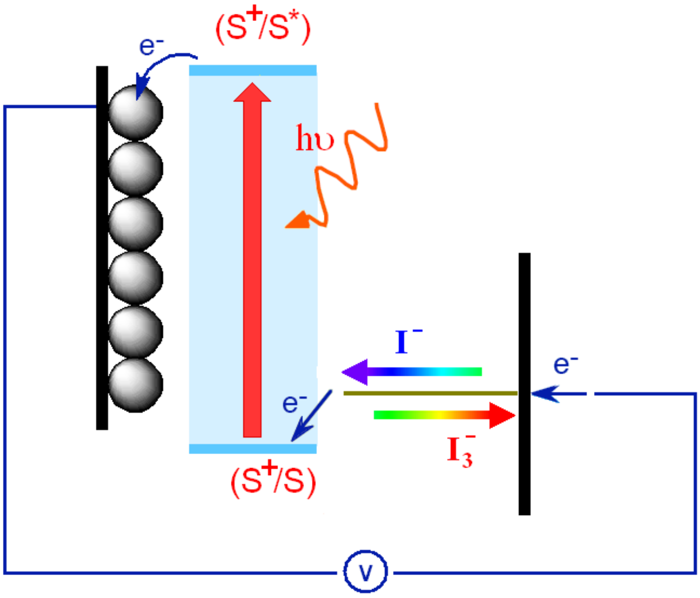

Figure 1.3 Principle of operation of the nanocrystalline TiO_2 dye-sensitized solar cells.

Following the above rationales, it is clear that photogeneration, separation and recombination take place nearly exclusively at the high-surface area heterointerface in nanocrystalline dye cells, and thus the properties of these interfaces are of critical importance to the conversion efficiency of the device.

1.2.2.2 Light absorption by the sensitizer monolayer on the mesoscopic semiconductor films

Sufficient absorption overlap of the solar spectrum is a prerequisite to any respectable power to electricity conversion for all photovoltaic devices. Due to the presence of a band gap, semiconductors only absorb light below a threshold wavelength λ_g, the fundamental absorption edge, which is related to the band gap energy, E_g, by Eq. 1.1

$$\lambda_g\ (\text{nm}) = 1240/\ E_g(\text{eV}) \qquad (1.1)$$

Given that only wide band-gap semiconductors with $E_g > 3$ eV are stable candidates to be used in DSCs,[30] these materials actually have no absorption in the solar spectrum apart from the ultraviolet regions. For example, TiO_2, the most widely used material for DSCs, has a band gap of 3.2 eV and thus an absorption edge of ~390 nm, lacking the access to the broad solar spectrum in visible and infrared regions. The surface anchored dyes greatly red-shift this absorption threshold to the near infrared (depending on the property of the sensitizers). The light harvesting efficiency (LHE) is given by Eq. (1.2)

$$\text{LHE}\ (\lambda) = 1 - 10^{-\Gamma\sigma(\lambda)} \qquad (1.2)$$

where Γ is the number of moles of sensitizer per square centimeter of projected surface area of the film and σ is the absorption cross section in units of $cm^2\ mol^{-1}$ obtained from the decadic extinction coefficient, ε (units of $M^{-1}\ cm^{-1}$) , by multiplying 1000 $cm^3\ L^{-1}$. Suppose on a planar electrode surface where there is a monolayer of the sensitizer with a high ε value of $10^5\ M^{-1}\ cm^{-1}$ and a low footprint of 1 nm^2 for each dye molecule, a simple calculation by Eq. 1.2 only gives an absorption of less than 4%, which is too small to achieve any respectable solar to electricity conversion, as was the case for early DSCs. State-to-art DSCs differ from their earlier counterparts in utilizing a mesoscopic semiconductor film. In a porous film consisting of typically 20 nm TiO_2 particles nowadays,[58] the roughness factor, defined as the ratio the *real* (true, actual) *surface (interface) area* to the *geometric surface (interface) area*,[59] can be as high as 138 for 1 µm film [60] and the effective surface area can be enhanced 1000-fold for a mere thickness of 7 µm. Still take the previous example with the flat surface, even a 500-fold increase in Γ will yield a close to unity absorption even with only a dye monolayer on each particle under the same conditions. Nature, in fact, shares the similarity of absorption enhancement by stacking the chlorophyll containing thylakoid membranes of the chloroplast to form the grana structures.[61]

To date, Ruthenium (II) polypyridyl complexes with the structure of $RuLL'(NCS)_2$ (L, L' stand for polypyridine ligands) are the most widely studied and used sensitizers due to their superior chemical stability and large visible light harvesting capacity. The N719 sensitizer, bis(tetrabutylammonium) cis-di(thiocyanato)-bis(2,2'-bipyridyl-4- carboxylate-4'-carboxylic acid)-ruthenium(II), was the first sensitizer that achieved the 10% conversion benchmark and now used as the standard sensitizer for cell evaluations.[46][58] It absorbs broadly in the visible region, with an absorption edge in the near infrared (~ 800 nm). Replacing the bipyridyl ligand with a terpyridyl ligand gives a panchromatic sensitizer, tri(thiocyanato)-2,2',2"-terpyridyl-4,4',4"- tricarboxylate)Ru(II), whose response extends 100 nm further into the IR and the photocurrent onset is close to 920 nm. The conversion of incident photons to electric currents is practically quantitative over the whole visible domain if reflection and absorption losses in the conducting glass are taken into account.[62] Recent advances in quaterpyridyl ligand red-shifted the threshold by another 10 to 15 nm, proving the concept.[63] An alternative strategy might be the ‘dye cocktail’ where a ruthenium sensitizer is absorbed together with another sensitizer that has a strong absorption in near infrared region, such as squaraines and phthalocyanines. The ultimate goal is to achieve a nearly vertical rise of the photocurrent close to the 920 nm absorption threshold that would yield a short circuit photocurrent of about 28 mA/cm^2 and a conversion efficiency of close to 15% if only light harvesting is the problem.[62]

1.2.3 Electron transfer processes in DSCs

1.2.3.1 A scheme of dynamics

DSCs are photoelectrochemical devices where several electron transfer (ET) processes are in parallel and in competition. Since the highest energy conversion efficiencies have been reported for a nanocrystalline TiO_2 film sensitized with ruthenium polypyridyl complexes and permeated with I^-/I_3^- as the electrolyte, the following discussion will primarily focus on DSCs with this configuration.

Figure 1.4 shows the typical time constants of processes involved in such a DSC device. Upon illumination, the sensitizer is photoexcited in a few femtoseconds (Eq. 1.3) and electron injection is ultrafast from S* to TiO_2 (Eq 1.4) on the subpicosecond time scale (intramolecular relaxation of dye excited states might complicate the injection process and change the timescale, see discussions in section **1.2.3.2**), where they are rapidly (less than 10 fs) thermalized by lattice collisions and phonon emissions. The nanosecond-ranged relaxation of S* (Eq 1.5) is rather slow compared to injection, ensuring the injection efficiency to be unity. The ground state of the sensitizer is then recuperated by I^- in the microsecond domain (Eq. 1.6), effectively annihilating S^+ and intercepting the recombination of electron in TiO_2 with S^+ (Eq. 1.7) that happens in the millisecond time range. This is followed by the two most important processes – electron percolation across the nanocrystalline film and the redox capture of the electron by the oxidized relay (back reaction, Eq. 1.8), I_3^-, within milliseconds or even seconds. The similarity in time constants of both processes induces a practical issue on achieving high conversion efficiencies in DSC. In a simple model, an electron collecting efficiency at short circuit can be defined as $\Phi_{col} = k_{trans} / (k_{trans} + k_{rec})$ where k_{trans} and k_{rec} are the first-order rate constants for the electron transportation and the back reaction, respectively, indicating that a fast electron transportation in TiO_2 and a slower back reaction are preferable.

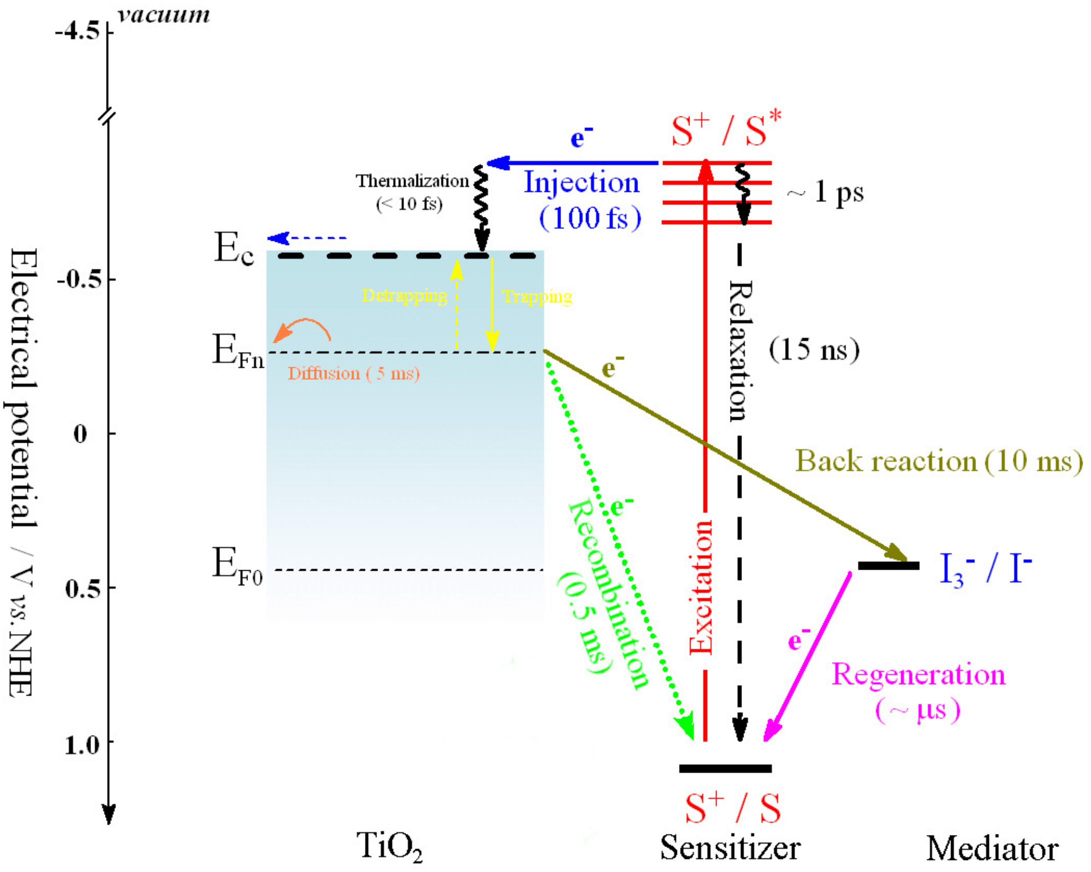

Figure 1.4 Dynamics of different electron transfer processes in the conversion of light to electric power by a DSC. The numbers in parentheses are representative values for each process.

$S\vert TiO_2 + hv \rightarrow S^*\vert\, TiO_2$	Photoexcitation	(1.3)
$S^*\vert\, TiO_2 \rightarrow S^+\vert\, TiO_2 + e^-_{cb}\,(TiO_2)$	Charge injection	(1.4)

$S^*|\ TiO_2 \rightarrow S|TiO_2$ Relaxation (1.5)

$S^+|TiO_2 + 2\ I^- \rightarrow S|TiO_2 + I_2^{-\bullet}$ Regeneration (1.6)

$S^+|\ TiO_2 + e^-(TiO_2) \rightarrow S|TiO_2$ Recombination (1.7)

$e^-(TiO_2) + I_2 \rightarrow I_2^{-\bullet}$ Back reaction (1.8)

1.2.3.2 Charge separation at semiconductor-dye interface

Charge separation in a DSC is achieved by photoinduced electron injection from the molecular excited state of the sensitizer to semiconductor nanoparticles, a process being described as ET between a discrete and localized molecular state and a continuum of ***k*** states in the semiconductor.[64][65] According to Marcus and Gerischer's theory, [34] [66]-[68] the total ET rate, k_{ET}, depends on the energetic overlap of donor (S*) and acceptor (semiconductor) states which are related to the density of states (DOS) at energy E relative to the conduction band edge, ρ(E), reorganization energy, λ_{reo}, and temperature, T. At a given temperature, the overlap increases with a higher ρ(E) and a smaller λ_{reo} and reaches a maximum when the entire donor distribution function lies above the conduction band edge, E_{c}. Significant overlap is associated with a fast k_{ET}. For example, for efficient sensitizers like $RuL_2(SCN)_2$ absorbed on nanocrystalline TiO_2 film, these complexes undergo strong metal-to-ligand charge transfer transitions (MLCT) under visible irradiation and the injecting molecular orbital is the π^* wave function of the carboxylated bipyridyl ligand. The interaction between carbxylate groups with the surface Ti(IV) ions results in good electronic coupling of the π^* wave function with the 3d orbital manifold of the conduction band of the TiO_2, leading to very rapid injection dynamics.[61]

Given the ultrafast rate of electron injection, it was not surprising that the dynamics were not well resolved until the advent of femtosecond laser spectroscopy in 1996.[69] [84] Soon there were many related publications reporting direct observation of subpicosecond electron injection from various dyes into TiO_2 nanoparticles.[71]-[89] Injections from the most studied Ru polypyridyl sensitizers are usually biphasic, consisting of a distinct <100 fs ultrafast component and one or more slower components on picosecond and longer timescales.[69][71][72] [75][76] This was attributed to injections from the singlet transfer (^{1}MLCT) and the triplet transfer (^{3}MLCT) state, the latter formed by intersystem crossing of the excited molecules. Since the energy of ^{3}MLCT is relatively low (1-2 eV lower than ^{1}MLCT) and near the semiconductor conduction band edge, injection from ^{3}MLCT is expected to be significantly slower than that from singlet due to the diminished overlap of the donor states with the rapidly decreased density of conduction band states near the band edge. Results from the excitation wavelength dependence of injection dynamics supported injection from unthermalized excited states, [80][83][86][87] while distinct singlet and triplet electron injection pathways have been identified with a RuN3/TiO_2 system. [80][83] However, recent experiments by Wenger et al. argued against the validity of this biphasic injection mechanism.[90]-[92] They believed the slow part of the injection was induced by dye aggregation. The slow part almost disappeared when a less aggregated sensitizer was used or the TiO_2 film was dyed from a diluted solution of sensitizer.[90] Impressively, a monophasic, <20 fs injection was observed from a dye containing a phosphonic acid group as an anchoring function. [92] Further experiments need to be conducted to develop a more quantitatively clear picture of the electron injection process.

1.2.3.3 Charge transportation and the back reaction

The driving force for electron transportation in semiconductors is the gradient of electrochemical potential, $\bar{\mu}_i$, or the quasi-Fermi levels (The word “quasi” is used here to describe the excess carrier distribution when external potential is applied to semiconductor and Fermi potential can not be used to describe the distributions of both electrons and holes). While conventional silicon junctions rely essentially on the space charge layer and “built-in field” to extract electrons, the TiO_2 nanoparticles of DSCs are usually too small to support any substantial space charge layer. For a spherical semiconductor particle, the potential difference between the center ($r = 0$) and at a distance r was derived to be [93]

$$\Delta\phi_{sc} = \frac{kT}{6e}\left(\frac{r-(r_0-W)}{L_D}\right)^2\left(1+\frac{2(r_0-W)}{r}\right) \qquad (1.9)$$

where $\Delta\phi_{sc}$ is the potential drop, $L_D = (\varepsilon_0\varepsilon kT/2e^2N_D)^{0.5}$ is the Debye length which depends on the number of ionized dopant molecules per cubic centimeter, N_D, r_0 is the radius of the particle and W is the width of the space charge layer. For nanoparticles, the total potential drop within the semiconductor becomes

$$\Delta\phi_{sc} = \frac{kT}{6e}\left(\frac{r_0}{L_D}\right)^2 \qquad (1.10)$$

Meanwhile, the high ionic strength electrolyte that interpenetrates the porous oxide network effectively shields photoinjected electrons. As a result, the electrical field in nanoparticles is negligible at normal doping levels (for example, $N_d = 10^{18}$ cm^{-3}) and the electron generation, transportation and collection can therefore be described by using the steady state continuity equation with the drift term omitted [94][95]

$$\frac{\partial n_c}{\partial t} = \eta_{inj}\alpha(\lambda)I_0 e^{-\alpha(\lambda)x} + D_n\frac{\partial^2 n_c}{\partial x^2} - \frac{n_c - n_{c0}}{\tau_n} = 0 \qquad (1.11)$$

Here n_c is the density of electrons in the oxide, n_{c0} is the conduction band electron concentration in the dark, η_{inj} is the injection efficiency, $\alpha(\lambda)$ is the absorption coefficient of the dye-sensitized medium at the wavelength λ, x is the distance from the substrate, I_0 is the photon flux at $x = 0$, D_n is the apparent diffusion coefficient and τ_n is the apparent lifetime of electrons. The photocurrent density is then given by

$$j_{photo} = qD_n\left.\frac{\partial n_c}{\partial x}\right|_{x=0} \qquad (1.12)$$

Typical values of D_n are in the range of 10^{-8} to 10^{-4} cm^{-2} s^{-1} [96][97] and found to increase with light intensities,[98]-[100] being much lower than the diffusion coefficient for electrons in the conduction band of the TiO_2 ($D_0 = 0.5$ cm^{-2} s^{-1}).[101] This is attributed to the multiple trapping event involved in the electron transporting process in the TiO_2, as is usually described by a trapping and a thermal release of electrons from shallow trap states in the energy distribution.[100][102] The electron concentration n_c in conduction band is always magnitudes lower than that of trapped electrons, n_t, and entirely related to the distribution and occupation of trap states. As we see later, the influence of this trapping/detrapping is also present in the loss channel of electrons, i.e. the back reaction (Eq. 1.8).

Due to the relatively small D_n and slow electron diffusion process (~ ms), electrons in TiO_2 may recombine with dye cation (Eq. 1.7), S^+, and/or the oxidized form of the redox couple in the electrolyte (Eq. 1.8), typically I_3^-. If we assume the S^+ is entirely intercepted by the redox couple and there is no electron loss to I_3^- via the substrate, the rate of electron transfer to I_3^- (the back reaction) may be expressed formally in terms of the concentrations of reactants (I_3^- and electrons) and the corresponding reaction orders a and b.

$$-\frac{dn}{dt} = kn^b[\mathrm{I_3^-}]^a \qquad (1.13)$$

Values between 1 and 2 have been reported for b,[100][103][104] while recent experiments suggest $b = 1$ and the reduction of tri-iodide is first order in electron concentration.[56] If we neglect the concentration variation of I_3^- (which is effectively constant), the electron lifetime, τ_n, can be defined as

$$\tau_n = \frac{1}{k[\mathrm{I}_3^-]^a} \tag{1.14}$$

Typical τ_n values are found in milliseconds, which are much higher than the conduction band electron lifetime τ_0 (tens of microseconds), and also dependant on the light intensities as is observed in the case of D_n. Meanwhile, it was interesting to find that the electron diffusion length

$$L_n = \sqrt{D_n \tau_n} \tag{1.15}$$

is almost independent (or only slightly) on light intensity.[100][105][106] An elegant explanation has been given by Bisquert and Vikhrenko by using a "quasistatic approximation" that considers that the stationary-state relationship between the densities of free and trapped electrons is maintained even when the system is displaced away from its initial state.[106] Then the apparent values of the electron diffusion coefficient, D_n, and electron lifetime, τ_n, are related to the conduction band values D_0 and τ_0 by

$$D_n = \left(\frac{\partial n_c}{\partial n_t}\right) D_0 \tag{1.16}$$

$$\tau_n = \left(\frac{\partial n_t}{\partial n_c}\right) \tau_0 \tag{1.17}$$

It then gives

$$L_n = \sqrt{D_n \tau_n} = \sqrt{D_0 \tau_0} \tag{1.18}$$

Eqs. (1.16) to (1.18) describe the dependence of D_n, τ_n and L_n on light intensity and are thus accepted in the dye cell community. Nonetheless, the origin and the location of the traps remain unclear. The traps are usually thought to be located at or near the surface of the oxide nanocrystals.[107] The difference of surface states and bulk trap states in electron transport and transfer are also pertinent for a better understanding of the trapping/detrapping process.

1.2.3.4 Dye regeneration

Fast dye regeneration is a prerequisite for an efficient DSC. In the presence of pure solvent, the lifetime of dye cation can be as long as milliseconds.[50] By introducing the most widely used $\mathrm{I}^-/\mathrm{I}_3^-$ system, dye cation quenching of down to microseconds has been observed. Dye regeneration is faster with increasing I^- concentrations and the lifetime of S^+ follows the Stern-Volmer equation:

$$\frac{\tau_{S^+}^0}{\tau_{S^+}} = 1 + k_q \tau_{S^+}^0 [Q] \quad \text{and} \quad \frac{1}{\tau_{S^+}} \propto [Q] \tag{1.19}$$

where k_q is the quenching constant, $[Q]$ is the concentration of quencher and $\tau_{S^+}^0$, τ_{S^+} are the lifetime of S^+ in the absence and presence of electrolyte, respectively. Normally, an I^- concentration of 0.6 M is thought to be fast enough to compete with recombination process (Eq. 1.7). There are also some studies on dye regeneration with redox couples other than I^-/I_3^-, providing kinetics on the same or even a faster time scale.[108],[109] On the contrary, dye regeneration in solid state DSCs has not been thoroughly studied and demands further pertinent work.

1.2.3.5 Electrolyte and hole conductor

To date, I^-/I_3^- system is still the best electrolyte for DSCs. Efficiencies of more than 11% with acetonitrile-based electrolyte and 8% long-term stability at 80 °C with a low volatile electrolyte have been achieved.[51] ,[110]-[113] Recently, room temperature ionic liquids (ILs) have attracted considerable interests as a potential candidate for replacing the volatile organic solvents due to their negligible vapor pressure and high ionic conductivity.[114]-[117] Stable DSC devices were obtained by using binary mixtures of the viscous, pure imidazolium I^-/I_3^- IL with a low viscosity, highly stable IL.[52] Following similar logics, quasi-solid electrolytes have been designed by gelating the electrolytes with aliphatic gels [118][119], polymers [50],[120][121] or even nanoparticles [122]. Other strategies for solidifying the electrolyte include introducing polymer cations [123][124] or plastic crystal [125].

Alternatives to the I^-/I_3^- system are always a topic of interest. Although Br_2/Br^- [126] and pseudohalogen systems of $(SCN)_2/SCN^-$ and $(SeCN)_2/SeCN^-$ [127][128] have been reported, the high corrosion and toxicity of these electrolyte hamper further research and application. Fast outer-sphere one-electron-transfer redox couples like ferrocene/ferrocinium and phenoxazine usually incur severe back reaction problems when subjected to DSC device tests.[129]-[131] Co(II) complexes show an impressive efficiency of 8% at a low light intensity but their performance drops markedly under full sun illumination. [132]-[134] A combination of two mediators, operating in series to regenerate the dye and transport the positive charges to the counter electrode has recently produced interesting results.[135] However to date, the solar to electric power conversion efficiency achieved with all these systems in full AM 1.5 sun light still remains well below 5%.

Hole conductors (HCs) are also a focus of current research since the majority of them are solids or nonvolatile liquids. Inorganic HCs of CuSCN,[136]-[138] CuI,[139]-[141] organic HCs of triarylamines[142] and polymer HCs of poly(3-alkyl thiophene),[143] polyaniline[144] have already been tested in DSCs. Among all the candidates, spiro-OMeTAD remains the best to date.[48][145] [146] The electron lifetime can be increased by reducing the doping level in the OMeTAD, but this also decreases its conductivity. Meanwhile, pore filling is still the most serious problem for increasing the efficiency and stability of the OMeTAD system.

1.2.3.6 Counter electrode

Counter electrode is the interface where the oxidized species in the electrolyte (or holes) is reduced and an equally important component of DSC. Normally, fluorine-doped tin oxide (FTO) glass is coated with platinum (by pyrolysis or sputtering, etc.) to afford more reversible electron transfer. Pt-free counter electrodes for the DSC include carbonaceous materials such as graphite,[147]-[149] carbon black, [147][150] carbon nanotubes, [150] activated carbon on FTO-glass and organic ion-doped conducting polymers of poly(3,4-ethylenedioxythiophene) (PEDOT) on both indium tin oxide (ITO) and FTO-glass [152],[153]. Over 9% efficiency under AM 1.5 simulated sunlight was achieved with carbon catalyst-based DSC recently,[150] rendering a new option with low cost and high corrosion resistance.

1.3 Objectives of the current work

The present work focuses on liquid electrolyte cells for a better understanding of DSCs. The interfacial phenomena between the nanocrystalline TiO_2 particles and electrolytes are scrutinized either by adding organic carboxylic/phosphonic acid or other functionalized acids. The effects of these molecules as coadsorbents on the photovoltaic properties of DSCs are examined and interpreted. The possibility of replacing the most widely used I^-/I_3^- system with alternatives is evaluated. Although this idea is not a new one, current experiments have shown interesting results and overcome some limits of the previous work. [154] The study is of an experimental nature and supported by different photochemical and electrochemical analytical techniques.

The thesis is then subdivided into mainly four parts: Chapter 2 addresses all the experimental and theoretical issues of device fabrication and characterization techniques and Chapter 3 shows the electronic effect of the light scattering layer of TiO_2 microparticles. Chapters 4 to 7 discuss the effects of different organic coadsorbents and the control of dark current across the TiO_2-electrolyte junction. Chapters 8 and 9 present recent results with iodide-free electrolytes based on fast, one-electron relays. A chapter of general conclusions (Chapter 10) is then made on the basis of all previous sections and the implications to DSC are also discussed.

1.4 References to Chapter 1

[1]. Energy Information Administration, *International Energy Outlook 2006*, June 2006 (www.eia.doe.gov/oiaf/ieo/index.html).
[2]. BP, *Statistical Review of World Energy*, June 2006.
[3]. Grätzel, M. *Nature* **2001,** *414*, 338.
[4]. Andrews, E. A. *A Latin Dictionary*, p845; Clarendon Press, **1879**, Oxford.
[5]. Becquerel, A. E. *C. R. Acad. Sci. Paris* **1839**, *9*, 561.
[6]. Smith, W. *J. Soc. Telegraph Eng.* **1873**, *2*, 31.
[7]. Smith, W. *Nature* **1873**, *7*, 303.
[8]. Adams, W. G.; Day, R. E. *Proc. R. Soc. Lond. A* **1877**, *25*, 113.
[9]. Siemens, W. *Van Nostrand's Eng. Mag.* **1885**, *32*, 392.
[10]. Planck, M. *Ann. Phys.* **1901**, *4*, 553.
[11]. Einstein, A. *Ann. Phys.* **1905**, *17*, 132.
[12]. Goldmann, A.; Brodsky, J. *Ann. Phys.* **1914**, *44*, 849.
[13]. Schottky, W. *Physik. Z.* **1930**, *31*, 913.
[14]. Copeland, A. W.; Black, O. D.; Garrett, A. B. *Chem. Rev.* **1942**, *31*, 177.
[15]. Czochralski, J. *Z. Phys. Chem.* **1917**, *92*, 219
[16]. Audubert, R.; Stora, C. *Compt. rend.* **1932**, *194*, 1124
[17]. Fuller, C. **10-7-53**, Book #24863, Loc. 123-09-01, *AT&T Archives*, Warren, NJ.
[18]. Chapin, D. **1-26-54** & **2-23-54**, Book #29349, Loc. 124-11-02, *AT&T Archives*, Warren, NJ.
[19]. "Sunlight Converted to Electricity", Sunday Globe, **Aug. 19, 1973**, Boston.
[20]. Luque, A. IEEE International Symposium on Industrial Electronics, **2007**, Vigo, Spain.
[21]. Luque, A. *Prog. Photovoltaics.* **2001**, *9*, 303.
[22]. Adapted from www.nrel.gov/pv/thin_film/docs/kaz_best_research_cells.ppt. Recent data are from Green, M. A.; Emery, K.; King, D. L.; Hishikawa, Y.; Warta, W. *Prog. Photovoltaics.* **2007**, *15*, 35.
[23]. West, W. *Photogr. Sci. Eng.* **1974**, *18*, 35.
[24]. J. Moser, *Monatsch. Chem.* **1887**, *8*, 373.
[25]. Namba, S.; Hishiki, Y. *J. Phys. Chem.* **1965**, *69*, 774.
[26]. Nelson, R. C. *J. Phys. Chem.* **1965**, *69*, 714.

[27]. Bourdon J., *J. Phys. Chem.* **1965**, *69*, 705.

[28]. Gerischer, H.; Tributsch, H. *Ber. Bunsenges. Phys. Chem.* **1968**, *72*, 437.

[29]. Gerischer, H.; Tributsch, H. *Ber. Bunsenges. Phys. Chem.* **1969**, *73*, 251.

[30]. Gerischer, H. *Electroanal. Chem. Interfac. Electrochem.* **1975**, *58*, 263.

[31]. Tsubomura, H.; Matsumura, M.; Noyamaura, Y.; Amamyiya, T. *Nature* **1976**, *261*, 402.

[32]. Clark, W. D. K.; Sutin, N. *J. Am. Chem. Soc.* **1977**, *99*, 4676.

[33]. Anderson, S.; Constable, E. C.; Dare-Edwards, M. P.; Goodenough, J. B.; Hamnett, A.; Seddon, K. R.; Wright, R. D. *Nature*, **1979**, *280*, 571.

[34]. Gerischer, H. *Photochem. Photobiol.* **1972**, 16, 243.

[35]. Memming, R. *Photochem. Photobiol.* **1972**, 16, 325.

[36]. Fujishima, A.; Watanabe, T.; Tatsuoki, O.; Honda, K. *Chem. Lett.* **1975**, *4*, 13.

[37]. Jayadevaiah, T. S. *Appl. Phys. Lett.*, **1974**, *25*, 399.

[38]. Hamnett, A.; Dare-Edwards, M. P.; Wright, R. D.; Seddon, K. R.; Goodenough, J. B. *J. Phys. Chem.*, **1979**, *83*, 3280.

[39]. Dare-Edwards, M. P.; Goodenough, J. B.; Hamnett, A.; Seddon, K. R.; Wright, R. D. *Faraday Discuss. Chem. Soc.*, **1980**, *70*, 285.

[40]. Fujishima, A.; Honda, K. *Bull. Chem. Soc. Jap.*, **1971**, *44*, 1148.

[41]. Fujishima, A.; Honda, K. *Nature*, **1972**, *238*, 37.

[42]. Duonghong, D.; Serpone, N.; Grätzel, M. *Helv. Chim. Acta*, **1984**, *67*, 1012.

[43]. DeSilvestro, J.; Grätzel, M.; Kavan, L.; Moser, J.; Augustynski, J. *J. Am. Chem. Soc.*, **1985**, *107*, 2988.

[44]. Vlachopoulos, N.; Liska, P.; Augustynski, J.; Grätzel, M. *J. Am. Chem. Soc.*, **1988**, *110*, 1216.

[45]. O'Regan B.; Grätzel, M. *Nature*, **1991**, *353*, 737.

[46]. Nazeeruddin, M. K.; Kay, A.; Rodicio, I.; Humphry-Baker, R.; Müller, E.; Liska, P. ; Vlachopoulos N.; Grätzel, M. *J. Am. Chem. Soc.* **1993**, *115*, 6382.

[47]. Nazeeruddin, M. K.; Pechy, P.; Grätzel, M. *Chem. Commun.*, **1997**, 1075.

[48]. Bach, U.; Lupo, D.; Comte, P.; Moser, J. E.; Weissortel, F.; Salbeck, J.; Spreitzer, H.; Grätzel, M. *Nature*, **1998**, *395*, 583.

[49]. Grätzel, M. *MRS Bull.* **2005**, *30*, 23.

[50]. Wang, P.; Zakeeruddin, S. M.; Moser, J. E.; Nazeeruddin, M. K; Sekiguchi, T.; Grätzel, M. *Nat. Mater.*, **2003**, *2*, 402.

[51]. Wang, P.; Klein, C.; Humphry-Baker, R.; Zakeeruddin, S. M.; Grätzel, M. *J. Am. Chem. Soc.* **2005**, *127*, 808.

[52]. Kuang, D. B.; Wang, P.; Ito, S.; Zakeeruddin, S. M; Grätzel, M. *J. Am. Chem. Soc.* **2006**, *128*, 7732.

[53]. Kuang, D.; Klein, C.; Ito, S.; Moser, J. E.; Humphry-Baker, R.; Evans, N.; Duriaux, F.; Grätzel, C.; Zakeeruddin, S. M.; Grätzel, M. *Adv. Mater.*, **2007**, *19*, 1133.

[54]. Gregg, B. A.; Hanna, M. C. *J. Appl. Phys.*, **2003**, *93*, 3605.

[55]. Gregg, B. A. *J. Phys. Chem. B*, **2003**, *107*, 4688.

[56]. Peter L. M. *J. Phys. Chem. C*, **2007**, *111*, 6601.

[57]. Grätzel, M. *Chem. Lett.* **2005**, *34*, 8

[58]. Barbé, C. J.; Arendse, F.; Comte, P.; Jirousek, M.; Lenzmann, F.; Shklover, V.; Grätzel, M. *J. Am. Ceram. Soc.* **1997**, *80*, 3157.

[59]. IUPAC Compendium of Chemical Terminology, Electronic version,

http://goldbook.iupac.org/R05419.html.

[60]. Ito, S.; Liska, P.; Comte, P.; Charvet, R. L.; Pechy, P.; Bach, U.; Schmidt-Mende, L.; Zakeeruddin, S.M.; Kay, A.; Nazeeruddin, M. K.; Grätzel, M. *Chem. Commun.* **2005**, 4351.

[61]. Hagfeldt, A.; Grätzel, M. *Chem. Rev.* **1995**, *95*, 49.

[62]. Grätzel, M. *Prog. Photovoltaics.* **2000**, *8*, 171.

[63]. Barolo, C.; Nazeeruddin, M. K; Fantacci, Simona; Di Censo, D.; Comte, P.; Liska, P.; Viscardi, G.; Quagliotto, P.; Filippo De Angelis; Ito, S.; Grätzel, M. *Inorg. Chem.* **2006**, *45*, 4642.

[64]. Watson, D.; Meyer, G. *Annu. Rev. Phys. Chem.* **2005**, *56*, 119.

[65]. Anderson, N.; Lian, T. *Annu. Rev. Phys. Chem.* **2005**, *56*, 491.

[66]. Gerischer H. *Surf. Sci.* **1969**, *18*, 97.

[67]. Marcus R. A. *J. Chem. Phys.* **1956**, *24*, 966.

[68]. Marcus R. A. *Annu. Rev. Phys.Chem.* **1964**, *15*, 155.

[69]. Tachibana, Y.; Moser, J. E.; Grätzel, M.; Klug, D. R.; Durrant, J. R. *J. Phys. Chem.* **1996,** *100*, 20056-20062.

[70]. Rehm J. M., McLendon G. L., Nagasawa Y., Yoshihara K., Moser J., Grätzel, M. *J. Phys. Chem.* **1996**, *100*, 9577.

[71]. Hannappel, T.; Burfeindt, B.; Storck, W.; Willig, F. *J. Phys. Chem. B* **1997,** *101*, 6799.

[72]. Ellingson, R. J.; Asbury, J. B.; Ferrere, S.; Ghosh, H. N.; Sprague, J. R.; Lian, T. Q.; Nozik, A. J. *J. Phys. Chem. B* **1998,** *102*, 6455.

[73]. Das, S.; Kamat, P. V. *J. Phys. Chem. B* **1998,** *102*, 8954.

[74]. Durrant, J. R.; Tachibana, Y.; Mercer, I.; Moser, J. E.; Grätzel, M.; Klug, D. R. *Z. Phys. Chem.* **1999,** *212*, 93.

[75]. Asbury, J. B.; Ellingson, R. J.; Ghosh, H. N.; Ferrere, S.; Nozik, A. J.; Lian, T. Q. *J. Phys. Chem. B* **1999,** *103*, 3110.

[76]. Heimer, T. A.; Heilweil, E. J.; Bignozzi, C. A.; Meyer, G. J. *J. Phys. Chem. A* **2000,** *104*, 4256.

[77]. Tachibana, Y.; Haque, S. A.; Mercer, I. P.; Durrant, J. R.; Klug, D. R. *J. Phys. Chem. B* **2000,** *104*, 1198.

[78]. Asbury, J. B.; Hao, E.; Wang, Y. Q.; Ghosh, H. N.; Lian, T. Q. *J. Phys. Chem. B* **2001,** *105*, 4545.

[79]. Tachibana, Y.; Haque, S. A.; Mercer, I. P.; Moser, J. E.; Klug, D. R.; Durrant, J. R. *J. Phys. Chem. B* **2001,** *105*, 7424.

[80]. Kallioinen, J.; Benkö, G.; Sundström, V.; Korppi-Tommola, J. E. I.; Yartsev, A. P. *J. Phys. Chem. B* **2002,** *106*, 4396.

[81]. Kuciauskas, D.; Monat, J. E.; Villahermosa, R.; Gray, H. B.; Lewis, N. S.; McCusker, J. K. *J. Phys. Chem. B* **2002,** *106*, 9347.

[82]. Tachibana, Y.; Nazeeruddin, M. K.; Grätzel, M.; Klug, D. R.; Durrant, J. R. *Chem. Phys.* **2002,** *285*, 127.

[83]. Benkö, G.; Kallioinen, J.; Korppi-Tommola, J. E. I.; Yartsev, A. P.; Sundström, V. *J. Am. Chem. Soc.* **2002,** *124*, 489.

[84]. Chergui, M., *ChemPhysChem* **2002,** *8*, 713.

[85]. Benkö, G.; Myllyperkiö, P.; Pan, J.; Yartsev, A. P.; Sundström, V. *J. Am. Chem. Soc.* **2003,** *125*, 1118.

[86]. Asbury, J. B.; Anderson, N. A.; Hao, E. C.; Ai, X.; Lian, T. Q. *J. Phys. Chem. B* **2003,** *107*, 7376.

[87]. Anderson, N. A.; Ai, X.; Lian, T. *J. Phys. Chem. B* **2003,** *107*,14414.

[88]. Benkö, G.; Kallioinen, J.; Myllyperkiö, P.; Trif, F.; Korppi-Tommola, J. E. I.; Yartsev, A. P.; Sundström, V. *J. Phys. Chem. B* **2004,** *108*, 2862.

[89]. Kallioinen, J.; Benkö, G.; Myllyperkiö, P.; Khriachtchev, L.; Skårman, B.; Wallenberg, R.; Tuomikoski, M.; Korppi-Tommola, J.; Sundström, V.; Yartsev, A. P. *J. Phys. Chem. B* **2004,** *108*, 6365.

[90]. Wenger, B.; Grätzel, M.; Moser, J. *J. Am. Chem. Soc.* **2005**, *127*, 12150.

[91]. Wenger, B.; Grätzel, M.; Moser, J. E. *Chimia* **2005**, *59*, 123.

[92]. Wenger, B. École Polytechnique Fédérale de Lausanne, **2006**, thesis *No. 3447*.

[93]. Albery, W. J.; Bartlett, P. N. *J. Electrochem. Soc*. **1984**, *131*, 31.

[94]. Peter, L. M.; Vanmaekelbergh, D. *Adv. Electrochem. Sci. Eng.*, **1999**, *6*, 77.

[95]. Peter, L. M. *Phys. Chem. Chem. Phys.* **2007**, *9*, 2630.

[96]. Solbrand, A.; Lindström, A.; Rensmo, H.; Hagfeldt, A.; Lindquist, S. E. *J. Phys. Chem. B* **1997,** *101*, 2514.

[97]. Tirosh, S.; Dittrich, T.; Ofir, A.; Grinis, L.; Zaban, A. *J. Phys. Chem. B* **2006**, *110*, 16165.

[98]. Schlichthörl, G.; Park, N. G.; Frank, A. J. *Z. Phys. Chem.***1999**, *212*, 45.

[99]. Duffy, N. W.; Peter, L. M.; Wijayantha, K. G. U. *Electro. Commun.* **2000**, *2*, 262

[100]. Fisher, A. C.; Peter, L. M.; Ponomarev, E. A.; Walker, A. B.; Wijayantha, K. G. U. *J. Phys. Chem. B* **2000**, *104*, 949.

[101]. Savenije, T. J.; de Haas, M. P.; Warman, J. M. *Z. Phys. Chem.* **1999**, *212*, 201.

[102]. Bisquert, J.; Zaban, A.; Salvador, P. *J. Phys. Chem. B* **2002**, *106*, 8774.

[103]. Huang, S. Y.; Schlichthorl, G.; Nozik, A. J.; Grätzel, M.; Frank, A. J. *J. Phys. Chem. B* **1997**, *101*, 2576.

[104]. Duffy, N. W.; Peter, L. M.; Rajapakse, R. M. G.; Wijayantha, K. G. U. *J. Phys. Chem. B* **2000**, *104*, 8916.

[105]. Kruger, J.; Plass, R.; Grätzel, M.; Cameron, P. J.; Peter, L. M. *J. Phys. Chem. B* **2003**, *107*, 7536.

[106]. Bisquert, J.; Vikhrenko, V. S. *J. Phys. Chem. B* **2004**, *108*, 2313.

[107]. Kopidakis, N.; Neale, N. R.; Zhu, K.; van de Lagemaat, J.; Frank, A. J. *Appl. Phys. Lett.* **2005**, *87*.

[108]. Cazzanti, S.; Caramori, S.; Argazzi, R.; Elliott, C.M.; Bignozzi, C.A. *J. Am. Chem. Soc.* 2006, *128*, 9996

[109]. Nusbaumer, H.; Zakeeruddin, S. M.; Moser, J.-E.; Grätzel, M. *Chem. Eur.J.* 2003, *9*, 3756.

[110]. Grätzel, M. *J. Photochem. Photobio. A* **2004**, 164, 3.

[111]. Y. Chiba, A. Islam, Y. Watanabe, R. Komiya, N. Koide, L. Han, *Jap. J. Appl. Phys. Part 2: Lett. & Express Lett.* **2006**, *45*, L638-L640.

[112]. Wang, P.; Klein, C.; Humphry-Baker, R.; Zakeeruddin, S. M.; Grätzel, M. *Appl. Phys. Letts.* **2005**, *86*, 123508.

[113]. Kuang, D.; Klein, C.; Ito, S.; Moser, J. E.; Humphry-Baker, R.; Zakeeruddin, S. M.; Grätzel, M. *Adv. Func. Mater.* **2007**, *17*, 154.

[114]. Wasserscheid, P.; Welton, T. *Ionic Liquids in Synthesis*; Wiley: Weinheim, Germany, 2002.

[115]. Dogers, R. D.; Seddon, K. R. *Science* **2003**, *302*, 792.

[116]. Dupont, J.; de Souza, R. F.; Suarez, P. A. Z. *Chem. Rev*. **2002**, *102*, 3667.

[117]. Xu, W.; Angell, C. A. *Science* **2003**, *302*, 422.

[118]. Kubo, W.; Murakoshi, K.; Kitamura, T.; Wada, Y.; Hanabusa, K.; Shirai, H.; Yanagida, S. *Chem. Lett*. **1998**, *27*, 1241.

[119]. Kubo, W.; Kambe, S.; Nakade, S.; Kitamura, T.; Hanabusa, K.; Wada, Y.; Yanagida, S. *J. Phys. Chem. B,* **2003**, *107,* 4374.

[120]. Wang, P.; Zakeeruddin, S. M.; Exnar, I.; Grätzel, M. *Chem. Commun.* **2002**, 2972.

[121]. Cao, F.; Oskam, G.; Searson, P. C. *J. Phys. Chem*., **1995**, *99*, 17071.

[122]. Wang, P.; Zakeeruddin, S. M.; Comte, P.; Exnar, I.; Grätzel, M. *J. Am. Chem. Soc.*, **2003**, *125*, 1166.

[123]. Nogueira, A. F.; Durrant, J. R.; De Paoli, M. A. *Adv. Mater.* **2001**, *13,* 826.

[124]. Longo, C.; Nogueira, A. F.; De Paoli, M.; Cachet, H. *J. Phys. Chem. B* **2002**, *106*, 5925.

[125]. Wang, P.; Dai, Q.; Zakeeruddin, S. M.; Forsyth, M.; MacFarlane, D. R.; Grätzel M. *J. Am. Chem. Soc.* **2004**, *126*, 13590.

[126]. Desilvestro, J.; Grätzel, M.; Kaven, L.; Moser, J. *J. Am. Chem. Soc.* **1985**, *107*, 2988.

[127]. Oskam, G.; Bergeron, B. V.; Meyer, G. J.; Searson, P. C. *J. Phys. Chem. B* **2001**, *105*, 6867.

[128]. Wang, P.; Zakeeruddin, S. M.; Moser, J.; Humphry-Baker, R.; Grätzel, M. *J. Am. Chem. Soc.* **2004**, *126*, 7164.

[129]. Gregg, B. A.; Pichot, F.; Ferrere, S.; Fields, C. R. *J. Phys. Chem. B* **2001**, *105*, 1422.

[130]. Gregg, B. A. *Coord. Chem. Rev*. **2004**, *248*, 1215.

[131]. Argazzi, R.; Bignozzi, C. A.; Heimer, T. A.; Castellano, F. N.; Meyer, G. J. *J. Phys. Chem. B* **1997**, *101*, 2591.

[132]. Nusbaumer, H.; Moser, J.-E.; Zakeeruddin, S. M.; Nazeeruddin, M. K.; Grätzel, M. *J. Phys. Chem. B* 2001, *105*, 10461.

[133]. Nusbaumer, H.; Zakeeruddin, S. M.; Moser, J.-E.; Grätzel, M. *Chem. Eur.J.* 2003, *9*, 3756.

[134]. Sapp, S. A.; Elliott, C. M.; Contado, C.; Caramori, S.; Bignozzi, C. A. *J. Am. Chem. Soc.* 2002, *124*, 11215

[135]. Cazzanti, S.; Caramori, S.; Argazzi, R.; Elliott, C.M.; Bignozzi, C.A. *J. Am. Chem. Soc.* 2006, *128*, 9996.

[136]. O'Regan, B.; Lenzmann, F. *J. Phys. Phys. Chem. B* **2004**, *108*, 4342.

[137]. O'Regan, B.; Lenzmann, F.; Muis, R.; Wienke, J. *Chem. Mater.* **2002**, *14*, 5023.

[138]. O'Regan, B.; Schwartz, D. T.; Zakeeruddin, S. M.; Grätzel, M. *Adv. Mater*. **2000**, *12*, 1263.

[139]. Taguchi, T.; Zhang, X. T.; Sutanto, I.; Tokuhiro, K.; Rao, T. N.; Watanabe, H.; Nakamori, T.; Uragami, M.; Fujishima, A. *Chem. Comm.* **2003**, 2480.

[140]. Konno, A.; Kitagawa, T.; Kida, H.; Kumara, G. R. A.; Tennakone, K. *Cuur. Appl. Phys*. **2005**, *5*, 149.

[141]. Kumara, G. R. A.; Konno, A.; Shiratsuchi, K.; Tsukahara, J.; Tennakone, K. *Chem. Mater.* **2002**, *14*, 954.

[142]. Snaith, H.; Zakeeruddin, S. M.; Wang, Q.; Pechy, P.; Grätzel, M. *Nano Lett*, **2006**, *6*, 2000.

[143]. Gebeyehu, D.; Brabec, C. J.; Sariciftci, N. S. *Thin Solid Film*, **2002**, *403-404*, 271.

[144]. Tan, S.; Zhai, J.; Wan, M.; Meng, Q.; Li, Y.; Jiang, L.; Zhu, D. *J. Phys. Chem. B,* **2004**, *108*, 18693.

[145]. Kruger, J.; Plass, R.; Grätzel, M.; Cameron, P. J.; Peter, L. M. *J. Phys. Chem. B* **2003**, *107,* 7536.

[146]. Schmidt-Mende, L.; Kroeze, J. E.; Durrant, J. R.; Nazeeruddin, M. K.; Grätzel, M. *Nano Lett,* **2005**, *5*, 1315.

[147]. Kay, A.; Grätzel, M. *Sol. Energy Mater. Sol. Cells* **1996**, *44*, 99.

[148]. Lindstrom, H.; Holmberg, A.; Magnusson, E.; Lindquist, S. E.; Malmqvist, L.; Hagfeld, A. *Nano Lett.* **2001**, *1*, 97.

[149]. Imoto, K.; Takatashi, K.; Yamaguchi, T.; Komura, T.; Nakamura, J.; Murata, K. *Sol. Energy Mater. Sol. Cells*, **2003**, *79*, 459.

[150]. Murakami, T. N.; Ito, S.; Wang, Q.; Nazeeruddin, M. K.; Bessho, T.; Cesar, I.; Liska, P.; Humphry-Baker, R.; Comet, P.; Pechy, P.; Grätzel, M. *J. Electro. Soc.* **2006**, *153*, A2255.

[151]. Suzuki, K.; Yamamoto, M.; Kumagai, M.; Yanagida, S. *Chem. Lett.* **2003**, *32*, 28.

[152]. Saito, Y.; Kitamura, T.; Wada, Y.; Yanagida, S. *Chem. Lett.*, **2002**, *31*, 1060.

[153]. Saito, Y.; Kubo, W.; Kitamura, T.; Wada, Y.; Yanagida, S. *J. Photochem. Photobiol. A* **2004**, *164*, 153.

[154]. Nusbaumer, H. École Polytechnique Fédérale de Lausanne, **2004**, thesis *No. 2955*.

2. Experimental Methods and Device Preparation

The chapter describes the relevant theoretic and experimental issues of device preparation, characterization and analysis in this work. Details of glass substrates, mesoscopic TiO_2 pastes, sensitizers, electrolytes and counter electrodes are shown in the first part, as well as the assembling procedure of the whole device. In the second part, setups and theories of spectroscopic methods such as photovoltaic current-voltage characterization, electrochemical measurements, phototransient voltage and current decay experiments, electrochemical impedance spectroscopy (EIS) are explained.

2.1 Materials and Reagents

2.1.1 Conductive glass

Highly fluorine-doped transparent conducting oxide (TCO) films deposited on glass plates (SnO_2:F) were purchased from either Nippon Sheet Glass (NSG, Solar) or Pilkington (TEC-8, TEC-15), distributed in Switzerland by Hartford. The parameters of both substrates are listed in Table 2.1.

Table 2.1 Parameters of TCO substrates used for fabricating DSC devices. Values are provided by the producers of the respective TCO substrates.

Sample name	Resistance (Ω / □)	T550 (%) [a]	Thickness (mm)
NSG	~10	90	4
TEC-8	8	80	3
TEC 15	15	82	2.3

a. Transmission at 550 nm

NSG showed an excellent transmission of ≥90% from 380 nm to 800 nm. A close to unity transmission at 550 nm was observed with the aid of anti-reflective coatings.[1] Considering this excellent transparency, NSG was normally used for device fabrication.

2.1.2 Precursor solutions for compact TiO_2 deposition

A thin compact TiO_2 layer was deposited on FTO substrate when necessary. The layer was prepared by spray pyrolysis with 0.02 M precursor solution of diisopropoxy-titaniumbis(acetylacetonate) (DPTAA, Aldrich) in ethanol.

2.1.3 Preparation of mesoscopic TiO_2 pastes

TiO_2 pastes for nanocrystalline transparent layers were synthesized by P. Comte, LPI, EPFL by the reported sol-gel process.[2] This involved hydrolysis of $Ti(OCH(CH_3)_2)_4$ in water at 250 ℃ (70 atms) for 12 hours, followed by conversion of the water to ethanol by three-times centrifugation and the exchange of ethanol with α-terpineol by sonication and evaporation. The particle size was around 20 nm and the porosity of the paste was 0.68. This paste was found to have the best performance in DSCs and always be used as a standard condition for evaluating new systems. In combination with this paste, a light diffusive paste was often employed in order to enhance the light absorption via multiple scattering. The diffusive paste was prepared by a similar procedure with the TiO_2 anatase particles (400 nm in diameter) from Catalysts & Chemicals Ind. Co. Ltd. (CCIC), Japan.

To study the particle size effect in one-electron transfer redox system, we further made TiO_2 pates with particles of 30 nm and 60nm in diameter. The procedure is illustrated in Figure 2.1. The 30 and 60 nm TiO_2 particles were from Showa Denko K.K., Japan. Liquids were added drop by drop into the mortar during the preparation. The ultrasonic homogenization was performed with using a Ti-horn-equipped sonicator (Vibra cell 72408, Bioblock scientific). Anhydrous terpineol (Fluka) and the mixture solution of two ethyl celluloses in ethanol were added, followed by stirring and sonication. The contents of the dispersion were concentrated by evaporator at 35 ℃. The pressure was evacuated until 10 mbar. The pastes were finalized with a three-roller-mill grinder (EXAKT).[3]

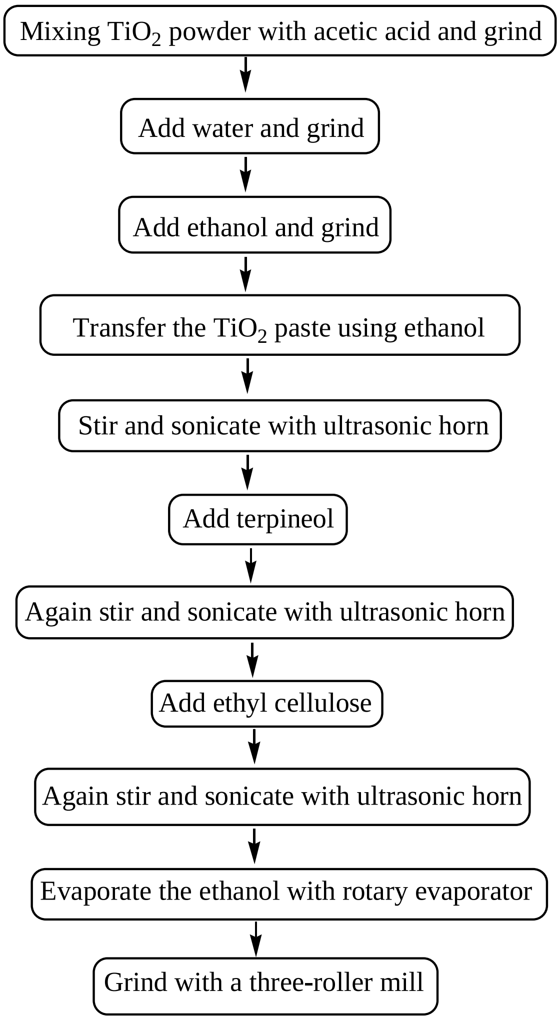

Figure 2.1 Preparation scheme of screen-printing paste TiO_2 from Showa Denko particles.

2.1.4 Chemicals

Unless otherwise specified, all the chemicals (puriss. grade) were of puriss quality and purchased from Fluka or Aldrich.

Common solvents, such as acetonitrile (AcCN) and methoxypropionitrile (MPN) were distilled before use to remove water.

As the iodide source, 1-methyl-3-propylimidazolium iodide (PMII) was prepared according to the literature method [4] and its purity was confirmed by ^1H NMR spectrum.

N-methylbenzimidazole (NMB) was purchased from Aldrich and recrystallized from diethyl ether before use. N-butylbenzimidazole (NBB) was synthesized in our lab by Dr. Evans and used as received.

Guanidinoacetic acid, 4-guanidinobutyric acid and 6-guanidinohexanoic acid were purchased from Fluka. Due to the poor solubility of ω-guanidinoalkyl acid zwitterions in the dye solvent mixture (acetonitrile / *tert*-butyl alcohol, volume ratio of 1:1), hydrochloric acid was added to an aqueous solution of these compounds till pH = 2.5 to yield guanidinoacetic acid hydrochloride (GAAHCl), 4-guanidinobutyric acid hydrochloride (GBAHCl) and 6-guanidinohexanoic acid hydrochloride (GHAHCl). 3-Guanidinopropylphosphonic acid was prepared according to the literature method [5] and treated with an equimolar amount of aqueous tetrabutylammonium hydroxide to give tetrabutylammonium 3-guanidinopropylphosphonate (GPA).

2-[2,2';5',2"]Terthiophen-5-ylmethylene-malonic acid (3TMMA) was synthesized by Professor Officer's Group in New Zealand.

2.1.4 Preparation of mesoscopic TiO_2 electrodes

FTO glass was first cut to plates of 3.5 cm × 10 cm dimension and cleaned in a detergent solution using an ultrasonic bath for 15 min, and then rinsed with water and ethanol. After treatment in a UV-O_3 system (Model No. 256-220, Jelight Company, Inc.) for 20 min, a layer of paste was coated on the FTO glass plates by screen printing (90T, Estal Mono, Schweiz. Seidengazefabrik AG Thal), kept in a clean box for 3 min with ethanol so that the paste could relax to reduce the surface irregularity, and then dried for 6 min at 125 ℃. The screen-printing procedure (with coating, storing and drying) was repeated to the desired thickness if needed. For the double-layer electrode, the second layers of diffusive paste for the light-scattering layer were deposited by screen printing to 4-5 µm thickness. A double-layer film denoted as "7+5" simply meant the film comprised a 5-µm-thick layer of light-scattering particles on top of a 7-µm-thick layer of 20-nm-sized TiO_2 nanoparticles. This "7+5" film was the state-to-art configuration and all the experiments were performed with this film unless otherwise specified. The electrodes coated with the TiO_2 pastes were gradually heated under an air flow at 325 ℃ for 5 min, at 375 ℃ for 5 min, at 450 ℃ for 15 min and 500 ℃ for 15 min. The as-prepared film was then processed with a $TiCl_4$ treatment, immersing it into a 40 mM $TiCl_4$ aqueous solution for 30 min, to give the final TiO_2 electrodes.

2.1.5 Sensitizers

Heteroleptic ruthenium bipyridyl complexes were used as the sensitizers in this work. These molecules were synthesized and purified by Dr. Zakeeruddin in our lab.[6]-[8] Table 2.1 lists the molecular formula and short codes for these sensitizers (See Appendix I for the structures).

Table 2.1 Ruthenium sensitizers

Code	Molecular formula
Z-907	NaRu (4-carboxylic acid-4'-carboxylate-2,2'-bipyridine)(4,4'-dinonyl-2,2'-bipyridine)$(NCS)_2$
K-19	Ru (4,4'-dicarboxylic acid-2,2'-bipyridine)(4,4'-bis(p-hexyloxystyryl)-2,2'-bipyridine)$(NCS)_2$
K-51	NaRu(4-carboxylic acid-4'-carboxylate-2,2'-bipyridine)(4,4'-bis[(triethylene glycol methyl ether) methyl ether]-2,2'-bipyridine)$(NCS)_2$
K-73	Ru (4,4'-dicarboxylic acid-2,2'-bipyridine)(4,4'-bis(p-methoxystyryl)-2,2'-bipyridine)$(NCS)_2$
Z-973	NaRu (4,4'-dicarboxylic acid-2,2'-bipyridine)(4,4'-dinonyl-2,2'-bipyridine)$(CN)_2$

Some organic sensitizers with a high molar extinction coefficient were also employed when enhanced light absorption was needed. Indoline sensitizers coded as D-102 and D-149 were provided by Prof. Uchida at University of Tokyo and used as received. The structures of these sensitizers are shown in Figure 2.2.

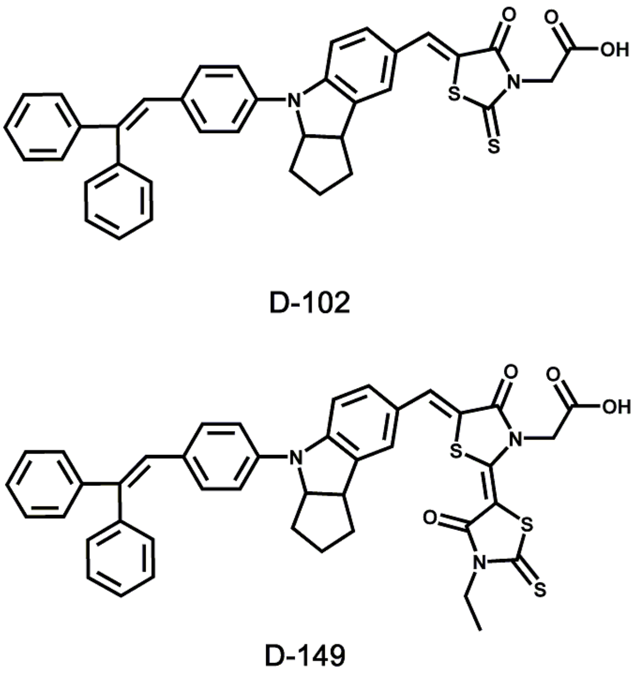

D-102

D-149

Figure 2.2 Structures of indoline sensitizers used in this work.

2.1.6 Molecules as redox mediators

For studying alternative redox systems, several series of organic molecules were investigated, including derivatives of triarylamine, phenoxazine, piperidinyloxy and tetrathiafulvalene. *N*-(methoxyethoxyethyl)-phenoxazine (MEEP), *N*-(methoxyethoxyethyl)-3,7-dimethoxy-phenoxazine (MeOMEEP), *N*-(methoxyethoxyethyl)-3, 7-dibromo-phenoxazine (BrMEEP), *N*-(methoxyethoxy ethyl)-3-methyl-phenoxazine (MeMEEP), and *N*-(methoxyethoxyethyl)-3,7-dimethyl-phenoxazine (DMeMEEP) were synthesized by Dr. Evans at LPI. 2,2,6,6-tetramethyl-1-piperidinyloxy (TEMPO) and 2,2,6,6-tetramethyl-4-methoxy-1-piperidinyloxy (MeOTEMPO) were purchased from Fluka. Tetrathiafulvalene (TTF) and bis(4,5-dihydro naphtho[1,2-*d*])tetrathiafulvalene (BDHN-TTF) were bought from Aldrich and used as received.

2.2 Device fabrication

2.2.1 Photoanodes

FTO was used as the support for TiO_2 photoanodes. The most commonly used electrodes were of a double layer configuration, a nanocrystalline TiO_2 particle layer for ample dye adsorption and a larger TiO_2 particle light scattering layer for better light harvesting. Due to the high doping level and metallic behavior of FTO substrate, electron transfer may take place between FTO and redox couple in the electrolyte and shant the device. Thus, a TiO_2 compact layer between FTO and TiO_2 nanoporous layer might be necessary to block this reaction. Fortunately, I^-/I_3^- was known to have very slow electron transfer processes on FTO and the direct contact with FTO did not cause a big effect on photovoltaic parameters of the device (There are still debates about this issue, however, experimentally, this compact layer has not produced significant improvements in efficiency with I^-/I_3^- electrolytes [9]). While for studying one-electron alternative redox couples, the compact TiO_2 layer was essential, due to the considerably large exchange current densities of these couples on FTO (in the range of several mA cm^{-2}), and thus present in all the photoanodes used.

To prepare the TiO_2 underlayer, spray-pyrolyzed TiO_2 was deposited by a published process.[10] Briefly, 0.02 M precursor solution of DPTAA in ethanol was sprayed through the nozzle at a distance of about 20 cm over the conducting glass surface that was heated and maintained at 450 °C on a temperature-controlled hotplate. Oxygen was used as the carrier gas to improve the reproducibility.[11] Glass slides were used as the mask to protect the fringe of FTO surfaces so that the surface where collecting contact was made would not be covered by compact TiO_2. The treated glass plates were further fired at 450 °C for another 30 min to remove remaining organic traces after underlayer deposition. After it cooled to room temperature, different nanocrystalline TiO_2 pastes were then screen-printed onto the underlayer coated FTO, following the procedure discussed in Section **2.1.4**, to give the final electrodes. Table 2.2 shows the physical parameters of different TiO_2 paste used in this work. The roughness factor (*RF*) of the photoelectrodes was calculated by Eq. 2.1

$$RF = (1 - p) * d_{\mathrm{TiO_2}} * SSA \qquad (2.1)$$

where p stands for the porosity of the film, *SSA* is the specific surface area and the density of TiO_2 equals 3.84 g cm^{-3}.

Table 2.2 Characteristics of different nanocrystalline TiO_2 layers after $TiCl_4$ treatment

Name	Porosity	Particle diameter (nm)	*SSA* (m^2 g^{-1})	*RF* (μm^{-1})
Standard	0.56	18.3	79.7	138 ± 2
HPW 400c	0.67	400	27.1	35 ± 1
F2	0.53	60	35.7	65
F4 [a]	0.64	30	57.6	81

a. This was measured before $TiCl_4$ treatment

Photovoltaic experiments in this work were conducted by using the above mentioned layers (or their combinations) and these conditions will be specified in relevant experiments.

2.2.2 Sensitization

To achieve sensitization, the TiO_2 electrode was first sintered at 500 °C for 25 minutes and naturally cooled to 80 °C. Then it was immersed into the 0.3 mM dye solution in acetonitrile/*tert*-butyl alcohol mixture (Volume to volume ratio of 1:1) at room temperature for 12 h. The dyed film was then taken out from the dye solution, rinsed with acetonitrile to remove loosely anchored sensitizer on TiO_2 surface and dried in a box with continuous dry air flows.

2.2.3 Counter electrode and electrolytes

Counter electrodes were prepared by thermal decomposition of platinum precursor. Usually, a drop of 5 to 10 mM solution of hexacholorplatinic(IV) acid hexahydrate in anhydrous isopropanol was put on clean FTO substrate, spread with pipette and dried in air. Coated electrodes were heated with fire gun to a temperature of 385 °C and stabilized at the temperature for 15 min. It was then gradually cooled to room temperature. The obtained counter electrode was optically transparent and of highly dispersed platinum particles for catalyzing I^-/I_3^- redox reaction.

Electrolytes were prepared by dissolving/mixing different components in the solvent. Mainly, AcCN and MPN were used as the solvent. Based on the volatility of the solvent, electrolytes were classified as volatile (AcCN solvent) and nonvolatile (MPN solvent). Generally, apart from the redox couples, NMB or NBB was added to increase the open-circuit voltage of the device. LiTFSI was incorporated in non-iodine electrolytes to enhance the charge collection efficiency. Detailed composition of each electrolyte can be found in pertinent parts where its photovoltaic performance is reported.

2.2.4 Device assembly

All cells were carefully sealed before photoelectrochemical measurement. The sensitized photoanodes and the counter electrode were separated by a 25-µm-thick Surlyn® or 35-µm-thick Bynel® hot-melt ring (DuPont, USA) and sealed by heating. The internal space was evacuated, then filled with electrolyte through a filling hole made by a sandblasting drill on the counter electrode glass substrate. The electrolyte introduction hole was subsequently sealed with a Bynel sheet under a thin glass cover by heating. Finally, tin was deposited on the FTO surface to make the contact and reduce the series resistance of the device. The whole fabrication process is illustrated in Figure 2.3.

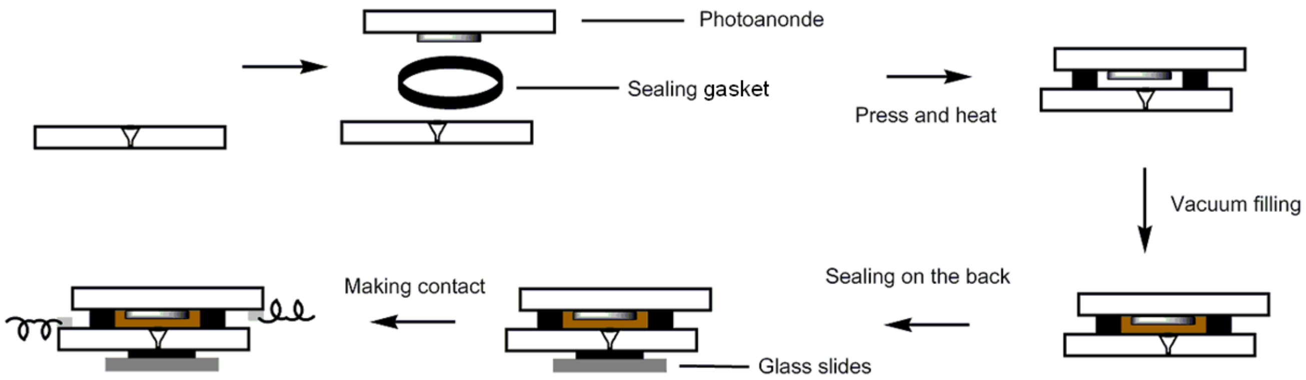

Figure 2.3 Flow chart of device assembly.

2.2.5 Device storage for stability experiment

Some of experiments in this work demanded a long term stability test under thermal stress. Two kinds of conditions were adopted: for moderate thermal stress under visible light soaking experiments, the cells were kept at 60 °C, covered with a 50 µm-thick polyester film (Preservation Equipment Ltd, UK) as a UV cutoff filter (below 400 nm) and irradiated at open circuit under a Suntest CPS plus lamp (ATLAS GmbH, 100 mW cm^{-2}, 60 °C). This procedure was referred as “60 °C light soaking” process. Or else, cells might be kept at 80 °C in the oven in darkness, a procedure denoted as “80 °C aging” process. In both cases, cells were taken from the solar simulator or the oven at a weekly interval to monitor the evolution of photovoltaic parameters. If the cell maintained 90 % of its initial efficiency after a 1,000 hour test under one of the above mentioned conditions, it was regarded as a stable cell under that condition.

For non-iodide electrolytes, some cells were also stored at room temperature in the dark drawer. This will be specified wherever stability of these electrolytes is discussed.

2.3 Electrochemical Measurements

Cyclic voltammetry measurements were performed on a computer-controlled Autolab P20 electrochemical workstation (Eco Chimie, Netherlands) in combination with a conventional three-electrode, one-compartment electrochemical cell. The working electrode was usually a Pt disk, paired with an Ag disk as the counter electrode. In the cases when a dye-coated nanocrystalline TiO_2 film was used as the working electrode, a clean FTO glass was then employed as the reference electrode. Ag/AgCl reference electrode was used as the reference and it was calibrated by measuring the redox potential of ferrocene dissolved in the solvent and the redox potentials were converted to those versus a normal hydrogen electrode (NHE) reference scale always by adding a constant of 0.55 V.[12] The only exception was in one of our earlier pubilications,[13] i.e. Chapter 4, where a reference value of 0.67 V was used (We made no correction so as to preserve the intactness of the publication, however, more importantly, the simple variation in choosing the reference value would not change the comparison and experimental conclusions in the chapter). The supporting electrolyte was 0.1 M tetrabutylammonium tetrafluoroborate (TBATBF) solution in acetonitrile.

To determine the half wave potential of the redox couples, differential pulse voltammetry was used. The voltage interval and amplitude was set as 0.001 V and 10 mV, respectively. The potential was first expressed against the ferrocene/ferrocium redox scale and then converted to NHE scale.

For measuring diffusion coefficient and flux of the redox species, a 5.0 μm radius Pt ultramicroelectrode (Bioanalytical Systems, MF-2005),was used as working electrode and a Pt foil as counter electrode. The apparent diffusion coefficient D_{app} was related to the steady current I_{ss} by Eq. 2.2,

$$I_{ss} = 4ncr_aFD_{app} \tag{2.2}$$

where n is the electron-transfer number per molecule, F is the Faraday constant, c is the bulk concentration of electroactive species and r_{a} is the radius of the microelectrode. Alternatively, D_{app} can also be determined by measuring the peak current during the forward sweep of the first cycle at different scan rates. For reversible redox couples, The peak current, i_{p}, was directly proportional to the square root of the scan rate, $\nu^{1/2}$, as described by the Randles-Sevcik equation (Eq. 2.3),

$$i_p = 2.69\ \times\ 10^5 n^{3/2} A D_{app} c \nu^{1/2} \tag{2.3}$$

where i_{p} is peak current in A, A is the electrode area in cm^2, D_{app} is in cm^2 s^{-1}, c is the concentration in mol cm^{-3} and v is scan rate in V s^{-1}.

Electrochemical impedance spectroscopy (EIS) was performed with a computer controlled potentiostat (EG&G, Model 273) equipped with a frequency response analyzer (EG&G, Model 1025). The frequency range was usually 0.005-100 KHz and the magnitude of the modulation signal was 10 mV. The obtained spectra were fitted with Z-View software (v2.1b, Scribner Associates Inc.) in terms of appropriate equivalent circuits.

2.4 Spectroscopic Measurements

2.4.1 Infrared Spectroscopy

Attenuated Total Reflection (ATR) infrared spectroscopy was used for the analysis of the surface of

TiO_2 films. The sampling surface was pressed into intimate optical contact with the top surface of the crystal with a high refractive index, through which the infrared radiation passed and got reflected within the ATR element several times before it was collected at the output end of the crystal. Fourier-Transform (FT) was used to increase the sensitivity and resolution of data acquisition. The ATR-FTIR spectra were measured using a FTS 7000 FTIR spectrometer (Digilab, USA). Spectra were derived from 64 scans at a resolution of 2 cm^{-1}. All samples were measured under identical mechanical force used to push the mesoscopic TiO_2 films in contact with the diamond window. For a better signal to noise ratio, a Germanium crystal was used together with a highly sensitive charge-coupled device (CCD) detector under liquid nitrogen cooling. The dye-loaded electrodes were rinsed in acetonitrile and dried prior to measuring the spectra. No ATR correction was applied to the data. The obtained data were further processed with a home-built software to subtract the absorption of the crystal, surface water and carbon dioxide for purpose of clarity.

2.4.2 UV-visible absorption and photoluminescence spectra

UV-visible absorption spectra of solutions were measured in a 1 cm or 2 mm path length quartz cell on a Cary 5 spectrophotometer. For measuring the absorption of dyed TiO_2 films, the samples were attached to a center apertured sample holder by double-sided tapes. The beam was then incident from the glass side.

Photoluminescence was recorded on Spex Fluorolog 112 spectrofluorometer. The emitted light was detected with a Hamamatsu R928 photomultiplier operated in single photon counting mode. The emission spectrum was photometrically corrected with a calibrated 200 W tungsten lamp as a reference source.

2.4.3 Photoelectrochemical and phototransient measurement

For photoelectrochemical measurements, a 450 W xenon light source (Oriel, USA) was used to give an irradiance of 100 mW cm^{-2} (the equivalent of one sun at AM 1.5) at the surface of the solar cell. The spectral output of the lamp was matched in the region of 350-750 nm with the aid of a Schott K113 Tempax sunlight filter (Präzisions Glas & Optik GmbH, Germany) so as to reduce the mismatch between the simulated and true solar spectra to less than 4%. Various incident light intensities were regulated with neutral wire mesh attenuators. The current voltage characteristics of the cell under these conditions were obtained by applying an external potential bias to the cell and measuring the generated photocurrent with a Keithley model 2400 digital source meter (Keithley, USA). A mask with an aperture of 0.158 cm^2 was applied on each cell and this area was used to calculate the short circuit current density (mA cm^{-2}).

Photovoltage transients were observed using an exciting pulse generated by a ring of red light emitting diodes (LEDs, Lumiled) controlled by a fast solid-state switch. Pulse widths of 200 ms were used. The pulse was incident on the photoanode side of the device and its intensity was controlled to keep the modulation of the voltage below 5 mV. A white bias light, also incident on the same side of the device, was supplied by white diodes. Usually, transients were measured at different white light intensities ranging from 150 % to 0.01 % sun via tuning the voltage applied on the bias diodes.

2.4.4 Nanosecond Laser Transient Absorbance Measurements

Laser flash photolysis was conducted to study the sensitizer regeneration process. The dye was excited by pulsed laser photolysis at wavelengths where its absorbance was relatively low to assure a homogeneous absorption profile throughout the dye-sensitized TiO_2 layer. The excited state decay of the dye or the recovery of its fundamental state was then monitored by the change of the absorbed continuous wave light. Experimentally, dye-sensitized, 8 μm thick transparent nanocrystalline TiO_2 films were irradiated by nanosecond laser pulses produced by a Powerlite 7030 frequency-tripled Q-switched Nd:YAG laser (Continuum, USA) pumping an OPO-355 optical parametric oscillator (GWU, Germany) tuned at $\lambda = 600$ nm (30 Hz repetition rate, pulse width at half-height of 5 ns). To inject on the average less than one electron per nanocrystalline TiO_2 particle, the pulse fluence was attenuated to a maximum of 25 μJ cm^{-2} by use of absorptive neutral density filters. The probe light from a Xe arc lamp was passed through an interference filter monochromator, various optical elements, the sample, and a grating monochromator before being detected by a fast photomultiplier tube. Averaging over *ca.* 2,000 laser shots was necessary to obtain satisfactory signal/noise ratios.

2.5 Photovoltaic characterization and analysis

2.5.1 Basics of photovoltaics

2.5.1.1 The solar resource and Air Mass

The solar spectrum is a mixture of light with different wavelengths, ranging from ultraviolet, visible and infrared regions of the electromagnetic spectrum. According to the black-body radiation, the energy density per wavelength $de_\gamma/d\lambda$ can be expressed as a function of λ by Eq. 2.4.

$$\frac{de_\gamma(\lambda)}{d\lambda} = \frac{2\,hc_0 d\Omega}{\lambda^5}\,\frac{1}{\exp(hc_0/\lambda k_B T) - 1} \tag{2.4}$$

where dΩ is solid angle element, c_0 is the velocity of light in the medium, k_B and h is the Boltzmann constant and Planck constant, respectively. By taking $d^2e_\gamma/d\lambda^2 = 0$, the maximum value of $de_\gamma/d\lambda$ is at a wavelength

$$\lambda_{max} = \frac{hc_0}{4.965\,k_B T} = 0.2497\,\frac{\mu\text{m eV}}{k_B T} \tag{2.5}$$

The power density at the sun's surface is 62 MW m^{-2} and it reduces to 1353 W m^{-2} at the point just outside the Earth's atmosphere since the solid angle subtended by the sun, Ω_s, is as small as 6.8×10^{-5} sr. On passing through the atmosphere, the spectrum is partially attenuated by the absorption of oxygen, ozone in the ultraviolet region and water vapor, carbon dioxide, methane in the infrared. This attenuation is described by the 'Air Mass' factor since the absorption increases with the mass of air through which the radiation passes. For a thickness of l_0 of the atmosphere, the path length l through the atmosphere for radiation at an incident angle α relative to the normal to the earth's surface is given by

$$l = l_0/\cos\alpha \tag{2.6}$$

The ratio l/l_0 is called the Air Mass factor. The spectrum outside the atmosphere is denoted as AM0 and that on the surface of the earth for perpendicular incidence as AM1. The standard spectrum for moderate weather is AM 1.5, which corresponds to a solar incident angle of 48^o relative to the surface normal and gives a mean irradiance of 1,000 W m^{-2}. Figure 2.4 shows the comparison between the spectrum of a 5900 K black body and those of AM0 and AM1.5. The actual irradiation varies with seasons, climates, day time and the position of the sun. Averaged over the year, the global mean energy current density ranges from less than 100 W m^{-2} at high latitude areas to around 300 W m^{-2} in Saudi Arabia. It is a little more than 100 W m^{-2} in central Europe, where the amount of energy incident to a normal surface in a year is about 1000 kWh m^{-2} and also known as 1000 sun hours per year.

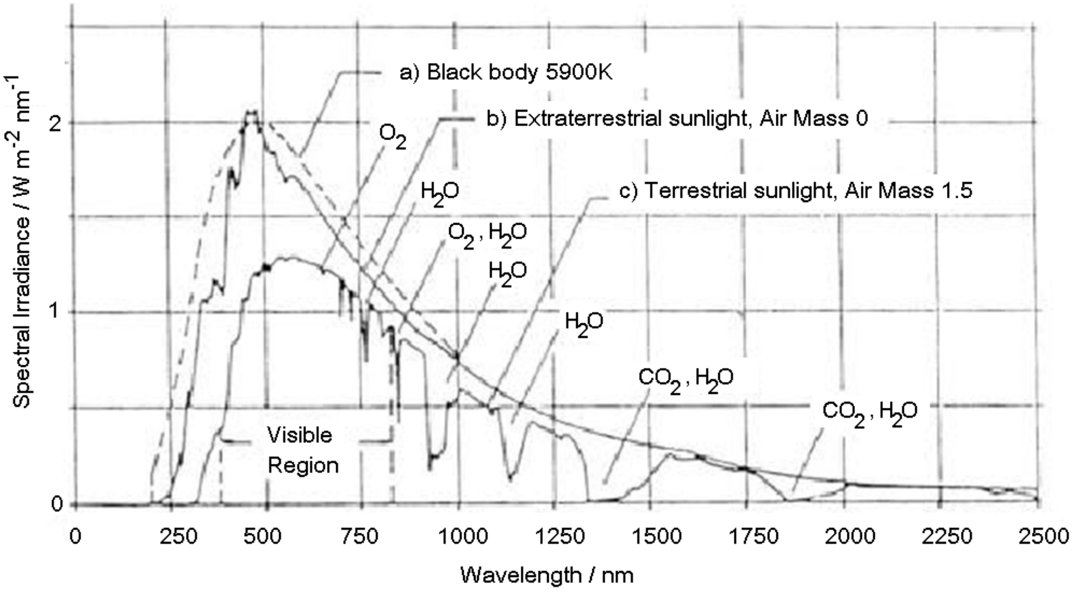

Figure 2.4 Spectra of a) Black body 5900K (attenuated by a factor of 6×10^5 in intensity), b) AM0 and c) AM1.5.

2.5.1.2 Current-voltage characterization

Standard current-voltage measurement of a DSC determines the current voltage response of the device, i.e. current-voltage characteristics, in the dark and under different light intensities. In the dark, the applied voltage, *bias*, on the device generates a current that flows in the direction opposite to that of the photocurrent. This reverse current is usually called the dark current. For an ideal diode, the dark current I_{dark} relates to voltage with Eq. 2.7.

$$I_{dark} = I_s\left(\mathrm{e}^{qV/k_BT} - 1\right) \tag{2.7}$$

where I_s is the saturation current of the diode (typically 10^{-7}-10^{-9} A), V is the voltage applied on the terminals of the cell and q is the elementary charge.

Under illumination, the current-voltage characteristics follow

$$I = I_{ph} - I_s(\mathrm{e}^{qV/k_BT} - 1) = I_{ph} - I_s(\mathrm{e}^{V/V_T} - 1) \tag{2.8}$$

where I_{ph} is the photocurrent that depends on irradiation intensity and V_{T} is often referred to as the thermal voltage that equals $k_{\mathrm{B}}T/q$. For non-ideal devices, an ideality factor, m, is used to describe the weaker dependence of dark current on voltage.

$$I = I_{ph} - I_s\,(\mathrm{e}^{V/mV_T} - 1) \tag{2.10}$$

An experimental *I-V* curve is shown in Figure 2.5, together with the power curve. The following parameter can be derived with the *I-V* curve.

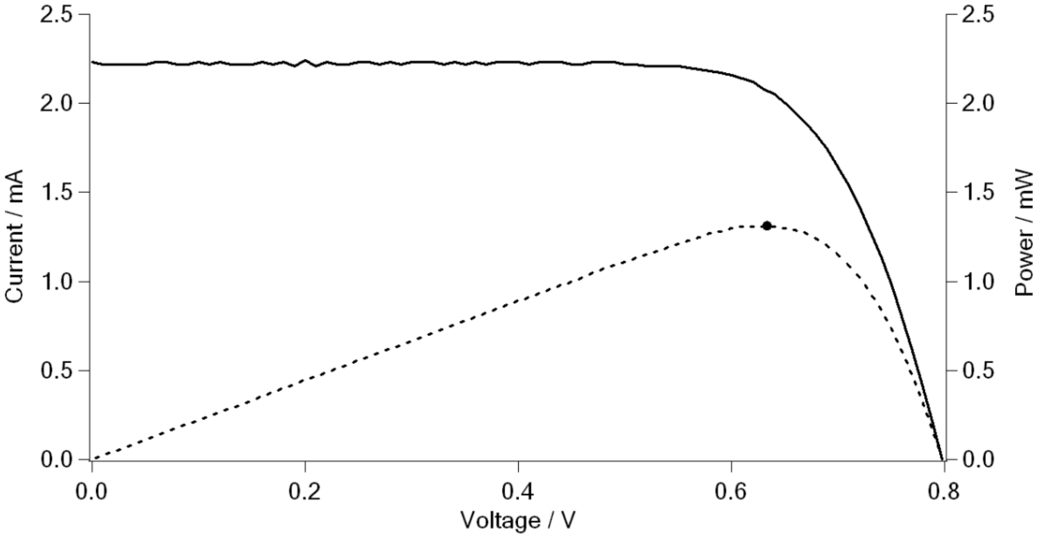

Figure 2.5 A typical I-V curve in the experiment. The dotted line shows the power output at different bias. The dot indicates the maximum power point.

Open-circuit voltage (V_{oc})

The V_{oc} is measured under the condition when there is no external load connected, i.e. the circuit is broken or open. In this condition, there is no external current flow between the two terminals of the device, i.e. $I = 0$ and $V = V_{oc}$. From Eq. 2.10,

$$I_{ph} - I_s(\mathrm{e}^{V_{oc}/mV_T} - 1) = 0 \tag{2.11}$$

$$V_{oc} = mV_T\ \ln\left(\frac{I_{ph}}{I_s} + 1\right) \cong mV_T\ \ln\left(\frac{I_{ph}}{I_s}\right) \tag{2.12}$$

V_{oc} increases logarithmically with the photocurrent and light intensity.

Short-circuit current (I_{sc})

The I_{sc} is measured at the condition when the applied voltage, V, equals zero. From Eq. 2.10,

$$I_{sc} = I_{ph} \tag{2.13}$$

I_{sc} increases linearly with the light intensity.

Fill factor (FF)

The power is calculated as the product of $I \times V$ and the maximum power point is labeled with the dot. At this point, the device delivers the highest power output with the voltage, V_m and current, I_m.

$$V_m = V_{oc} - mV_T \ln\left(\frac{V_m}{V_T} + 1\right) \tag{2.14}$$

The fill factor (*FF*) is defined as the ratio

$$FF = \frac{V_m I_m}{V_{oc} I_{sc}} \tag{2.15}$$

to describe how the maximum power rectangle fits under the *I*-*V* characteristics. Combining Eqs. 2.14 and 2.15, we obtain the approximation for *FF* in Eq. 2.16.

$$FF = \frac{V_{oc}/mV_T - \ln\left(1 + V_{oc}/mV_T\right)}{1 + V_{oc}/mV_T} \tag{2.16}$$

Typical *FF* of DSC ranges from 0.6 to 0.8 depending on the individual device and usually increases with the decreasing light intensity. It is also influenced by the series resistance (R_s) arising from the internal resistance and resistive contacts of the cell and parallel resistance (R_{sh}) from the leakage of the current. Figure 2.6a illustrates a simplified equivalent circuit for DSC in which R_s and R_{sh} are present. For an efficient solar cell, we need a small R_s but a large R_{sh} since a large R_s and a small R_{sh} decrease the *FF* dramatically.

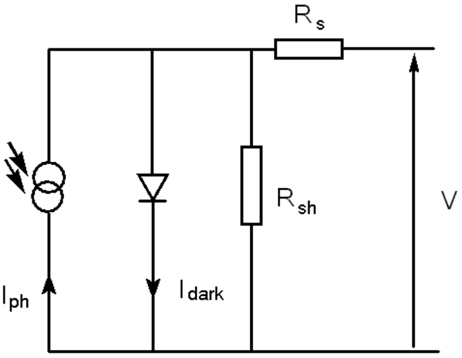

Figure 2.6 A simplified equivalent circuit for DSC. Series and shunt resistances are taken into account.

When R_s and R_{sh} are taken into account, a more precise diode equation is given by eq. 2.17.

$$I = I_{ph} - I_s\left(e^{(V+IR_s)/mV_T} - 1\right) - (V + IR_s)/R_{sh} \tag{2.17}$$

Solar-to-electric-power conversion efficiency (η)

The efficiency η of the device is the parameter that is associated with the performance of the device. It is defined as the ratio of the maximum power (P_{max}) to the incident sunlight power (P_s).

$$\eta = \frac{V_m\, I_m}{P_s} = \frac{V_{oc}\, I_{sc}\, FF}{P_s} \tag{2.18}$$

P_s is an important experimental parameter and in order to compare different results, standard test condition is always used for all the devices in this work. This condition includes AM 1.5 spectrum illumination with an incident power density of 100 mW cm^{-2} and a test temperature of 298 K.

2.5.1.3 Incident photon-to-current conversion efficiency (IPCE)

The incident photon-to-current conversion efficiency (*IPCE*) is defined as the number of light-generated electrons in the external circuit divided by the number of incident photons at a certain wavelength.

$$IPCE = \frac{N_{electron}}{N_{photon}} = \frac{qN_{electron}/s}{qN_{photon}/s} = \frac{I_{ph}(amp)}{qN_{photon}/s} \tag{2.19}$$

The incident power

$$P_{in}(Watt) = P_{in}\left(\frac{Joule}{s}\right) = \frac{N_{photons}}{s}\, hv = \frac{N_{photons}}{s}\,\frac{hc_0}{\lambda} \tag{2.20}$$

With Eq. 2.20, Eq. 2.19 can be rewritten as

$$IPCE = \frac{I_{ph}}{\frac{qP_{in}\lambda}{hc_0}} = \frac{I_{ph}}{P_{in}}\,\frac{hc_0}{q}\,\frac{1}{\lambda} = \frac{I_{ph}}{P_{in}} \times \frac{1240}{\lambda\,(nm)} \times 100\% \tag{2.21}$$

2.6 Data Analysis

2.6.1 Theories

2.6.1.1 Free and trapped electrons in nanocrystalline TiO$_2$

As partly mentioned in Sec. 1.2.3.3, the majority of photoinjected electrons are localized in the trap states and transported to the external circuit via multiple trapping/detrapping events. This type of behavior greatly affects the experimental observation of rate constants for charge transfer and makes it quite different from that expected by simply considering conduction band electrons. Due to the large surface area of the nanoporous films, these traps are assumed to be located primarily at the particle surface. For simplicity, we thus discriminate electrons in the TiO$_2$ nanoparticles as “free” electrons in the conduction band and trapped electrons in the bandgap.

According to Fermi-Dirac distribution, the average occupancy in semiconductor, *f(E)*, is given by

$$f(E) = \frac{1}{1 + \exp\,[(E - E_F)/k_B T\,]} \tag{2.22}$$

In the dark, the TiO_2 film is thermally equalized with the electrolyte and the quasi-Fermi level of TiO_2, E_{F0}, equals the redox Fermi level of I^-/I_3^- in the electrolyte, E_{redox}, i.e. $E_{F0} = E_{redox}$. Under these conditions, TiO_2 film is an insulator and the concentration of conduction band electrons, n_{c0}, is very small. $n_{c,0}$ can be related to the effective conduction band states, N_c by

$$n_{c0} = N_c f(E_c) = N_c\,\frac{1}{1 + \exp\,[(E_c - E_{F0})/k_B T\,]} \tag{2.23}$$

where E_c is the conduction band energy. Typical values of N_c and E_c are 1×10^{21} cm^{-3} and 1.0 eV versus E_{redox}, respectively.

The occupancy of states at E_c is usually well approximated by the Boltzmann limit where $E_c - E_F >> k_B T$ and $f <<1$. Eq. 2.23 can be rewritten as

$$n_{c0} = N_c \exp\,[(E_{redox} - E_c)/k_B T\,] \tag{2.24}$$

When the light sheds on the device, n_c increases with the upward displacement of E_F towards the conduction band. Then,

$$n_c = N_c \exp\,[(E_{Fn} - E_c)/k_B T\,] \tag{2.25}$$

The photovoltage

$$qV_{photo} = E_{Fn} - E_{redox} \tag{2.26}$$

From Eqs. 2.25, 2.26 and 2.27,

$$n_c = n_{c0} \exp\,[qV_{photo}/k_B T\,] \tag{2.27}$$

The electron trapping states in nanocrystalline TiO_2 layers are generally approximated by an exponential distribution as a function of energy. Tailing from the conduction band electron states, the density of the traps are higher for shallow ones near the conduction band but much lower for deep traps that were energetically far away from the conduction band. Eq. 2.28 shows a good description of this type of distribution.

$$\frac{\partial n_t}{\partial E} = g(E) = \frac{N_t}{k_B T_c} \exp\,[(E - E_c)/k_B T_c] \tag{2.28}$$

Here, $g(E)$ is the density of trapped states below the conduction band at the energy E, N_t is total density of trapped states and T_c is the tailing parameter that describes the shape of the exponential distribution. Normally, coefficient β or "effective mass" m_c was used to state the same feature of this distribution, where $\beta = T/T_c$ and $m_c = k_B T_c$. β is usually in the range of 0.2 to 0.5 and a β of 1 simply denotes that all the electrons are located in the conduction band. Figure 2.7 illustrates how $g(E)$ is influenced by different T_c values. As E_F descends from the conduction band, the density of trapped states drops more rapidly for a smaller T_c, i.e. a larger β.

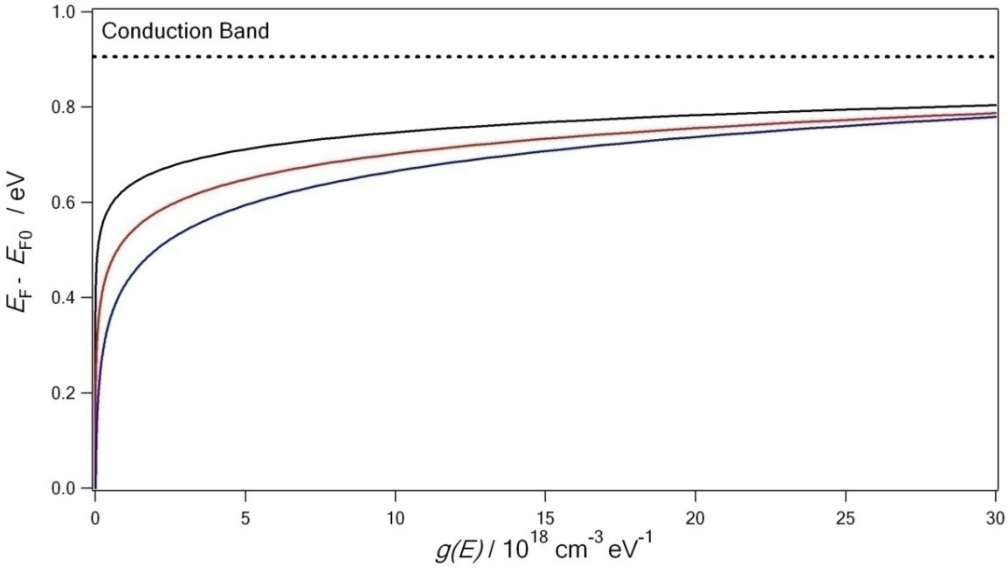

Figure 2.7 Density of states distributions for electron traps showing the effect of the parameter T_c. T_c is 600 K (Black), 900 K (Red) and 1200 K (Blue), respectively. Other values for the calculation: N_t =10^{19} cm^{-3} eV^{-1}, $E_c - E_{F0}$ = 0.9 eV.

The derivative $\partial n_t/\partial n_c$ is related to the density of states function for electron traps $g(E)$ by

$$\frac{\partial n_t}{\partial n_c} = \frac{\partial n_t}{\partial E}\frac{\partial E}{\partial n_c} = g(E)\frac{\partial E}{\partial n_c} \tag{2.29}$$

Note that from Eq. 2.25,

$$\frac{\partial n_c}{\partial E_F} = \frac{N_c}{k_B T}\exp\left[\frac{E_F - E_c}{k_B T}\right] = \frac{n_c}{k_B T} \tag{2.30}$$

Thus,

$$\frac{\partial n_t}{\partial n_c} = \frac{k_B T}{n_c}\, g(E) = \beta\,\frac{N_t}{N_c^{\beta}}\, n_c^{\beta-1} \tag{2.31}$$

Integration of the trap density between the limits of E_{redox} and $E_{redox} + qV_{photo}$ will give the true density of trapped electrons as

$$n_t = \int_{E_{redox}}^{E_{redox}+\,qV_{photo}} g(E)\,f(E)d(E) \tag{2.32}$$

By using zero-Kelvin approximation of Fermi-Dirac distribution, n_t is given by

$$n_t = N_t\exp\left[\frac{E_{redox} - E_c}{k_B T_c}\right]\left[\exp\left(\frac{qV_{photo}}{k_B T_c}\right) - 1\right] \tag{2.33}$$

Together with Eq. 2.27,

$$n_t = N_t \exp\left[\frac{E_{redox} - E_c}{k_B T_c}\right]\left[\left(\frac{n_c}{n_{c0}}\right)^{T/T_c} - 1\right] \cong \frac{N_t}{N_c^{\beta}}\, n_c^{\beta} \tag{2.34}$$

The derivative of Eq. 2.34 gives the same result as Eq. 2.31.

For a calculation of n_t at a finite temperature, this involves the numerical integration of the product $g(E)\, f(E)$ up to the conduction band energy.

Under the short-circuit condition, the continuity equation (Eq. 1.11) can be solved by omitting the recombination term and taking the boundary condition of the boundary condition of zero electron flux at the outermost TiO_2/redox electrolyte interface ($J_n(d) = 0$).[14] The steady-state free electron concentration n_c at a distance of x from FTO substrate is given by Eq. 2.35

$$n_c(x) = n_{c0} + \frac{\eta_{inj} I_0}{\alpha(\lambda) D_0}\left[1 - \alpha(\lambda) x e^{-\alpha(\lambda) d} - e^{-\alpha(\lambda) x}\right] \tag{2.35}$$

where d is the film thickness and D_0 is the diffusion coefficient of conduction band electrons. Figure 2.8 shows the electron concentration profiles for an 8-µm-thick TiO_2 film and it is apparent that n_t is orders of magnitude higher than n_c. The corresponding electron quasi-Fermi level is also plotted versus the film thickness. The quasi-Fermi level is found to be rather flat across the whole film until the near proximity of the FTO substrate.

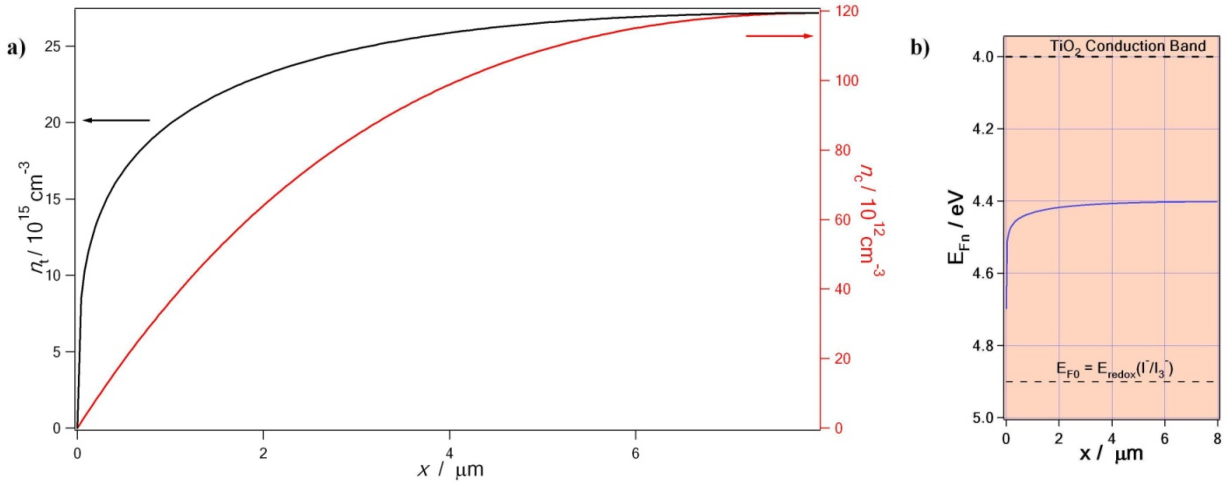

Figure 2.8 a) Profiles of conduction band electron density (n_c, shown in red) and trapped electron density (n_t, shown in black) calculated for short-circuit condition. $N_c = 10^{21}$ cm^{-3} eV^{-1}, $N_t = 10^{19}$ cm^{-3} eV^{-1}, $I_0 = 2\times10^{17}$ cm^{-2} s^{-1}, $\eta_{inj} = 1$, $E_c - E_{F0} = 0.9$ eV, $\alpha = 2250$ cm^{-1}, $D_0 = 0.4$ cm^{-2} s^{-1}. b) Corresponding electron quasi-Fermi level across the film. NHE is taken as 4.5 V versus vacuum level and the redox potential of I^-/I_3^- is 0.4 V versus NHE.

A general definition of chemical capacitance, C_{ch}, is introduced to describe the capacity to store energy with a thermodynamic displacement. The chemical capacitance per volume is given by

$$C_{ch} = q^2 \frac{\partial N_i}{\partial \mu_i} \tag{2.36}$$

to reflect the capability of a system to accept or release additional carriers with density N_i due to a change in their chemical potential, μ_i.[15] For an ideal system, $\mu_i = \mu_0 + k_B T \ln N_i$. Then Eq. 2.36 can be described by

$$C_{ch} = q^2 \frac{N_i}{k_B T} \tag{2.37}$$

For conduction band electrons,

$$C_{ch}{}^{(cb)} = q^2 \frac{n_c}{k_B T} \tag{2.38}$$

For trapped electrons, by the zero-Kelvin approximation of the Fermi function,

$$C_{ch}{}^{(tr)} = q^2 g(E_F) = q^2 \frac{\alpha N_t}{k_B T} \exp\left[\alpha(E_F - E_c)/k_B T\right] \tag{2.39}$$

The total chemical capacitance

$$C_{ch} = q^2 \frac{\partial (n_c + n_t)}{\partial \mu_n} = C_{ch}{}^{(cb)} + C_{ch}{}^{(tr)} \tag{2.40}$$

Considering the fact that $n_c << n_t$, the experimentally measured C_{ch} are dominated by $C_{ch}{}^{(tr)}$ and it is roughly taken as C_{ch}.

2.6.1.2 Quasistatic approximation under small perturbation[16]

A quasistatic process is a thermodynamic process that happens infinitely slowly. In practice, such processes can be approximated by performing them ‘very slowly’ to achieve the change in a sequence of equilibrium states. In current case, we consider a system consisting of two types of electronic states (free and trapped). The system initially at equilibrium (under bias or illumination) and perturbed by a small perturbation superimposed on the system.

With the external perturbation on the equilibrium at E_F, the variation of $\partial n_c/\partial t$ and $\partial n_t/\partial t$ are ruled by the instantaneous occupancies and transition rates.

$$\frac{\partial n_c}{\partial t} = -\frac{\partial J}{\partial x} - \gamma n_c f(E) + \delta N_t[1 - f(E)] \tag{2.41}$$

$$\frac{\partial n_t}{\partial t} = \frac{\partial N_t[1 - f(E)]}{\partial t} = \gamma n_c f(E) - \delta N_t[1 - f(E)] \tag{2.42}$$

Here, J is diffusive flux of conduction band electrons, γ is electron capture rate constant and δ is rate constant for electron thermal release from the trap to the conduction band. γ and δ are related by Shockley-Read-Hall statistics.[17]

A particular kind of evolution as that which obeys the quasistatic condition was defined by Bisquert and Vikhrenko [16]

$$\frac{\partial n_t}{\partial t} = \frac{\partial n_t}{\partial n_c}\frac{\partial n_c}{\partial t} \tag{2.43}$$

Combining Eqs. 2.41 to 2.43, we get

$$\frac{\partial n_c}{\partial t} = -\frac{\partial J}{\partial x} - \frac{\partial n_t}{\partial n_c}\frac{\partial n_c}{\partial t}$$

$$\frac{\partial n_c}{\partial t} = \frac{1}{\left(1+\frac{\partial n_t}{\partial n_c}\right)}\left(-\frac{\partial J}{\partial x}\right) \tag{2.44}$$

A new diffusion coefficient, as is called chemical (or apparent) diffusion coefficient,[18] D_n is thus defined by

$$D_n = \frac{1}{\left(1+\frac{\partial n_t}{\partial n_c}\right)} D_0 \tag{2.45}$$

where D_0 is the diffusion coefficient of conduction band electrons.

By taking $\partial n_t/\partial n_c >> 1$ and Eq. 2.31

$$D_n = \frac{N_c^{\beta}}{\alpha N_t} n_c^{1-\beta} D_0 \tag{2.46}$$

Following the same logic that $n_c << n_t$, $n_{total} = n_c + n_t \cong n_t$. D_n is then related to n_{total} by replacing n_c in Eq. 2.46 with Eq. 2.34

$$D_n = \frac{N_c}{\alpha N_t^{1/\beta}} n_{total}^{(1-\beta)/\beta} D_0 \tag{2.47}$$

Eq. 2.47 nicely correlates D_n with the total electron concentration in the film and thus explains the measured power law dependence of D_n on light intensities.

Meanwhile, if we assume that the back capture of electrons in TiO_2 with I_3^- mainly takes place from conduction band and in a pseudo-first order reaction, the measured electron lifetime (response time), τ_n, has the form of

$$\tau_n = \left(1+\frac{\partial n_t}{\partial n_c}\right)\tau_0 \cong \beta\,\frac{N_t}{N_c^{\beta}}\, n_c^{\beta-1}\tau_0 \tag{2.48}$$

Electron diffusion coefficient and electron lifetime are important parameters that render a better understanding of the photovoltaic system. The quasistatic approximation provides a feasible method to measure D_n and τ_n via a small perturbation induced by modulated signals (light or electrical). Experimentally, techniques of intensity-modulated photocurrent/voltage spectroscopy (IMPS/IMVS), open-circuit decay measurement, transient photocurrent/voltage decay measurement and electrochemical impedance spectroscopy (EIS) have been employed. In this work, the last three methods were mostly used to study different DSC systems and devices.

2.6.2 Phototransient-based measurements

The idea of phototransient measurement is to use a light transient of small amplitude to probe the device that is under equilibrium and monitor the decay kinetics. In practice, this is achieved by using red light emitting diodes as a probe to generate a voltage perturbation about the V_{oc} of the cell under the white bias light produced by an array of white light emitting diodes and measuring the voltage decay process thereafter. The red diodes are driven by a pulse generated by the computer that allows synchronization with the switching of the cell between open and short circuits. Figure 2.9 shows the basic setup of the whole experiment. Green and blue diodes are available to probe the system if the light absorption of the device is weak in the spectrum of the red diode. Oscilloscope has to be used for rapid decaying systems that are faster than 0.1 ms.

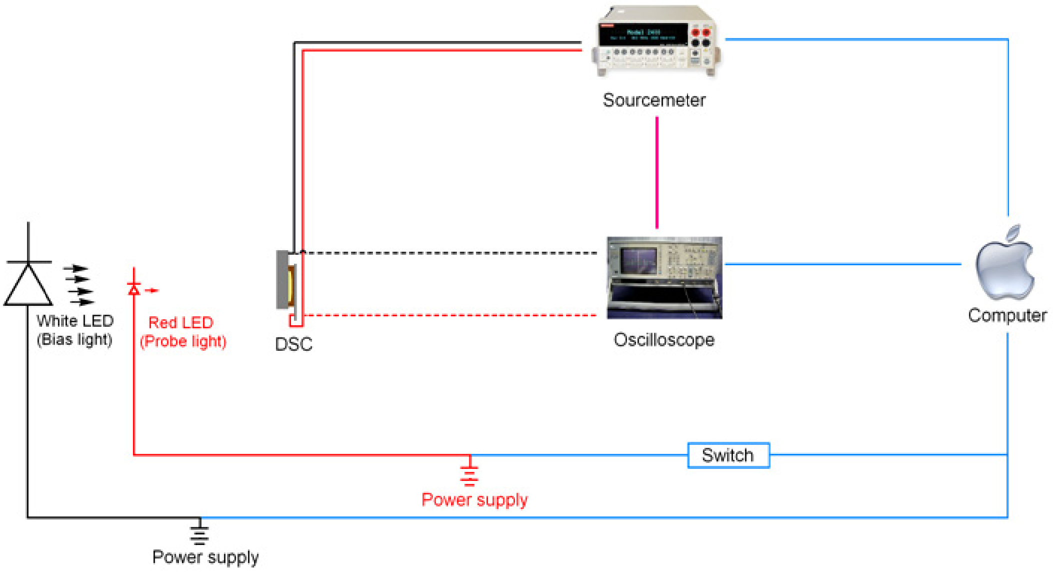

Figure 2.9 Setup of the phototransient measurement.

Normally, the photovoltage decay closely follows a pseudo single exponential form, thus the recombination rate constant, k_{rec}, can be extracted from the slope of the semi-logarithmic plot. Since the back reaction is usually taken as the pseudo-first order reaction, k_{rec} is related to electron lifetime τ_{n} by

$$k_{\mathrm{rec}} = 1/\tau_n \tag{2.49}$$

Similarly, the experiment can be done by monitoring the photocurrent decay under short-circuit condition. A characteristic electron transport time, τ_{c}, can be extrapolated from the decay curve. The electron diffusion coefficient D_{n} is then calculated from τ_{c} by a three-dimension diffusion model

$$D_{\mathrm{n}} = \frac{d^2}{2.8\tau_c} \tag{2.50}$$

where d is the thickness of the TiO_2 film.[19] Typical photovoltage and photocurrent decay curves are shown in Figure 2.10.

The recombination rate constant at short-circuit condition is determined by monitoring the transient photovoltage decay of the device under the condition that it is biased with a countercurrent equal to the short-circuit current but in the opposite direction. The decay process is found to be very slow compared to the transport process under the short-circuit condition.

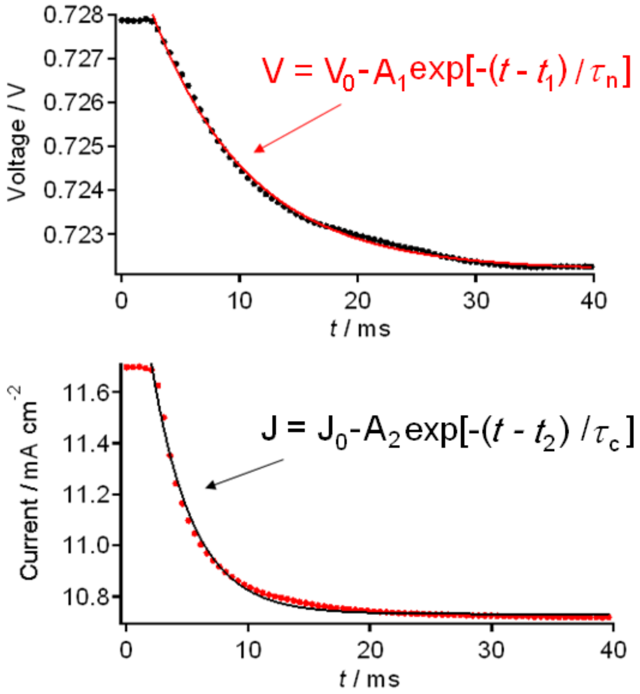

Figure 2.10 Photovoltage (up) and photocurrent (down) decay measurements. Raw data are shown in dotted lines and the fittings with indicated equations are presented in solid lines.

The chemical capacitance of the TiO_2/electrolyte interface at the V_{oc} is calculated as $C = \Delta Q/\Delta V$, where ΔV is the peak height of the photovoltage transient and ΔQ is the number of electrons injected during the light flash. The latter is determined by integrating a photocurrent transient at short circuit generated from an identical pulse. Since the bias intensity can be manipulated by controlling the voltage applied on the white light emitting diodes, the same experiment is done at different light intensities from 150% to 0.01% Sun to tune the TiO_2 Fermi level of the device and get the curvature of the capacitance. This method may underestimate the actual injected charge by the fraction of electrons that are lost to recombination during transport at short circuit, yet it will affect only the magnitude but not the shape of the calculated capacitance versus the potential curves.[20],[21]

The number of electrons in the TiO_2 film can be measured by a charge extraction method.[22] The bias applied on the two terminals of the device is controlled by the sourcemeter and can vary from open-circuit to short-circuit conditions. Briefly, the measurement sequence is as follows. The device is initially poised at short-circuit condition in the dark and then switched to open-circuit and the white light emitting diodes array is switched on for 200 ms. The increase in the photovoltage relative to the open-circuit voltage is recorded. The light is subsequently shut off and the decay of the photovoltage is recorded as well. The voltage decay is carried on for a certain time before the circuit is switched back to short-circuit condition. The whole charge extraction curve is measured at different points along the photovoltage decay curve by varying the delay between shutting off the light and switching to short circuit. The extracted electrons manifest themselves as the current pulse collected when the cell is switched from open circuit to short circuit. The delay between shutting off the light and switching to short circuit can be varied from 100 μs to 10 s by tuning the integration time of the sourcemeter.

Open-circuit voltage decay measurement is also performed to obtain the electron lifetime. Briefly, the white bias light is illuminated on the device for a certain time to a steady voltage and then turned off. At the same time, the open-circuit voltage decay of the device is recorded by the sourcemeter. Typically, the interval of the measurement is set in a logarithmic scale, ranging from 100 μs to seconds. The decay data is fitted by a quadruple exponential model and then differentiated against time. The apparent electron lifetime τ_n is obtained by Eq. 2.51.[23]

$$\tau_\mathrm{n} = -\frac{k_B T}{q}\left(\frac{dV_{oc}}{dt}\right)^{-1} \tag{2.51}$$

2.6.3 Electrochemical impedance spectroscopy (EIS)

The principle of using EIS to study response of the device resembles that of the phototransient experiment except that an electrical signal is used as the probe. In EIS experiments, the device is first poised by an external potential bias and then subjected to a harmonically modulated low-amplitude voltage, $\Delta U = U_{\mathrm{amp}}\, \mathrm{e}^{i\omega t}$, as a small perturbation. An increase of ΔU on the device will cause a current flow of $\Delta i = i_{\mathrm{amp}}\, \mathrm{e}^{i(\omega t-\theta)}$ by a delay of phase angle θ. The impedance of the device is thus given by

$$Z_{EIS} = \left|\frac{\Delta U}{\Delta I}\right| = \left|\frac{U_{\mathrm{amp}}}{i_{\mathrm{amp}}}\right| e^{i\theta} \tag{2.52}$$

The interpretation of the EIS spectrum of a DSC has been thoroughly discussed recently.[15],[24]-[33] Generally, a transmission line model is used to describe the system, as is shown in Figure 2.11.[28][31]

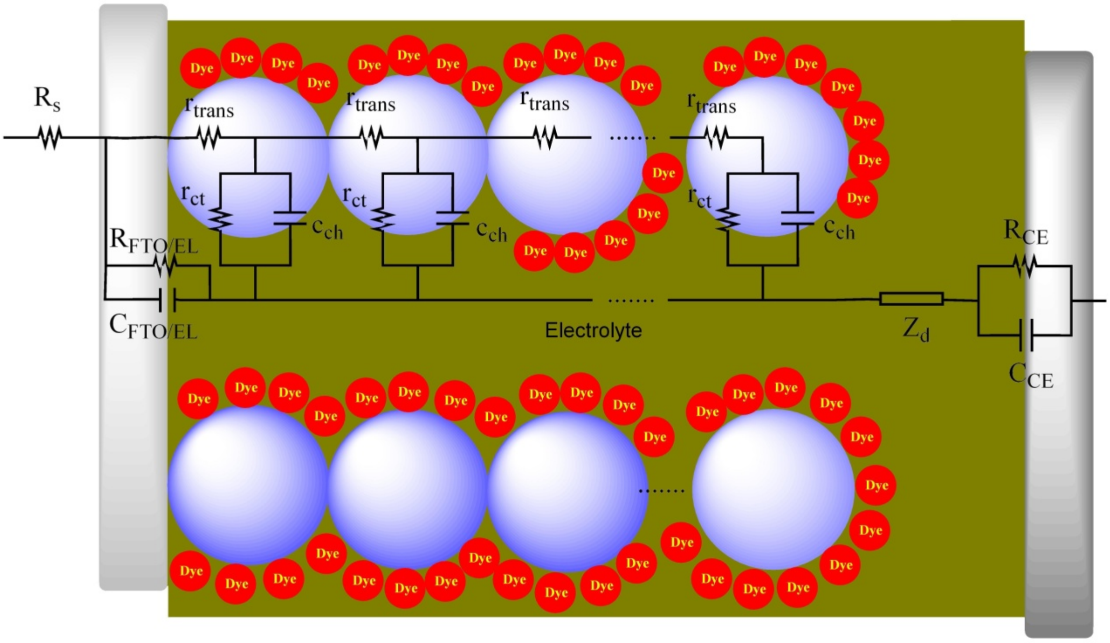

Figure 2.11 Transmission line model for DSCs.

Here, the whole mesoscopic TiO_2 film is treated as an interconnected network. Under a forward bias, electrons are injected from FTO substrate into the TiO_2 and the film is charged by electron propagation through individual particles with a resistance of r_{trans}. Some of the injected electrons recombine with the oxidized species in the electrolyte, characterized by a charge transfer resistance of r_{ct} and a capacitance of c_{ch}, and the rest of the electrons are then recaptured by the FTO current collector during the opposite phase of the sinusoidal voltage modulation. The two channels for electron transportation through TiO_2 and that of the I_3^- through the electrolyte are coupled in series. Taking d as the thickness of the mesoscopic TiO_2 film, the electron transport resistance is $R_t = r_t \times$ d, the interfacial charge recombination resistance is $R_{ct} = r_{ct} / d$ and the chemical capacitance of the film is $C_{\mathrm{ch}} = c_{\mathrm{ch}} \times d$, where the lower case letters represent resistances and capacitance that are normalized to the film thickness.[33] $R_{\mathrm{FTO/EL}}$ and $C_{\mathrm{FTO/EL}}$ stand for the charge transfer resistance and the corresponding double layer capacitance at exposed FTO/electrolyte interface and change with surface conditions (blocking layer and cleanliness). Due to the irreversibility of I^-/I_3^- couple on FTO, $R_{\mathrm{FTO/EL}}$ is usually very large. The diffusion of I_3^- within a thin layer cell is described by a Nernst diffusion impedance Z_d. Regeneration of I_3^- at the counter electrode is characterized by R_{CE} and C_{CE}, which are the charge transfer resistance and double layer capacitance at the platinized FTO, respectively.

The fitting of the experimental data is realized in the Zview software application version 2.8 by the following equivalent circuit in Figure 2.12.

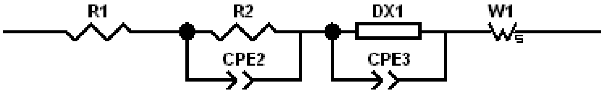

Figure 2.12 Equivalent circuit of DSC in Zview software.

Compared with Figure 2.11, R1 is the series resistance R_s, R2 is the charge transfer resistance at the counter electrode R_{CE}, CPE2 is the Constant Phase Element representing C_{CE}, DX1 is the Extended Distributed Element that models the TiO_2 network,[34][35] CPE3 is the $C_{\mathrm{FTO/EL}}$ and W1 is the Finite-Length Warburg element for Z_{d}. Instead of a capacitor, CPE is used here for an improved fitting. However, the CPE exponent δ is found to be close to an ideal capacitor value, $\delta \cong 1$ in most cases.

Typical EIS spectra are shown in Figure 2.13 and the measured data are presented in squares. The upper curve displays real part (Z') versus the imaginary part (Z") of the impedance, usually known as the Nyquist plot. The lower curve is the Bode plot where the phase angel θ is plotted against frequency. It is apparent that the Nyquist plot consists of three semicircles. The small semicircle occurring at highest frequencies represents redox charge transfer at the platinum counter electrode, the larger one at intermediate frequencies stands for the electron transport in the TiO_2 layer, the electron transfer at the oxide/electrolyte interface and the third one at lower frequencies is attributed to ion diffusion within the electrolyte. Accordingly, there are three peaks in the Bode plot, corresponding to the RC time constants shown in the Bode plot. Based on the equivalent circuit in Figure 2.12, fairly satisfactory fittings can be obtained as the solid lines shown in Figure 2.13.

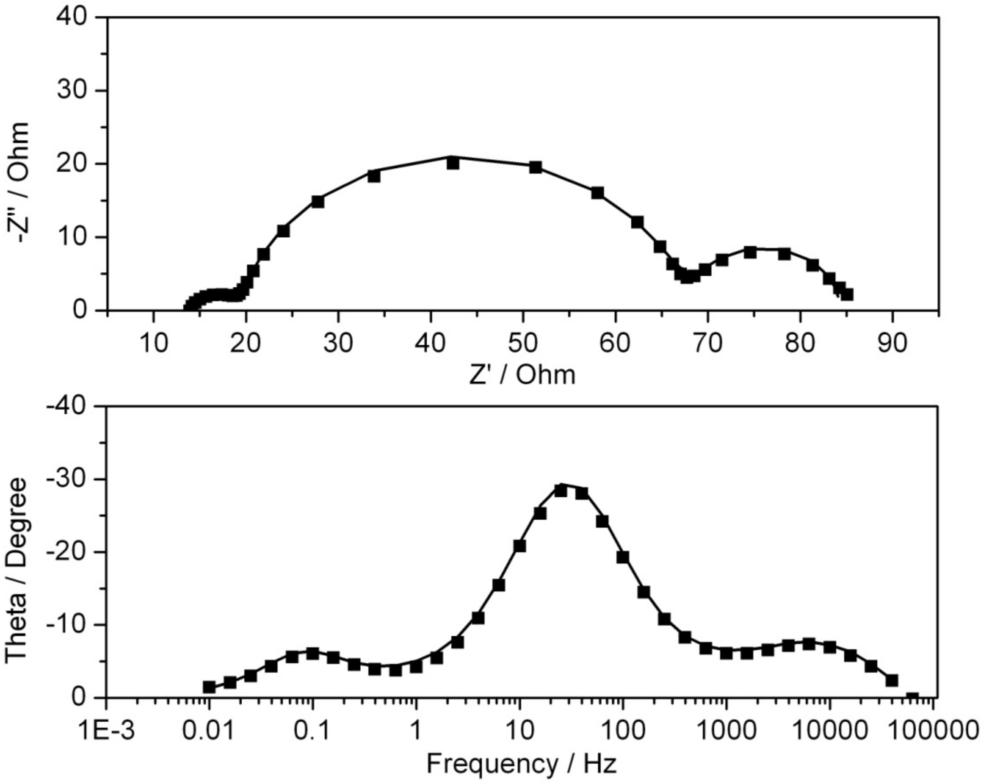

Figure 2.13 Typical curves of impedance spectra for a DSC. Experimental data are plotted in black squares and the fitting is in solid lines. The data was measured at -0.7 V bias in the dark.

The data fitting gives key parameters of the device, such as the series resistance, information about the counter electrode and electron transport and recombination, i.e. values of R1, R2, CPE2, R_{trans}, R_{ct} and C_{ch}. The diffusion coefficient D_{n} is then calculated by $D_{\mathrm{n}} = d^2 / (R_{\mathrm{trans}}C_{\mathrm{ch}})$ while the electron lifetime τ_{n} is obtained by $\tau_{\mathrm{n}} = R_{\mathrm{tr}}C_{\mathrm{ch}}$. The electron diffusion length L_{n} is given by Eq. 2.53.

$$L_n = \sqrt{D_n \tau_n} = d\sqrt{\frac{R_{ct}}{R_{trans}}} \tag{2.53}$$

It should be noted there are certain important points in the above method.[33] First, in the dark IR drop during the impedance measurement is negligible due to the small dark current and the Fermi level is significantly below the conduction band edge (>> $k_{\mathrm{B}}T$). Hence, the external bias potentials are directly taken as that applied on the junction without further corrections. Second, the capacitance measured by impedance spectroscopy is in fact a sum of capacitances contributed by chemical capacitance (C_{ch}) and space charge (C_{sc}) of the semiconductor film as well as the Helmholtz layer (C_H) and surface adsorbed ionic species (C_{ad}) at the interface with the electrolyte. The C_{ch} and C_{sc} as well as C_H and C_{ad} are connected in parallel ($C_{ch}//C_{sc}$-$C_H//C_{ad}$). Due to the lack of a depletion layer in nanocrystalline TiO_2 mesoscopic films, C_{sc} is neglected in the experimental potential range. The double layer capacitance ($C_H//C_{ad}$) only contributes slightly to the total capacitance at the higher bias potentials. Similarly, a contribution from $R_{TCO/EL}$ and $C_{TCO/EL}$ under high bias potentials is also neglected and only becomes more significant at much lower biases.

2.7 References and notes to Chapter 2

[1]. Ito S.; Zakeeruddin, S. M.; Humphry-Baker, R.; Liska, P.; Charvet, R.; Comte, P.; Nazeeruddin, M. K.; Péchy, P.; Takata, M.; Miura, H; Uchida, S.; Grätzel, M. *Adv. Mater.* **2006**, *18*, 1202.

[2]. Barbé, C. J.; Arendse, F.; Comte, P.; Jirousek, M.; Lenzmann, F.; Shklover, V.; Grätzel, M. *J. Am. Ceram. Soc.* **1997**, *80*, 3157.

[3]. Ito, S.; Chen, P.; Comte, P.; Nazeeruddin, M. K.; Liska, P.; Péchy, P.; Grätzel, M. *Progress in Photovoltaics*, *Res. Appl.* **2007**, *15*, 603.

[4]. Wang, P.; Zakeeruddin, S. M.; Humphry-Baker, R.; Moser, J.-E.; Grätzel, M. *Adv. Mater.* **2003**, *15*, 2101.

[5]. Cameron, D. G.; Hudson, H. R.; Pianka, M. *Phosphorus, Sulfur Silicon Relat. Elem.* **1993**, *83*, 21.

[6]. Wang, P.; Zakeeruddin, S. M.; Moser, J. E.; Nazeeruddin, M. K; Sekiguchi, T.; Grätzel, M. *Nat. Mater.*, **2003**, *2*, 402.

[7]. Wang, P.; Klein, C.; Humphry-Baker, R.; Zakeeruddin, S. M.; Grätzel, M. *J. Am. Chem. Soc.* **2005**, *127*, 808.

[8]. Kuang, D.; Klein, C.; Ito, S.; Moser, J. E.; Humphry-Baker, R.; Evans, N.; Duriaux, F.; Grätzel, C.; Zakeeruddin, S. M.; Grätzel, M. *Adv. Mater.*, **2007**, *19*, 1133.

[9]. Ito, S.; Liska, P.; Comte, P.; Charvet, R.; Péchy, P.; Bach, U.; Schmidt-Mende L.; Zakeeruddin, S. M.; Kay, A.; Nazeeruddin, M. K; Grätzel, M. *Chem. Commun.*, **2005**, 4351.

[10]. Kavan, L.; Grätzel, M. *Electrochim Acta* **1995**, *40*, 643.

[11]. Snaith, H. J.; Grätzel, M. *Adv. Mater.*, **2006**, *18*, 1910.

[12]. Bard, A. J.; Faulkner, L. R. *Electrochemical Methods: Fundamentals and Applications*, second ed., John Wiley and Sons Inc., New York, 2001.

[13]. Zhang, Z.; Zakeeruddin, S. M.; O’Regan, B. C.; Humphry-Baker, R.; Grätzel, M. *J. Phys. Chem. B* **2005**, *109*, 21818.

[14]. Van de Lagemaat, J.; Frank, A. J.; *J. Phys. Chem. B* **2000**, *104*, 4293.

[15]. Bisquert, J. *Phys. Chem. Chem. Phys.* **2003**, *5*, 5360.

[16]. Bisquert, J.; Vikhrenko, V. S. *J. Phys. Chem. B* **2004**, *108*, 2313.
[17]. Shockley, W.; Read, W. T. J. *Phys. Rev*. **1952**, *87*, 835.
[18]. Bisquert, J. *J. Phys. Chem. B* **2004**, *108,* 2323.
[19]. Personal correspondence between Prof. L. M. Peter and Dr. R. Humphry-Baker.
[20]. O'Regan, B. C.; Lenzmann, F. *J. Phys. Chem. B* **2004**, *108,* 4342.
[21]. O'Regan, B. C.; Scully, S.; Mayer, A. C.; Palomares, E.; Durrant, J. *J. Phys. Chem. B* **2005**, *109,* 4616.
[22]. Duffy, N. W.; Peter, L. M.; Rajapakse, R. M. G.; Wijayantha, K. G. U. *J. Phys. Chem. B* **2000**, *104*, 8916.
[23]. Zaban, A.; Greenshtein, M.; Bisquert, J. *Chemphyschem*, **2003**, *4*, 859.
[24]. Kern, R.; Sastrawan, R.; Ferber, J.; Stangl, R.; Luther, J. *Electrochim. Acta* **2002**, *47,* 4213.
[25]. Hauch, A.; Georg, A. Elec*trochim. Acta* **2001**, *46,* 3457.
[26]. Zaban, A.; Meier, A.; Gregg, B. A. *J. Phys. Chem. B* **1997**, *101,* 7985.
[27]. Schwarzburg, K.; Willig, F. *J. Phys. Chem. B* **2003**, *107,* 3552.
[28]. Bisquert, J. *J. Phys. Chem. B* **2002**, *106,* 325.
[29]. Fabregat-Santiago, F.; Garcia-Canadas, J.; Palomares, E.; Clifford, J. N.; Haque, S. A.; Durrant, J. R.; Garcia-Belmonte, G.; Bisquert, J. *J. Appl. Phys.* **2004**, *96*, 6903.
[30]. Pitarch, A.; Garcia-Belmonte, G.; Mora-Sero, I.; Bisquert, J. *Phys. Chem. Chem. Phys.* **2004**, *6,* 2983.
[31]. Fabregat-Santiago, F.; Bisquert, J.; Garcia-Belmonte, G.; Boschloo, G.; Hagfeldt, A. *Sol. Energ. Mat. Sol. C.* **2005**, *87*, 117.
[32]. Wang, Q.; Moser, J.; Grätzel, M. *J. Phys. Chem. B* **2005**, *109*, 14945.
[33]. Wang, Q.; Ito, S.; Grätzel, M.; Fabregat-Santiago, F.; Mora-Seró, I.; Bisquert, J.; Bessho, T.; Imai, H. *J. Phys. Chem. B* **2006**, *110,* 25210.
[34]. Bisquert, J.; Garcia-Belmonte, G.; Fabregat-Santiago, F.; Compte, A. *Elec. Commun.* **1999**, *1*,429.
[35]. Bisquert, J. *Phys. Chem. Chem. Phys.* **2003**, *2*, 4185.

3. Silica Coated and Insulated TiO_2 Microparticles as Light-Scattering Layer: Electronic Function of TiO_2 Light-Scattering Layer in Dye-Sensitized Solar Cells

Published in *Z. Phys. Chem.* **2007**, *221*, 319-328.

Zhipan Zhang[†], *Seigo Ito*[†], *Brian O'Regan*[§], *Daibin Kuang*[†], *Shaik Mohammed Zakeeruddin*[†], *Paul Liska*[†], *Raphaël Charvet*[†], *Pascal Comte*[†], *Mohammad Khaja Nazeeruddin*[†], *Peter Péchy*[†], *Robin Humphry-Baker*[†], *Tsuguo Koyanagi*[‡], *Takaki Mizuno*[‡] *and Michael Grätzel*[*,†],

Laboratory for Photonics and Interfaces, Institute of Chemical Sciences and Engineering, Swiss Federal Institute of Technology, CH-1015 Lausanne, Switzerland; Electronic Materials and Devices, Department of Chemistry and Physics, Imperial College, SW7 2AZ London, United Kingdom and Catalysts & Chemicals Ind. Co. Ltd.(CCIC), 13-2, Kitaminato-machi, Wakamatsu-ku, Kitakyushu-shi, 808-0027, Japan

† Swiss Federal Institute of Technology

§ Imperial College

‡ Catalysts & Chemicals Ind. Co. Ltd.(CCIC)

[*] To whom the correspondence should be made.

3.1 Abstract

Dye-sensitized solar cells have been fabricated with different kinds of TiO_2 films including silica coated and SiO_2 coated TiO_2 microparticles as light-scattering layer (LSL). Results show that the LSL barely affected the cell's dark current, whereas under illumination, it made a significant contribution to the total photocurrent. Photo-voltage decay measurements performed under bias

illumination show the density of electronic states (*DOS*) of the LSL to be two times smaller than that of a transparent nanoparticle layer (TNL). DSCs fabricated only with a 4.5 μm thick LSL showed an impressive conversion efficiency of 5% despite being pale pink in color.

3.2 Introduction

The dye-sensitized solar cell (DSC) has attracted considerable scientific and industrial interests during the past decade. Efficiencies exceeding 11% under AM 1.5 simulator have already been achieved.[1]-[6] As an economically feasible alternative to conventional photovoltaic devices, they offer relatively low-cost solar devices with a high light-to-power conversion efficiency. DSCs comprise a dye-sensitized nanoporous TiO_2 film infiltrated with a hole transporting material, typically a liquid electrolyte containing the iodide/triiodide (I^-/I_3^-) redox couple. Under illumination, ultrafast electron injection takes place from the photoexcited dye molecules into the conduction band of the oxide semiconductor, followed by dye regeneration and hole transport to the counter electrode. The injected electrons then diffuse through the oxide film to the conducting oxide (TCO) current collector and pass subsequently via the external circuit to the counter electrode, where the reduction of the hole carrier, e.g. triiodide ions, completes the cycle of events effecting electric power generation from sunlight.

Sufficient light absorption is a prerequisite to attain a high efficiency for such a cell. To maximize the light-harvesting, nanoporous TiO_2 films with a large surface area are usually selected as photoanode to increase the amount of surface-anchored sensitizers. However, this transparent layer of nanoparticles cannot be thickened without adversely affecting the film’s mechanical properties, limiting the mass transport in the electrolyte and reducing the open circuit photovoltage (V_{oc}) of the cell by augmenting the dark current, which is proportional to the surface area of the film. As an alternative strategy to enhance the harvesting of sunlight the molar extinction coefficient of ruthenium sensitizers has been improved by extending the conjugated system of the donating ligand.[7],[8] The other approach is to deposite large light-scattering TiO_2 microparticles on top of the nano-particle layer in order to increase the average optical path length of the light within the film. The optical effect of the light-scattering layer has been studied by theoretical and experimental methods. Ferber and Luther, using computer simulations, reported that incorporating large particles in a porous material composed of small particles leads to a gain in photon absorption of around 20% for a 15 μm film sensitized by the standard N-719 dye.[9] Rothenberger et al. used a modified 4-flux model to analyze the double layer film. Compared to a 10 μm thick single layer of transparent nanoparticles, a 6% increase in absorbed flux between 400 and 800 nm was found with a double layer configuration consisting of 5 μm transparent nanoparticles plus 5 μm scattering colloids.[10] Recently, Arakawa et al. tuned the TiO_2 photoelectrode morphology and investigated different structures with layers of nanoparticles, light-scattering particles, and mixture of both particles on the conducting glass for a desirable sequence and thickness.[11] The data confirmed the superiority of the double-layer structure with regards to a mono-layer configuration.

The present study examines the electronic and optical function of the light-scattering layer (LSL) in the DSC by measuring the film's photovoltaic performance and relates it to its chemical capacitance. The latter was determined using phototransient methods.

3.3 Experimental section

Scheme 1 depicts the structure of film used in the present work. Four types of TiO_2 electrodes were screen-printed on fluorine-doped transparent tin oxide (FTO) (10 Ω/m, Nippon Sheet Glass) by a screen printing method. The first type of film, denoted as "TNL-TiO_2 / LSL-TiO_2", is the well-known double layer of mesoscopic TiO_2 with $TiCl_4$ post treatment (diameter of anatase TiO_2 nanoparticles: 20 nm, thickness: 3.4 μm; diameter of anatase TiO_2 microparticles: 400 nm, thickness: 4.5 μm, 20% weight of 10 nm anatase TiO_2 nanoparticles in diameter were added for a better adhesion between the microparticles). This film structure could be regarded as the control while the following three types of electrodes are modifications to this prototype. The second kind of electrode noted as "TNL-TiO_2 / SiO_2 coated LSL-TiO_2" was prepared by replacing the normal TiO_2 microparticles by SiO_2 coated TiO_2 microparticles (CCIC, thickness of SiO_2 *ca.* 20 nm). The insertion of a 1.5 μm SiO_2 insulating layer of 10 nm SiO_2 nanoparticles between the nano-TiO_2 layer and micro-TiO_2 layer led to the third configuration designated as "TNL-TiO_2 / SiO_2 / LSL-TiO_2". The last type of film was made of TiO_2 microparticles alone with a thickness of 4.5 μm and is referred to as "LSL-TiO_2". For the sake of clarity, cells made with different films of TNL-TiO_2 / LSL-TiO_2, TNL-TiO_2 / SiO_2 coated LSL-TiO_2, TNL-TiO_2 / SiO_2 / LSL-TiO_2 and LSL-TiO_2 were denoted as cell **a**, **b**, **c** and **d**, respectively. A reference cell was also fabricated with 3.4 μm TiO_2 nanoparticles, referred to as TNL-TiO_2, and denoted as cell **e**.

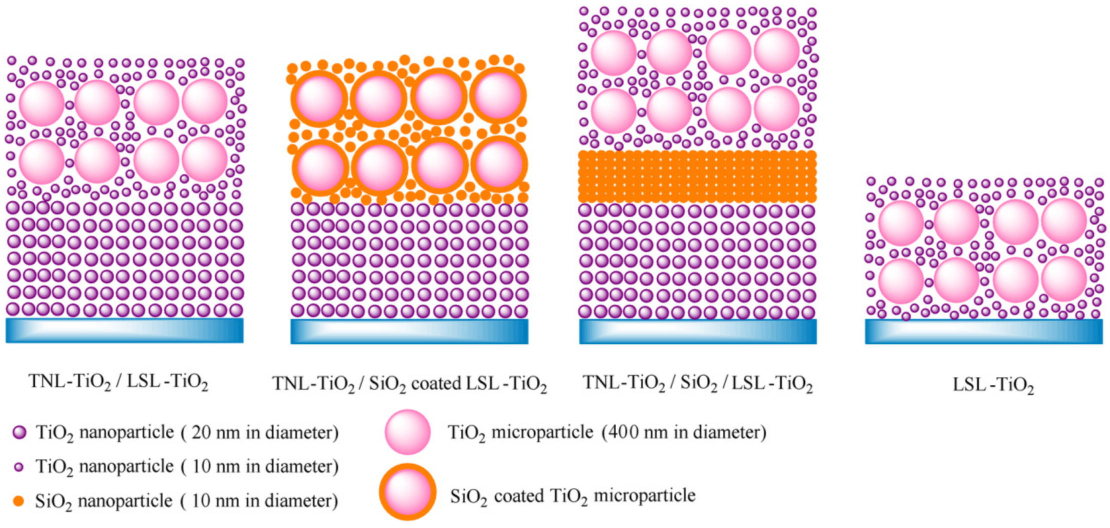

Scheme 1. Schematic diagram showing the structures of TiO_2 electrodes used in present work.

The N719: Ru dye [12] was adsorbed by soaking the above electrodes after sintering in a 0.5 mM Ru dye solution in acetonitrile/tert-butanol (50/50, v/v) for 24 h. The Pt counter electrodes were prepared by spreading a drop of H_2PtCl_6 solution on the FTO and heating at 400 °C for 15 min. Cells were sealed by using hot-melt ionomer films of Surlyn 1702 (DuPont). The electrolyte contained 0.60 M 1-methyl-3-butyl- imidazolium iodide, 0.03 M I_2, 0.10 M guanidinium thiocyanate and 0.50 M 4-tertbutylpyridine in a mixed solvent of acetonitrile and valeronitrile (volume ratio: 85 : 15). To improve and stabilize the photovoltaic performances, an anti-reflection and UV-cut off film ($\lambda < 380$ nm, ARKTOP, ASAHI GLASS) was attached to the DSC surface.

3.4 Result and Discussion

Figure 1 shows the current-voltage characteristics of different cells (**a** to **e**) fabricated with the five types of TiO_2 electrodes. Cell **a**, **b** or **c** exhibited quite similar dark current over the whole potential range, while cell **d** showed much smaller dark current at the same forward bias voltage. The result indicated that the TiO_2-TNL dominated the dark current of the DSC and that the LSL contributed little dark current. This is reasonable since the dark current in DSC scales with the surface area, which due to the larger particle size is significantly smaller for the light scattering layer had than the transparent layer.

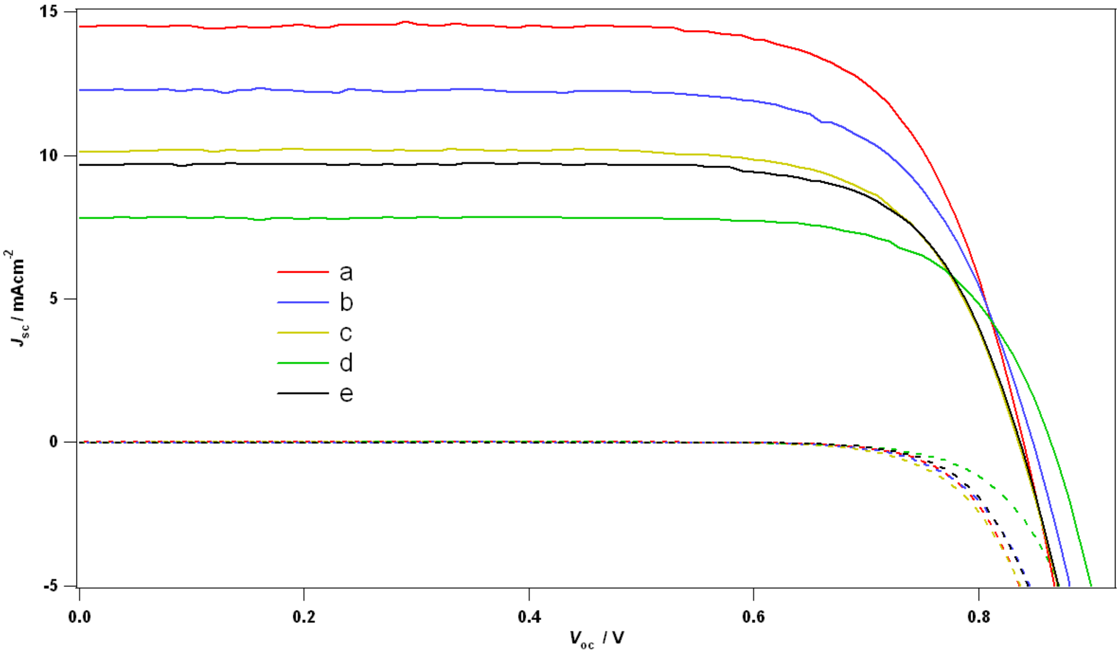

Figure 1. Current-voltage characteristics of different cells in the dark (dash line) and under simulated illumination (AM 1.5, 100 mW cm^{-2}). Cells were fabricated with films of a) TNL-TiO_2 / LSL-TiO_2, b) TNL-TiO_2 / SiO_2 coated LSL-TiO_2, c) TNL-TiO_2 / SiO_2 / LSL-TiO_2, d) LSL-TiO_2 and e) TNL-TiO_2.

The photovoltaic performance data of these four cells under AM 1.5 simulated illumination are summarized in Table 1. Champion cells are typically made with much thicker films than cell **a**, i.e. a double layer comprised of a 14 μm layer of 20 nm sized TiO_2 particles covered by a 4 μm thick layer of TiO_2 microparticles.[13] As a result, the latter exhibits a lower J_{sc} (14.5 mA cm^{-2} as compared to 18.7 mA cm^{-2}) but a higher V_{oc} (840 mV compared to 798 mV) than the former DSC type. It was striking to find that decreasing the thickness of TiO_2 nanoparticle layer by as much as a factor of 4, i.e. from 14 μm to 3.4 μm, reduced the power conversion efficiency only by 12 percent, i.e. from 10.1 % to 8.8 %.[13] The loss in the short circuit photo-current is partially offset by an augmentation of the V_{oc} both effects resulting from the lower surface area decreasing the surface area and the amount of adsorbed dye.

Table 1. Photovoltaic characteristics of dye-sensitized solar cells made with four different kinds of TiO_2 electrode. Data were averaged on three cells.

Cell	Electrodes	J_{sc} / mA cm^{-2}	V_{oc} / mV	*FF*	η / %

a	TNL-TiO_2 / LSL-TiO_2	14.5 ± 0.2	840 ± 6	0.72 ± 0.01	8.8 ± 0.1
b	TNL-TiO_2 / SiO_2 coated LSL-TiO_2	12.6 ± 0.3	845 ± 5	0.71 ± 0.01	7.6 ± 0.2
c	TNL-TiO_2 / SiO_2 / LSL-TiO_2	10.1 ± 0.1	836 ± 5	0.73 ± 0.01	6.2 ± 0.1
d	LSL-TiO_2	7.8 ± 0.1	864 ± 4	0.75 ± 0.01	5.0 ± 0.1
e	TNL-TiO_2	9.7 ± 0.1	834 ± 3	0.74 ± 0.04	6.0± 0.0

Cell **d** showed a J_{sc} of 7.8 mA cm^{-2} and an impressive efficiency of 5%. The open circuit voltage of cell **d** was ~25 mV higher than other cells (**a**, **b, c** and **e)**, which results again from the lower surface area of the LSL layer reducing the dark current. Comparing the currents of cell **a** to **e**, it is evident that the light scattering layer enhanced the light absorption enhancing the J_{sc} value. Though cell was only pale pink in color, multiple scattering contains the photons in the TiO_2 electrode extending the effective optical length. Thus in cell **d** the surface-anchored dye molecules could still absorb enough light to attain a respectable light-to-power conversion efficiency.

The light-scattering and electrical effects of the LSL-TiO_2 deposited on the TNL-TiO_2 were discriminated by using SiO_2 coating on the LSL-TiO_2 (fig. 1**b**) or a SiO_2 layer between the TNL-TiO_2 and LSL-TiO_2 layer (fig. 1**c**). The insulating SiO_2 layer (for electrode **c**) was examined with a configuration of FTO/SiO_2-layer/LSL-TiO_2. In this structure, the SiO_2 layer became an effective electrical insulator, blocking 99.5% of the photocurrent, the J_{sc} being reduced (from 7.8 mA cm^{-2} to 0.04 mA cm^{-2}. SiO_2 coating on the LSL-TiO_2 (electrode **b**) reduced the surface-dye loading from $8.0 \times 10^{-9} cm^{-2}\ \mu m^{-1}$ to $3.0 \times 10^{-9} cm^{-2}\ \mu m^{-1}$.[14] The electrical insulating effect of the SiO_2 coating was examined separately using the SiO_2-coated LSL-TiO_2 particles on the FTO substrate. The J_{sc} was 0.8 mA cm^{-2} for this configuration. Hence, the SiO_2 coating reduces the surface-dye loading and the DSC photocurrent by a factor of 2.7 and 10 respectively. From these results, the difference in DSC photocurrent between cell **b** and **c** is predicted to be 0.8 mA cm^{-2}. However, the observed decrease in J_{sc} was 2.5 mA cm^{-2}. Considering only a thin TNL-TiO_2 are used in both cells and incident light can not be fully absorbed in this nanoporous layer, such a three fold difference of photocurrent from the prediction is possibly due to the diminished dye adsorption by silica-coated LSL in cell **b**, since in the case of cell **c**, LSL is electronically insulated with the beneath TNL and the injected electrons therein can not be transported to the collecting electrode.

In order to calculate the electron state density of the light scattering layer, transient measurements were employed to study cells **a** to **d**.[15],[16] We used a millisecond pulse from a red diode to increase the concentration of charge carriers producing small voltage increase near the V_{oc} of the cell under bias light and measured the voltage decay process thereafter. The capacitance of the TiO_2/electrolyte interface and *DOS* at the V_{oc} were derived from the relation $C = \Delta Q/\Delta V$, where ΔV is the peak of the transient voltage, and ΔQ is the number of electrons injected during the light flash. The latter was determined by integrating the photocurrent transient at short circuit condition generated from an identical pulse.

Figure 2 depicts the capacitance of the cell *vs.* the open-circuit voltage, the curves being fitted to a single exponential, as has been found previously.[17]-[19] Over the whole V_{oc} range, cell **a** had the largest capacitance, followed by cell **b** and **c** and cell **d** which had the lowest capacitance. This was consistent with the trend observed for the short circuit current. The *DOS* (in electron states / cm^3 V) was then calculated from *C* using the equation [16],

$$DOS = (6.24\times 10^{18})\frac{C}{d(1-p)} \tag{1}$$

where *d* and *p* represent the thickness and porosity of the TiO_2 film, respectively. Figure 2 shows the curves of *DOS* vs. V_{oc} for TiO_2 TNL and LSL. The *DOS* of the LSL was found to be about 50% of the TNL. It should also be noted that the method used here may overestimate the *DOS* of LSL. The *DOS* was calculated from the cell capacitance of cell **d** purely made with LSL material, and for this type of film, light scattering effect was more pronounced than the double layer configuration (as cell **a**), because in the latter case, the incident light was first absorbed and thus attenuated by dye-stained TiO_2 TNL before it could be scattered by LSL. However, this would not greatly affect the above discussion to the benefit of LSL.

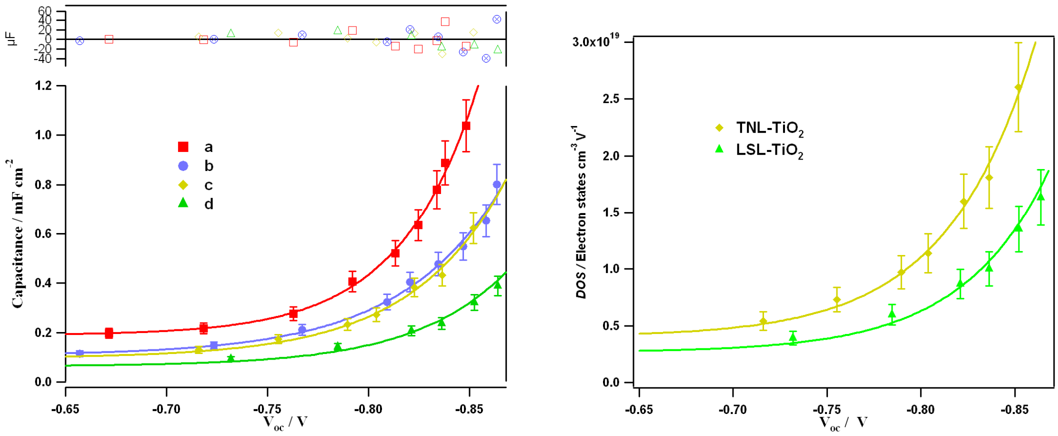

Figure 2. Results of phototransient voltage measurements with above-mentioned cells (**a** to **d**). Left: Capacitance *vs.* Open-circuit potential; Right: *DOS* of TiO_2 TNL and LSL *vs*. Open-circuit potential. The capacitance is calculated in term of cell area.

Table 2. Characteristics of TiO_2 transparent nanoparticle layer (TNL) and light-scattering layer (LSL). Data was calculated as the average of three samples, except for the BET measurements: specific surface area and average pore size. The roughness factor was obtained by multiplying specific surface area and TiO_2 weight. *DOS* values were taken at an open-circuit voltage of 0.85 V on the fitting curve.

	TNL-TiO_2	LSL-TiO_2
Thickness / µm	3.4	4.5
Specific surface area / m^2 g^{-1}	79.7	27.1
Porosity	0.56	0.67
Roughness factor / μm^{-1}	138 ± 2	35 ± 1
DOS / electron states cm^{-3} V^{-1}	$(2.6 \pm 0.4) \times 10^{19}$	$(1.4 \pm 0.2) \times 10^{19}$

We have elucidated the opto-electronic function of the TiO_2 light-scattering layer in dye-sensitizer solar cells. This layer barely affected dark current, while it contributed considerable photocurrent under illumination. A cell made purely with light-scattering material showed an impressive efficiency of 5% at AM 1.5 illumination and phototransient measurements showed that the *DOS* of light-scattering layer is about 50% that of TiO_2 transparent nanoparticle layer. The present study confirmed the beneficial effect of light-scattering layer in DSCs, which should foster its widespread application for enhancing the efficiency of this kind of solar cell in the future.

In conclusion the present study shows that the LSL barely affected the DSC dark current, whereas under illumination (AM 1.5, 100 mW cm^{-2}), it made a significant contribution to the total photocurrent. The density of states of the light scattering layer was two times smaller than that of the transparent nanoparticle layer. A DSC fabricated only with a 4 μm scattering layer material showed an impressive efficiency of 5% even though the cell was pale pink in color.

3.5 References and Notes

[1]. O'Regan, B.; Grätzel, M. *Nature* **1991,** *353*, 737.

[2]. Grätzel, M. *Nature* **2001,** *414*, 338.

[3]. Hagfeldt, A.; Grätzel, M. *Chem. Rev.* **1995**, *95*, 49.

[4]. Grätzel, M. *J. Photochem. Photobio. A* **2004**, 16*4*, 3.

[5]. Grätzel, M. *Chem. Lett.* **2005**, *34*, 8.

[6]. Nazeeruddin, M.K.; De Angelis, F.; Fantacci, S.; Selloni, A.; Viscardi, G.; Liska, P; Ito, S.; Takeru, B.; Grätzel, M. *J. Am. Chem. Soc.* **2005**, *127*, 16835.

[7]. Wang, P.; Zakeeruddin, S. M.; Moser, J. E.; Comte, P.; Aranyos, V.; Hagfeldt, A.; Nazeeruddin, M. K.; Grätzel, M. *Adv. Mater.* **2004**, *16*, 1806.

[8]. Wang, P.; Klein, C.; Humphry-Baker, R.; Zakeeruddin, S. M.; Grätzel, M. *J. Am. Chem. Soc.* **2005**, *127*, 808.

[9]. Ferber, J.; Luther, J. *Sol. Energy Mater. Sol. Cells* **1998**, *54*, 265.

[10]. Rothenberger, G; Comte, P.; Grätzel, M. *Sol. Energy Mater. Sol. Cells* **1999**, *58*, 321.

[11]. Wang, Z. S.; Kawauchi, H.; Kashima, T.; Arakawa, H. *Coordin. Chem. Rev.* **2004**, *248*, 1381.

[12]. Nazeeruddin, M.K.; Zakeeruddin, S.M.; Humphry-Baker, R.; Jirousek, M; Liska, P.; Vlachopoulos, N.; Shklover, V.; Fischer, C.H.; Grätzel, M. *Inorg. Chem.* **1999**, *38*, 6298,

[13]. Ito, S.; Liska, P.; Comte, P; Charvet, R. L.; Pechy, P.; Bach, U.; Schmidt-Mende, L.; Zakeeruddin, S.M.; Kay, A.; Nazeeruddin, M. K.; Grätzel, M. *Chem. Commun.* **2005**, 4351.

[14]. First, films of LSL (thickness of 4.5 µm) and SiO_2 coated LSL (thickness of 4.5 µm) were dyed overnight with N 719 solution. The dye amount was determined by dissolving the absorbed dyes by putting the films in 0.1 M *tetra*-butyl ammonium hydroxide solution and measuring the absorbance of this solution at 518 nm. The molar extinction coefficient of N 719 at 518 nm was 1.3×10^{-4} M^{-1} cm^{-1} (from reference 12).

[15]. O'Regan, B. C.; Lenzmann, F. *J. Phys. Chem. B* **2004**, *108*, 4342.

[16]. O’Regan, B. C.; Scully, S.; Mayer, A. C.; Palomares, E.; Durrant, J. *J. Phys. Chem. B* **2005**, *109*, 4616.

[17]. Van de Lagemaat, J.; Park, N.-G.; Frank, A. J. *J. Phys. Chem. B* **2000**, *104*, 2044.

[18]. Willis, R. L.; Olson, C.; O’Regan, B.; Lutz, T.; Nelson, J.; Durrant, J. R. *J. Phys. Chem. B* **2002**, *106*, 7605.

[19]. Duffy, N. W.; Peter, L. M.; Rajapakse, R. M. G.; Wijayantha, K. G. U. *Electrochem. Commun.* **2000**, *2*, 658.

4. Influence of 4-Guanidinobutyric Acid as Coadsorbent in Reducing Recombination in Dye-Sensitized Solar Cells

Published in J. Phys. Chem. B **2005,** 109, 21818-21824.

Zhipan Zhang[†], *Shaik M. Zakeeruddin*[†], *Brian C. O'Regan*[§], *Robin Humphry-Baker*[†] *and Michael Grätzel*[*,†]

Laboratory for Photonics and Interfaces, Institute of Chemical Sciences and Engineering, Swiss Federal Institute of Technology, CH-1015 Lausanne, Switzerland, and Electronic Materials and Devices, Department of Chemistry and Physics, Imperial College, SW7 2AZ London, United Kingdom

† Swiss Federal Institute of Technology

§ Imperial College

[*] To whom the correspondence should be made.

4.1 Abstract

Dye-sensitized solar cells based on nanocrystalline TiO_2 have been fabricated with an amphiphilic ruthenium sensitizer [Ru (4,4'-dicarboxylic acid-2,2'-bipyridine) (4,4'-bis(p-hexyloxystyryl)-2,2'-bipyridine)$(NCS)_2$], coded as K-19, and 4-guanidinobutyric acid (GBA) as coadsorbent. The cells showed a ~50 mV increase in open circuit voltage and a negligible current decrease in comparison with cells without GBA co-grafting. The performance of both types of devices was evaluated on the basis of their photocurrent-voltage characteristics, dark current measurements, cyclic voltammetry, electrochemical impedance spectroscopy and phototransient decay methods. The results indicate that GBA shifted the conduction band of TiO_2 towards a more negative potential and reduced the interfacial charge transfer reaction from conduction band

electrons to triiodide in the electrolyte (also known as the back reaction). In addition, the devices with GBA co-grafting showed an excellent stability with a power conversion efficiency of 8% under simulated full sunlight (air mass 1.5, 100 mW cm^{-2}) during visible light soaking at 60 °C.

4.2 Introduction

The success of dye-sensitized solar cells (DSCs) has increasingly fostered scientific and industrial research on the photovoltaic properties of wide band gap oxides, mainly TiO_2 based, solar cells during the past years.[1]-[3] Unlike conventional p-n junction solar devices, a DSC employs interconnected inorganic semiconductor nanocrystals to form a “bulk” junction with a huge surface area at the semiconductor/electrolyte interface and, thus, provides sufficient anchoring sites for sensitizers to attain effective light-harvesting and energy conversion. Achieving more than 11% efficiency with acetonitrile- based electrolyte and 8% long-term stability at 80 °C with a low volatile electrolyte have transformed DSC into a more attractive candidate as a substitute for conventional silicon solar cells.[4]-[6]

However, the ideal of a “bulk” junction is impaired by the occurrence of interfacial charge recombination of photoinjected electrons, the main processes being depicted in Scheme 1. Under illumination, the sensitizer is excited and injects electrons into the conduction band of the mesoscopic TiO_2 film. Electron transfer from a donor, most typically the iodide, then regenerates the dye ground state. The transportation of the electrons in TiO_2 is strongly influenced by trapping (1) and detrapping (2) effects. Previous results showed that trapping is about 3 orders faster than detrapping, so nearly all photoinjected electrons are located in trap states.[7] The source of recombination includes the recapture of injected electrons in these traps by the oxidized sensitizer (S^+) anchored on the TiO_2 surface (3) or back reaction with the oxidized component of the redox couple present in the electrolyte, I_3^- (4). Considering the relatively fast regeneration of dye by iodide, the latter would be expected to be the predominant recombination channel in DSCs. Apart from the very large area of the junction, the recombination is favored by the fact that the size of the nanoparticles is too small to support enough band bending which would generate an internal electric field that is believed to be essential to afford charge separation in photo-electrochemical devices.[3] Theoretically, the back reaction can be blocked by surface modifications such as introducing an insulating layer on the solvent-exposed parts of the nanoporous electrode in order to passivate the interface [9,10] or when core-shell structured particles were used instead of bare TiO_2.[11]-[14] Coating of TiO_2 nanoparticles with a shell material of a slightly more negative CB will result in an energy barrier that assists electron injection while retarding its diffusion in the opposite direction. In both of these cases, the devices showed higher values of short-circuit current density (J_{sc}), open-circuit voltage (V_{oc}) and fill factor (*FF*), and, thus, better performance.

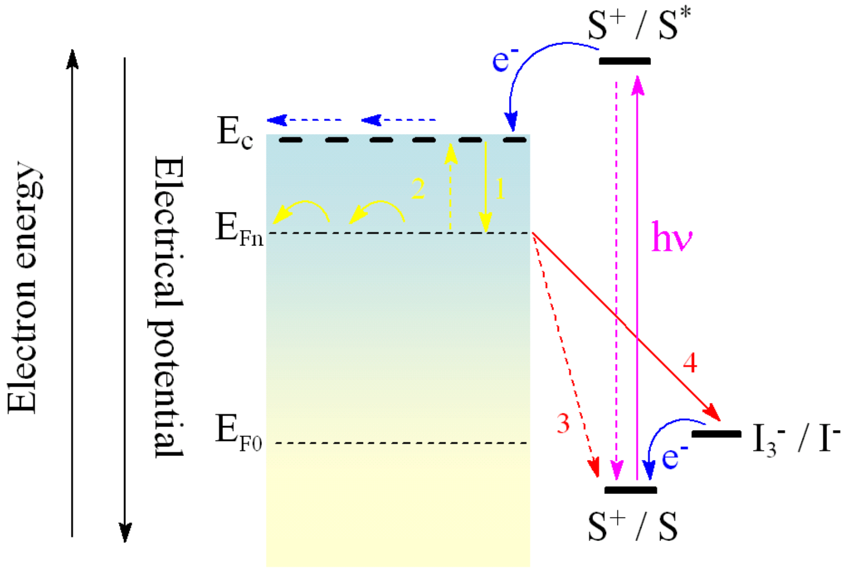

Scheme 1. Schematic diagram showing electron transportation and recombination processes in a dye- sensitized nanocrystalline solar cell with a liquid-based I_3^- / I^- electrolyte. Trapping (1) and detrapping (2) of electrons in TiO_2; Recombination of trapped electrons with the oxidized sensitizer S^+ (3) and with the redox couple (4).

Co-grafting of dyes with amphiphilic molecules containing carboxylic or phosphonic end groups were reported to considerably enhance the stability and the performance of DSCs.[6],[15]-[17] The coadsorption leads to the formation of a more compact monolayer, comprised of the dye and coadsorbent, than the adsorption of dye alone. This insulating molecular layer effectively shields the back electron transfer from the TiO_2 conduction band to triiodide and gives a higher open circuit voltage. In this paper, an amphiphilic ruthenium sensitizer coded as K-19 is coadsorbed with 4-guanidinobutyric acid (GBA), a combination which enhances the open circuit voltage by 50 mV and increases the overall conversion efficiency by 10%. Photovoltage transient measurements and electrochemical impedance spectroscopy techniques were applied in order to understand the role of the coadsorbent in the enhancement of the efficiency and open circuit potential. The results have shown that the presence of the coadsorbent resulted in a small negative shift of the conduction band edge of TiO_2 nanocrystals as well as a decrease in the back reaction rate constant.

4.3 Experimental Section

Reagents and Electrolytes. All chemicals and solvents used in the present work were of puriss quality. *N*-methylbenzimidazole (NMBI) was purchased from Aldrich and recrystallized from diethyl ether before use. GBA was purchased from Fluka and used as obtained. 3-Methoxypropionitrile (MPN) puriss quality was obtained from Fluka and distilled before use. K-19 was synthesized as reported in our earlier publication [17] and the structure is shown in Figure1. 1-Methyl-3-propylimidazolium iodide (PMII) was prepared according to the literature method [15] and its purity confirmed by ^{1}H NMR spectrum. Sephadex LH-20 was obtained from Pharmacia (Sweden). 400-nm-sized TiO_2 particles were received as a gift from CCIC (Japan). The electrolyte contained 0.8 M 1-propyl-3-methylimidazolium iodide, 0.15 M I_2, 0.1 M guanidinium thiocyanate, and 0.5 M *N*-methylbenzimidazole in MPN.

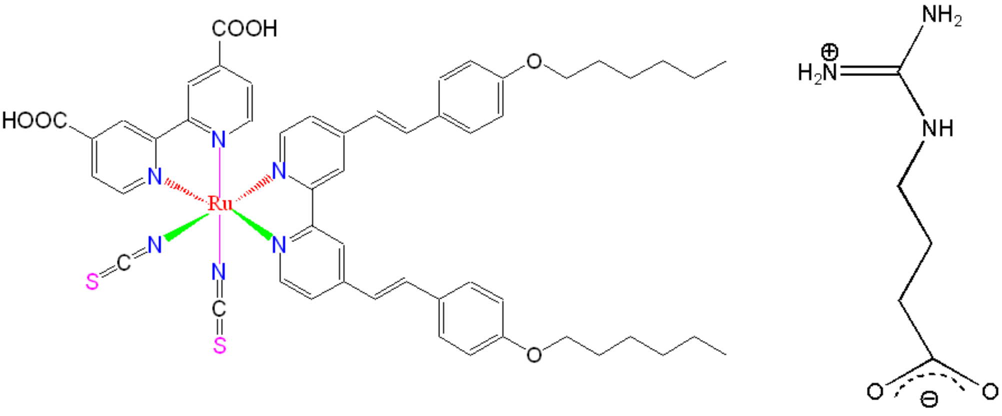

K -19

GBA

Figure 1. Structure of the K-19 sensitizer and GBA.

Spectroscopic Measurements. IR spectra were measured using a FTS 7000 FTIR spectrometer (Digilab, USA). Spectra were derived from 64 scans at a resolution of 2 cm^{-1}. All samples were measured under identical mechanical force used to push the mesoscopic TiO_2 films in contact with the diamond window. No ATR correction has been applied to the data. The dye-loaded electrodes were rinsed in acetonitrile and dried prior to measuring the spectra.

For photoelectrochemical measurements, a 450 W xenon light source (Oriel, USA) was used to give an irradiance of 100 mW cm^{-2} (the equivalent of one sun at AM 1.5) at the surface of solar cell. The spectral output of the lamp was matched in the region of 350-750 nm with the aid of a Schott K113 Tempax sunlight filter (Präzisions Glas & Optik GmbH, Germany) so as to reduce the mismatch between the simulated and true solar spectra to less than 2%. Various incident light intensities were regulated with neutral wire mesh attenuators. The current voltage characteristics of the cell under these conditions were obtained by applying an external potential bias to the cell and measuring the generated photocurrent with a Keithley model 2400 digital source meter (Keithley, USA).

Photovoltage transients were observed using a pump pulse generated by a ring of red LEDs controlled by a fast solid-state switch. Pulse widths of 100 µs were used, with a rise and fall time of ≤ 2 µs. The pulse was incident on the photoanode side of the cell and its intensity was controlled to keep the modulation of the voltage below 10 mV. White bias light, also incident on the same side of the cell, was supplied by 10 W “Solarc” lamps (WelchAllyn) that are also of the metal-halogen type. The bias light was attenuated when needed by neutral-density filters. When the pulse intensity from the red diodes was insufficient to give voltage signals greater than 0.5 mV, a white flash lamp was used. The flash time was also 100 µs, with a fall half time of 20 µs. The time resolution of the potentiostat is 20 µs; thus, transient phenomena with time constants ≥ 40 µs could be measured. It is important to note the Solarc light sources contain a UV component similar to that found in sunlight.

Cyclic voltammetry measurements were performed on a computer-controlled Autolab P20 electrochemical workstation (Eco Chimie, Netherlands) in combination with a conventional three-electrode, one-compartment electrochemical cell. A dye-coated nanocrystalline TiO_2 film in the absence (Electrode A) or presence (Electrode B) of GBA co-grafting was employed as the working electrode. A Pt foil and an Ag disk were used as counter and reference electrodes, respectively. The reference electrode was calibrated by measuring the redox potential of ferrocene dissolved in 1-methyl-3-ethylimidazolium bis (trifluoromethyl) sulfonyl) imide (EMITFSI) and the redox potentials were converted to those versus a normal hydrogen electrode (NHE) reference scale by adding a constant of 0.67 V (See Section **2.3** for remarks).

Impedance measurements were performed with a computer controlled potentiostat (EG&G, Model 273) equipped with a frequency response analyzer (EG&G, Model 1025). The frequency range is 0.005-100 KHz and the magnitude of the modulation signal is 10mV. The obtained spectra were fitted with Z-View software (v2.1b, Scribner Associates Inc.) in terms of appropriate equivalent circuits.

Device Fabrication. A double-layer TiO_2 mesoscopic film was used as the photoanode. An 8-μm thick transparent layer of 20-nm-sized TiO_2 particles was first printed on the fluorine-doped SnO_2 conducting glass electrode and further coated with a 5 μm thick second layer of 400 nm light scattering anatase particles. The details for the preparation of mesoscopic TiO_2 film has been described elsewhere.[16],[18] The double-layer structured TiO_2 electrode was first sintered at 500 °C for 20 minutes and cooled at ambient temperature down to 80 °C. It was then immersed into the dye solution at room temperature for 12 h before assembly with a thermally platinized conducting glass counter electrode. For the present work, two kinds of sensitizer solution were used. Solution A consisted of 0.3 mM K-19 dye in acetonitrile and *tert*-butyl alcohol (volume ratio, 1:1), while solution B contained 0.3 mM K-19 dye and 0.3 mM GBA as coadsorbent in the same solvent. To prepare solution B, GBA was first dissolved in 10% water and ethanol mixture (30 mM) then added to the dye solution to bring it to 0.3 mM GBA. The electrodes were separated by a 35-μm-thick Bynel hot-melt ring (DuPont, USA) and sealed by heating. The internal space was evacuated, then filled with electrolyte through a filling hole made by a sandblasting drill on the counter electrode glass substrate. Finally, the electrolyte introduction hole was sealed with a Bynel sheet under a thin glass cover by heating to produce device A without and device B with GBA co-grafting.

Stability Test. Hermetically sealed cells were used for longterm stability tests under moderate thermal stress and visible light soaking. After a short thermal aging in the oven, the cells were covered with a 50 μm-thick polyester film (Preservation Equipment Ltd, UK) as a UV cutoff filter (below 400 nm) and irradiated at open circuit under a Suntest CPS plus lamp (ATLAS GmbH, 100 mW cm^{-2}, 60 °C).

Analysis. Electrochemical impedance spectroscopy (EIS) is a well-known technique for characterization of electrochemical systems. As a steady-state method, it modulates the external voltage bias and measures the synchronized response as a function of frequency. Recently, several groups have reported interesting results by using EIS to evaluate the performance of DSCs including our own publication.[19]-[28] In principle, the modulation of external voltage results in a fluctuation of the quasi-Fermi level of the TiO_2 electrode, which changes i) the population of surface and bulk states with electrons and ii) the recombination current across the TiO_2 / electrolyte interface. Hence, analyzing EIS measured in the dark with an appropriate model proposed by Bisquert [24] yields parameters of chemical capacitance C_μ and charge transfer resistance R_{rec} corresponding to effect i) and ii), respectively. In the present work the EIS spectra of the cell were measured at forward biases near its V_{oc}, C_μ is taken as the TiO_2 film capacitance which is proportional to the density of states (DOS) including both surface and bulk traps. R_{rec} reflects the direct transfer of electrons from the oxide conduction band to the triiodide in the electrolyte. The product of these two quantities gives a time constant, the observed electron lifetime, $\tau_r = R_{rec}C_\mu$. This τ_r relates more properly to the *response time* with a general meaning of the characteristic time for the decay under a small perturbation,[25] yet it is often interpreted as the *electron lifetime* and we used the latter term in our discussion.

In transient photovoltage experiments, we used red diodes as a probe to generate a perturbation near the V_{oc} of the cell under the bias light and measured the voltage decay process thereafter. Normally, the decay follows closely a single exponential form, thus the recombination rate constant, k, can be extracted from the slope of the semi-logarithmic plot. The capacitance of the TiO_2/electrolyte interface and DOS at the V_{oc} are calculated as $C = \Delta Q/\Delta V$, where ΔV is the peak of the transient, and ΔQ is the number of electrons injected during the light flash. The latter is determined by integrating a photocurrent transient at short circuit condition generated from an identical pulse. This method may underestimate the actual injected charge by the fraction of electrons that are lost to recombination during transport. The error is thought to be less than 30% in the worst case, and more critically, it will affect only the magnitude but not the shape of the calculated capacitance *vs.* potential curves.[29],[30]

4.4 Results and Discussion

Figure 2 shows the attenuated total reflectance FTIR (ATR-FTIR) spectra of nanoporous TiO_2 electrode A and electrode B with typical peaks of K-19 sensitizer as we have reported before.[17] the single feature at 2103 cm^{-1} arises from the thiocyanato group, the bands at 1625 cm^{-1} and1385 cm^{-1} are for the asymmetric and symmetric stretching modes of carboxylate groups, and the signals observed at 2932 and 2862 cm^{-1} correspond to the asymmetric and symmetric stretching modes of the CH_2 units. The sharp absorption at 1597 cm^{-1} is attributed to the vibration mode of the double bond between two aromatic rings. The peaks located at 1538 and 1429 cm^{-1} are ascribed to the aromatic modes of bipyridyl while the broad band centered at 3440 cm^{-1} is due to adsorbed water presumably from the dye solution since the TiO_2 film is heated prior to staining.

Spectrum b was measured with electrode B, which was stained from the solution consisting of K-19 sensitizer and GBA at equal concentrations. It is well established that the characteristic peak of the thiocyanato group at 2103 cm^{-1} is a sensitive measure of the adsorbed amount of sensitizer. The fact that the intensity of this peak for K-19 showed a decrease by about 25% indicates that one fourth of the dye has been replaced by GBA during coadsorption. The decrease in the concentration of dye on the surface of the TiO_2 electrode is also confirmed by measuring the transparent films by UV visible spectroscopy. Due to the presence of GBA on electrode B several new bands are observed. The peak at *ca*. 1668 cm^{-1} is due to the asymmetric stretching of the carboxylate group of GBA. In comparison with its counterpart resulting from the pure K-19 sensitizer, the carboxylate group of GBA does not exhibit conjugation with the pyridine ring and, consequently, the absorption appears at higher wave numbers. Likewise, two conspicuous peaks centered at 3174 cm^{-1} and 3344 cm^{-1} correspond to the N-H stretching modes of the guanidino group. These spectroscopic data are convincing evidence that a mixed layer of K-19 and GBA has been co-grafted onto electrode B.

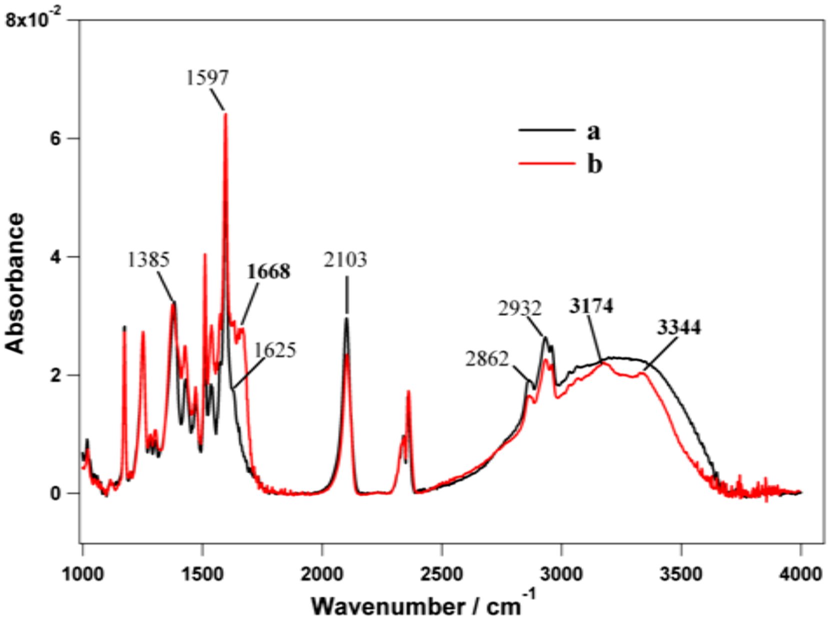

Figure 2. ATR-FTIR spectra for TiO_2 films stained with (a) K-19 dye alone and (b) K-19 dye and GBA.

Figure 3 shows the corresponding photocurrent density *vs.* voltage curves of device A and device B at full sun illumination and in the dark. The parameters of short-circuit current density (J_{sc}), open-circuit voltage (V_{oc}), fill factor (FF) for both cells and photovoltaic conversion efficiency (η)

are listed in Table 1. Compared with device A, device B has similar current and fill factor, but a higher open-circuit voltage making device B superior to device A. This result is further corroborated by measurements at different light intensities. Using GBA as coadsorbent enhances the overall power conversion efficiency due to an increase in the open-circuit voltage of the device without significant penalty in photocurrent.

TABLE 1. Current/Voltage Parameters of DSCs (Device A and Device B).

	η (%) at different light intensities [a]			Current/voltage characteristics at 1.0 sun		
Device	0.1 sun	0.5 sun	1.0 sun	V_{oc} (mV)	J_{sc} (mA cm^{-2})	*FF*
A	7.9	7.6	6.9	719	14.5	0.671
B	8.7	8.4	7.5	767	14.3	0.682

[a] The spectral distribution of the xenon lamp simulates air mass 1.5 solar light. 1.0 sun corresponds to ~100 mW cm^{-2}. The cell active areas were 0.158 cm^{-2}.

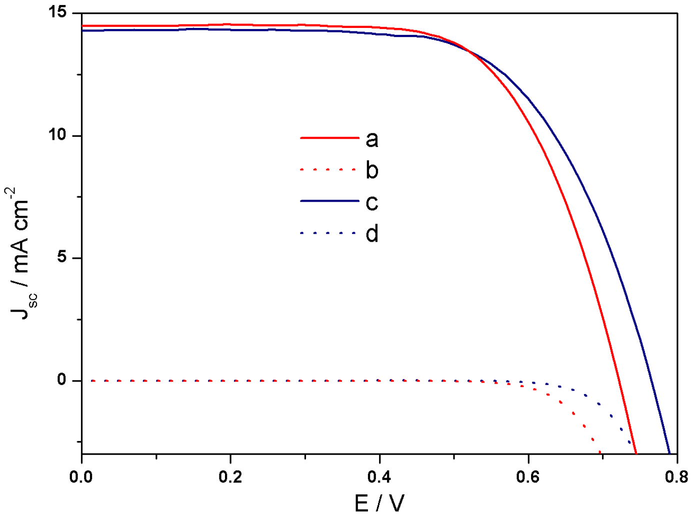

Figure 3. Current density-voltage characteristics of a) device A and c) device B under AM 1.5 simulated sunlight (100 mW cm^{-2}) illumination. Dark current data for device A and device B are shown as curves b) and d), respectively.

The dark current is not a good simulation of the recombination current under illumination due to the localized variation in electrolyte concentration and potential distribution through the TiO_2 electrode. However, it can be used as an estimate of the extent of reduction of triiodide with conduction band electrons. The dark current data in Figure 3 suggest that the mixed monolayer of K-19 and GBA is more effective in retarding this back reaction, a finding consistent with the ~50 mV increase in V_{oc}. Since V_{oc} is determined by the difference between the quasi-Fermi level and the redox potential of triiodide/iodide couple in the electrolyte, a higher V_{oc} implies a negative shift of the quasi-Fermi level of TiO_2 induced by GBA coadsorbent.

Cyclic voltammograms of electrode A and electrode B were measured in the ionic liquid EMITFSI. The choice of EMITFSI as the electrolyte for these studies is based upon the insolubility of K-19 sensitizer in this medium, thus avoiding any dye desorption from the TiO_2 electrode over the entire potential range investigated during the electrochemical measurement. Applying an increasing negative potential, i.e. a forward bias, on the TiO_2 layer in the EMITFSI ionic liquid moved the quasi-Fermi level closer towards its conduction band and led to a capacitive current as shown in Figure 4A. In principle, for a perfect n-type semiconductor-electrolyte junction, charge injection will commence once the quasi-Fermi level reaches the lower edge of conduction band. However, due to the presence of coordinatively unsaturated Ti species on the surface of TiO_2 nanoparticles, some electronic levels exist at energies below the conduction band edge.[3],[31] These surface states trap electrons injected under forward bias producing a gradual onset of the capacitive current in the forward scan as shown in Figure 4a. For the reverse scans, the current approached zero at the more positive potentials, indicating recovery of the injected negative charge and regeneration of most surface states.[32]

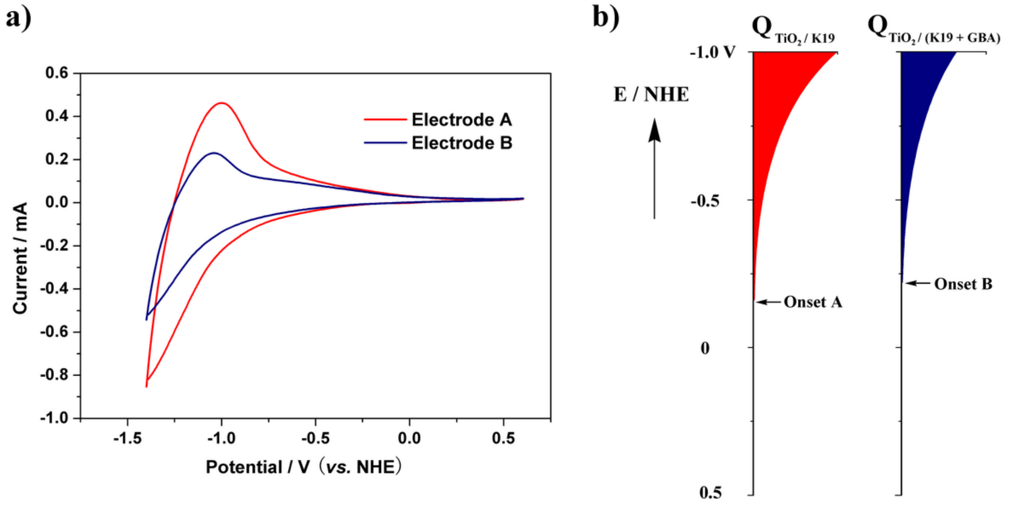

Figure 4. a) Cyclic voltammograms of TiO_2 electrode A (K-19 grafted only) and electrode B (GBA co-grafted) in EMITFSI. Straight red line for Electrode A, coated with K-19 sensitizer alone; blue line for Electrode B, K-19 / GBA co-grafted. The scan rate is 0.05 V/s. (B) Energy levels at the mesoscopic TiO_2 / EMITFSI interface.

The energetic distribution of the traps at the surface of a TiO_2 electrode can be deduced from the cyclic voltammograms via the following equations

$$\frac{dQ}{dV} = \mathrm{DOS}\frac{N_A}{F} \tag{1}$$

$$dQ = \frac{1}{v} I(V) dV \tag{2}$$

where Q is the total injected charge, N_A is Avogadro constant, F is Faraday’s constant , $I(V)$ is the current, V is the potential applied on the electrode and v represents the constant scanning rate in the cyclic voltammetry measurements. Dividing the derivative dQ/dV by elementary charge in equation (1) yields DOS, while the integration of equation (2) will give Q the total number of surface states as plotted versus applied potential in Figure 4b. The onset is around -0.15 V (*vs.* NHE) for electrode A whereas in the case of electrode B, it moves to -0.20 V (*vs.* NHE), indicating that the edge of conduction band of TiO_2 moved negatively towards the vacuum level. Since there is not a steep gradient, Q for electrode B increases much more slowly than Q for electrode A under increasing forward bias. This phenomenon is due to better surface passivation. TiO_2 nanocrystals are not fully covered by the dye molecules and, consequently, there are some surface areas directly in contact with the electrolyte. The use of GBA as coadsorbent passivates these surface areas, resulting in a decrease in trap states.

Figure 5 shows typical electrochemical impedance spectra of device A and B measured in the dark. The figure is presented in the forms of a) Nyquist plots and b) Bode plots. For clarity of comparison, an identical forward bias of -0.72 V, which is the V_{oc} of device A, was applied to both cells. In figure 5a, the Nyquist plots consist of two semicircles. The smaller semicircle occurring at higher frequencies represents redox charge transfer at the platinum counter electrode, while the larger one at lower frequencies is attributed to the electron transport in the TiO_2 layer, the electron transfer at the oxide/electrolyte interface and ion diffusion within the electrolyte. Fitting the low frequency semicircle subsequently gives C_μ and R_{rec}. Comparing device B with device A, C_μ decreased from 2600 μF cm^{-2} to 2000 μF cm^{-2} while R_{rec} increased sharply from 54.8 Ω to 254.7 Ω, yielding a larger τ_r of 127.6 ms for device B than that for device A, i.e. 35.6 ms. These results are supported by the Bode plots shown in Figure 5b. Here, the frequency value of the phase angle peak approximately equals the reciprocal of τ_r. Following this principle, the τ_r extracted for device A and device B are ~50 ms and ~ 200 ms, respectively, in fair agreement with the results from the Nyquist plots.

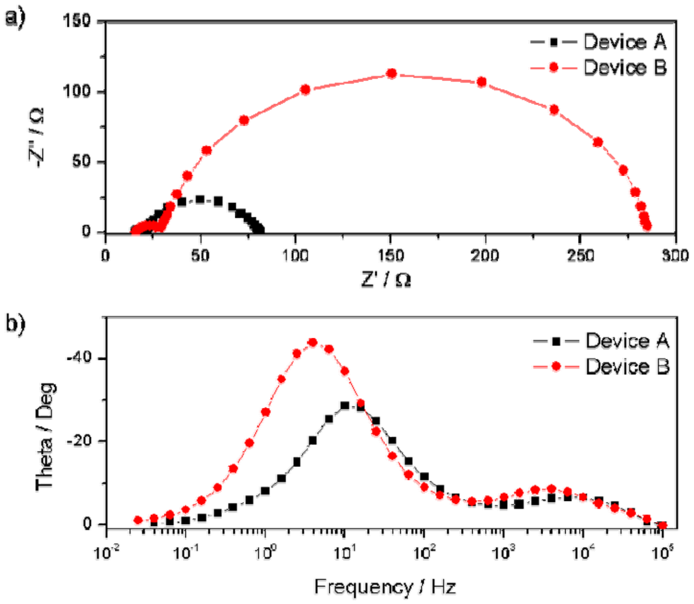

Figure 5. Typical electrochemical impedance spectra of device A and B in the forms of a) Nyquist plots and b) Bode plots. The spectra were measured with an external potential of -0.72V in the dark.

In order to elucidate the underlying mechanisms connected to these differences, impedance spectra were also measured by varying the applied potential at equal intervals in the vicinity of V_{oc}. The values of C_{μ}, R_{rec} and τ_r are plotted in Figure 6. C_{μ} follows a characteristic exponential rise with increasing forward bias. This behavior is generally analyzed to yield the chemical capacitance of nanostructured TiO_2 utilizing the following model [20],[33],[34]

$$C = C_a \exp[-\beta eV / k_B T] + C_b \tag{3}$$

where k_B is the Boltzmann constant, T is the temperature, e is the elementary charge, V is the applied potential, C_a is the prefactor of the exponential increase, C_b is the quasi-constant capacitance at low potentials and β is a coefficient describing either the Boltzmann occupancy of the conduction band capacitance ($\beta = 1$) or an exponential distribution of trap states ($\beta < 1$). We found β of 0.24 for device A and 0.17 for device B respectively, results very similar to those reported in previous work yielding β values of 0.2 ~ 0.3.[27],[33]

The plot of electron lifetime (response time), versus bias potential is shown in Figure 6d. It is interesting that device B has a much longer response time than device A at any given potential. This increase in τ_r is associated with a pronounced rise in the charge transfer resistance indicating that the co-grafting of GBA decreases the interfacial rate constant for electron capture by triiodide ions. GBA assists probably the self assembly of the K-19 dye at the TiO_2 surface producing a more compact monolayer than when the sensitizer is adsorbed alone that blocks the access of I_3^- to the interface impairing the back reaction.

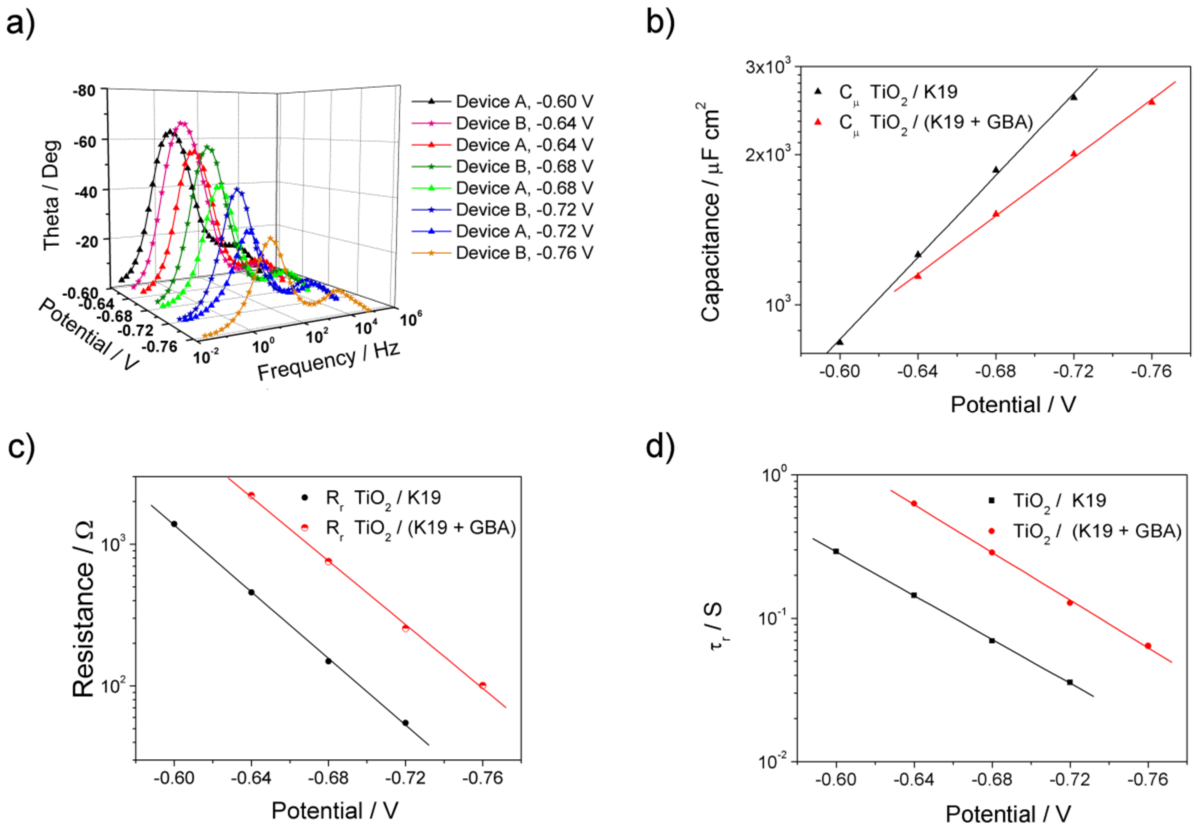

Figure 6. a) Electrochemical impedance spectra of device A (TiO_2 electrode coated with K-19 dye alone) and device B (TiO_2 film stained with K-19 and GBA) measured at different forward bias near their open circuit potentials. The fitted results are plotted as b) film capacitance C_μ, c) charge transfer resistance R_{rec} and d) electron lifetime τ_r with respect to the externally controlled potential.

GBA also lowers the film capacitance, C_μ due to the passivation of surface states and induces a negative band edge movement reducing the number of recombination centers available at a given cell potential. Both effects augment the quasi-Fermi level of the conduction band electrons in the titania film and increase therefore the open circuit photovoltage of the solar cell.

The treatment of the titania surface with agents such as with 4-*tert*-butylpyridine or ammonia also produces an increase in open circuit voltage. However, a significant drop in photocurrent generally accompanies this effect.[35] The main role of such additives is to depronotate the TiO_2 surface, synchronously displacing the quasi-Fermi energy and conduction band edge towards the vacuum level. This negative shift of conduction band hampers electron injection from the excited sensitizer explaining the decrease in the photocurrent. While such a shift occurs also with GBA as coadsorbent, it is small enough not to affect the electron injection from the excited sensitizer into the conduction band of titania. The main effect of GBA is to block the electron recapture by the redox electrolyte allowing higher electron concentrations in the mesoscopic TiO_2 films and hence a higher V_{oc} to be reached under illumination.

Finally it should be noted that GBA has a significant dipole moment, which can alter the energetics of the TiO_2/sensitizer interface unless it is locally compensated by solvent molecules. Further investigations are presently carried out to unravel the detailed reasons for the favorable effect that GBA exerts on the performance of the DSC.

Transient photovoltage measurements were also performed for comparison. The recombination rate constant (k) of dye-sensitized cells is known to be dependent on the electrode potential. This effect was scrutinized, adjusting the V_{oc} by varying the intensity of the bias light. Figure 7a shows the logarithmic plot of k with respect to V_{oc}. The recombination rate constant, k, is apparently exponentially dependent on V_{oc}, and linear fits to all of the data give a similar slope value of 11.7 ± 0.3 for both cells, with or without of GBA coadsorption. This slope corresponds to ~90 mV per decade, which is slightly smaller than the value of 120 mV per decade obtained for solid-state cells.[30] Once again, the cell fabricated with a dye/GBA co-grafted TiO_2 film exhibits slower recombination at all potentials. However, the coadsorption does not influence the slope value, suggesting that the underlying recombination mechanism is not changed. It should be noted that the electron lifetimes obtained here (for example, at an open-circuit potential of -0.72V, 14 ms for device A and 24 ms for device B) are smaller than those observed by EIS measurements. This divergence should be attributed to the local concentration difference in electron capturing species, I_3^-, due to the fact that the EIS was measured in the dark where the concentration of I_3^- is much less than that under illumination.[28]

As discussed in analysis section, the capacitance can be calculated from the transient voltage data taken at each $V_{oc.}$ The curve of capacitance *vs.* open-circuit potential is shown in Figure 7b for two typical cells fabricated with TiO_2 film in the absence and the presence of GBA co-grafting. The curve is well fit by a single exponential, as has been found by other authors. [34],[36],[37] The cell with GBA coadsorption is found to have less capacitance at all potentials, which is in agreement with the EIS experiments.

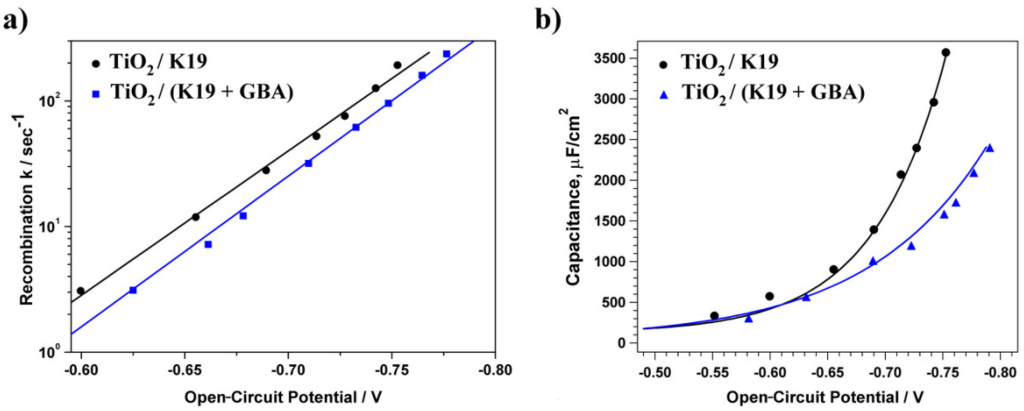

Figure 7. Results of phototransient voltage measurements with cells made by nanoporous TiO_2 films in the absence and presence of GBA co-grafting. a) recombination rate constant *vs.* open-circuit potential and b) capacitance *vs.* open-circuit potential.

Stability Test. Device B showed excellent light soaking stability when subjected to the accelerated experimental conditions in the solar simulator at 60 °C covered by an ultraviolet absorbing polymer film. Following 1,000 h of light soaking under these conditions, there is no degradation in the device efficiency (Figure 8) as compared to the initial values. With nearly constant *FF* values (changes less than 2% were observed), the extraordinary stability is mainly due to the fact that the decrease in V_{oc} is well compensated by the increase in J_{sc}. At the end of the light soaking test the J_{sc} was even larger than the initial value. These results also confirmed that the styryl structure in the K-19 sensitizer molecules can remain intact under the longtime visible light soaking as mentioned previously, and, thus, paves the way for future designs of sensitizer with a high molar extinction coefficient exhibiting good thermostability.

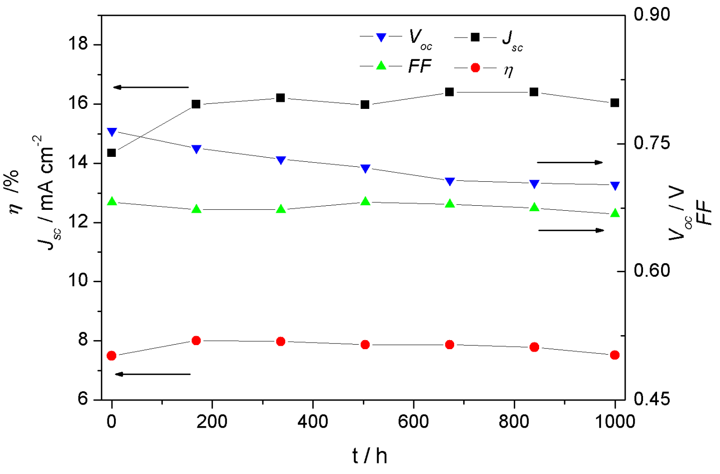

Figure 8. Detailed temporal evolution of photovoltaic parameters of device B under successive 1.0 sun visible-light soaking at 60 °C.

4.5 Conclusions

The experiments disclosed in this study show that the coadsorption of K-19 sensitizer with 4-guanidinobutyric acid onto nanocrystalline TiO_2 films remarkably increases the photovoltage without suffering significant current penalty, thus, enhancing the total power conversion efficiency. Results from cyclic voltammetry, electrochemical impedance spectroscopy and photovoltage transient measurements demonstrate that this increase in photovoltage is generated from the negative shift of the quasi-Fermi level of TiO_2 nanocrystals as well as the inhibition of charge transfer from electrons in TiO_2 to the triiodide in the electrolyte primarily resulting from the shielding of surface traps due to the addition of GBA as a dye coadsorbent. The device showed a long-term stability exhibiting approximately 8% power conversion efficiency under the dual stress of both thermal aging and light-soaking. Studies are now underway to optimize the chain length and the structure of this type of coadsorbent for further improvement of cell performance.

Acknowledgement. We are grateful to P. Comte and R. Charvet for the film fabrication, Dr. Carole K. Grätzel, Dr. Augstin McEvoy and Dr. Qing Wang for helpful discussions and T. Koyanagi (CCIC, Japan) for a free sample of the 400 nm sized light scattering anatase particles. The Swiss Science Foundation, the Swiss Federal Office for Energy (OFEN), the European Office of U.S. Air Force under Contract No. F61775–00–C0003 and the Swiss Commission of Technology and Innovation (CTI) under Contract No. 7019.1 NMS-NM have supported this work.

4.6 References and Notes

[1]. O'Regan, B.; Grätzel, M. *Nature* **1991,** *353,* 737.
[2]. Grätzel, M. *Nature* **2001,** *414,* 338.
[3]. Hagfeld, A.; Grätzel, M. *Chem. Rev.* **1995**, *95*, 49.
[4]. Grätzel, M. *J. Photochem. Photobio. A* **2004**, 16*4*, 3.
[5]. Grätzel, M. *Chem. Lett.* **2005**, *34,* 8.
[6]. Wang, P.; Klein, C.; Humphry-Baker, R.; Zakeeruddin, S. M.; Grätzel, M. *Appl. Phys. Letts.* **2005**, *86*, 123508.
[7]. Fischer, A. C.; Peter, L. M.; Ponomarev, E. A.; Walker, A. B.; Wijayantha, K. G. U. *J. Phys. Chem. B* **2000**, *104*, 949.
[8]. Shkrob I.A.; Sauer, M.C. *J. Phys. Chem. B* **2004**, *108*, 12497.

[9]. Tennakone, K.; Perera, V. P. S.; Kottegoda, I. R. M.; De Silva, L. A. A.; Kumara, G.; Konno, A. *J. Electron. Mater.* **2001**, *30*, 992.

[10]. Gregg, B. A.; Pichot, F.; Ferrere, S.; Fields, C. L. *J. Phys. Chem. B* **2001**, *105*, 1422.

[11]. Kumara, G.; Tennakone, K.; Perera, V. P. S.; Konno, A.; Kaneko, S.; Okuya, M. *J. Phys. D Appl. Phys.* **2001**, *34*, 868.

[12]. Zaban, A.; Chen, S. G.; Chappel, S.; Gregg, B. A. *Chem. Commun.* **2000**, 2231.

[13]. Chappel, S.; Chen, S. G.; Zaban, A. *Langmuir* **2002**, *18*, 3336.

[14]. Palomares, E.; Clifford, J. N.; Haque, S. A.; Lutz, T.; Durrant, J. R. *J. Am. Chem. Soc.* **2003**, 125, 475.

[15]. Wang, P.; Zakeeruddin, S. M.; Humphry-Baker, R.; Moser, J.-E.; Grätzel, M. *Adv. Mater.* **2003**, *15*, 2101.

[16]. Wang, P.; Zakeeruddin, S. M.; Comte, P.; Charvet, R.; Humphry-Baker, R.; Grätzel, M. *J. Phys. Chem. B* **2003**, *107*, 14336.

[17]. Wang, P.; Klein, C.; Humphry-Baker, R.; Zakeeruddin, S. M.; Grätzel, M. *J. Am. Chem. Soc.* **2005**, *127*, 808.

[18]. Barbé, C. J.; Arendse, F.; Comte, P.; Jirousek, M.; Lenzmann, F.; Shklover, V.; Grätzel, M. *J. Am. Ceram. Soc.* **1997**, *80,* 3157.

[19]. Kern, R.; Sastrawan, R.; Ferber, J.; Stangl, R.; Luther, J. *Electrochim. Acta* **2002**, *47,* 4213.

[20]. Bisquert, J. *Phys. Chem. Chem. Phys.* **2003**, *5,* 5360.

[21]. Hauch, A.; Georg, A. Elec*trochim. Acta* **2001**, *46,* 3457.

[22]. Zaban, A.; Meier, A.; Gregg, B. A. *J. Phys. Chem. B* **1997**, *101,* 7985.

[23]. Schwarzburg, K.; Willig, F. *J. Phys. Chem. B* **2003**, *107,* 3552.

[24]. Bisquert, J. *J. Phys. Chem. B* **2002**, *106,* 325.

[25]. Fabregat-Santiago, F.; Garcia-Canadas, J.; Palomares, E.; Clifford, J. N.; Haque, S. A.; Durrant, J. R.; Garcia-Belmonte, G.; Bisquert, J. *J. Appl. Phys.* **2004**, *96*, 6903.

[26]. Pitarch, A.; Garcia-Belmonte, G.; Mora-Sero, I.; Bisquert, J. *Phys. Chem. Chem. Phys.* **2004**, *6*, 2983.

[27]. Fabregat-Santiago, F.; Bisquert, J.; Garcia-Belmonte, G.; Boschloo, G.; Hagfeldt, A. *Sol. Energ. Mat. Sol. C.* **2005**, *87*, 117.

[28]. Wang, Q.; Moser, J.; Grätzel, M. *J. Phys. Chem. B* **2005**, *109,* 14945.

[29]. O'Regan, B. C.; Lenzmann, F. *J. Phys. Chem. B* **2004**, *108,* 4342.

[30]. O’Regan, B. C.; Scully, S.; Mayer, A. C.; Palomares, E.; Durrant, J. *J. Phys. Chem. B* **2005**, *109,* 4616.

[31]. Moser, J.; Punchihewa, S.; Infelta, P. P.; Grätzel, M. *Langmuir* **1991**, *7*, 3012.

[32]. Wang, Q.; Zakeeruddin, S. M.; Cremer, J.; Bäuerle, P.; Humphry-Baker, R.; Grätzel, M. *J. Am. Chem. Soc.* **2005**, *127*, 5706.

[33]. Fabregat-Santiago, F.; Mora-Seró, I.; Garcia-Belmonte, G.; Bisquert, J. *J. Phys. Chem. B* **2003**, *107*, 758.

[34]. Van de Lagemaat, J.; Park, N.-G.; Frank, A. J. *J. Phys. Chem. B* **2000**, *104*, 2044.

[35]. Schlichthörl, G.; Huang, S. Y.; Sprague, J.; Frank, A. J. *J. Phys. Chem. B* 1997, *101,* 8141.

[36]. Willis, R. L.; Olson, C.; O’Regan, B.; Lutz, T.; Nelson, J.; Durrant, J. R. *J. Phys. Chem. B* **2002**, *106*, 7605.

[37]. Duffy, N. W.; Peter, L. M.; Rajapakse, R. M. G.; Wijayantha, K. G. U. *Electrochem. Commun.* **2000**, *2,* 658.

5. Guanidino-coadsorbent in Dye-sensitized Solar Cells to Increase the Photovoltage

5.1 Introduction

Due to the fact that the dark current caused by the recombination of electrons in TiO_2 films with the oxidized species in the electrolyte (usually I_3^-) is the major electron loss channel in DSC, controlling the dark current is important to obtain a high open circuit photovoltage. This interfacial recombination processes can be inhibited by modifying the interface via a core-shell design of the photoelectrode [1]-[5] or a physical protecting layer [6] as illustrated in Figure 5.1.

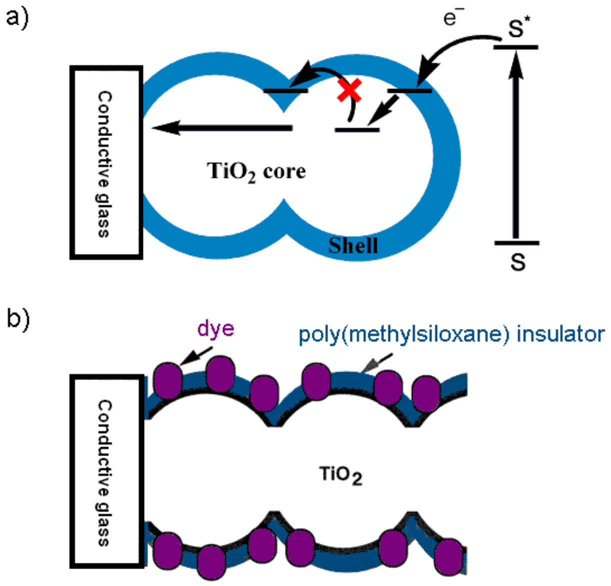

Figure 5.1 A cartoon depicting the two methods of interfacial passivation by: a) fabrication of core matrix-shell structures with composite materials and b) coating exposed oxide surfaces with poly(methylsiloxane).

Molecular-scale interface engineering is a more attractive way to inhibit interfacial recombination. Since the sensitizer molecules are anchored on the TiO_2 in the form of a self-assembled monolayer, the packing mode of the sensitizer is important for the photovoltaic performance. Judicious selections of the sensitizer and other adsorbents to modify the TiO_2 surface may lead to the formation of an ultra thin, electrically insulating layer between the TiO_2/electrolyte interface and decrease the dark current. In Chapter 4, we used 4-guanidinobutyric acid (GBA) as the coadsorbent with K-19 and an increase of ~50 mV in V_{oc} was observed. In this chapter, we follow this initial success and continue the study on the effect of this guanidino-coadsorbent.

5.2 Decrease in dark current by coadsorption

The idea of coadsorption is to use small molecules of amphiphilic acids to passivate the TiO_2 surface that is not covered by dye molecules so as to mitigate the back reaction. Figure 5.2 shows the structures for some of the coadsorbents studied in this chapter.

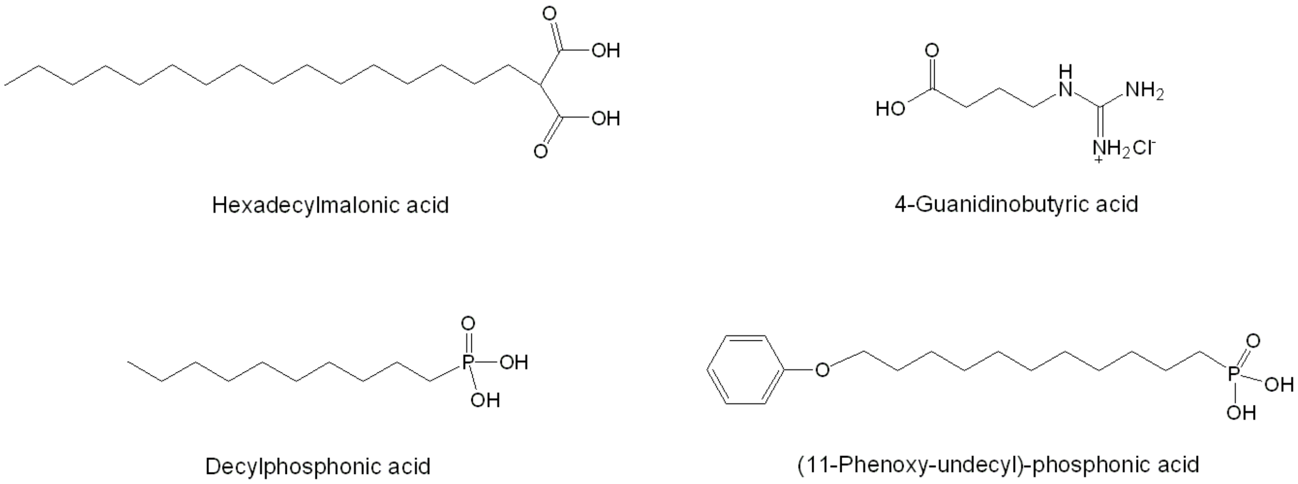

Hexadecylmalonic acid

4-Guanidinobutyric acid

Decylphosphonic acid

(11-Phenoxy-undecyl)-phosphonic acid

Figure 5.2 Molecular structures for some coadsorbents

The effects of coadsorbents on TiO_2 photoelectrodes were first studied in the absence of the sensitizer on the TiO_2 surface. The electrodes were dipped into a 0.3 mM solution of one of the above acids and the dark *I*-*V* characteristics of modified electrodes are plotted in Figure 5.3. Compared to the control experiment shown in black squares at the same voltage, all the coadsorbents decreased the dark current. Hexadecylmalonic acid (HDMA) and GBA modification showed a similar moderate blocking effect, while the decylphosphonic acid (DPA) and (11-phenoxy-undecyl)-phosphonic acid (PUPA) decreased the dark current more pronouncedly, presumably due to the well-known strong bindings of alkyl phosphonic acids to the TiO_2 surface via the formation of P-O-metal bonds.[7],[8]

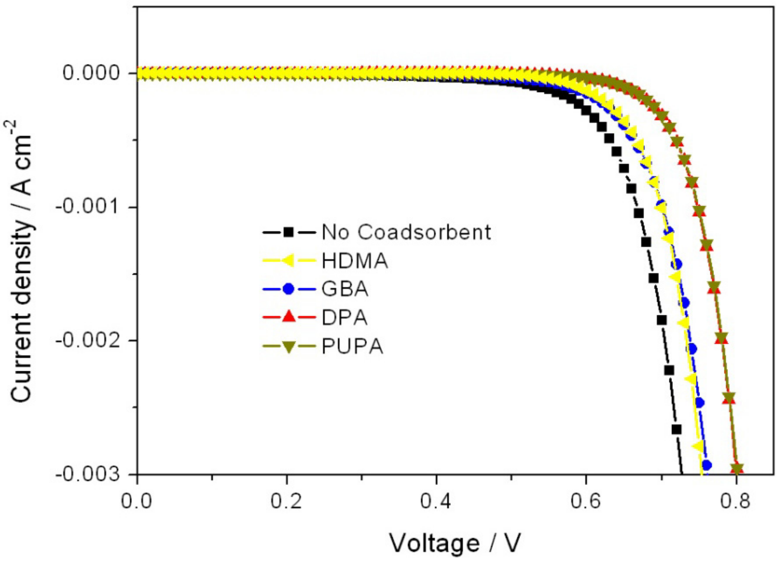

Figure 5.3 Dark currents of the devices based on bare TiO_2 films (no sensitizers on the surface) modified by different coadsorbents. The electrolyte was Z-208.

We then turned to the situation when a sensitizer was co-grafted on the TiO_2 surface. Due to the extreme difficulties we met during the purification process of K-19, we chose a more widely used amphiphilic ruthenium sensitizer, Z-907. This sensitizer was featured with two nonyl groups on the *para*-positions of bipyridine ligand and showed excellent stability under longtime high-temperature (80 ℃) thermal stresses.[9] Later experiments on coadsorption were mostly done with this sensitizer.

Figure 5.4 demonstrates the dark currents of the corresponding devices based on TiO_2 films sensitized with Z-907 in the presence of coadsorbents. Coadsorption did decrease the dark current in all cases, whereas the GBA was found to have the most obvious effect instead of the phosphonic acids. Apparently, effects other than simple passivation were involved with GBA coadsorption.

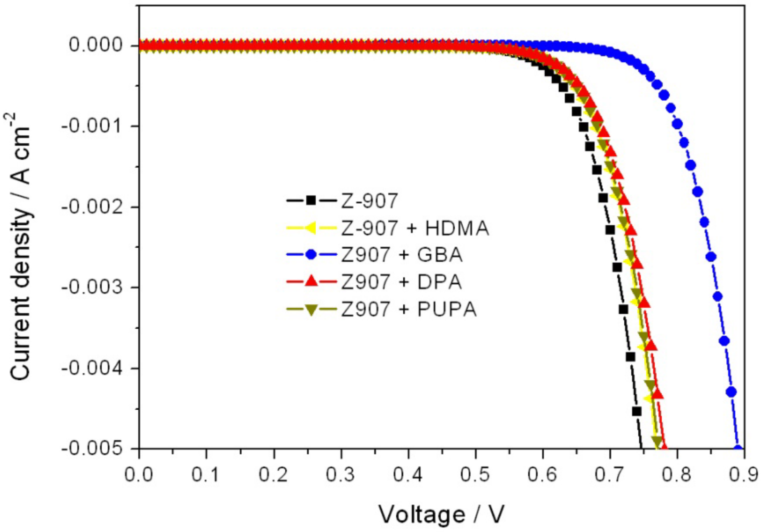

Figure 5.4 Dark current studies of the devices TiO_2 films sensitized with Z-907 in the presence of coadsorbents. The dye-to-coadsorbent molar ratio was 1:1 for GBA and 4:1 for HDMA, DPA and PUPA, respectively. The electrolyte was Z-208.

Figure 5.5 shows the *I-V* characteristics of the above devices under the simulated illumination of AM 1.5 sunlight at 100 mW cm^{-2}. The device sensitized with Z-907 itself gave a J_{sc} of 11.1 mA cm^{-2} and a V_{oc} of 710 mV. From the perspective of V_{oc}, coadsorption of HDMA, DPA and PUPA did not induce a big change in the V_{oc} (~ 20 mV). Small increases in J_{sc} were observed when HDMA or DPA was used as the coadsorbent, as was reported and attributed to the decrease in back reaction by Wang et. al.[10],[11] The most interesting fact was the high V_{oc} (832 mV) and small current loss resulted from the GBA coadsorption, suggesting the benefits of using this molecule as the coadsorbent. Since the structure of GBA was only different to the other acids by the ω-guanidino group, the large increase in V_{oc} was thought to be associated with this functional group and more studies were carried out on this aspect in the following two chapters by choosing and designing molecules having similar molecular structures as the coadsorbents for Z-907 sensitizer.

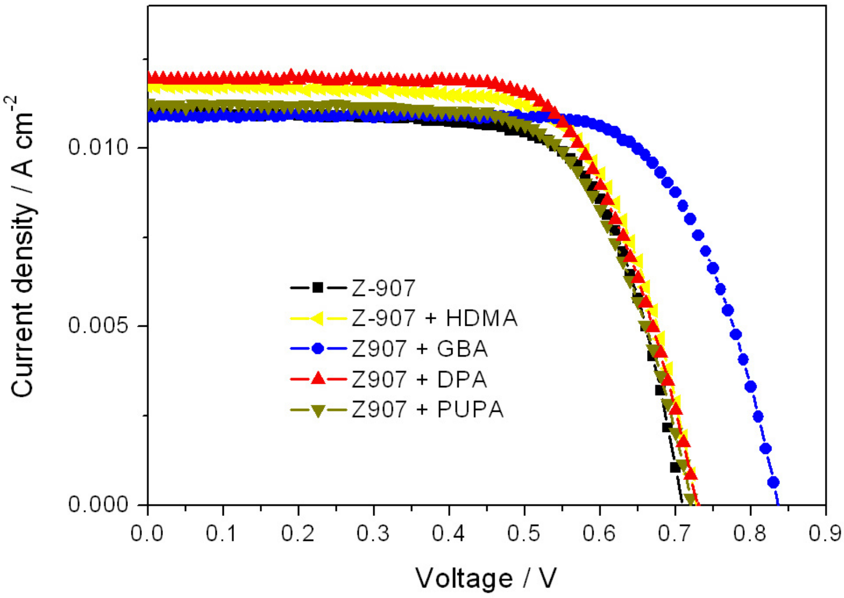

Figure 5.5 *I-V* characteristics of the corresponding devices in Figure 4.4 under the simulated illumination of AM 1.5 sunlight at 100 mW cm^{-2}. Cell area: 0.158 cm^{2}.

5.3 Electrolyte optimization

The importance of using amphiphilic polypyridyl ruthenium sensitizer such as Z-907 for the DSC device stability was first demonstrated with a non-volatile, lithium-free 3-methoxyproprionitrile (MPN)-based electrolyte.[9],[12]-[14] Compared to acetonitrile solvent, these non-volatile electrolytes showed a somewhat lower but much more stable conversion efficiency under prolonged thermal stress at elevated temperatures. In this section, a series of MPN-based electrolytes were prepared with different concentrations of PMII. With Z-907 as the sensitizer, the concentration effect of PMII on the photovoltaic performance and stability of DSC was studied.

When the concentration of triiodide is fixed in the electrolyte, the reaction rate for the back reaction of injected electrons with triiodide is constant. Then the recombination of injected electrons with oxidized sensitizer can become another loss channel if the regeneration of the dye by iodide is not fast enough. Electrolytes with iodide concentrations ranging from 0.5 to 2.5 M was employed in these experiments. The limiting anodic current of the electrolyte was measured using an ultramicroelectrode technique. The apparent diffusion coefficient D_{app} of iodide was calculated from the anodic steady-state currents (I_{ss}) using Eq. 2.2. D_{app} values of different electrolytes as a function of PMII concentration (keeping a constant iodine concentration of 0.15 M in all the electrolytes) are presented in Figure 5.6. As the PMII concentration changed from 0.5 to 2.5 M, I_{ss} increased linearly from 229 to 817 nA, while D_{app} dropped from 5.53×10^{-6} to 4.17×10^{-6} $\mathrm{cm}^2\ \mathrm{s}^{-1}$. The existence of Grothus exchange mechanism for diffusing operating in parallel to the conventional mass transport has been proposed for electrolytes containing the I^-/I_3^- redox couple.[15] For this case the apparent diffusion coefficient D_{app} is described by the Dahms-Ruff equation: [16]-[20]

$$D_{app} = D_{phys} + D_{ex} = D_{phys} + k_{ex}\delta^2 c/6 \qquad (5.1)$$

where D_{phys} is the physical diffusion coefficient, k_{ex} is the exchange-reaction rate constant, and c and δ are the concentration and center-to-center intersite distance between redox species at the exchange reaction. The observed linear decrease of D_{app} corresponds to the change of viscosity-dependent D_{phys} term and excludes any significant contribution from D_{ex}. The lack of any significant contribution of D_{ex} is mainly due to the low I_3^-/I^- ratio employed in Figure 5.6, in agreement with the results of Wanatabe et al.[21],[22]

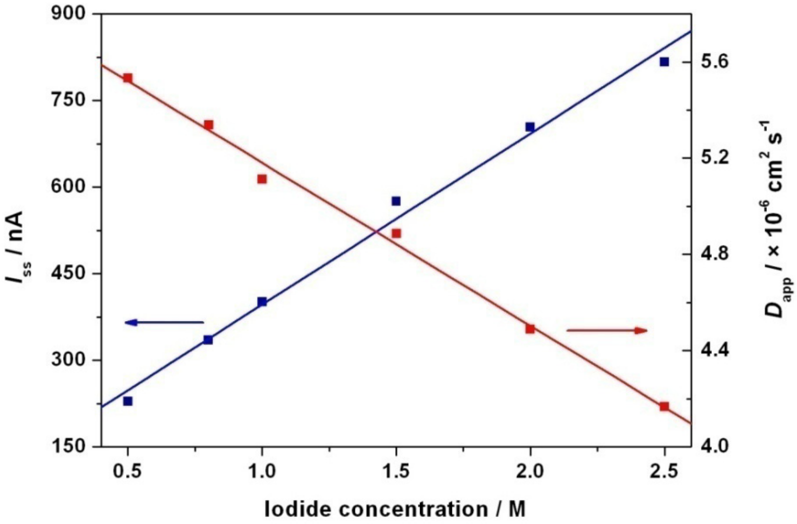

Figure 5.6. Dependence of steady-state current and iodide diffusion coefficient on the concentration of PMII in the electrolyte. Measurements employed a Pt microelectrode as described in the experimental section.

A complete set of photovoltaic parameters for these electrolytes under simulated illumination of AM 1.5 sunlight (100 mW cm^{-2}) is summarized in Table 5.1. As shown in Figure 5.7, the short-circuit current densities (J_{sc}) for PMII concentrations of 0.5, 0.8 and 1.5 M under AM 1.5 sun illumination at 100 mW cm^{-2} were 12.0, 13.2 and 14.3 mA cm^{-2}, respectively. The corresponding photovoltaic efficiencies were 5.9 %, 6.6 % and 7.4 %, respectively, following the trend observed in I_{ss}. Meanwhile, the open-circuit voltage (V_{oc}) and the fill factor (FF) only slightly changed for a few percent. Both J_{sc} and η reached a plateau at a PMII concentration of 1.5 M and further increase did not yield a higher value.

Table 5.1. A complete set of photovoltaic parameters for DSCs based on Z907 sensitizer and different electrolytes with various PMII concentrations measured under AM 1.5 full sunlight (100 mW cm^{-2}) irradiation.

PMII concentration (M)	J_{sc} (mA cm^{-2})	V_{oc} (mV)	FF	η (%)
0.5	12.0 ± 0.3	720 ± 10	0.66 ± 0.03	5.9 ± 0.3
0.8	13.2 ± 0.4	745 ± 10	0.65 ± 0.02	6.6 ± 0.2
1	13.8 ± 0.4	735 ± 15	0.67 ± 0.03	7.0 ± 0.2
1.5	14.3 ± 0.4	735 ± 10	0.68 ± 0.02	7.4 ± 0.3
2	14.3 ± 0.3	735 ± 10	0.69 ± 0.02	7.3 ± 0.3
2.5	14.2 ± 0.4	740 ± 10	0.69 ± 0.02	7.3 ± 0.3

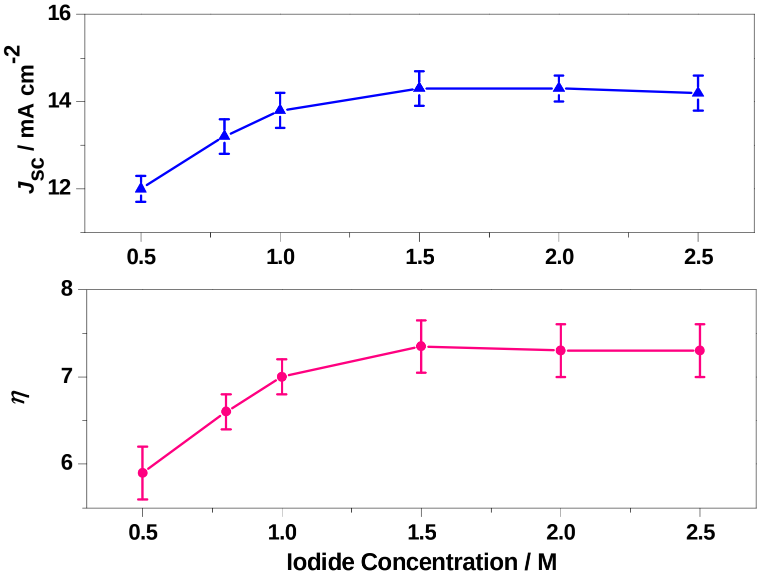

Figure 5.7. Dependence of photocurrent density and power conversion efficiency of devices under the AM 1.5 full sunlight (100 mW cm^{-2}) on the concentration of PMII. The iodine concentration is kept at 0.15 M**.**

Laser transient absorbance measurements were performed to scrutinize the dynamics of the recombination of the electrons injected in the conduction band of TiO_2 (e^-_{cb}) with the oxidized dye (S^+) and the dye regeneration reaction with iodide. Kinetic competition between these two charge-transfer processes (Eqs 1.6 and 1.7) controls, to a large extent, the photon-to-current conversion efficiency of the device. Figure 5.8 displays the temporal evolution of the absorbance measured at $\lambda = 680$ nm of a transparent Z-907 dye-sensitized TiO_2 film upon pulsed laser excitation ($\lambda = 600$ nm; pulse duration 5 ns; pulse fluence, 25 μJ cm^{-2}). The charge injection (Eq. 1.4) produced the immediate appearance of a positive transient signal recorded at 680 nm, which was mainly due to light absorption by the oxidized sensitizer (S^+) species. In the absence of iodide donor, this signal decayed (trace a) as a consequence of back transfer of conduction band electrons to the oxidized dye (Eq. 1.7).

The kinetics of S^+ transient absorbance decay through charge recombination in pure MPN solvent displayed a typical half-reaction time ($t_{1/2}$) of the order of 400 μs. In the presence of 0.5 M iodide (trace b), the decay of the oxidized dye signal was accelerated ($t_{1/2} \sim 80$ μs), indicating that the mediator intercepted back-electron transfer to S^+ (Eq. 1.6). The decay of S^+ transient absorbance was observed to be faster with an increasing iodide concentration (trace c), yielding $t_{1/2} \sim 30$ μs for a

PMII concentration of 0.8 M. In combination with photovoltaic results, it is apparent that the electrolyte with insufficient dye regeneration took place in electrolytes of 0.5 or 0.8 M PMII. Dynamics of an incomplete dye regeneration was reported in a similar system containing 0.6 M 1,2-dimethyl-3-propylimidazolium iodide (DMPII) and 0.1 M iodine in MPN, where $t_{1/2} \approx 30$ µs was observed and 10 - 15% of the initial Z-907 cations (S^+) population was estimated to undergo recombination with conduction-band electrons.[9] This limited the quantum conversion efficiency and the maximum photocurrent density obtainable in practice as seen in our current devices with electrolytes of 0.5 or 0.8 M PMII. Increasing the iodide concentration in the electrolyte was expected to expedite the interception of charge recombination. In the presence of 1.5 M PMII in the electrolyte (trace d), S^+ species decayed with $t_{1/2} \sim 20$ µs and only a very small portion of dye cations survive for 100 µs, which was sufficiently fast compared to the time frame of charge recombination in the range of 200 µs - 1 ms (trace a). Further increase of iodide concentration to 2.0 and 2.5 M yielded $t_{1/2}$ of 10 µs and 6 µs (traces e and f), respectively, yet this acceleration seemed to be redundant and had a negligible effect on photocurrent density of the device as well (Figure 5.7).

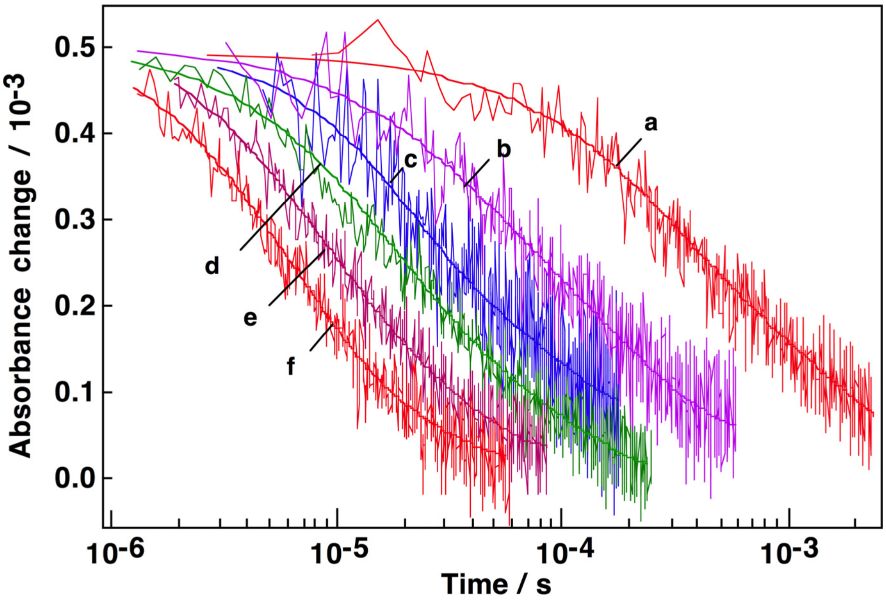

Figure 5.8. Transient absorbance decay kinetics of the oxidized state of Z-907 dye adsorbed on nanocrystalline TiO_2 films in pure MPN solvent (a), and in the presence of electrolytes of increasing I^- concentration: 0.5 M (b), 0.8 M (c), 1.5 M (d), 2.0 M (e), and 2.5 M (f). Absorbance changes were measured at a probe wavelength of 680 nm, employing 600 nm pulsed laser excitation (5 ns fwhm pulse duration, 25 µJ cm^{-2} pulse fluence). Solid lines drawn on top of experimental data are double exponential fits of the transient decays.

On the basis of above discussion, carefully sealed devices with electrolytes comprising 1.0, 1.5, and 2.0 M PMII were fabricated and stored in oven at 80 °C for long-term thermal stress tests. The present study permitted for the first time a study of the iodide concentration effect on DSC thermal stability as plotted in Figure 5.9. It appeared that the device with electrolyte of 1.0 M PMII showed superior stability to the others, with less than 10 % decrease in short-circuit photocurrent density and photovoltaic conversion efficiency being witnessed in 35 days of aging at 80 °C. The 1.5 and 2 M PMII electrolytes showed relatively inferior stability, with a ~15 % decrease in efficiency at the same time. The results suggested that higher iodide concentration was rather detrimental to device thermal stability which might be caused by dye desorption due to the high ionic liquid concentration as was implicated by the continuous drop in short-circuit photocurrent density of devices with 2.0 M PMII containing electrolytes.

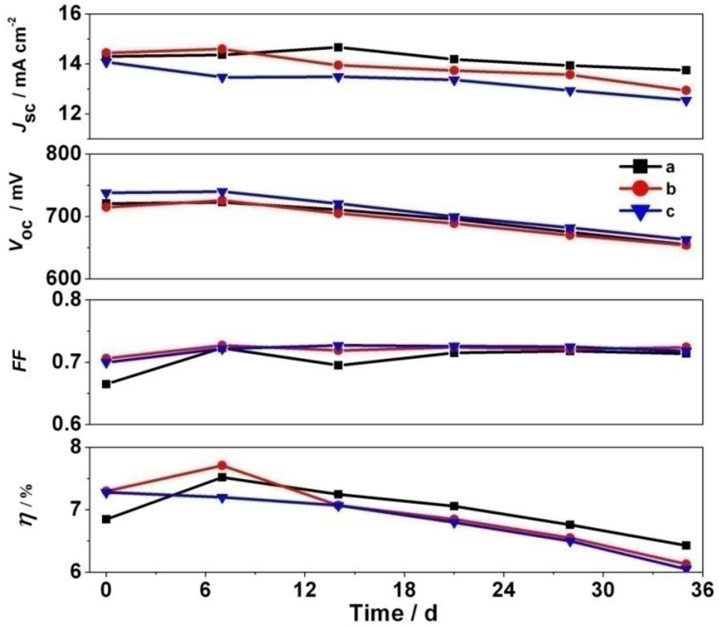

Figure 5.9 Temporal evolution of normalized photovoltaic parameters of devices fabricated with electrolytes containing a) 1.0, b) 1.5 and c) 2.0 M PMII during successive thermal aging at 80 °C.

In summary, the diffusion coefficient of iodide ions determined by microelectrode techniques was found to decrease linearly with the increase of PMII concentration. Judicious selection of PMII concentration of 1.5 M led to a power conversion efficiency of 7.4 % at full sunlight, a high value for Z-907 sensitizer based devices with MPN based electrolytes. Laser flash results demonstrated that at PMII concentrations lower than 1.5 M was responsible for the low dye regeneration rate.

Additionally, further increase in iodide concentration became kinetically redundant for intercepting charge transfers between oxidized dye sensitizer and electrons in the conduction band of TiO_2. The device with electrolyte composed of 1.0 M PMII showed good stability during thermal aging at 80 °C.

5.4 Coadsorbent for thermal aging studies at 80 °C

As shown in Chapter 4, the device with GBA coadsorption showed good stability under light soaking conditions at 60 °C for a 1,000-hour test. We now turn to the more challenging goal of obtaining longtime stable systems under aging process at 80 °C. Figure 5.10a plots the stability data of a device sensitized with K-19 and GBA coadsorption under the thermal aging at 80 °C. Contrary to the fairly constant J_{sc} over the whole aging process, the V_{oc} decreased continuously over time, leading to a decrease in conversion efficiency. Compared to the control experiment in the absence of GBA coadsorption, the two stability data shared similar features in voltage degradation process, implying a possible desorption of coadsorbed GBA from the TiO_2 surface. FT-IR studies were performed to monitor this change. Due to the low penetration length of the infrared signal used in ATR FT-IR studies, a single layer of 3-μm-thick nanocrystalline TiO_2 particles was selected as the electrode. The TiO_2 electrodes were first sensitized with K-19 and GBA as the coadsorbent, assembled to devices and then aged under light soaking at 60 °C or dark thermal aging at 80 °C for three days before the devices were disassembled and the TiO_2 films were examined with FT-IR. Figure 5.11 shows IR spectra of the electrodes after different aging conditions. Traces a (control) and b (60 °C aging) were almost identical while in trace c (80 °C aging), there was an obvious decrease in the peak at *ca.* 1665 cm^{-1}, which was attributed to the asymmetric stretching of the carboxylate group of GBA. The decrease in this peak in trace c indicated that GBA firmly anchored on the surface during 60°C aging but underwent some desorption under 80°C aging, impairing the beneficial effect of GBA along the aging process.

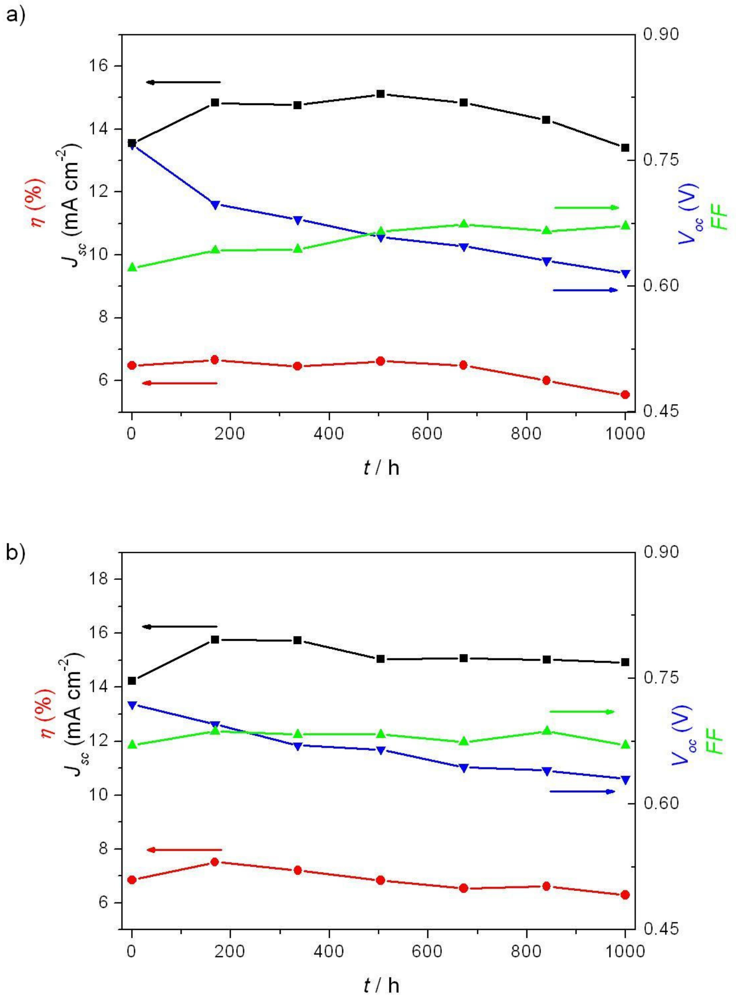

Figure 5.10 Detailed temporal evolution of photovoltaic parameters of devices under successive dark thermal aging at 80 °C. The devices were based on double layer (7+5) TiO_2 films sensitized with K-19 sensitizer in the a) presence and b) absence of GBA as the coadsorbent.

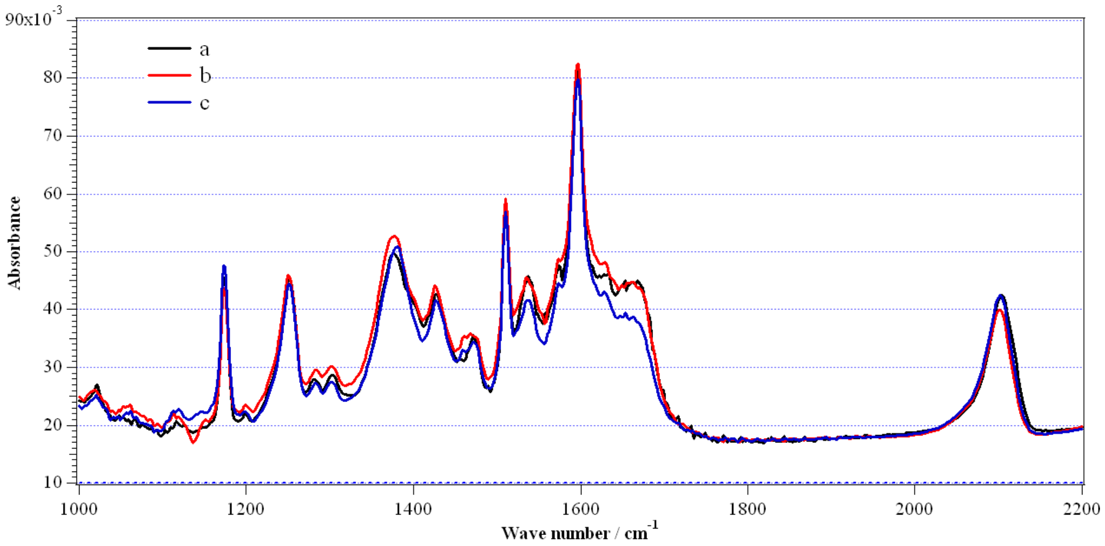

Figure 5.11 ATR-FTIR spectra for a mesoporous TiO_2 film before (a) and after aging (b, c). Two films were coated with Z-907 dye and GBA as coadsorbent with a coadsorbent-to-dye ratio of 1:4 and two devices were made with these films after measuring curve (a). Curves (b) and (c) were measured by opening the devices after they had undergone thermal aging for 3 days under light-soaking at 60 °C and in an oven at 80 °C, respectively.

Phosphonic acids have demonstrated their function as the coadsorbent to enhance the device stability under thermal aging at 80 °C.[9] In this aspect, a better coadsorbent could be an analog to GBA that has an anchoring group of phosphonic acid. Tetrabutylammonium 3-guanidinopropylphosphonate (GPA) was thus synthesized and studied in Chapters 6 and 7.

5.5 References to Chapter 5

[1]. Kumara, G.; Tennakone, K.; Perera, V. P. S.; Konno, A.; Kaneko, S.; Okuya, M. *J. Phys. D Appl. Phys.* **2001**, *34*, 868.

[2]. Zaban, A.; Chen, S. G.; Chappel, S.; Gregg, B. A. *Chem. Commun.* **2000**, 2231.

[3]. Chappel, S.; Chen, S. G.; Zaban, A. *Langmuir* **2002**, *18*, 3336.

[4]. Palomares, E.; Clifford, J. N.; Haque, S. A.; Lutz, T.; Durrant, J. R. *J. Am. Chem. Soc.* **2003**, *125*, 475.

[5]. Fabregat-Santiago, F.; Garcia-Canadas, J.; Palomares, E.; Clifford, J. N.; Haque, S. A.; Durrant, J. R.; Garcia-Belmonte, G.; Bisquert, J. *J. Appl. Phys.* **2004**, *96*, 6903.

[6]. Gregg, B. A.; Pichot, F.; Ferrere, S.; Fields, C. L. *J. Phys. Chem. B* **2001**, *105*, 1422.

[7]. Gawalt, E. S.; Lu G.; Bernasek, S. L.; Schwartz, J. *Langmuir* **1999**, *15*, 8929.

[8]. Hofer, R.; Textor, M.; Spencer, N. D. *Langmuir* **2001**, *17*, 4014.

[9]. Wang, P.; Zakeeruddin, S. M.; Moser, J. E.; Nazeeruddin, M. K; Sekiguchi, T.; Grätzel, M. *Nat. Mater.*, **2003**, *2*, 402.

[10]. Wang, P.; Zakeeruddin, S. M.; Humphry-Baker, R.; Moser, J.-E.; Grätzel, M. *Adv. Mater.* **2003**, *15*, 2101.

[11]. Wang, P.; Zakeeruddin, S. M.; Comte, P.; Charvet, R.; Humphry-Baker, R.; Grätzel, M. *J. Phys. Chem. B* **2003**, *107*, 14336.

[12]. Wang, P.; Klein, C.; Humphry-Baker, R.; Zakeeruddin, S. M.; Grätzel, M. *J. Am. Chem. Soc.* **2005**, *127*, 808.

[13]. Wang, P.; Klein, C.; Humphry-Baker, R.; Zakeeruddin, S. M.; Grätzel, M. *Appl. Phys. Letts.* **2005**, *86*, 123508.

[14]. Kuang D. B.; Klein C.; Snaith H. J.; Moser J. E.; Humphry-Baker R.; Comte P.; Zakeeruddin S. M.; Grätzel, M. *Nano Lett.* **2006**, *6*, 769.

[15]. Kubo, W.; Murakoshi, K.; Kitamura, T.; Yoshida, S.; Haruki, M.; Hanabusa, K.; Shirai, H.; Wada, Y.; Yanagida, S. *J. Phys. Chem.* **2001**, *105*, 12809.

[16]. Dahms, H. *J. Phys. Chem.* **1968**, *72*, 362.

[17]. Ruff, I.; Botar, L. *J. Chem. Phys.* **1985**, *83*, 1292.

[18]. I. Ruff, I.; Friedrich, V. J. *J. Phys. Chem.* **1971**, *75*, 3297.
[19]. Ruff, I.; Friedrich, V. J.; Csillag, K. *J. Phys. Chem.* **1972**, *76*, 162.
[20]. Majda, M. In Molecular Design of Electrode Surfaces; Murray, R. W., Ed.; John Wiley and Sons: New York, 1992; p 166.
[21]. Kawano, R.; Watanabe, M. *Chem. Commun.* **2003**, 330.
[22]. Kawano R.; Matsui H.; Matsuyama C.; Sato A.; Susan M. A. B. H.; Tanabe N.; Watanabe M. *J. Photochem. Photobio. A* **2004**, 164, 87.

6. Effects of ω-Guanidinoalkyl Acids as Coadsorbents in Dye-sensitized Solar Cells

Published in *J. Phys. Chem. C* **2007**, *111,* 398-403.

*Zhipan Zhang, Nick Evans, Shaik M. Zakeeruddin, Robin Humphry-Baker and Michael Grätzel**

Laboratory for Photonics and Interfaces, Institute of Chemical Sciences and Engineering, Swiss Federal Institute of Technology, CH-1015 Lausanne, Switzerland

* To whom the correspondence should be made

6.1 Abstract

Dye-sensitized solar cells (DSCs) based on nanocrystalline TiO_2 have been fabricated with an amphiphilic ruthenium sensitizer NaRu(2,2'-bipyridine-4-carboxylic acid-4'-carboxylate)(4,4'-dinonyl-2,2'-bipyridine)$(NCS)_2$, coded as Z-907 and a series of ω-guanidinoalkyl acids as coadsorbents. The addition of guanidinoalkyl acids as coadsorbents increased the open-circuit voltage of the DSCs and had no adverse effect on the photocurrent if an appropriate amount was used. Phototransient measurements showed that the addition of these guanidino coadsorbents slowed down the charge recombination and that the increase in the open-circuit voltage was due to suppression of the recombination and/or an upward shift of the TiO_2 band-edge to negative potentials. Thus, for the first time, a class of coadsorbents has been demonstrated to not only shield the surface electrons against recombination but also to shift the band edge to negative potentials, which is essential for future improvements in the performance of DSCs.

6.2 Introduction

The dye-sensitized mesoscopic nanocrystalline TiO_2 solar cell (DSC) has attracted intense scientific and industrial interest ever since its first successful demonstration in 1991.[1]-[5] As a low-cost alternative to conventional p-n junction solar devices, the DSC employs interconnected TiO_2 nanocrystals to form a “bulk” junction with a large surface area at the semiconductor/electrolyte interface and thus provides sufficient anchoring sites for sensitizers to attain effective light-harvesting and energy conversion. Under illumination, ultrafast electron injection takes place from the photoexcited dye molecules into the conduction band of the oxide semiconductor, followed by dye regeneration and hole transport to the counter electrode. The injected electrons diffuse through the oxide film to the current collector and pass subsequently via the external circuit to the counter electrode, where the reduction of the hole carrier, e.g. triiodide ions, completes the cycle of events generating electric power from sunlight. The open-circuit voltage (V_{oc}) of the device is determined by the difference between the quasi-Fermi level of TiO_2 and the potential of the redox couple in the electrolyte and is strongly dependent on both the rate of recombination and the band-edge position of TiO_2.[6]

The large interfacial area of the junction also favors charge recombination, of which the predominant channel in DSCs is the recapture of injected electrons by the oxidized species of the redox couple present in the electrolyte (eg. I_3^-), impairing the total light-to-electrical energy conversion efficiency of the device. Much effort has been devoted to surface modification of TiO_2 in order to suppress the adverse effect of this back reaction or to induce a negative shift of the band edge relative to vacuum, as a means of enhancing the photovoltage of the device. Examples of surface passivation include the introduction of an insulating layer on the solvent-exposed parts of the nanoporous electrode [7],[8] and the application of core-shell structured particles instead of bare TiO_2,[9]-[12] which were shown to improve the V_{oc} and performance of the device. Meanwhile, higher V_{oc} have also been reported for the treatment of the TiO_2 surface with bases (4-*tert*-butylpyridine or ammonia),[6] organic dipoles [13],[14] and amphiphilic coadsorbents,[15]-[17] resulting from upward manipulation of TiO_2 band-edge movement towards negative potentials.

We recently reported the effects of an interesting coadsorbent, 4-guanidinobutyric acid, on the photovoltaic parameters of DSCs.[18] We found that addition of this coadsorbent decreased the rate of recombination and produced a higher photovoltage. The mechanism was interpreted as a combination of surface passivation and an upward shift of the TiO_2 conduction band edge to more negative potentials. In the work presented here, we have employed four ω-guanidinoalkyl acids, with different chain lengths and anchoring groups, as coadsorbents with an amphiphilic sensitizer NaRu(2,2'-bipyridine-4-carboxylic acid-4'-carboxylate)(4,4'-dinonyl-2,2'-bipyridine)($NCS)_2$, coded as Z-907, and investigated their effects on DSCs with the aid of photochemical, impedance and phototransient measurements.

We note that during the final stage of preparation of the present manuscript, a paper of A. J. Frank appeared investigating the effect of guanidinium thiocyanate addition to the redox electrolyte of a DSC sensitized by the N-719 dye.[19] While the guanidinium cations were found to passivate recombination, this effect was largely compensated by a downward shift in the band-edge of the conduction band position of the TiO_2, resulting in a small overall V_{oc} gain of 20 mV. By contrast, our present study uses a surface bound guanidinium derivaties in conjugation with the amphiphilic Z-907 sensitizer, producing both a reduction of the recombination rate and an upward shift of the band edge and resulting in a larger gain in V_{oc}.

6.3 Experimental Section

Reagents and electrolytes. All chemicals and solvents used in the present work were of puriss quality. *N*-Methylbenzimidazole (NMBI) was purchased from Aldrich and recrystallized from diethyl ether before use. 3-Methoxypropionitrile (MPN) was obtained from Fluka and distilled before use. Guanidinoacetic acid, 4-guanidinobutyric acid and 6-guanidinohexanoic acid were purchased from Fluka. Due to the poor solubility of ω-guanidinoalkyl acid zwitterions in the dye solvent mixture (acetonitrile / *tert*-butyl alcohol, volume ratio of 1:1), hydrochloric acid was added to an aqueous solution of these compounds till pH = 2.5 to yield guanidinoacetic acid hydrochloride (GAAHCl), 4-guanidinobutyric acid hydrochloride (GBAHCl) and 6-guanidinohexanoic acid hydrochloride (GHAHCl). 3-Guanidinopropylphosphonic acid was prepared according to the literature method [20] and treated with an equimolar amount of aqueous tetrabutylammonium hydroxide to give tetrabutylammonium 3-guanidinopropylphosphonate (GPA). 1-Methyl-3-propylimidazolium iodide (PMII) was prepared according to the literature method [21] and its purity confirmed by ^{1}H NMR analysis. 400 nm-sized TiO_2 particles were received as a gift from CCIC (Japan). The electrolyte contained 0.8 M 1-propyl-3-methylimidazolium iodide, 0.15 M I_2, 0.1 M guanidinium thiocyanate, and 0.5 M *N*-methylbenzimidazole in MPN. The structures of Z-907 and the guanidino coadsorbents are shown in Figure 1.

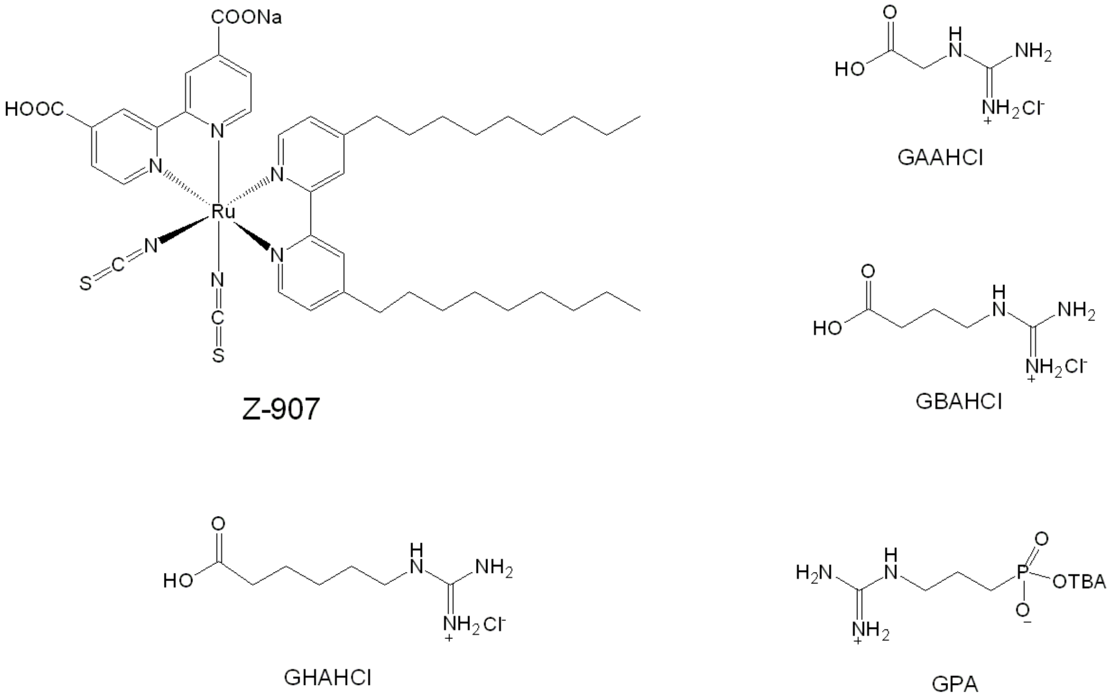

Figure 1. Structures of the sensitizer Z-907 and the coadsorbents used in this work.

Spectroscopic measurements. IR spectra were measured using a FTS 7000 FTIR spectrometer (Digilab, USA). Spectra were derived from 64 scans at a resolution of 2 cm^{-1}. All samples were measured under an identical mechanical force used to push the mesoscopic TiO_2 films in contact with the diamond window. A correction for attenuated total reflectance has not been applied to the data. The dye-loaded electrodes were rinsed in acetonitrile and dried prior to measuring the spectra.

For photoelectrochemical measurements, a 450 W xenon light source (Oriel, USA) was used to give an irradiance of 100 mW cm^{-2} (the equivalent of one sun at AM 1.5) at the surface of the solar cell. The spectral output of the lamp was matched in the region of 350-750 nm with the aid of a Schott K113 Tempax sunlight filter (Präzisions Glas & Optik GmbH, Germany) so as to reduce the mismatch between the simulated and true solar spectra to less than 2%. Various incident light intensities were regulated with neutral wire mesh attenuators. The current voltage characteristics of the device under these conditions were obtained by applying an external potential bias to the device and measuring the generated photocurrent with a Keithley model 2400 digital source meter (Keithley, USA).

Photovoltage transients were observed using an exciting pulse generated by a ring of red light emitting diodes (LEDs, Lumiled) controlled by a fast solid-state switch. Pulse widths of 200 ms were used. The pulse was incident on the photoanode side of the device and its intensity was controlled to keep the modulation of the voltage below 5 mV. A white bias light, also incident on the same side of the device, was supplied by white diodes. Usually, transients were measured at different while light intensities ranging from 150 % to 0.1 % sun via tuning the voltage applied on the bias diodes.

Impedance measurements were performed with a computer controlled potentiostat (EG&G, Model 273) equipped with a frequency response analyzer (EG&G, Model 1025). The frequency range is 0.005-100 KHz and the magnitude of the modulation signal is 10 mV. The obtained spectra were fitted with Z-View software (v2.8b, Scribner Associates Inc.) in terms of appropriate equivalent circuits.[22]-[24]

Device Fabrication. A double-layer TiO_2 mesoscopic film was used as the photoanode. A 7 µm-thick transparent layer of 20 nm-sized TiO_2 particles was first printed on the fluorine-doped SnO_2 conducting glass electrode and further coated with a 5 µm-thick second layer of 400 nm light scattering anatase particles. The details for the preparation of mesoscopic TiO_2 film have been described elsewhere.[15],[25] The double-layer structured TiO_2 electrode was first sintered at 500 °C for 25 minutes and cooled to about 100 °C in air. It was then immersed in the dye solution at room temperature for 12 h before assembly with a thermally platinized conducting glass counter electrode. The dye solution contained 0.3 mM Z-907 dye and various concentrations of an ω-guanidinoalkyl acid as the coadsorbent in acetonitrile and *tert*-butyl alcohol (volume ratio, 1:1). For the carboxylic acids GAAHCl, GBAHCl and GHAHCl, an equimolar concentration of 0.3 mM was used, whereas for GPA either 0.3 mM or 0.075 mM was employed. The electrodes were separated by a 35 µm-thick Bynel hot-melt ring (DuPont, USA) and sealed by heating. The internal space was evacuated, then filled with electrolyte through a filling hole made by a sandblasting drill on the counter electrode glass substrate. Finally, the electrolyte introduction hole was sealed with a Bynel sheet under a thin glass cover by heating.

Stability Test. Hermetically sealed cells were used for long-term stability tests under harsh thermal stress by keeping them in an oven (80 °C) in the dark. Before photoelectrochemical measurements, the cells were irradiated at open circuit under a Suntest CPS plus lamp (ATLAS GmbH, 100 mW cm^{-2}, 60 °C) with a 50 µm-thick polyester film (Preservation Equipment Ltd, UK) as a UV cutoff filter (below 400 nm) for 1 h and allowed to cool and equilibrate at room temperature for an hour.

Theory and analysis. In a transient photovoltage experiment, we used red light emitting diodes as a probe to generate a voltage perturbation about the V_{oc} of the cell under the white bias light and measured the voltage decay process thereafter. Normally, the decay closely follows a pseudo single exponential form, thus the recombination rate constant, k, can be extracted from the slope of the semi-logarithmic plot. The chemical capacitance of the TiO_2/electrolyte interface at the V_{oc} is calculated as $C = \Delta Q/\Delta V$, where ΔV is the peak of the transient, and ΔQ is the number of electrons injected during the light flash. The latter is determined by integrating a photocurrent transient at short circuit generated from an identical pulse. This method may underestimate the actual injected charge by the fraction of electrons that are lost to recombination during transport at short circuit, yet it will affect only the magnitude but not the shape of the calculated capacitance versus the potential curves.[26],[27]

Meanwhile, as proposed by Frank et al.,[6],[17],[28] the photoinduced charge density, n, at open circuit is calculated using the following equation:

$$n = J_{sc}\tau_r/(q_e d(1-p)) \qquad (1)$$

where J_{sc} is the short circuit current density, τ_r is the characteristic time of the exponential decay of the photovoltage at open circuit induced by the diode probe pulse, which equals the recombination lifetime of photocarriers at the bias light intensity, q_e is the elementary charge, and d and p are the thickness and porosity of the TiO_2 film, respectively. Band-edge movement can be determined by comparing the dependence of V_{oc} on n at open circuit in the absence and in the presence of the coadsorbent. As long as n solely determines the difference between the conduction band edge and the electron quasi-Fermi level under illumination, a higher or lower V_{oc} at a constant photoelectron density corresponds to negative or positive movement of the conduction band edge, respectively.[19] On the other hand, if the adsorbent does not affect the electron diffusion coefficient, the rate constant, k, will only depend on the change in recombination kinetics at the TiO_2/electrolyte interface. If the coadsorbent passivates the surface against recombination at a fixed J_{sc}, k will decrease and *n* will increase. Likewise, enhancement in recombination will yield a larger *k* and smaller *n*. Therefore, comparison between the plots of *n* versus the recombination current density, J_r, in cells with and without the coadsorbent is indicative of whether the adsorbent slows or enhances recombination. Considering the relatively slow recombination at short circuit, J_{sc} is used as a reasonable approximation for J_r at open circuit.[19],[29],[30] Again, it should be noted that this might underestimate J_r due to the fraction of electrons that are lost to recombination during transport at short circuit, which also takes place in the measurement of chemical capacitance.

6.4 Results and Discussions

FTIR Analysis. Figure 2 shows the attenuated total reflectance FTIR (ATR-FTIR) spectra of nanoporous TiO_2 electrodes stained with the Z-907 sensitizer alone (spectrum a) or in combination with different coadsorbents (spectra b to e). In spectrum a, the single feature at 2104 cm^{-1} arises from the thiocyanato group, the bands at 1597 cm^{-1} and 1378 cm^{-1} are for the asymmetric and symmetric stretching modes of carboxylate groups. The signals observed at 2926 and 2856 cm^{-1} correspond to the asymmetric and symmetric stretching modes of the CH_2 units arising from the dye. The peaks located at 1540 and 1427 cm^{-1} are ascribed to the aromatic modes of bipyridine while the broad band centered at 3440 cm^{-1} is due to adsorbed water, presumably from the dye solution since the TiO_2 film is heated prior to staining.

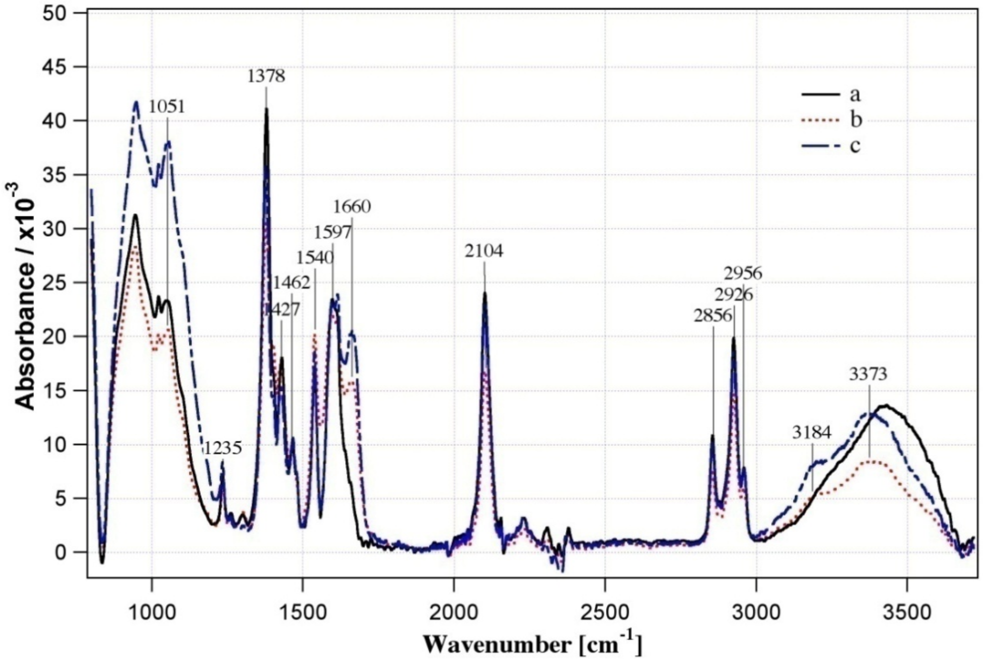

Figure 2. ATR-FTIR spectra for mesoporous TiO_2 films coated with (a) only the Z-907 dye or with the Z-907 dye and the guanidino coadsorbents (b) GBAHCl or (c) GPA. A TiO_2 reference film heated at 500 °C to remove surface-adsorbed water has been subtracted for clarity of presentation.

Spectrum b was measured with a TiO_2 electrode dyed from the solution consisting of the Z-907 sensitizer and GBAHCl at equal concentrations. Due to the presence of GBAHCl on the electrode, several new bands are observed. Two diagnostic peaks centered at 3184 cm^{-1} and 3373 cm^{-1} correspond to the N-H stretching modes of the guanidinium group. Likewise, the peak at 1660 cm^{-1} is due to the asymmetric stretching of the guanidinium group. Spectra of TiO_2 electrodes stained with Z-907 in the presence of either GAAHCl or GHAHCl as the coadsorbent resemble spectrum b (not shown here). Spectra c also shows the above mentioned bands in addition to a shoulder peak of P-O stretching mode centered at *ca.*1100 cm^{-1}. These spectroscopic data are convincing evidence that a mixed layer of Z-907 and guanidinoalkyl acid has been co-grafted onto the electrode.

Photovoltaic Characteristics. Figure 3 shows the current-voltage characteristics of dye-sensitized solar cells employing Z-907 alone (device **a**) or with different guanidino coadsorbents (devices **b** to **f**) under illumination of AM 1.5. The photovoltaic characteristic parameters of short-circuit current density (J_{sc}), open-circuit voltage (V_{oc}), fill factor (FF) and photovoltaic conversion efficiency (η) are listed in Table 1. Device **a** exhibits a J_{sc} of 14.0 mA cm^{-2}, V_{oc} of 740 mV and conversion efficiency of 7.2 %, which is excellent for cells with Z-907 dye and non-volatile electrolytes.[21] Coadsorption with guanidinocarboxylic acids leads to an increase in open-circuit voltage, yielding V_{oc} values of 776, 798 and 770 mV for devices **b**, **c**, and **d**, respectively. Meanwhile, although a certain amount of dye is replaced by the coadsorbents, small increases of 0.1 to 0.3 mA cm^{-2} in J_{sc} are observed for devices **b** to **d**, which agrees well with the corresponding IPCE spectra (Figure S1). Comparing these relatively high J_{sc} to that of device **a**, this implies that any expected reduction in light-harvesting by the sensitizer due to the dilution with co-grafted guanidinocarboxylic acids should be compensated by a smaller recombination loss during electron transportation across the nanocrystalline TiO_2 film. It is interesting to find that GBAHCl coadsorption increased the V_{oc} by 9 % and yielded a 15 % enhancement for the overall power conversion efficiency to 8.3 %, an unprecedented value for devices using Z-907 sensitizer. The effect is similar to our previous report on 4-guanidinobutyric acid coadsorption with a high-extinction-coefficient heteroleptic ruthenium sensitizer.[18]

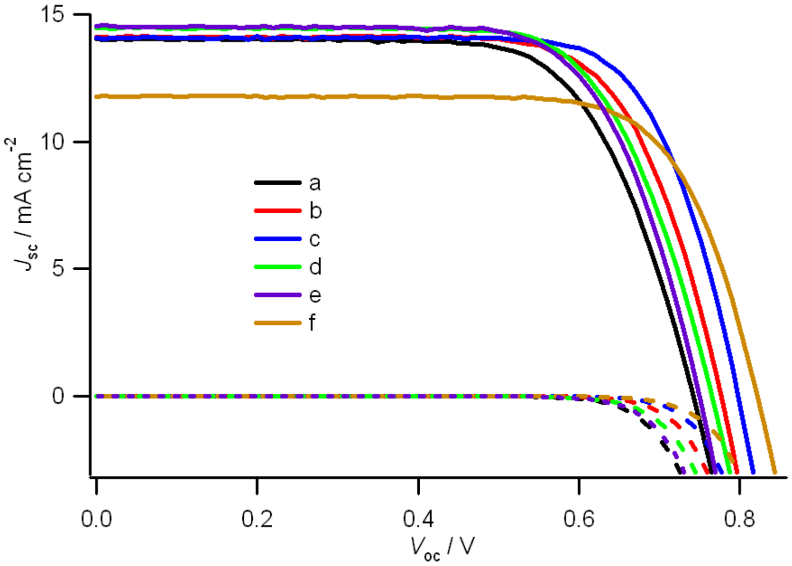

Figure 3. Current-voltage characteristics of different cells in the dark (dashed lines) and under simulated illumination (AM 1.5, 100 mW cm^{-2}, solid lines). Cells were fabricated from TiO_2 films stained with Z-907 alone (**a**) or with the guanidino coadsorbents GAA (**b**), GBA (**c**), GHA (**d**), and GPA (**e**, **f**). The molar coadsorbent-to-dye ratio is 1:1 except in (**e**) where 1:4 is used.

Table 1. Photovoltaic characteristics of dye-sensitized solar cells made with TiO_2 films stained in Z-907 solution containing different kinds of guanidino coadsorbents under illumination of AM 1.5. The number in round brackets shows the molar coadsorbent-to-dye ratio.

Device	Dye and coadsorbent	J_{sc} / mA cm^{-2}	V_{oc} / mV	*FF*	η / % [a]	Relative dye load [b]
a	Z 907	14.0	740	0.69	7.2	1
b	GAAHCl + Z 907 (1:1)	14.1	776	0.72	7.8	0.92
c	GBAHCl + Z 907 (1:1)	14.1	798	0.74	8.3	0.94
d	GHAHCl + Z 907 (1:1)	14.4	770	0.71	7.8	0.96
e	GPA + Z 907 (1:4)	14.5	761	0.69	7.7	0.92
f	GPA + Z 907 (1:1)	11.8	822	0.74	7.2	0.85

[a] The spectral distribution of the xenon lamp simulates air mass 1.5 solar light. 1.0 sun corresponds to ~100 mW cm^{-2}. The cell active areas were 0.158 cm^{-2}. [b] The dye loading is determined from the optical absorption of the TiO_2 film at 514 nm.

When GPA is applied as coadsorbent with a coadsorbent-to-dye ratio of 1:4 (device **e**), a moderate increase in V_{oc} and no adverse effect on photocurrent are observed. Increasing the coadsorbent concentration by four fold results in a 80 mV increase in V_{oc} and a 2 mA cm^{-2} drop in J_{sc} (device **f)**, which is probably induced by the larger amount of GPA anchored on the TiO_2 surface. GPA to dye ratios greater than 1:1 do not further enhance V_{oc} yet considerably impair J_{sc} and the power conversion efficiency, presumably due to the loss of sensitizer on the surface. Alkyl phosphonic acids are known to bind strongly to oxide surfaces via the formation of P-O-metal bonds,[31],[32] eliminating most of the hydrophilic surface sites that are available for water absorption and potential charge recombination in the DSC. The coadsorption of decylphosphonic acid (DPA) was reported to slightly increase the current and power efficiency of DSCs by suppression of the back electron transfer from the conduction band of TiO_2 to triiodide in the electrolyte,[21] a rationale which is also applicable in the current case. The addition of an ω-guanidinium group to an alkylphosphonic coadsorbent apparently helps its ability to enhance the DSC open-circuit voltage.

Phototransients. Photovoltage and photocurrent transients were performed to study the device**s**. The recombination rate constant (k) of dye-sensitized cells is known to be dependent on the electrode potential. This effect was scrutinized by adjusting the V_{oc} resulting from various bias light intensities. Figure 4 shows the logarithmic plot of k with respect to V_{oc}. The recombination rate constant, k, is apparently exponentially dependent on V_{oc}, as was pointed out by other authors.[33]-[35] Within experimental error, linear fits to all of the data give similar slope values in the range of 11.2 ± 0.5. This slope corresponds to ~90 mV per decade, which is slightly smaller than the value of 120 mV per decade obtained for solid-state cells.[27] Since the electron lifetime, τ_r, is the reciprocal of the recombination rate constant, τ_r is greater in devices **b** to **f** than in device **a**. Figure 5 shows the curve of chemical capacitance, C_μ, versus V_{oc} at different light intensities. C_μ follows a characteristic exponential rise with increasing forward bias. Apparently, a larger C_μ is found in device **a** than in any of the devices with guanidino coadsorbents. The decrease of C_μ might be due to either the negative shift of the conduction band or surface passivation from the coadsorption process, as will be discussed in the following section.

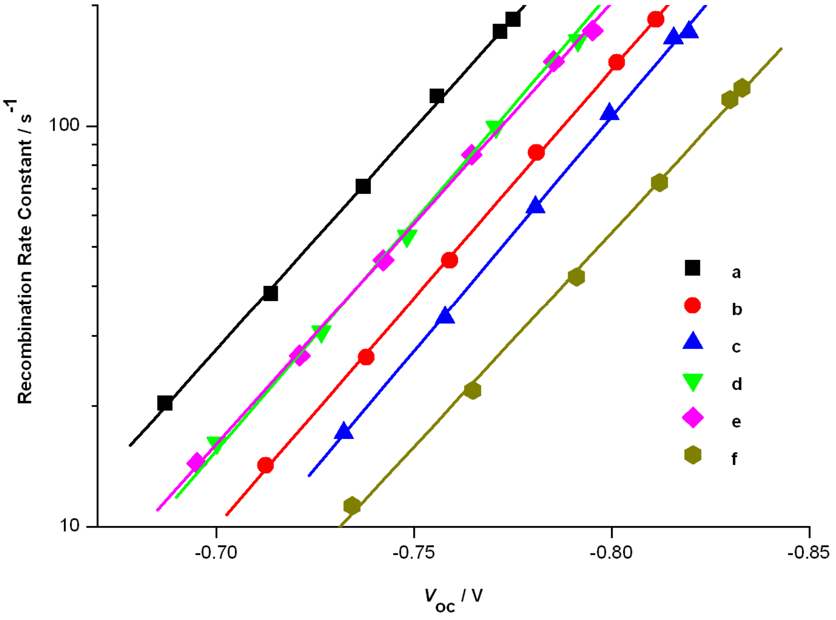

Figure 4. Recombination rate constants of devices **a** to **f** at open-circuit voltage under varying light bias.

We note that electron density in TiO_2 film can be calculated via an integration of the capacitance over the bias voltage and a comparison of this value with electron density obtained by equation (1) is performed. At the same bias voltage, for example, for cell **f** at -0.83 V, electron density values of 1.3 $\times 10^{18}$ and 1.9×10^{18} cm^{-3} are obtained, which is a fair agreement for kinetic analysis.

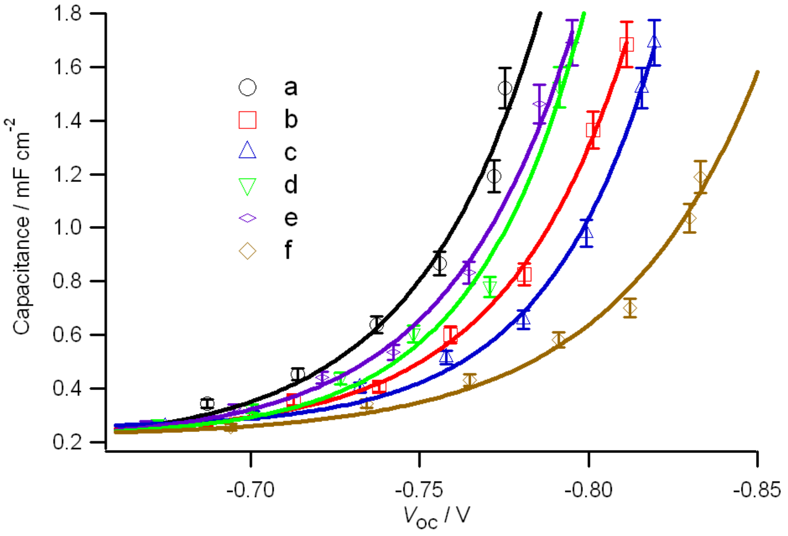

Figure 5. Chemical capacitance of devices **a** to **f** at open-circuit voltage under varying light bias.

Band-edge movement versus recombination. Figure 6 shows the effect of different coadsorbents on the photoinduced charge density at open circuit voltage with respect to J_{sc}. It is clear that all of the devices with coadsorbents have higher photoinduced charge densities for a given J_{sc} than does device

a, implying a suppression of recombination (eq. 1). All guanidinocarboxylic acids functionalize the surface to a similar extent, whereas GPA seems to exhibit a greater passivation of the surface (devices **e** and **f**), which might be due to its strong binding on TiO_2. Figure 7 displays the influence of guanidino coadsorbents on the photoinduced charge density at open circuit over a range of light intensities. The coadsorption of guanidinocarboxylic acids all move up the band-edge, with values of ~15 mV for GAAHCl (device **b**), ~35 mV for GBAHCl (device **c**) and ~15 mV for GHAHCl (device **d**). Considering the similar passivation effects of GAAHCl, GBAHCl and GHAHCl on the TiO_2 surface in Figure 6, the ~20 mV difference in band-edge movement well explains the higher V_{oc} of device **c** than those of devices **b** and **d** as seen in the above mentioned photovoltaic measurements. The negative shift does not seem to follow a monotonic trend on the chain length of the guanidino compounds, yielding GBAHCl as the most effective additive in increasing V_{oc}. In contrast, for GPA coadsorption with a coadsorbent-to-dye ratio of 1:4 (device **e**), no notable band shift (less than 10 mV) can be reliably detected within experimental errors, implying the measured increase of V_{oc} is achieved mostly through suppression of the recombination as shown in Figure 6. A further increase in the coadsorbent-to-dye ratio to 1:1 (device **f**) leads to a pronounced negative band-edge shift of ~30 mV, which indicates that the 80 mV gain of device **f** in V_{oc} is a result of the collective effects of negative band-edge shift and surface passivation. To the best of our knowledge, this is the first time that a class of adsorbent both shields the surface against recombination *and* shifts the band edge to negative potentials, which is the best condition one can expect for employing coadsorbent in DSCs.[19]

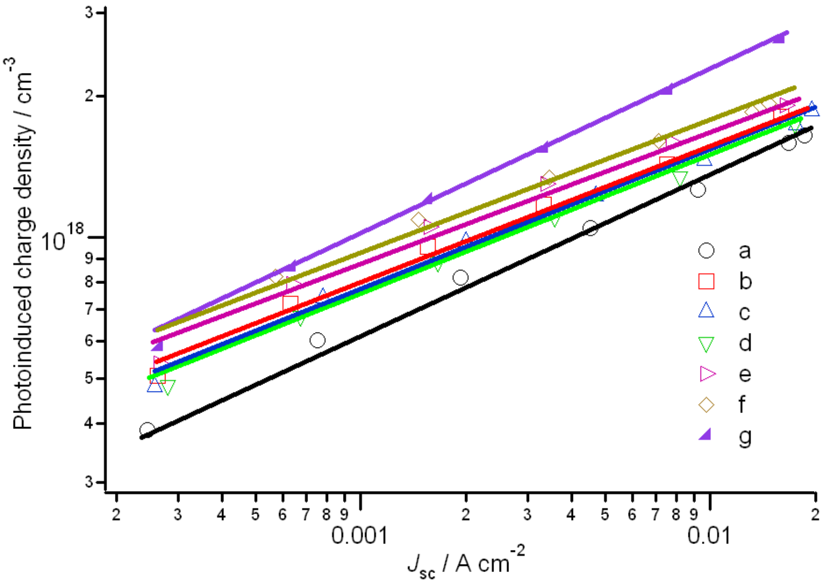

Figure 6. Effect of different coadsorbents on the photoinduced charge density at open circuit with respect to short-circuit current density (J_{sc}). The data were obtained from measurements of devices **a** to **f** over a range of light intensities. Device **g** was made with Z-907 sensitizer and decylphosphonic acid (DPA) with a coadsorbent-to-dye ratio of 1:4 for comparison.

Finally, device **g** was made with Z-907 sensitizer and decylphosphonic acid (DPA) with a coadsorbent-to-dye ratio to 1:4. Compared with device **a**, device **g** showed a small improvement in the short-circuit density and an unchanged open-circuit voltage, as has been reported before.[21] Phototransient measurements were also performed for device **g** and the results are summarized in Figure 6 and 7. Clearly, a strong suppression of recombination and a *positive* conduction band shift of ~40 mV can be seen. The surface passivation well offsets the unfavorable downward band-edge movement, yielding the unchanged open-circuit voltage for device **g**. It is interesting to find that the addition of an ω-guanidinium group to an alkylphosphonic coadsorbent completely changes the properties of the coadsorbent, presumably due to the dipole that is pointing towards the TiO_2 surface and pushing the band-edge to more negative potentials. Furthermore, it should be noted that the photoinduced charge density, *n*, calculated using equation (1) is probably lower than the actual total electron concentration due to the recombination under short-circuit conditions (see **Theory and analysis** section), the difference appears to be constant factor for dye solar cells, yet it is unclear if differences between cells may exist. However, in the present case, considering the short-circuit current of cells investigated here is fairly close to predicted values by IPCE or theoretical calculations, the assumption that negligible recombination takes place under short-circuit conditions could be achieved to a good approximation and more importantly, this will not change our current conclusion on the effects of ω-guanidinoalkyl acids.

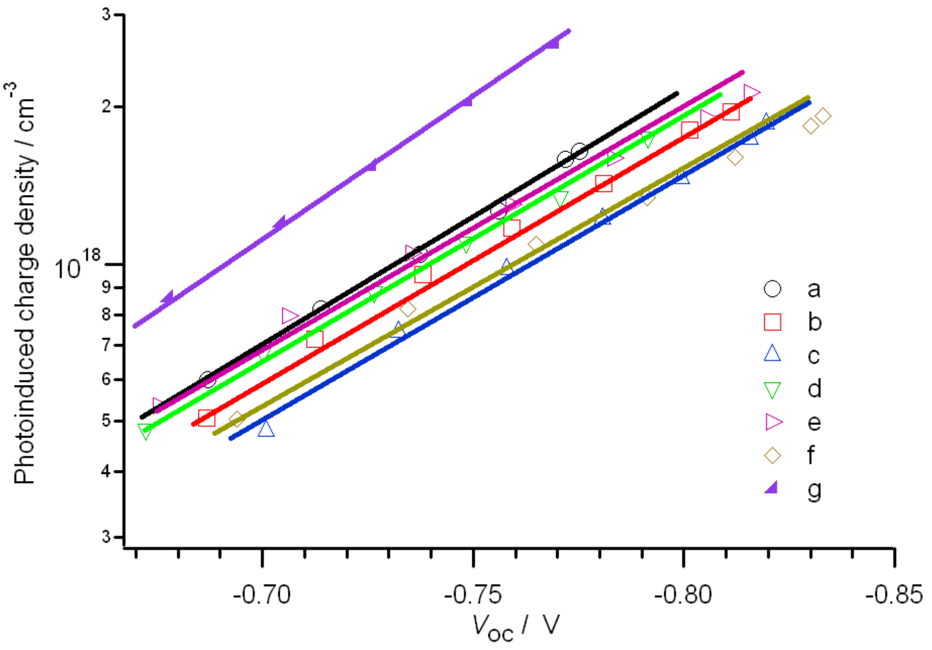

Figure 7. Effect of different coadsorbents on the photoinduced charge density at open circuit over a range of open-circuit voltage (V_{oc}). The data were obtained from measurements of devices **a** to **f** over a range of light intensities. Device **g** was made with Z-907 sensitizer and decylphosphonic acid (DPA) with a coadsorbent-to-dye ratio of 1:4 for comparison.

Stability tests. Hermetically sealed devices were stored in an oven at 80 °C for long-term thermal stress tests and their photovoltaic parameters were monitored at intervals. In addition to the cell made only with Z-907 as the control (cell **I**), cell **II,** which was fabricated with GPA as coadsorbent (a coadsorbent-to-dye ratio of 1:4 was used) is chosen for comparison, since ATR-FTIR results demonstrate that GPA is able to bind strongly to the TiO_2 surface during long-term thermal aging at 80 °C (Figure S2) whereas ω-guanidinocarboxylic acids cannot, as the guanidinium peaks vanished with aging (not shown here). Detailed temporal evolution of photovoltaic parameters of cell **I** and cell **II** are shown in Table S1. Both devices show good stability following 1,000 h of aging under these conditions; a modest decrease is observed in the power conversion efficiency due to the drop in V_{oc}. Electrochemical impedance measurements were used to study these two devices after 1,000 h aging. Figure 8 shows typical electrochemical impedance spectra of the aged cells **I** (black) and **II** (red) measured in the dark. The figure is presented in the form of Bode (top) and Nyquist plots (bottom). For clarity of comparison, an identical forward bias of -0.72 V was applied to both cells. Data fitting shows that compared with cell **I**, cell **II** has a slightly smaller C_{μ} (1500 μF cm^{-2} to 1610 μF cm^{-2}) but a higher R_{rec} (26.8 Ω vs. 13.3 Ω), yielding a larger τ_r of 14.7 ms than that of cell **I**, 8.7 ms. The longer electron lifetime measured in the aged cell **II** should be attributed to suppression of recombination by the presence of the remaining GPA on the surface of TiO_2 after 1000 h high temperature aging, as is supported by the ATR-FTIR spectra in Figure S2.

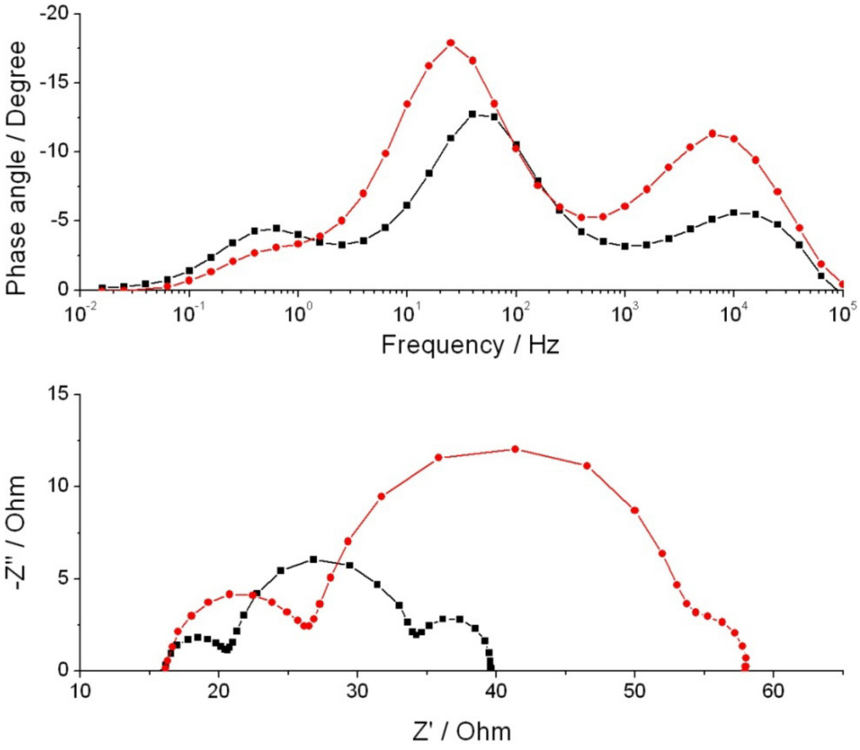

Figure 8. Typical electrochemical impedance spectra of cell **I** (black) and cell **II** (red) in the form of Bode plots (top) and Nyquist plots (bottom). The spectra were measured at an external potential of -0.72 V in the dark after these two devices had been aged at 80 °C in the oven for 1000 h.

Conclusions. In summary, a series of guanidinoalkyl acids was employed as coadsorbents with the Z-907 sensitizer and the effects on dye-sensitized solar cells were investigated. The addition of guanidino coadsorbents increased the open-circuit voltage of the DSCs and had no adverse effect on the photocurrent if a proper amount was used. Up to a 15 % increase in total power conversion efficiency was achieved by using GBA as the coadsorbent and its efficiency of 8.3 % under AM 1.5 illumination is unprecedented for devices with the Z-907 sensitizer. Phototransient measurements showed that the increase in open-circuit voltage for guanidinocarboxylic acids is a collective effect of suppression of surface recombination *and* negative band-edge movement. In contrast, 3-guanidinopropylphosphonic acid at low concentration only suppresses the surface recombination, whereas at a higher concentration it also induces a negative band shift to ~30 mV, which is opposite to the effect of decylphosphonic acid that leads to a *positive* band-edge shift of 40 mV. This study shows for the first time that a class of coadsorbent can not only shield the surface against recombination but also shift the band edge to more negative potentials, which is ideal for future improvements in the performance of DSCs.

Acknowledgements. We are grateful to Mr. P. Comte for film preparation and Dr. Qing Wang for helpful discussions.

Supporting Information Available. IPCE spectra for devices **a** to **f**, additional ATR-FTIR spectra and detailed temporal evolution of photovoltaic parameters. This material is available free of charge via the Internet at http://pubs.acs.org.

6.5 References

[1]. O'Regan, B.; Grätzel, M. *Nature* **1991,** *353*, 737.
[2]. Grätzel, M. *Nature* **2001,** *414*, 338.
[3]. Hagfeldt, A.; Grätzel, M. *Chem. Rev*. **1995**, *95*, 49.
[4]. Grätzel, M. *J. Photochem. Photobio. A* **2004**, 16*4*, 3.
[5]. Grätzel, M. *Chem. Lett.* **2005**, *34*, 8.
[6]. Huang, S. Y.; Schlichthörl, G.; Nozik, A. J.; Grätzel, M.; Frank, A. J. *J. Phys. Chem. B* **1997**, *101*, 2576.
[7]. Tennakone, K.; Perera, V. P. S.; Kottegoda, I. R. M.; De Silva, L. A. A.; Kumara, G.; Konno, A. *J. Electron. Mater.* **2001**, *30*, 992.
[8]. Gregg, B. A.; Pichot, F.; Ferrere, S.; Fields, C. L. *J. Phys. Chem. B* **2001**, *105*, 1422.
[9]. Kumara, G.; Tennakone, K.; Perera, V. P. S.; Konno, A.; Kaneko, S.; Okuya, M. *J. Phys. D Appl. Phys.* **2001**, *34*, 868.
[10]. Zaban, A.; Chen, S. G.; Chappel, S.; Gregg, B. A. *Chem. Commun.* **2000**, 2231.
[11]. Chappel, S.; Chen, S. G.; Zaban, A. *Langmuir* **2002**, *18*, 3336.
[12]. Palomares, E.; Clifford, J. N.; Haque, S. A.; Lutz, T.; Durrant, J. R. *J. Am. Chem. Soc.* **2003**, 125, 475.
[13]. Krüger, J.; Bach, U.; Grätzel, M. *Adv. Mater.* **2002**, *12*, 447.
[14]. Rühle, S.; Greenshtein, M.; Chen, S.-G.; Merson, A.; Pizem, H.; Sukenik, C. S.; Cahen, D.; Zaban, A. *J. Phys. Chem. B* **2005**, *109*, 18907.

[15]. Wang, P.; Zakeeruddin, S. M.; Comte, P.; Charvet, R.; Humphry-Baker, R.; Grätzel, M. *J. Phys. Chem. B* **2003**, *107*, 14336.

[16]. Kay, A.; Grätzel, M. *J. Phys. Chem.* **1993**, *97*, 6272.

[17]. Neale, N. R.; Kopidakis, N.; van de Lagemaat, J.; Grätzel, M.; Frank, A. J. *J. Phys. Chem. B* **2005,** *109*, 23183.

[18]. Zhang, Z.; Zakeeruddin, S. M.; O'Regan, B. C.; Humphry-Baker, R.; Grätzel, M. *J. Phys. Chem. B* **2005**, *109*, 21818.

[19]. Kopidakis, N.; Neale, N. R.; Frank, A. J. *J. Phys. Chem. B* **2006,** *110*, 12485.

[20]. Cameron, D. G.; Hudson, H. R.; Pianka, M. *Phosphorus, Sulfur Silicon Relat. Elem.* **1993**, *83*, 21.

[21]. Wang, P.; Zakeeruddin, S. M.; Humphry-Baker, R.; Moser, J.-E.; Grätzel, M. *Adv. Mater.* **2003**, *15*, 2101.

[22]. Bisquert, J. *Phys. Chem. Chem. Phys.* **2003**, *5*, 5360.

[23]. Bisquert, J. *J. Phys. Chem. B* **2002**, *106*, 325.

[24]. Wang, Q.; Moser, J.; Grätzel, M. *J. Phys. Chem. B* **2005**, *109*, 14945.

[25]. Barbé, C. J.; Arendse, F.; Comte, P.; Jirousek, M.; Lenzmann, F.; Shklover, V.; Grätzel, M. *J. Am. Ceram. Soc.* **1997**, *80*, 3157.

[26]. O'Regan, B. C.; Lenzmann, F. *J. Phys. Chem. B* **2004**, *108*, 4342.

[27]. O'Regan, B. C.; Scully, S.; Mayer, A. C.; Palomares, E.; Durrant, J. *J. Phys. Chem. B* **2005**, *109*, 4616.

[28]. Frank, A. J.; Kopidakis, N.; van de Lagemaat, J. *Coord. Chem. Rev.* **2004**, *248*, 1165.

[29]. Kopidakis, N.; Schiff, E. A.; Park, N.-G.; van de Lagemaat, J.; Frank, A. J. *J. Phys. Chem. B* **2000**, *104*, 3930.

[30]. van de Lagemaat, J.; Frank, A. J. *J. Phys. Chem. B* **2001**, *105*, 11194.

[31]. Gawalt, E. S.; Lu G.; Bernasek, S. L.; Schwartz, J. *Langmuir* **1999**, *15*, 8929.

[32]. Hofer, R.; Textor, M.; Spencer, N. D. *Langmuir* **2001**, *17*, 4014.

[33]. Van de Lagemaat, J.; Park, N.-G.; Frank, A. J. *J. Phys. Chem. B* **2000**, *104*, 2044.

[34]. Willis, R. L.; Olson, C.; O'Regan, B.; Lutz, T.; Nelson, J.; Durrant, J. R. *J. Phys. Chem. B* **2002**, *106*, 7605.

[35]. Duffy, N. W.; Peter, L. M.; Rajapakse, R. M. G.; Wijayantha, K. G. U. *Electrochem. Commun.* **2000**, *2*, 658.

Supporting information

Effects of ω-Guanidinoalkyl Acids as Coadsorbents in Dye-sensitized Solar Cells

*Zhipan Zhang, Nick Evans, Shaik M. Zakeeruddin, Robin Humphry-Baker and Michael Grätzel**

Laboratory for Photonics and Interfaces, Institute of Chemical Sciences and Engineering, Swiss Federal Institute of Technology, CH-1015 Lausanne, Switzerland

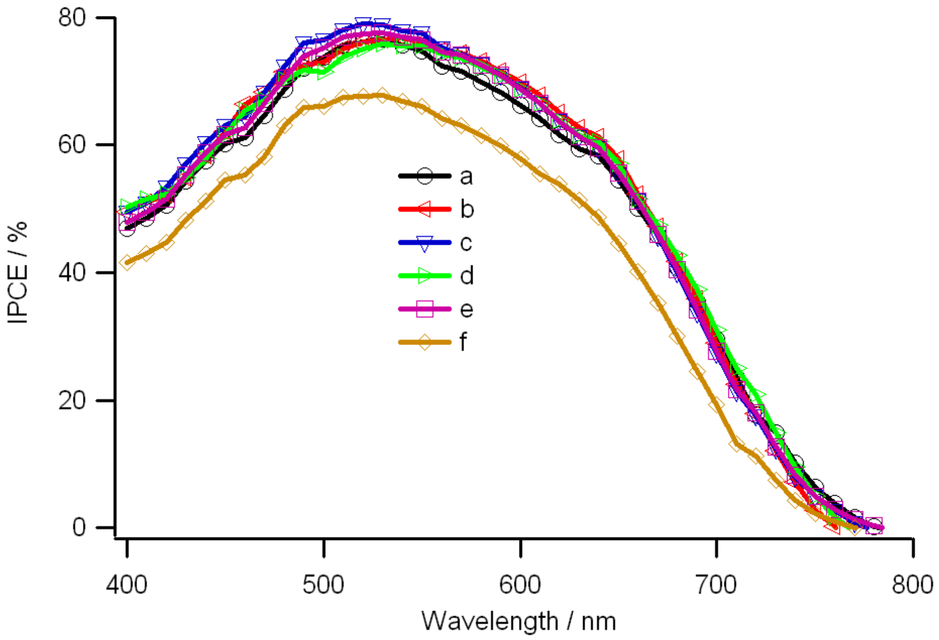

Figure S1.IPCE spectra for devices **a** to **f**. Cell active area: 0.158 cm^2.

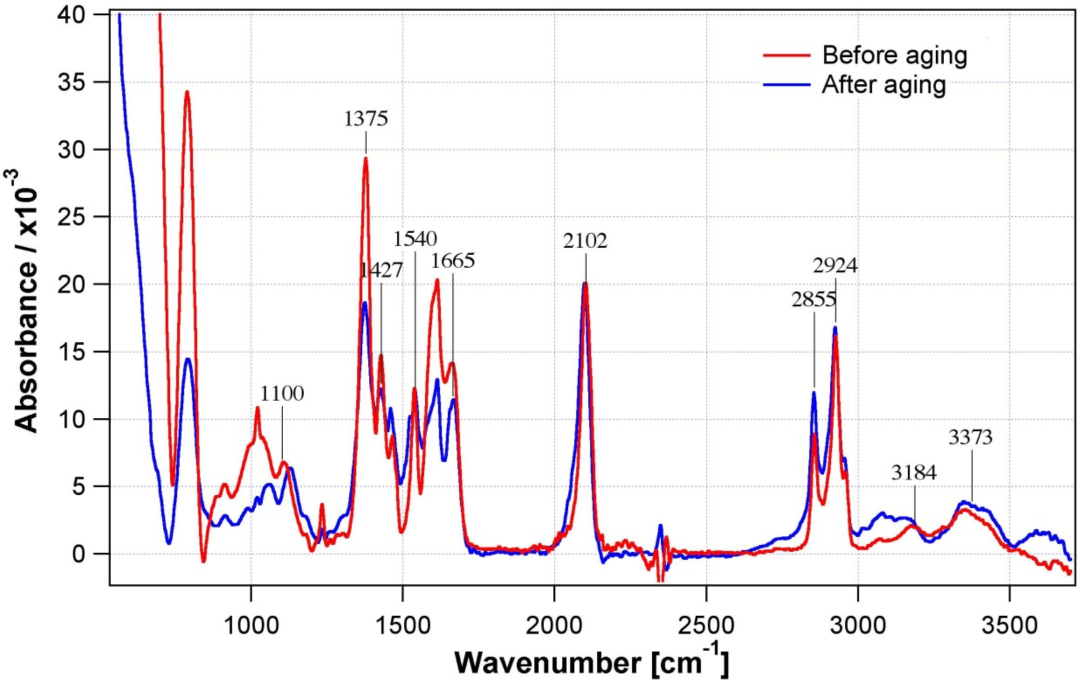

Figure S2. ATR-FTIR spectra for a mesoporous TiO_2 film before (red) and after (blue) aging. The film was coated with Z-907 dye and GPA as coadsorbent with a coadsorbent-to-dye ratio of 1:4 and a device was made with this film after measuring the red curve. The blue curve was measured by opening the device after it had undergone thermal aging for 5 weeks in an oven at 80 °C, in which the N-H stretching modes of the guanidinium group centered at 3184, 3373 cm^{-1} and the P-O stretching mode centered at *ca.*1100 cm^{-1}can still be clearly seen. A TiO_2 reference film heated at 500 °C to remove surface-adsorbed water has been subtracted for clarity of presentation.

Table S1. Detailed temporal evolution of photovoltaic parameters of cell **I** and cell **II** measured under an illumination of AM 1.5.

	Cell **I**				Cell **II**			
t / h	J_{sc} / mA cm^{-2}	V_{oc} / mV	*FF*	η / % [a]	J_{sc} / mA cm^{-2}	V_{oc} / mV	*FF*	η / % [a]
0	14.3	714	0.68	6.9	14.8	752	0.66	7.3
168	14.8	724	0.71	7.6	15.3	742	0.68	7.7
340	14.8	675	0.71	7.1	15.1	716	0.68	7.3
1000	14.0	630	0.71	6.3	14.0	675	0.69	6.5

[a] The spectral distribution of the xenon lamp simulates air mass 1.5 solar light. 1.0 sun corresponds to ~100 mW cm^{-2}. The cell active areas were 0.158 cm^{-2}.

7. Influence of Coadsorbent Structure on the Photovoltage

7.1 Band-edge shift versus recombination, another perspective on guanidino-coadsorbent effects

In Chapter 6, we separated the photovoltage increase induced by coadsorption into band-edge movement and suppression in back reaction with a simple and approximate calculation in charge density.[1],[2] The main drawback of this calculation was applying apparent lifetime of electrons (τ_n) rather than the free electron lifetime (τ_c) to obtain total charge density in TiO_2 film. The calculation was valid for conduction band electrons, while it gave a bit wrong estimation of the trapped electrons.[3] As charge extraction was known as a reliable way to determine the electron concentration in the film,[3] we used charge extraction techniques together with the decay measurements to quantify the coadsorbent effect.

A new program was complied to measure the charge density by charge extraction at the same light intensity where the photocurrent and photovoltage decays were measured. Briefly, the device was illuminated under a certain light bias and the C_{ch} and τ_n were first determined by recording the phototransient decays. Before the LEDs switched to the next light intensity, a charge extraction routine was executed to measure the electron density in the film. Unlike the normal charge extraction measurement that extracted charges at different points with different delay time, this charge extraction was measured only at one point with a fixed delay of around 1 millisecond. By varying the light intensities from 150% to 0.06% sun, the routine was repeated at each light intensity to give an electron concentration evolution with light intensity. Together with the measured C_{ch} and τ_n, this enabled us to discriminate the contributions from band-edge shift and recombination change to the enhancement in V_{oc}.

Figure 7.1 shows the charge density in the TiO_2 film versus the photovoltage of the devices based on Z-907 dye alone and with GBA or GPA as the coadsorbent. The electrolyte used here was Z-889, which contained no guanidinium thiocyanate in order to simplify the analysis. For a certain charge density, the devices with GBA or GPA coadsorption corresponded to a higher photovoltage, indicating an obvious negative shift of the conduction band-edge. The shift was about 50 mV for GPA and 70 mV for GBA coadsorption, both with a coadsorbent-to-dye ratio of 1:1.

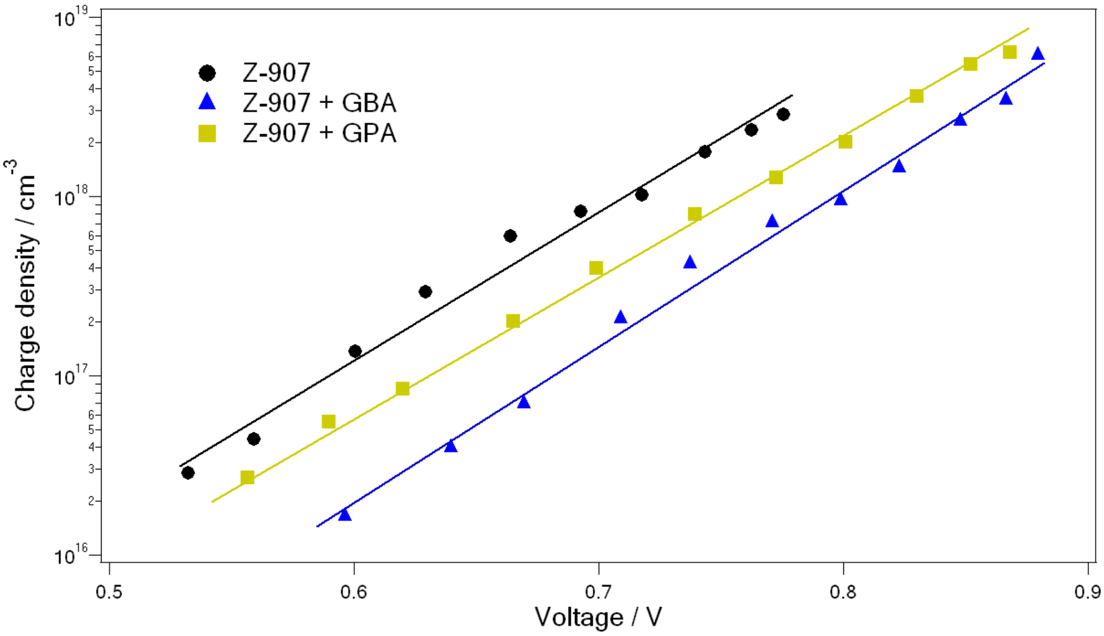

Figure 7.1 Effect of GPA and GBA coadsorption on the charge density over a range of photovoltages. The data were obtained from the charge extraction measurements of corresponding devices over a range of light intensities. Devices were based on Z-907 alone and with GBA or GPA as the coadsorbent at a coadsorbent-to-dye ratio of 1:1. TiO_2 film: 7+5. Electrolyte: Z-889.

Figure 7.2 plots the recombination rate constants versus the charge density in the film for the corresponding devices. As the reciprocal of the apparent electron lifetime τ_n, the recombination rate constant k_{rec} was a direct measure of the recombination reaction of electrons in TiO_2 with the triiodide species in the electrolytes. For a certain charge density, the devices with GBA or GPA coadsorption had a lower recombination rate constant than that of the device sensitized with Z-907 alone. Although the effect was not a lot (a factor of 2 to 3), this helped the devices with GPA and GBA coadsorption to accumulate a higher charge density at the open-circuit and induced a larger increase in V_{oc} than the simple band-edge shift, a conclusion similar to that reached by an approximate method in Chapter 6.

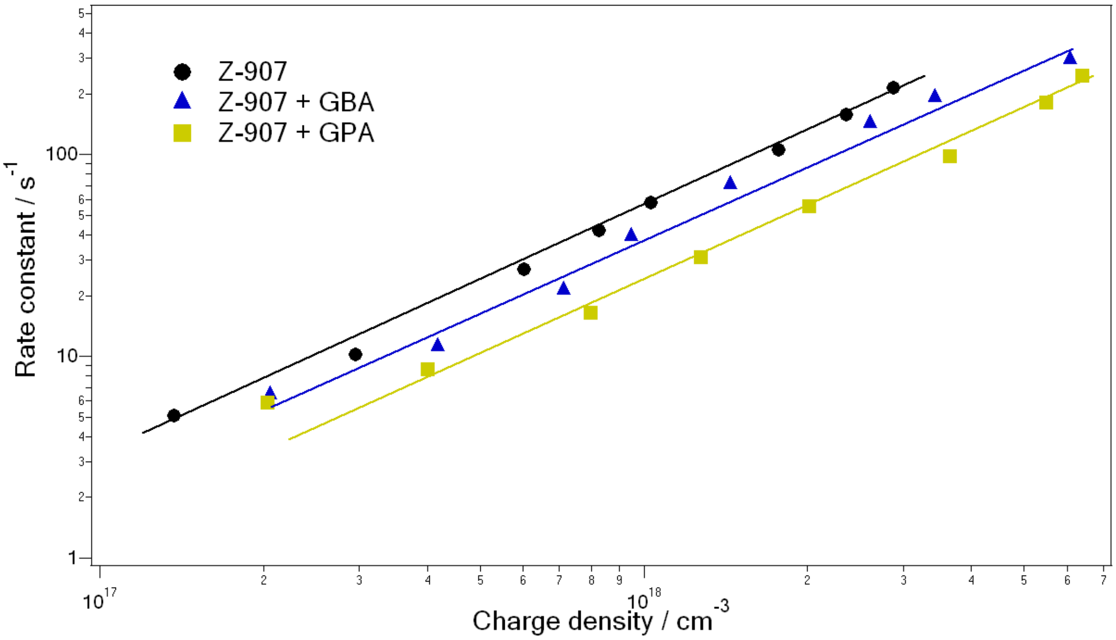

Figure 7.2 Effect of GPA and GBA coadsorption on the recombination rate constant over the charge density. Devices were based on Z-907 alone and with GBA or GPA as the coadsorbent at a coadsorbent-to-dye ratio of 1:1. TiO_2 Film: 7+5. Electrolyte: Z-889.

7.2 Coadsorbent-induced increase in photovoltage

7.2.1 Protons of the sensitizer

The negative shift of conduction band-edge is believed to be associated with the surface deprotonation. Thus, the protons of the sensitizer might play a role in the overall effect. Figure 7.3 shows the concentration effect of GPA in the solution of Z-907 which is a one-proton sensitizer. The V_{oc} of the device increased with increasing GPA molar ratio in the dye solution until reaching a plateau over a fraction of 0.5, while J_{sc} was almost the same till a fraction of 0.2, slightly lower for a fraction of 0.5 and then dropping dramatically with further increase of GPA, indicating too high a surface concentration of GPA that led to a strong disturbance to the dye anchorage. We note the photovoltaic parameters with this GPA concentration profile shows a slightly higher J_{sc} and a slightly lower V_{oc} for a dye-to-GPA ratio of 1:1 than those of devices under identical GPA concentration conditions presented in Chapter 6, presumably due to the thicker films used here and some small variations in the titration process of guanidinopropyl phosphonic acid to GPA.

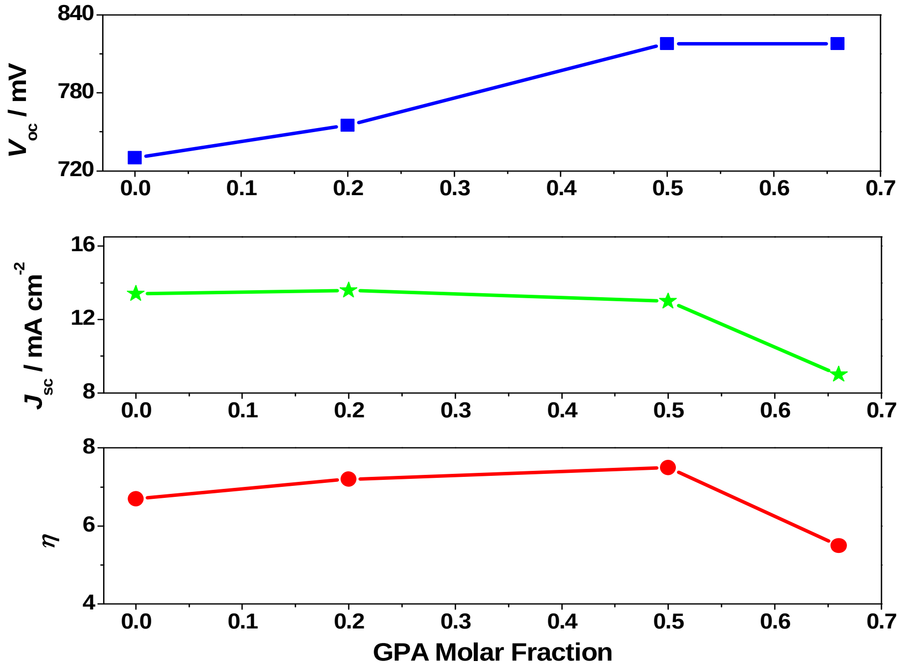

Figure 7.3 Dependence of photovoltaic parameters of the DSC on the GPA molar fraction in the dye solution. Sensitizer: Z-907. TiO_2 Film: 10+4. Electrolyte: Robust.

While K-60, a two-proton dye, was used as the sensitizer with the same coadsorbent GPA, only an intermediate increase of ~ 40 mV in photovoltage was observed for a GPA molar fraction up to 0.5, suggesting that a higher proton content of the sensitizer was against a large negative shift of the conduction band-edge. Possibly, the extra protons formed a surface reservoir of protons, counterbalancing the deprotonation process and decreasing the negative band-edge movement.

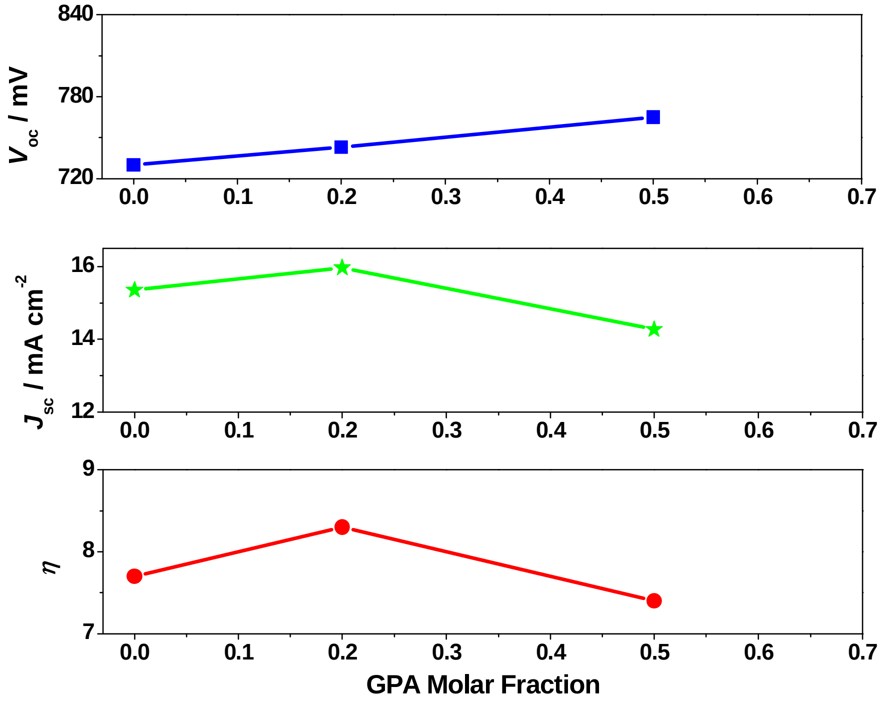

Figure 7.4 Dependence of photovoltaic parameters of the DSC on the GPA molar fraction in the dye solution. Sensitizer: K-60, a two-proton dye. TiO_2 Film: 7+4. Electrolyte: Robust.

7.2.2 Structure of the coadsorbent

To study the structural influence of the coadsorbent on the photovoltage increment, acid molecules with similar functional groups were tested, including 4-aminobutyric acid (ABA), 3-aminopropionic phosphonic acid (APA), salicylic acid (SA), phthalic acid (PhA) and Arginine (Arg) as shown in Figure 7.5. The photovoltaic parameters of devices based on Z-907 dye and the above mentioned coadsorbents are listed in Table 7.1. Within experimental errors, there was no notable increase in V_{oc} for the coadsorption of SA, PhA and APA. ABA gave an increase of ~40 mV in V_{oc} and this increase was about half of that observed in GBA or GPA coadsorption under a similar coadsorbent-to-dye ratio in the solution. Similar results were also found with K-19 sensitizer based DSCs, where ABA and PhA barely changed the photovoltage.

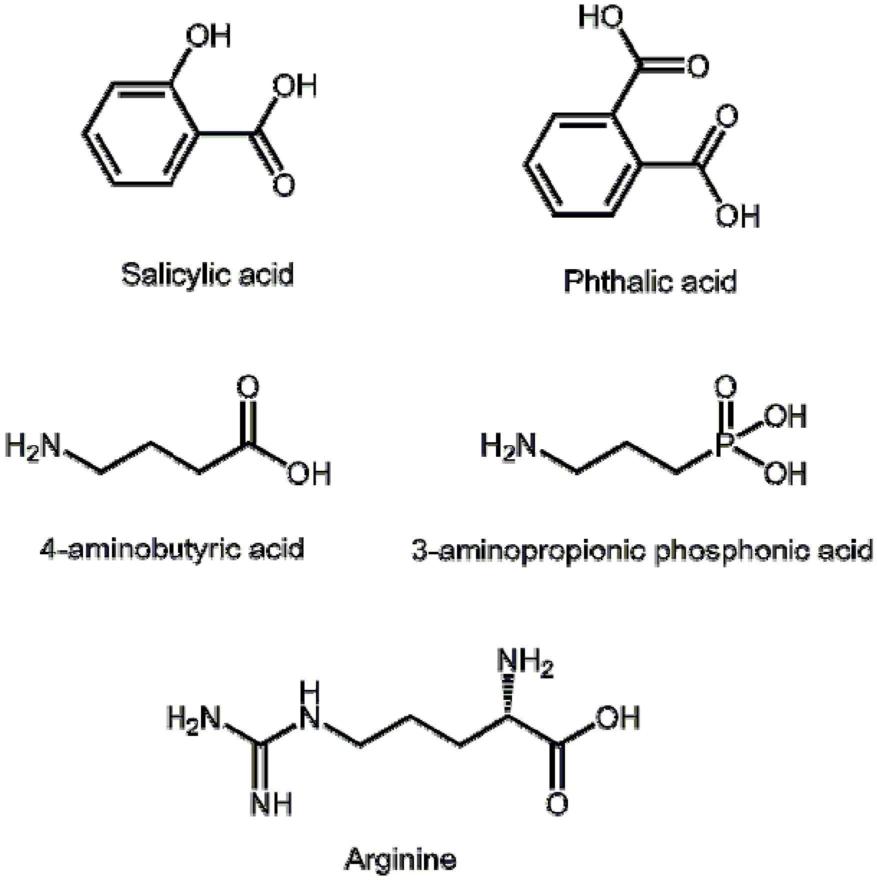
Salicylic acid

Phthalic acid

4-aminobutyric acid

3-aminopropionic phosphonic acid

Arginine

Figure 7.5 Structure of the coadsorbents SA, PhA, ABA, APA and Arg.

Table 7.1. Photovoltaic characteristics of dye-sensitized solar cells made with TiO_2 films (7+5) stained in Z-907 solution containing ABA, APA, SA or PhA under illumination of AM 1.5. The number in round brackets shows the molar coadsorbent-to-dye ratio.

Dye and coadsorbent	J_{sc} / mA cm^{-2}	V_{oc} / mV	FF	η / %
Z 907	14.0	730	0.66	6.8
ABA + Z 907 (1:1)	12.9	769	0.63	6.2
APA + Z 907 (1:4)	13.9	725	0.69	6.9
PhA+ Z 907 (1:4)	12.4	728	0.71	6.3
SA + Z 907 (1:4)	12.7	737	0.66	6.2

On the other hand, Arginine (Arg) showed quite a strong effect in increasing the V_{oc}. Arg is an α-amino acid with a structure similar to that of GBA, except that it has an amino group at the α position that makes the whole molecule more basic. The effect of Arg was studied in a system where a ruthenium sensitizer with a high extinction coefficient, K-73, was used. Figure 7.6 summarizes the concentration effect of Arg. With the increase of the Arg molar percentage in the dye solution, the open-circuit voltage of the device rose up gradually from 740 mV to 880 mV while in the meantime, the short-circuit current density dropped from 15.8 to 5.0 mA cm^{-2}. With a small variation in the fill factor, the solar-to-electricity conversion efficiency decreased continuously from 8.3 % to 3.2%. The increment in V_{oc} was higher for Arg coadsorption than that of GBA coadsorption where the V_{oc} of the device only increased to 810 mV with a GBA molar fraction of 0.5 (Figure 7.7). The opposite trends in the change of photocurrent and photovoltage indicated that the Arg functioned merely as a surface buffer, strongly deprotonating the TiO_2 surface at a higher concentration and possibly leading to an adverse effect on the electron injection process. In this sense, GBA and GPA were fairly mild bases that appeared not to disturb the electron injection.

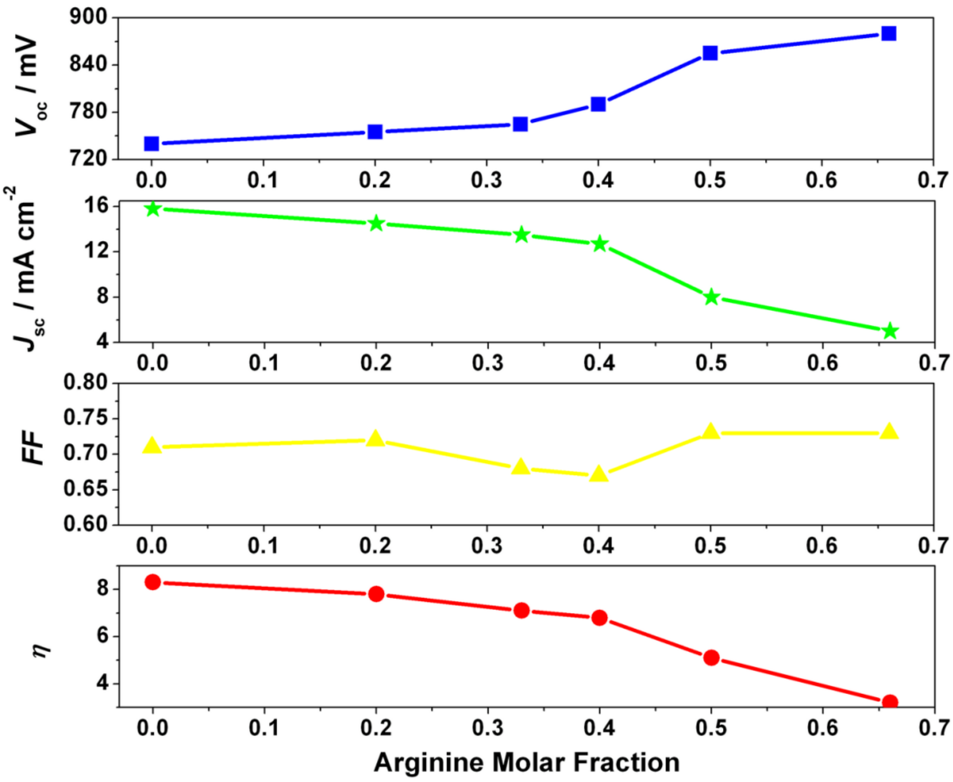

Figure 7.6 Dependence of photovoltaic parameters of the DSC on the Arginine molar fraction in the dye solution. Sensitizer: K-73. TiO_2 Film: 7+5. Electrolyte: Robust.

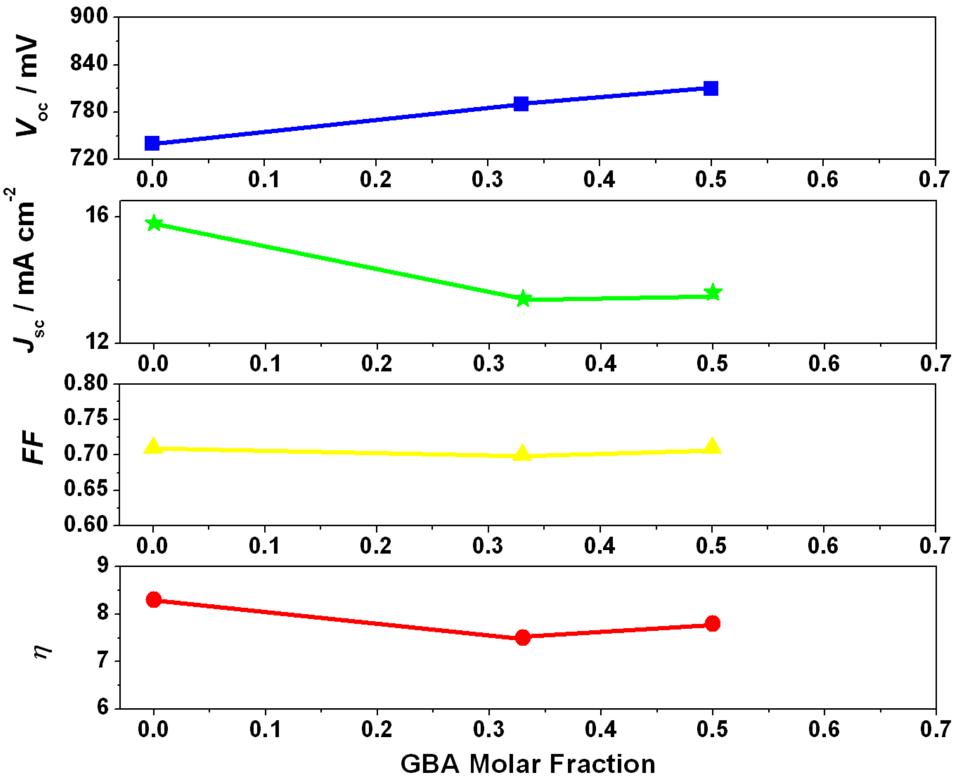

Figure 7.7 Dependence of photovoltaic parameters of the DSC on the GBA molar fraction in the dye solution. Sensitizer: K-73. TiO_2 Film: 7+5. Electrolyte: Robust.

One interesting phenomenon was that the large increase (> 50 mV) in photovoltage was only associated with guanidino-coadsorbents, such as GBA, but not with any other structure like SA or PhA. DPA itself did not induce any increase in V_{oc}, however, by introducing a guanidino group to the end of the alkyl chain, GPA had an obvious improvement on the photovoltage and, similarly, Arg demonstrated the strongest effect on increasing the V_{oc}, predominately due to the more basic feature of Arg. These results indicated that the guanidino group had quite special properties for this large increase in photovoltage while other functional groups such as amino group were not effective since ABA and APA showed mild increases in the photovoltage. The guanidino group is known to be strongly basic and remains protonated except in strongly alkaline solution. Thus for the guanidino coadsorbents of GBA, GPA and Arg, they actually existed in the zwitterions form in the solution. Upon the anchorage of guanidino-coadsorbents on the surface of TiO_2, this might produce a dipole moment favoring the negative band-edge shift. Although the high ionic strength electrolytes used in DSCs should screen all the charges and wipe out the dipoles in all directions, available results implied that the dipole induced by these molecules still had some local effects on the photovoltage in view of the large increase in V_{oc} associated with guanidino-coadsorbents.

7.2.3 Photoresponsive coadsorbents

Another idea was to select molecules with a photovoltaic activity as the coadsorbents. As has been discussed above, coadsorbent molecules behaved as an electron protecting rather than electron generating layer. If, in the mean time, the molecule had photovoltaic activity, extra current could be collected. However, this ideal situation was based on three assumptions: i) the molecule could be immobilized on the oxide film and have similar blocking effect shown as other coadsorbents; ii) the size of the molecule should be moderate so that the coadsorption process would not cause adverse effects on dye adsorption and iii) the molecule will not interfere with the normal photovoltaic effect of the sensitizer during the operation of the solar cell. These requirements demanded a judicious selection of the molecule. Molecules with oligo-thiophene unit such as 2-[2,2';5',2"]Terthiophen-5-ylmethylene-malonic acid (3TMMA) were designed and synthesized. The malonic acid substructure enabled the molecule to have an intimate contact with the oxide surface. Figure 7.8 illustrates the *I-V* characteristics of a device sensitized with 3TMMA. The device showed a fairly good photoresponse, with a J_{sc} of 7.3 mA cm^{-2} and a conversion efficiency of 3.2% at a simulated AM 1.5 illumination of 100 mW cm^{-2} (trace c). The IPCE took its maximum of 50% at 480 nm. However, the V_{oc} of 580 mV was a bit low for DSC, due to the large dark current for 3TMMA as the sensitizer (trace a).

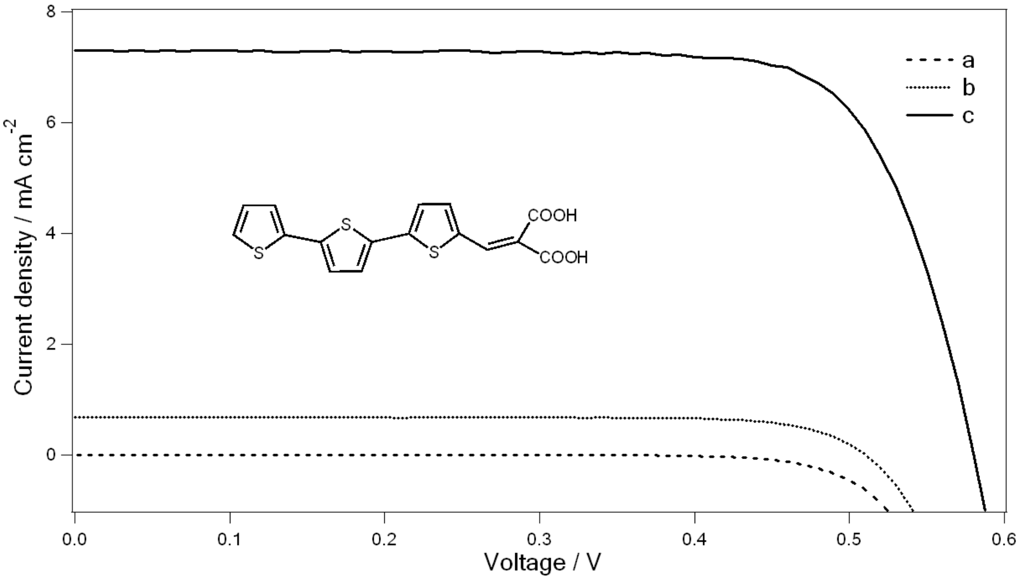

Figure 7.8 *I-V* characteristics of a 3TMMA-sensitized device in the dark (a) and under simulated AM 1.5 illuminations of 10 mW cm^{-2} (b) and 100 mW cm^{-2} (c). Insert shows the structure of 3TMMA. TiO_2 Film: 7+5. Electrolyte: Robust.

When 3TMMA was used as the coadsorbent with K-73 sensitizer with a coadsorbent-to-dye ratio of 1:4, both the J_{sc} (13.5 mA cm^{-2}) and V_{oc} (690 mV) were lower compared to those of a purely K-73 sensitized device shown in Figure 7.9. The lower J_{sc} was attributed to the decrease of K-73 surface concentration by the coadsorption of 3TMMA and the large spectrum overlap between K-73 and 3TMMA. The smaller V_{oc} was due to the higher dark current (trace a) induced by coadsorption of 3TMMA, as compared to the dark current of a purely K-73 sensitized device (trace c) and this increase in the dark current induced by 3TMMA was similar to recent results by O'Regan et al.,[5] where they suggested a catalytic effect of small organic sensitizers on the dark current of DSCs with I^- / I_3^- electrolytes. Comparable decreases in J_{sc} and V_{oc} were also observed when Z-907 sensitizer was used. These results indicated the coadsorption of 3TMMA onto TiO_2 film greatly interfered with dye adsorption process and no beneficial effects were observed.

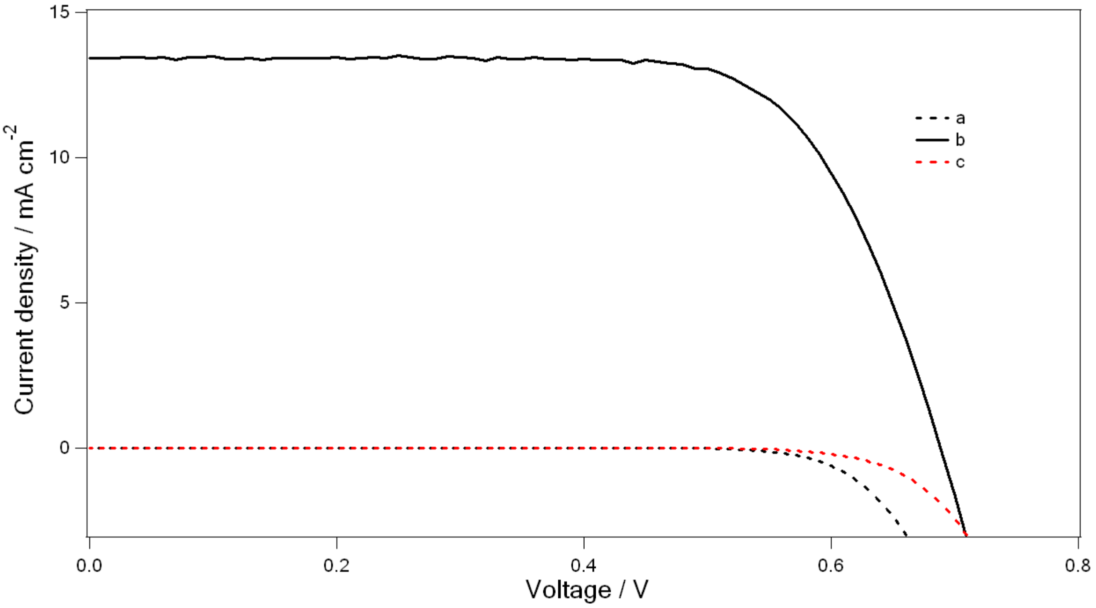

Figure 7.9 *I-V* characteristics of a DSC dyed with K-73 as the sensitizer and 3TMMA as the coadsorbent in the dark (a) and under simulated AM 1.5 illuminations of 100 mW cm^{-2} (b). Trace c is the dark current measured with a device sensitized with K-73 alone. TiO_2 Film: 7+5. Electrolyte: Robust.

7.2.4 Comparison to pretreatment and posttreatment

Alternative ways to use coadsorbents is to modify the surface of TiO_2 by the coadsorbents before the dye absorption (a pretreatment) or after the dye uptake process (a posttreatment). Control experiments were performed to study this effect. For pretreatment, the TiO_2 film was first dipped in a GPA solution for 2 hours and then transferred to Z-907 dye solution for overnight sensitization. While in a posttreatment, the TiO_2 film was first sensitized with Z-907 before putting into a GPA solution for 2 hours.

Figure 7.10 shows the *I-V* characteristics of the devices in the dark (dotted lines) and under the simulated AM 1.5 illumination at 100 mW cm^{-2} (full lines). The photoanodes of the devices were either pretreated (denoted as pre) or posttreated (referred as post) with different GPA solutions of 0.2, 0.5 and 1 M before the assembly of the device. It is clear that the dark current of the DSC dropped with both pretreatments and posttreatments and the decrease in the dark current was dependant on the concentration of GPA. The pretreatment was more effective in improving the photovoltage than the posttreatment since the GPA molecules had more difficulty to be absorbed on the surface with the formation of the sensitizer monolayer.

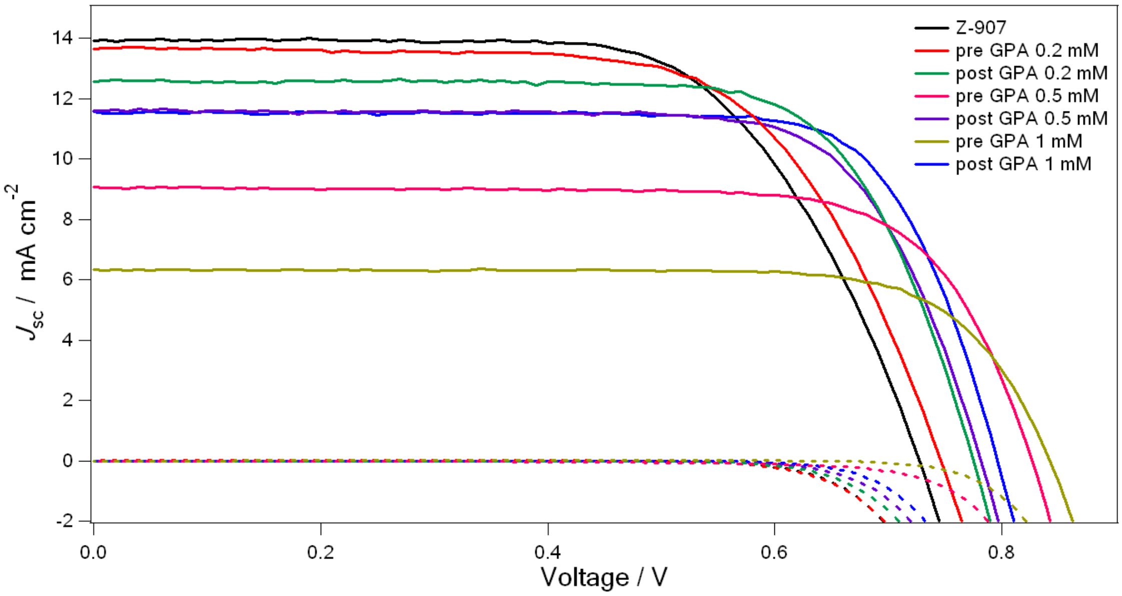

Figure 7.10 *I-V* characteristics of the devices in the dark (dotted lines) and under the simulated AM 1.5 illumination at 100 mW cm^{-2} (full lines). The photoanodes of the devices were either pretreated (denoted as pre) or posttreated (referred as post) with different GPA solutions of 0.2, 0.5 and 1 M before the assembly of the device. The black curve was the measurement based on a device without any GPA treatment. All the devices were made with a Z-907 sensitized 7+5 photoanode and Z-889 electrolyte.

The evolution of J_{sc} and V_{oc} of the device with the concentration of GPA is demonstrated in Figure 7.11. For pretreatment, the J_{sc} slightly increased until the GPA solution was higher than 0.2 mM while the V_{oc} showed a small increase (< 20 mV) in the same region. Further increase of GPA concentration was associated with a sharp decrease in J_{sc} and a large increase in V_{oc}, suggesting that a GPA-concentration-dependent effect was involved in the variation of the photovoltaic parameters. It is also interesting to note that the posttreatment also induced similar effects observed in the pretreatment, though the change was not as obvious. The increase in the V_{oc} of the device proved the mild basicity of GPA, which was also present in the coadsorption process and caused a negative displacement of the TiO_2 conduction band. One disadvantage with pretreatment and posttreatment was the relative large decrease in photocurrent accompanying the augmentation of photovoltage compared to the coadsorption process. One explanation could be that the dye and the coadsorbent might form a more ordered mixing layer and only weakly absorbed dye molecules that only made a slight contribution to the photocurrent were replaced by the coadsorbent. However, to achieve a large increase of photovoltage in the pretreatment and posttreatment, the GPA concentration was so high that it either blocked the access of the dye molecules to the surface or displaced some of the absorbed dye molecules which could make considerable photocurrent under the normal operation, leading to a weaker light harvesting and thus a lower observed J_{sc}.

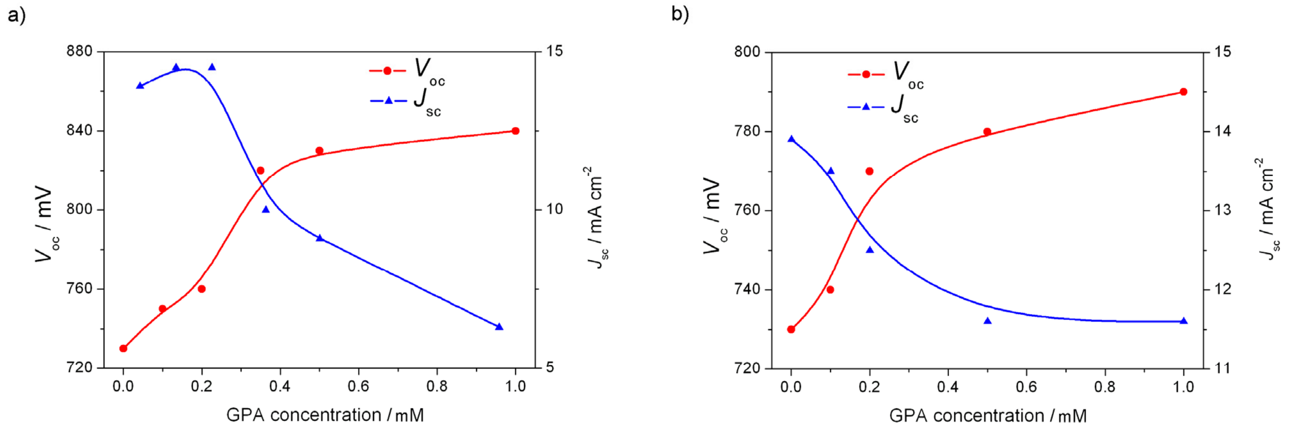

Figure 7.11 The evolution of J_{sc} and V_{oc} of the device with the concentration of GPA in the a) pretreatment and b) posttreatment process.

7.3 Conclusions

ω-Guinidino carboxylic and phosphonic acids have been employed as the coadsorbent in combination with two amphiphilic ruthenium sensitizers K-19 and Z-907. Judicious selection of the coadsorbent concentration increased the photovoltage without suffering significant current penalty and thus enhancing the total power conversion efficiency. Devices wth GBA showed a long-term stability exhibiting approximately 8% power conversion efficiency under the dual stress of both light-soaking and thermal aging at 60 °C. For the longtime thermal aging at an elevated temperature of 80 °C, FT-IR study indicated the desorption of GBA from the surface of TiO_2. Substituting the anchoring carboxylic group with the phosphonic group yielded the molecule of GPA that absorbed firmly on the TiO_2 surface and functioned all along the aging process at 80 °C.

Experiments with many coadsorbents showed that the large increase (>50 mV) in V_{oc} induced by the coadsorption was only present in guanidino compounds. When a high concentration was used, ~100 mV voltage increase was observed in the Z-907 sensitized devices. The absolute value of the increase was found to be related with the proton number of the dye and the basicity of the coadsorbent.

Systematic studies were carried out on the mechanism of the increase of the photovoltage by cyclic voltammetry, electrochemical impedance spectroscopy and photovoltage transient measurements. The guanidino-coadsorbent induced the negative shift of the quasi-Fermi level of TiO_2 nanocrystals, possibly behaving as a mild base and deprotonating the surface. Meanwhile, the coadsorbent formed a mixed layer with the amphiphilic sensitizer and slowed down the charge transfer from electrons in TiO_2 to the triiodide in the electrolyte, as suggested by the comparison in the evolution of recombination rate constant as a function of the carrier density in the film. In addition, pretreatment and posttreatment with the coadsorbent molecule were also performed and a high increment in the photovoltage was observed to be comcomitant with a large decease in photocurrent, a fact probably releated to the high concentration of the coadsorbent molecule used.

7.4 References to Chapter 7

[1]. Neale, N. R.; Kopidakis, N.; van de Lagemaat, J.; Grätzel, M.; Frank, A. J. *J. Phys. Chem. B* **2005,** *109,* 23183.

[2]. Frank, A. J.; Kopidakis, N.; van de Lagemaat, J. *Coord. Chem. Rev*. **2004**, *248*, 1165.

[3]. Personal correspondence of Dr. Humphry-Baker with Professor Laurie Peter, University of Bath.

[4]. Duffy, N. W.; Peter, L. M.; Rajapakse, R. M. G.; Wijayantha, K. G. U. *J. Phys. Chem. B* **2000**, *104*, 8916.

[5]. O'Regan, B. C.; López-Duarte, I.; Victoria Martínez-Díaz, M.; Forneli, A.; Albero, J.; Morandeira, A.; Palomares, E.; Torres, T.; Durrant, J. R. *J. Am. Chem. Soc.* **ASAP**, DOI 10.1021/ja078045o.

8. Alternative Redox Mediators for Dye-sensitized Solar Cells

8.1 Introduction

In the previous chapters, we have shown the effects of coadsorbents to increase the photovoltage. We now turn to the potential loss in the process of dye regeneration by the redox couple. Although the I^- / I_3^- couple works properly, there is a mismatch between the redox potential of the sensitizer cation (S^+), which is around 1 V versus NHE, and that of I^- / I_3^- (0.4 V vs. NHE). Since the photovoltage of DSC is determined by the difference between the quasi-Fermi level of the TiO_2 film and the Nernst potential of the redox couple, this mismatch leads to an excess driving force (~ 0.6 eV) for dye regeneration and thus a lower voltage. Therefore, it is of a great scientific interest to study alternative electrolytes to I^- / I_3^- with redox couples of having a more positive potential. Kinetically fast, one-electron transfer redox couples are good candidates for this purpose. Ferrocene/ferrocenium was shown to yield low photovoltages and low photocurrents in DSCs due to the rapid back reaction of injected electrons with Fe(III) species.[1],[2] Hence, a successful redox mediator should have fast electron exchange at the counter electrode to minimize the overvoltage loss, while it has to display relative slow electron transfer kinetics at TiO_2 in order to avoid recombination loss of photoinjected electrons with the oxidized species in the electrolyte. Other attempts of employing certain polypyridine Co(II) complexes showed an impressive efficiency of 8% at a low light intensity but a moderate efficiency at higher light intensities.[3]-[5] More recently, mediator mixtures containing a redox species with facile charge-transfer kinetics (for example, phenothiazine or ferrocene) and another co-mediator with very slow heterogeneous electron-transfer on semiconductor oxides were proposed. Unfortunately, the selected co-mediator was demonstrated to be less efficient (~1.5 % under 0.1 W/cm^2 Xe lamp irradiation) and the relatively high toxicity of metal-containing complexes hampered their practical applications.[6] In this chapter, we studied different one-electron transfer redox mediators, such as triarylamine, phenoxazine, piperidinyloxy and tetrathiafulvalene, and evaluated their potential usage as alternative electrolytes in DSCs. The Nernst potentials of some redox couples are summarized in Figure 8.1.

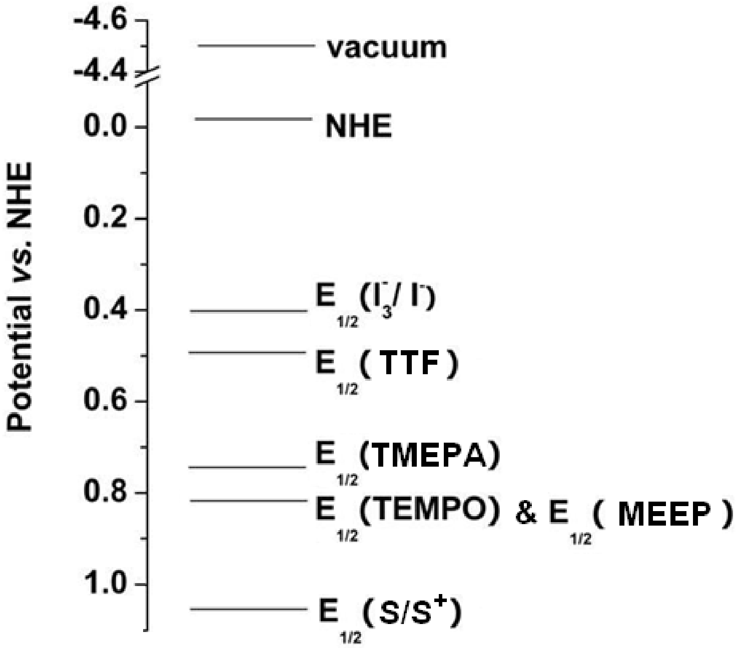

Figure 8.1 Nernst potentials of some representative redox couples.

8.2 Nitroxide radical based electrolytes

2,2,6,6-tetramethyl-1-piperidinyloxy (TEMPO) is a red-orange, sublimable solid first discovered by Lebelev and Kazarnowskii in 1960.[7] It is a well known remarkably stable radical and widely used as a radical trap in biochemistry, as a reagent in organic synthesis and as an initiator in polymer chemistry. The nitroxide radical usually displays two redox couples. At the cathodic side, it is reduced to an aminoxy anion while at the anodic side it is oxidized to an oxoammonium cation. In this section, we studied the possibility of using the radical/oxoammonium redox couple as a relay in the DSCs.

8.2.1 Electrochemistry

The electrochemical behavior of the nitroxide radical was initially examined on a platinum disc electrode. Figure 8.2 shows the cyclic voltammetry of 2 mM TEMPO at different scan rates ranging from 1 V s^{-1} to 0.002 V s^{-1}. The insert plots the anodic peak current ($i_{p,a}$) against the square root of the scan rate ($\upsilon^{1/2}$). The diffusion coefficient of TEMPO was calculated from the slope of $i_{p,a}$ - $\upsilon^{1/2}$ plot with Randles-Sevcik equation (Eq. 2.3) to be 1.2×10^{-5} cm^2 s^{-1}.

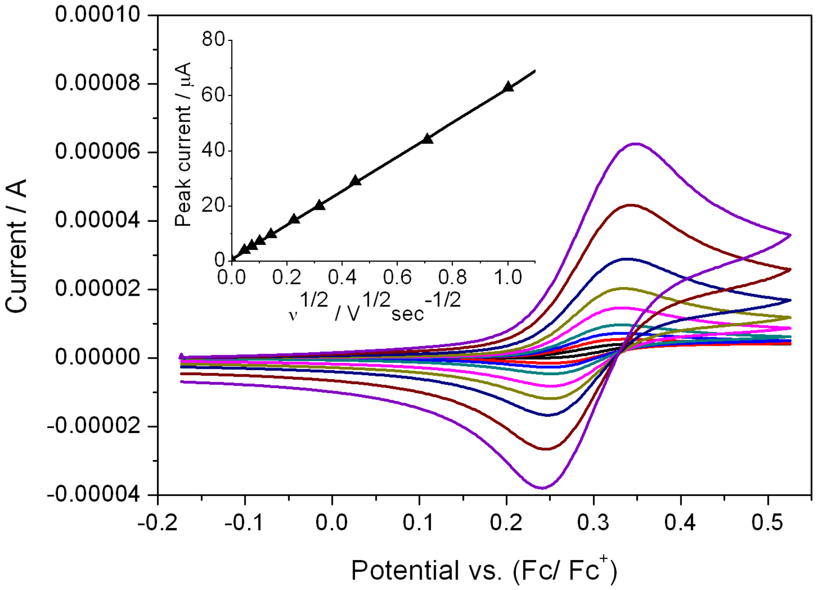

Figure 8.2 Typical cyclic voltammograms of 2 mM TEMPO on Pt disc electrode in acetonitrile solution containing 0.1 M tetrabutylamonium tetraboronfluoride (TBATBF) as the supporting electrolyte. Scan rates were changed from 1 to 0.002 V s^{-1}. The insert shows the anodic peak current versus the square root of the scan rate and diffusion coefficient of TEMPO was calculated by Eq. 2.3.

The standard Nernst potential of $TEMPO^+$/TEMPO was found to be 0.26 V versus Ferrocene/Ferrocium, i.e. around 0.8 V vs. NHE, which was about 400 mV more positive than that of the iodide/triiodide redox. The measurement of a structural analog, 4-methoxy-TEMPO (MeO-TEMPO), gave the same redox potential, indicating the redox potential was dictated by the radical center rather than the substituent at the *para*-position. In the following section, a ruthenium sensitizer K-51 and an organic sensitizer D-149 were used to evaluate the photovoltaic performance of the TEMPO based electrolytes. Since the potentials of the ruthenium sensitizers used in this thesis were about 1.1 V *vs.* NHE and the redox potential of the organic D-149 sensitizer was measured to be 1.05 V *vs.* NHE as shown in Figure 8.3, a driving force of ~ 0.3 eV for dye regeneration was anticipated in the DSCs employing this TEMPO/$TEMPO^+$ redox couple.

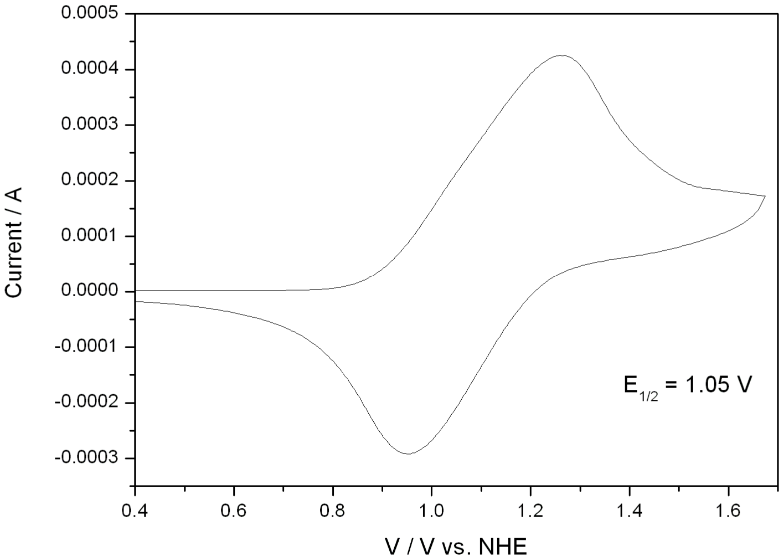

Figure 8.3 A cyclic voltammogram of D-149 sensitizer anchored on a 4-µm-thick transparent layer of nanocrystalline TiO_2 particles. The supporting electrolyte was 0.1 M TBATBF in acetonitrile. Scan rates was 0.1 V s^{-1}.

8.2.2 Photoelectrochemical study

8.2.2.1 Doping level of the electrolyte

DSCs were first fabricated with a transparent layer (2.4 µm in thickness) of 20-nm-sized (in diameter) TiO_2 particles sensitized with a ruthenium sensitizer K-51. The electrolyte contained 1M MeOTEMPO, 1.2 M LiTFSI and 0.5 M NBB in acetonitrile. To dope it, an oxidation degree of 1 % was used by the addition of $NOBF_4$ to the electrolyte. Figure 8.4 shows the current-voltage characteristics of the device under AM 1.5 illumination at a) 1.5 $mWcm^{-2}$, b) 10 $mWcm^{-2}$ and c) 50 $mWcm^{-2}$. Under 1.5 % sun irradiation, the device showed a common *I-V* curve (trace **a**), with a J_{sc} of 58 µA cm^{-2}, V_{oc} of 670 mV and a conversion efficiency of 1.2 %. When the light intensity increased to 10% sun, the J_{sc} only rose to 182 µA cm^{-2}, demonstrating a non-linear dependence of photocurrent on light intensity. *I-V* curve showed a notable increase in the vicinity of short-circuit, instead of a normally observed plateau in that region. This phenomenon was more obvious at a higher light intensity of 50 $mWcm^{-2}$ (trace **c**). Compared to the 35-fold increase in light intensity (from 1.5% to 50 % sun), the J_{sc} only increased by a factor of 8 (58 to 448 µA cm^{-2}). The V_{oc} of the device at 50% sun was as high as 850 mV, proving the concept of employing this redox couple in enhancing the photovoltage. However, the conversion efficiency dropped to 0.2 % at this light intensity due to the non-linearity in the photocurrent and the decrease in the fill factor.

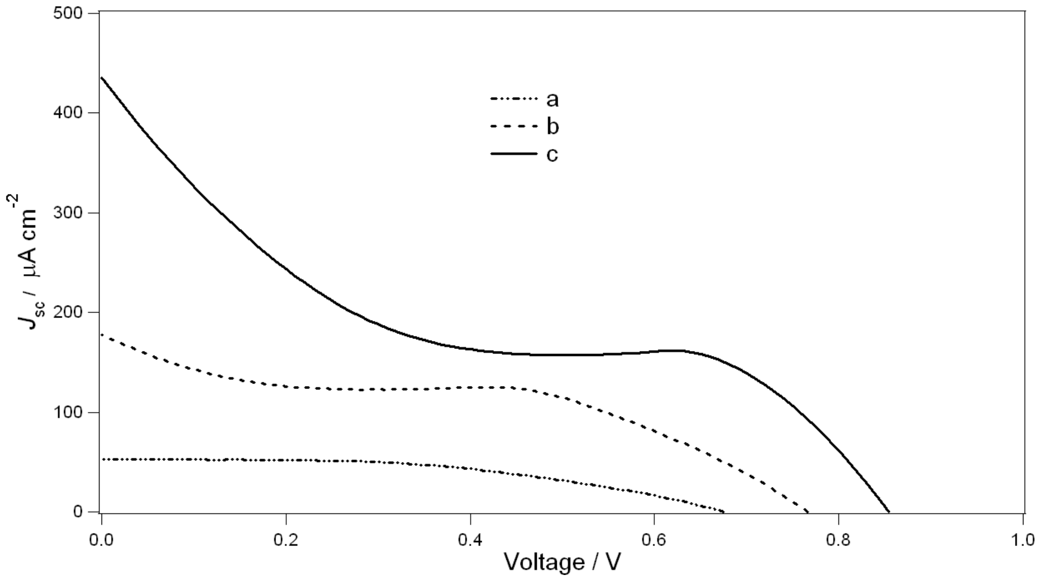

Figure 8.4 Current-voltage characteristics of the device under AM 1.5 illumination at a) 1.5 mWcm^{-2}, b) 10 mWcm^{-2} and c) 50 mWcm^{-2}. The device was fabricated with a 2.4-µm-thick nanocrystalline TiO_2 film dyed with K-51 sensitizer. Particle size: 20 nm in diameter. The electrolyte contained 1M MeOTEMPO with 1 % oxidized.

The problem was mitigated simply by adding more dopant to increase the amount of MeOTEMPO$^+$ to 5%. As displayed in Figure 8.5, the device showed a linear photocurrent response to light intensity up to 50% sun (trace **c**), mainly attributed to the increase in the concentration and thus the diffusion flux of MeOTEMPO$^+$. Under an irradiance of 50 mW cm^{-2}, the device showed a J_{sc} of 1.1 mA cm^{-2} and a conversion efficiency of 0.9%. However, similar limitation in mass-transfer was observed at full sunlight and the conversion efficiency dropped to 0.6% (trace **d**).

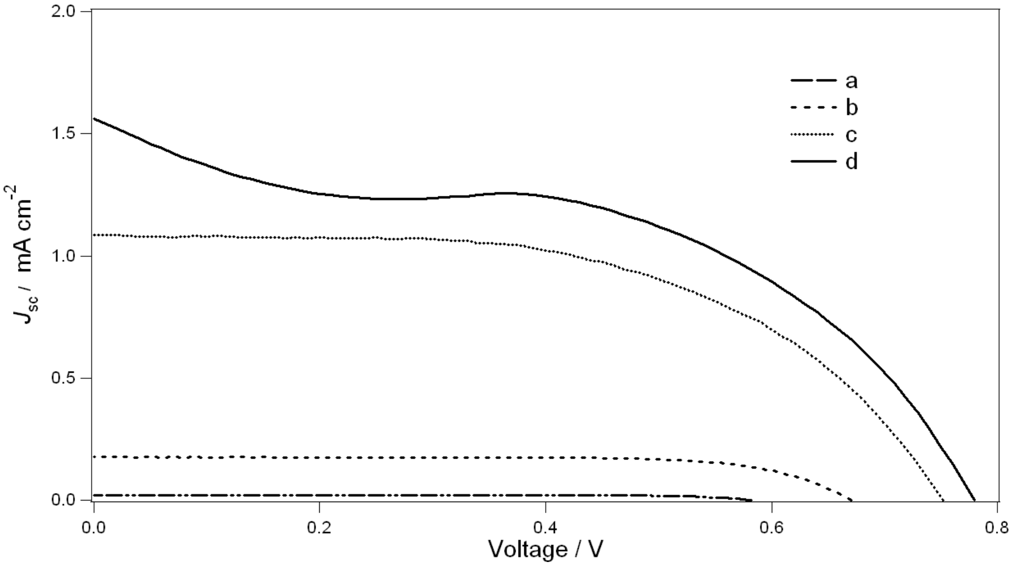

Figure 8.5 Current-voltage characteristics of the device under AM 1.5 illumination at a) 1.5 mWcm^{-2}, b) 10 mWcm^{-2}, c) 50 mWcm^{-2} and d) 100 mW cm^{-2}. The device was fabricated with a 2.4-µm-thick nanocrystalline TiO_2 film dyed with K-51 sensitizer. Particle size: 20 nm in diameter. The electrolyte contained 1M MeOTEMPO with an oxidation degree of 5 %.

Figure 8.6 plots the *I-V* characteristics of the device based on the same 1M MeOTEMPO electrolyte but with a higher oxidation degree of 10%. The short-circuit photocurrent almost increased linearly with the light intensity, showing the beneficial effect of increasing the concentration of TEMPO$^+$. At 100% sun irradiance, the device showed a J_{sc} of 2.2 mA cm^{-2}, a V_{oc} of 775 mV and a conversion efficiency of 1.1 %. Further increase in oxidization degree did not give a higher short-circuit photocurrent, suggesting that the mass-transfer was no longer an issue limiting the photocurrent at high light intensities for electrolytes with a fraction of 10% or higher oxidized species.

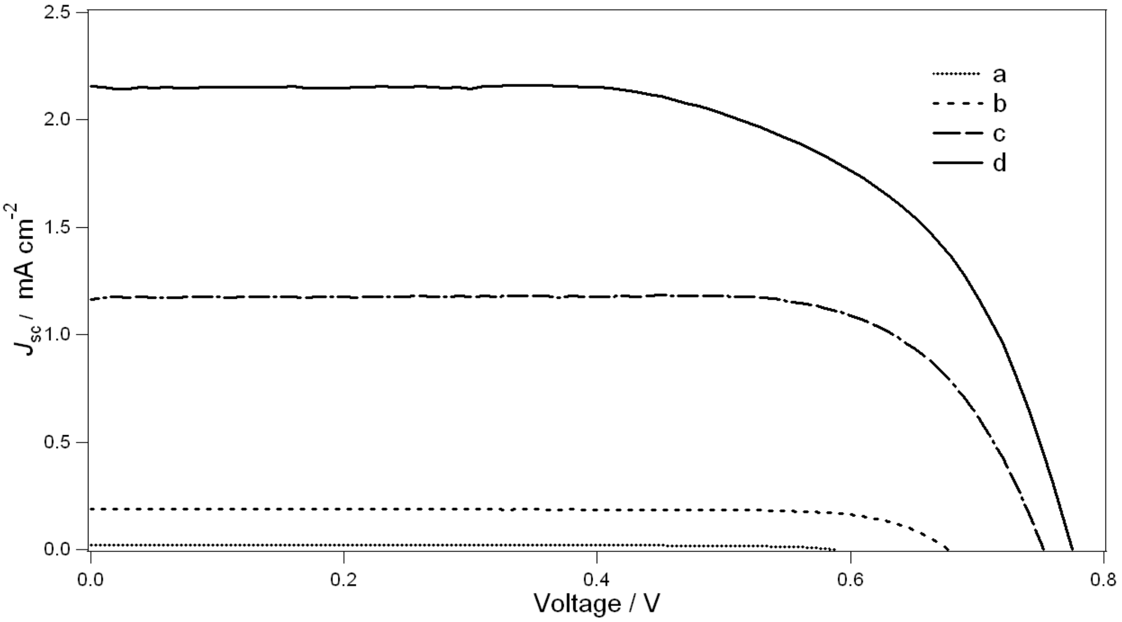

Figure 8.6 Current-voltage characteristics of the device under AM 1.5 illumination at a) 1.5 mWcm^{-2}, b) 10 mWcm^{-2}, c) 50 mWcm^{-2} and d) 100 mW cm^{-2}. The device was fabricated with a 2.4-µm-thick nanocrystalline TiO_2 film dyed with K-51 sensitizer. Particle size: 20 nm in diameter. The electrolyte contained 1M MeOTEMPO with an oxidation degree of 10 %.

8.2.2.2 Enhancing the light absorption

The device based on 10% oxidized TEMPO electrolyte showed the normal *I-V* characteristics, however, the J_{sc} of 2.2 mA cm^{-2} at 1 sun was rather low compared to the normal I^-/I_3^- redox. The low light harvesting of a thin nanocrystalline TiO_2 layer sensitized with a ruthenium dye could be enhanced by using a thicker film or a sensitizer with a higher molar extinction coefficient. With previous results, a similar electrolyte based on TEMPO was investigated in consideration of the simpler structure and great availability. Figure 8.7 shows the *I-V* characteristics of the devices under AM 1.5 simulated irradiation at 100 mW cm^{-2}. The devices were based on a nanotransparent TiO_2 film of a) 2.4 and b) 5.8 µm and an electrolyte with 1M TEMPO in which 10% of TEMPO was oxidized by $NOBF_4$. The J_{sc} of the device with 2.4-µm-thick film was 1.7 mA cm^{-2} (trace a), while it increased to 3.3 mA cm^{-2} for the device with a film thickness of 5.8 µm (trace b). With a V_{oc} of 760 mV, the latter device showed a conversion efficiency of 1.5% at 100 mW cm^{-2}.

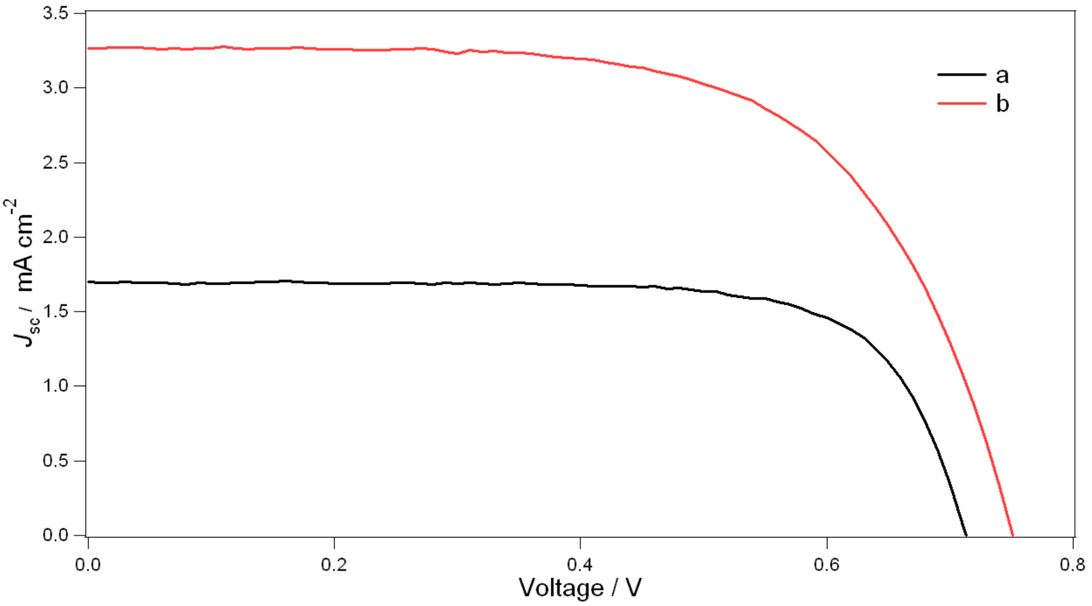

Figure 8.7 Current-voltage characteristics of the devices under AM 1.5 illumination at 100 mW cm^{-2}. The device was fabricated with a) 2.4-µm-thick and b) 5.8-µm-thick nanocrystalline TiO_2 film dyed with K-51 sensitizer. Particle size: 20 nm in diameter. The electrolyte contained 1M TEMPO with an oxidation degree of 10 %.

Organic sensitizers were reported to have very high molar extinction coefficients and work well with a thin layer of TiO_2 film. An organic dye, D-149 was used to increase the light absorption in this system. The molar extinction coefficient of this sensitizer was 68, 700 M^{-1} cm^{-1} at 526 nm, which was about 5 times higher than that of K-51 sensitizer.[8][9] Figure 8.8 shows the current-voltage characteristics of the devices based on the above-mentioned 2.4 µm layer of 20-nm-sized TiO_2 particles sensitized with D-149. With this organic dye, the J_{sc} of the device increased to 7.0 mA cm^{-2}

and the conversion efficiency went up to 3.5% at 100 mW cm^{-2}, which was a fairly high value for non-iodine electrolytes under the simulated AM 1.5 illumination at full sun intensity.

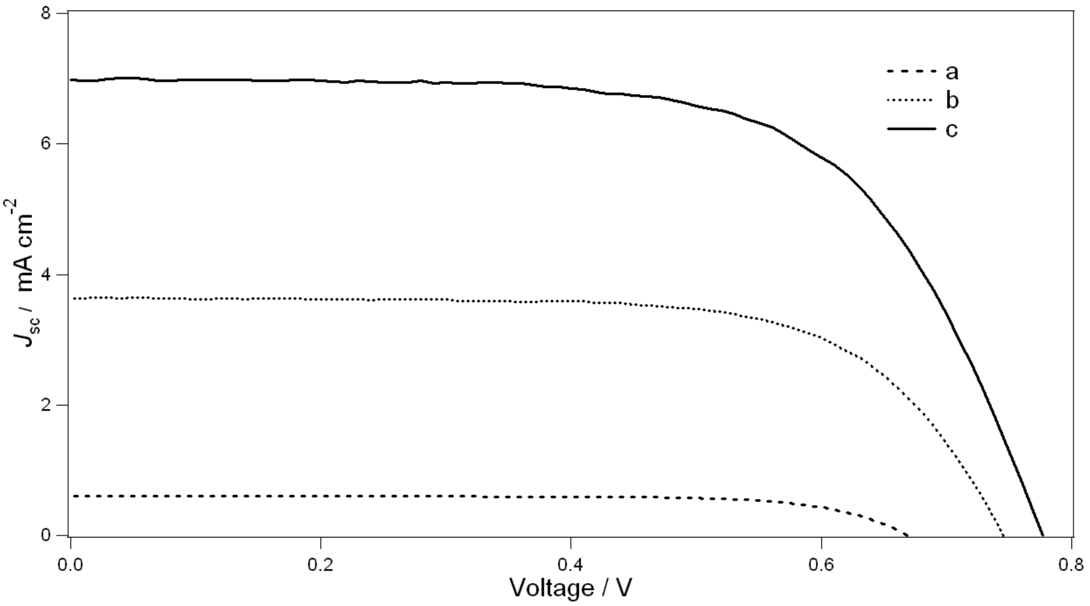

Figure 8.8 Current-voltage characteristics of the devices under AM 1.5 illumination at a) 10 mWcm^{-2}, b) 50 mWcm^{-2} and c) 100 mW cm^{-2}. The device was fabricated with a 2.4-µm-thick nanocrystalline TiO_2 film dyed with D-149 sensitizer. Particle size: 20 nm in diameter. The electrolyte contained 1M TEMPO with an oxidation degree of 10 %.

8.2.2.3 Particle size of TiO_2 and concentration of TEMPO

It was interesting to find that TEMPO-based electrolyte gave an acceptable efficiency for a non-iodide electrolyte. To further improve this redox system, one has to slow down the fast back reaction of injected electrons with TEMPO$^+$. Since the rate of this back reaction is proportional to the surface area of TiO_2 nanocrystalline film, TiO_2 pastes made of 60 nm-sized (Paste F2) particles were synthesized for this purpose. Figure 8.9 shows the current-voltage characteristics of the device under simulated AM 1.5 illumination at a) 10 mW cm^{-2} and b) 100 mW cm^{-2}. The device was made with a D-149 sensitized 6.0-µm-thick layer of 60-nm-sized TiO_2 nanoparticles and 1M TEMPO electrolyte. Strikingly, the device exhibited a good J_{sc} of 10.2 mA cm^{-2} at 100 mWcm^{-2} though the surface dye loading was reduced by the larger particles. The V_{oc} of this device is around 820 mV, a value which was considerably higher than those of devices with this organic dye in combination with iodide electrolytes.[9] The device showed a power conversion efficiency of 4.7% at 1.0 sun illumination (trace b) and 4.9 % efficiency at lower light intensities (trace a). The IPCE spectrum of the device was shown in the insert and found to be close to 60% from 550 nm to 600 nm.

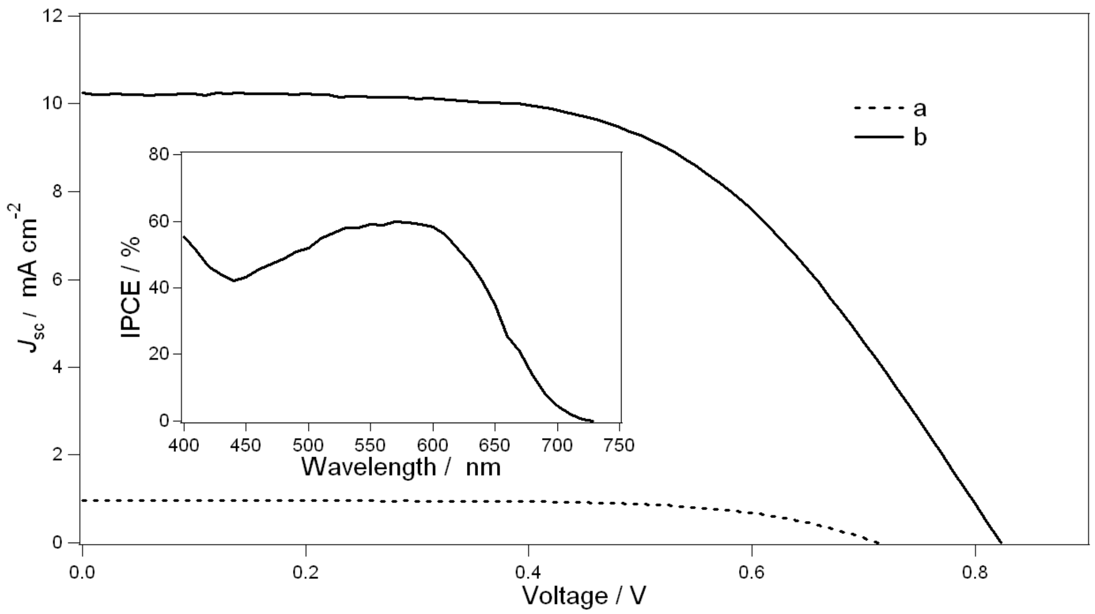

Figure 8.9 Current-voltage characteristics of a device under simulated AM 1.5 illumination at a) 10 and b) 100 mWcm^{-2}. The device was fabricated with a 6.0-μm-thick TiO_2 nanocrystalline film dyed with D-149 sensitizer. Nanoparticles are 60 nm in diameter. The insert shows the IPCE spectrum of the device.

To further study the effect of the concentration of this redox couple, electrolytes with a similar composition but different TEMPO concentrations were used. Table 8.1 summarizes all the photovoltaic parameters of the devices fabricated with different TEMPO electrolytes of 0.05, 0.1, 0.2, 0.5 and 1 M under simulated AM 1.5 sun illumination at 100 mW cm^{-2}. The devices were made with a D-149 sensitized 4.9-μm-thick layer of 60-nm-sized TiO_2 nanoparticles and TEMPO in all the electrolytes was 10% oxidized by adding $NOBF_4$. The V_{oc} of the device decreased from 920 mV for 0.05 M TEMPO electrolyte to 820 mV for 1 M TEMPO electrolyte, which could be explained by the increasing concentration of TEMPO$^+$ species that favored the back reaction and decreased the electron lifetime. Meanwhile, the J_{sc} increased from 7.2 mA cm^{-2} for 0.05 M electrolyte to 10.4 mA cm^{-2} for 0.5 M electrolyte and almost kept constant for electrolyte 1 M TEMPO. The fill factor of the devices scattered around 0.6 without obvious changes with respect to the concentration of TEMPO. We noted the J_{sc} of the device with 1M TEMPO electrolyte was about 1 mA cm^{-2} higher than that presented in our publication (Chapter 9) [10] and we attributed this increase in J_{sc} to the fluctuation of the experimental conditions, such as inevitable small variations in the film thickness, the acidity of the film between batches, electrolyte concentrations and the system error in *I-V* characterization etc. However, it was more important to find that the devices showed a similar conversion efficiency of (close to or over) 5% under simulated AM 1.5 sun illumination at 100 mW cm^{-2}, exceeding any other non-iodine redox couples at this light intensity.

Table 8.1 Complete set of photovoltaic parameters for DSCs based on D-149 sensitizer and a 4.9-µm-thick photoanode with electrolytes of different TEMPO concentrations. The devices were measured under AM 1.5 full sunlight (100 mW cm^{-2}) irradiation.

TEMPO concentration (M)	J_{sc} (mA cm^{-2})	V_{oc} (mV)	FF	η (%)
0.05	7.2	920	0.57	3.9
0.1	7.6	910	0.66	4.8
0.2	9.6	860	0.57	4.7
0.5	10.4	850	0.59	5.3
1	10.3	820	0.58	4.9

8.2.3 Kinetics of dye regeneration

Although the device based on D-149 sensitizer showed an impressive IPCE of ~60%, this was still lower than that of I^-/I_3^- electrolyte which was usually between 80% and 90%. Transient absorbance decay of the sensitizer cations (S^+) was monitored to better understand the system. Figure 8.10 shows the decay kinetics of the oxidized state of K-51 sensitizer adsorbed on nanocrystalline TiO_2 films in contact with a) pure MPN solvent and b) 0.1M TEMPO electrolyte. Absorbance changes were measured at a probe wavelength of 650 nm, employing 600 nm pulsed laser excitation (7 ns fwhm pulse duration, 40 µJ cm^{-2} pulse fluence). In the absence of TEMPO/TEMPO$^+$ redox electrolyte, the decrease of the absorption signal reflected the dynamics of recombination of the conduction band electrons with the oxidized dye (Eq. 1.7). The kinetics of the oxidized dye transient absorption decay could be well fitted by a single exponential, with a rate constant $k_0 = 4.2 \times 10^3$ s^{-1}.

When TEMPO/TEMPO$^+$ was present, the decay of the oxidized dye signal was greatly accelerated, suggesting that the recombination was efficiently intercepted by the mediator. The temporal behavior of the S^+ transient absorption was found again to follow a simple exponential. In the presence of 0.1 M TEMPO, the rate constant for the regeneration of the oxidized states S^+ of the sensitizer was determined to be $k_1 = 1.5 \times 10^7$ s^{-1}, a value of 150 times higher than the reciprocal half reaction time

$1/\tau_{1/2} = 10^5\ s^{-1}$ of the ground state recovery of the same sensitizer measured with 0.6 M 1-propyl-2,3-dimethylimidazolium iodide.[11] The fast dye regeneration was attributed to the facile electron transfer from TEMPO to S^+ and kinetics of the same time domain were also observed in the regeneration process of Z-907 sensitizer with ferrocene or phenothiazine species due to their low reorganization energy during the electron transfer.[6]

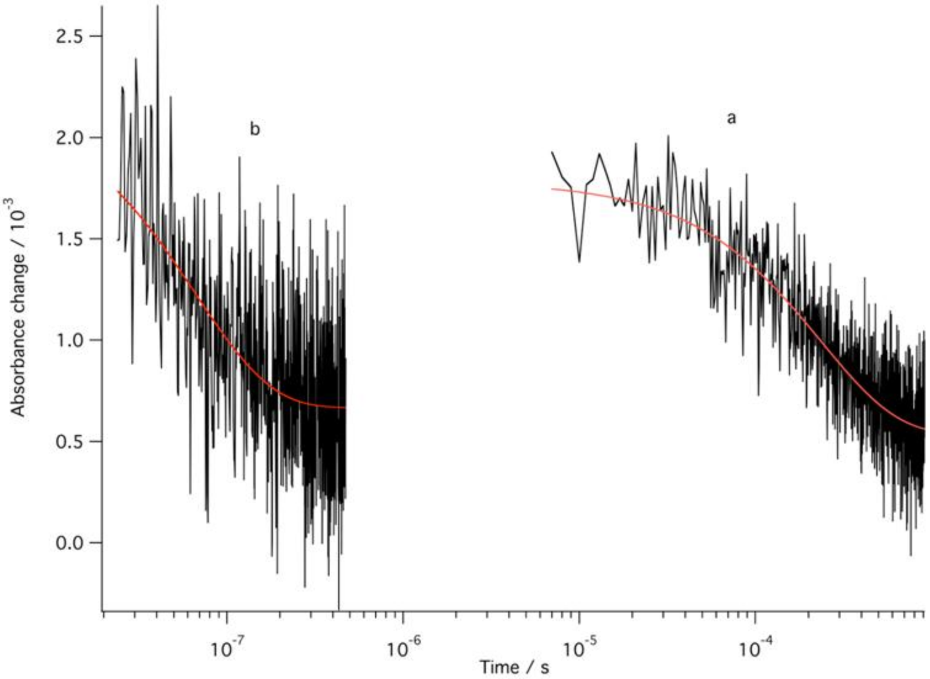

Figure 8.10 Transient absorbance decay kinetics of the oxidized state of K-51 dye adsorbed on nanocrystalline TiO_2 films a) in pure MPN solvent and b) in the presence of TEMPO electrolyte. Absorbance changes were measured at a probe wavelength of 650 nm, employing 600 nm pulsed laser excitation (7 ns fwhm pulse duration, 40 μJcm^{-2} pulse fluence). Continuous lines drawn on top of experimental data were monoexponential fitting curves with first-order rate constants of a) $k_0 = 4.2 \times 10^3\ s^{-1}$ and b) $k_1 = 1.5 \times 10^7\ s^{-1}$, respectively.

Despite the rapid dye regeneration by TEMPO, we observed a ~30%, remnant signal due to the oxidized state of the sensitizer survived up to hundreds of microseconds. To scrutinize this effect, FT-IR technique was used to monitor the change on the dyed TiO_2 after contacting with the electrolyte. Trace a in Figure 8.11 is the FR-IR spectrum measured with a nanotransparent layer of TiO_2 sensitized by K-51 dye. The sharp peak at 2100 cm^{-1} arose from the absorption of thiocyanato group and was considered to be an indication of the surface dye load. A drop of 0.1 M AcCN solution of TEMPO was then applied on the dyed film for 1 min before the film was rinsed with AcCN and measured to give trace b. There was no significant change in the position or the intensity of the peaks induced by the contact with TEMPO itself. However, the situation was a bit different if the drop of electrolyte contained TEMPO$^+$. Instead of applying a drop of pure AcCN solution of TEMPO on the film, we put a drop of 0.1 M TEMPO in AcCN where 10 mol percent of TEMPO was already oxidized by $NOBF_4$. The film was then rinsed and measured to give trace c. An obvious decrease in the peak height at 2100 cm^{-1} was observed, as well as a concomitant new feature at 2210 cm^{-1}. Meanwhile, the maximum in the absorption spectra of the film blueshifted to 490 nm, implying a partial formation of cyanide coordinated sensitizer. A possible explanation could be that the TEMPO$^+$ attacked the sulfur atom of the NCS group and decomposed it to a cyanide byproduct that changed the FT-IR and absorption spectrum of the film. At the first glance, this detrimental effect would instantly kill all the sensitizer molecules and stop the operation of the cell. However, as seen in FT-IR and UV-Vis absorption spectrum, the reaction was not complete and the absorption of the film was not drastically changed either. Yet this change in surface dye component might be strong enough to be detected in the sensitive laser flash photolysis experiment as the signal residue.

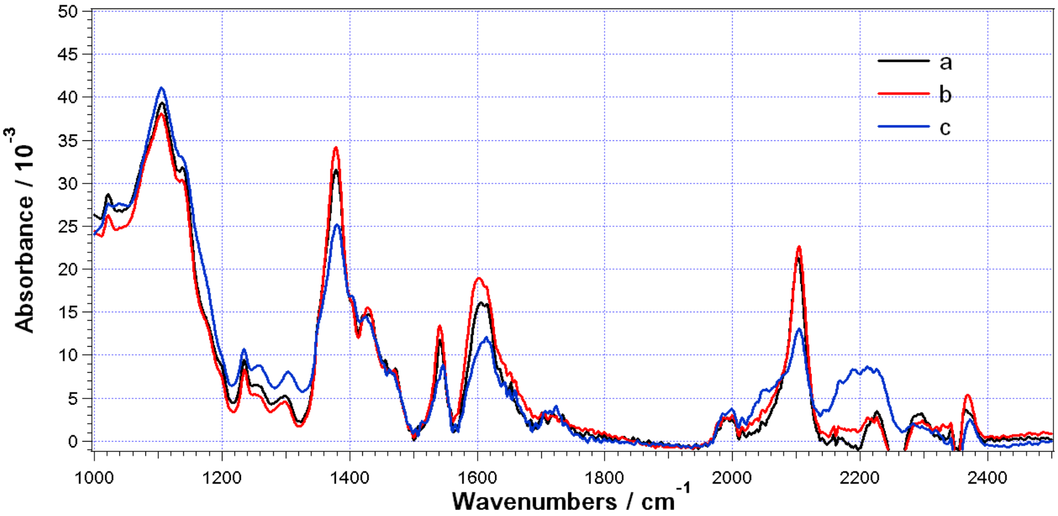

Figure 8.10 a) ATR-FTIR spectrum for mesoporous TiO_2 films coated with the K-51 sensitizer. The dyed film was then applied with a drop of b) 0.1 M AcCN solution of pure TEMPO or c) 10 % oxidized 0.1 M AcCN solution of TEMPO and rinsed before FT-IR measurement to give spectra b) and c). A TiO_2 reference film heated at 500 °C to remove surface-adsorbed water has been subtracted for clarity of presentation.

Given the fact that D-149 sensitizer gave the highest conversion efficiency with TEMPO/TEMPO$^+$ electrolyte, dye regeneration kinetics of D-149 sensitizer was monitored as well. Figure 8.11 plots the decay kinetics of the oxidized state of D-149 sensitizer adsorbed on nanocrystalline TiO_2 films in contact with a) pure MPN solvent and b) 0.1 M TEMPO electrolyte. Absorbance changes were measured at a probe wavelength of 700 nm, following a 530 nm pulsed laser excitation (7 ns fwhm pulse duration, 200 µJ cm^{-2} pulse fluence). In the absence of $TEMPO/TEMPO^+$ redox electrolyte, the decrease of the absorption signal could be fitted with a rate constant of $k_2 = 4.0 \times 10^3\ s^{-1}$, similar to that of the K-51 sensitizer. When $TEMPO/TEMPO^+$ was present, the signal of the oxidized dye decayed to 20 % of its initial value within 10 ns, indicating that the oxidized state of the sensitizer was ultrafast (< 7 ns) regenerated by the mediator. Unfortunately, we could not resolve the rate constant for this process with our nanosecond laser setup due to the experimental limitations and this would demand further experiments on a new picosecond laser that is being built at the moment. Again, a 15% residual signal of dye cation was observed up to 400 µs. Since there is no NCS group in the molecule of D-149, the signal residue was not thought to be associated with the decomposition of the sensitizer. FT-IR spectra in Figure 8.12 showed no notable difference in the peak positions between the samples without or with the addition of $TEMPO^+$ on the dyed film. The slight change in signal intensity was probably due to the small variation of the applied pressure on different samples. It should be noted that we could not rule out the possibility that reactions might take place between $TEMPO^+$ and D-149 sensitizer that were not be detected by FT-IR measurement. However, this seemed not to be supported by the available results where a high IPCE and a fast regeneration of the ground state of the sensitizer were observed.

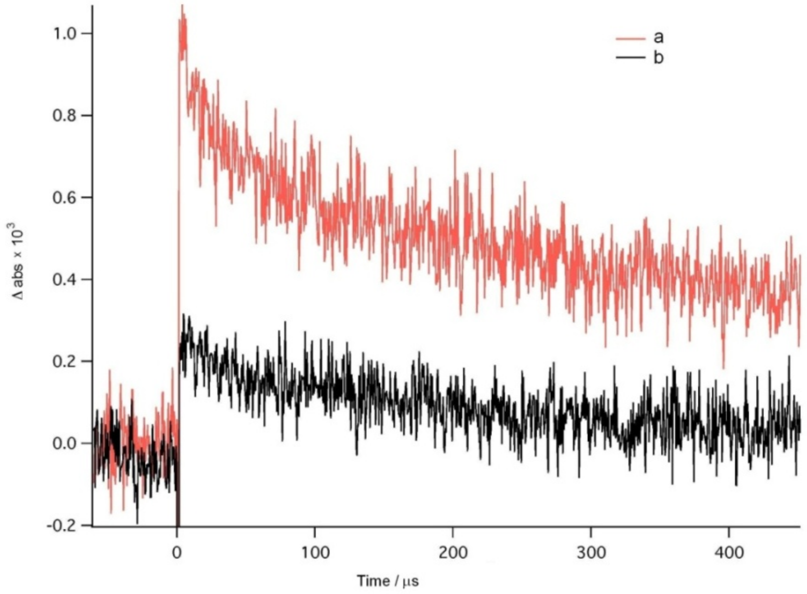

Figure 8.11 Transient absorbance decay kinetics of the oxidized state of D-149 dye adsorbed on nanocrystalline TiO_2 films a) in pure MPN solvent and b) in the presence of 0.1 M TEMPO electrolyte. Absorbance changes were measured at a probe wavelength of 700 nm, employing 530 nm pulsed laser excitation (7 ns fwhm pulse duration, 200 μJcm^{-2} pulse fluence).

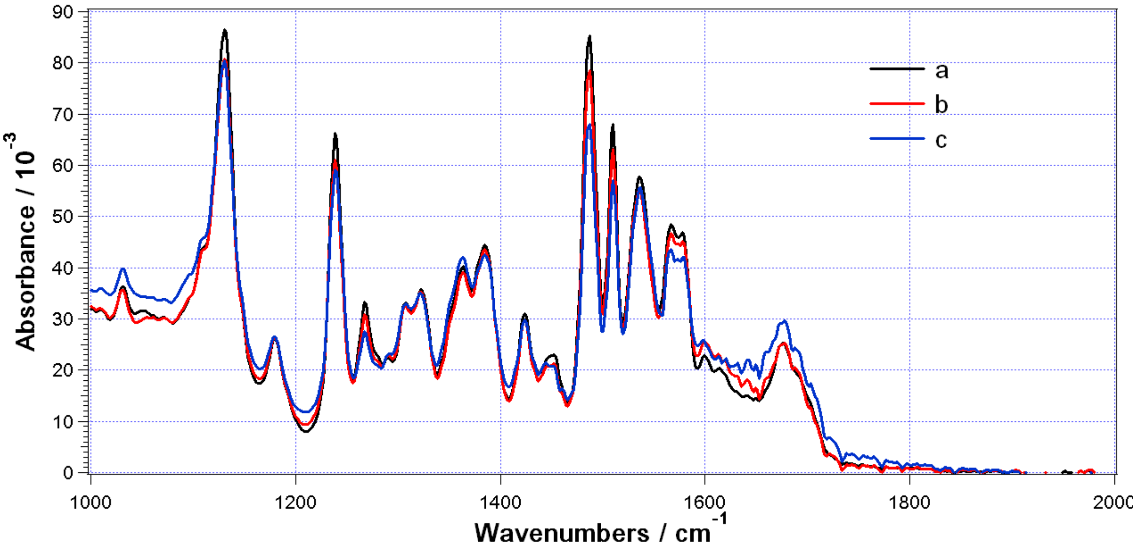

Figure 8.12 a) ATR-FTIR spectrum for mesoporous TiO_2 films coated with the D-149 sensitizer. The dyed film was then applied with a drop of b) 0.1 M AcCN solution of pure TEMPO or c) 10 % oxidized 0.1 M AcCN solution of TEMPO and rinsed before FT-IR measurement to give spectra b) and c). A TiO_2 reference film heated at 500 °C to remove surface-adsorbed water has been subtracted for clarity of presentation.

8.2.4 TEMPO electrolyte with a cyanide dye

Finally, to avoid the NCS decomposition problem with $TEMPO^+$, a cyanide dye Z-973 was used as the sensitizer to study the $TEMPO/TEMPO^+$ redox couples. This sensitizer had a similar structure to Z-907 sensitizer except that the NCS ligands in Z-907 were replaced by the cyano group. The introduction of cyano ligand increased the energy of the LUMO and blueshifted the absorption maximum of the molecule from 510 nm to 480 nm. Apart from small variations in signal intensities, FT-IR spectra in Figure 8.13 demonstrates the same peak features, regardless of the presence of TEMPO and $TEMPO^+$ and proves that this dye was not influenced by $TEMPO^+$, at least within the ATR-IR detection limit. The photovoltaic performance of this sensitizer was first evaluated with the standard I^-/I_3^- redox system by using electrolyte Z-646 and a double-layered TiO_2 film of 7+5. Figure

8.14 shows the current-voltage characteristics of the device under simulated AM 1.5 illumination at 100 mW cm^{-2}. Due to the blue shift of the dye spectrum, the device showed a much smaller J_{sc} than that of the device based on the Z-907 sensitizer and an IPCE spectrum with a maximum of 70% at 490 nm.

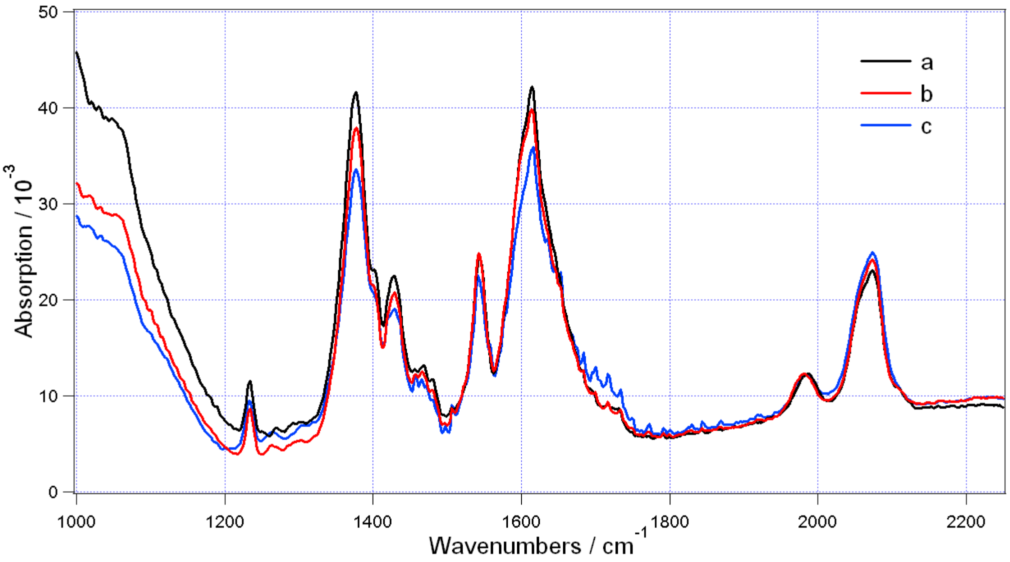

Figure 8.13 a) ATR-FTIR spectrum for mesoporous TiO_2 films coated with the Z-973 sensitizer. The dyed film was then applied with a drop of b) 0.1 M AcCN solution of pure TEMPO or c) 10 % oxidized 0.1 M AcCN solution of TEMPO and rinsed before FT-IR measurement to give spectra b) and c). A TiO_2 reference film heated at 500 °C to remove surface-adsorbed water has been subtracted for clarity of presentation.

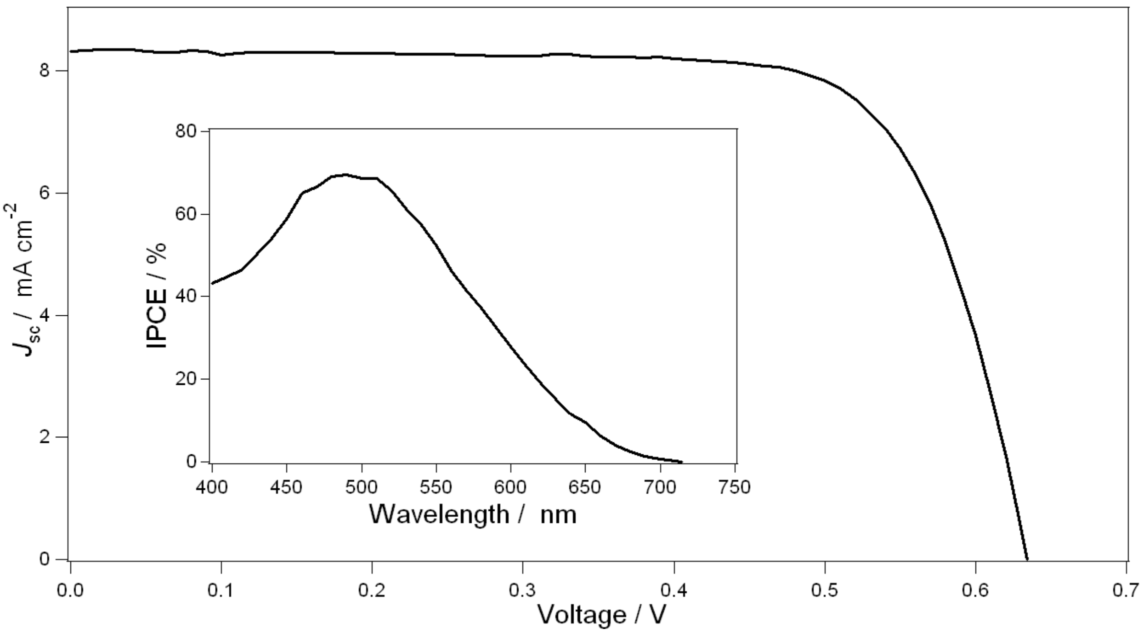

Figure 8.14 Current-voltage characteristics of a Z-973 sensitized device under simulated AM 1.5 illumination at 100 mWcm^{-2}. The photoanode was 7+5. Electrolyte: Z-646. The insert shows the IPCE spectrum of the device.

Figure 8.15 is the current-voltage characteristics of a device based on Z-973 sensitizer and 0.1 M TEMPO electrolyte under simulated AM 1.5 illumination at 100 mW cm^{-2}. The device showed a J_{sc} of 6.2 mA cm^{-2}, a V_{oc} of 890 mV and a power conversion efficiency of 3.1%. Despite of the lower J_{sc} of this device compared to that of the device in Figure 8.14, the IPCE spectrum of this device showed a maximum of 66% at 480 nm, well approaching the value observed in the iodide cells. It is also interesting to note that even the molar extinction coefficient of Z-973 sensitizer was much lower than that of the D-149 sensitizer, the IPCE maximum of the device based on Z-973 was even higher than that of D-149, indicating the beneficial effect of using a cyanide dye in combination with the TEMPO electrolyte.

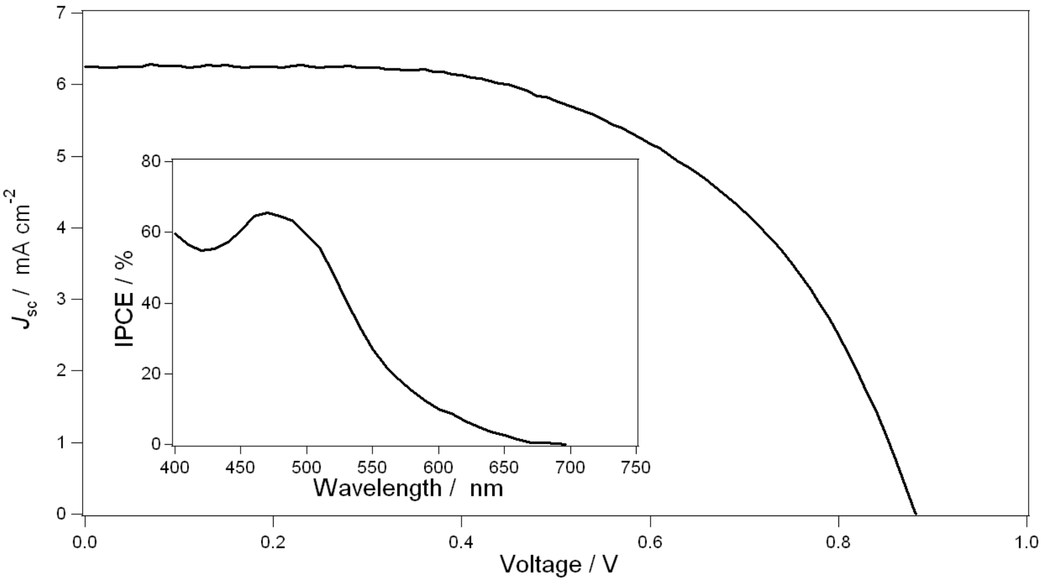

Figure 8.15 Current-voltage characteristics of a Z-973 sensitized device under simulated AM 1.5 illumination at 100 mWcm^{-2}. The device was based on a 5.8-µm-thick photoanode made of standard TiO_2 paste. The electrolyte contained 0.1 M TEMPO, 1.2 M LiTFSI and 0.5 M NBB in acetonitrile. $NOBF_4$ was added to oxidize 10 mol percent of the TEMPO to TEMPO$^+$. The insert shows the IPCE spectrum of the device.

8.3 Electrolytes based on Phenoxazine (POZ)

8.3.1 Electrochemistry of phenoxazine

POZ has been known as the chromophore of actinomycins and a structural analog to phenothiazine (PTZ) which has also a fast redox. To increase the solubility of the molecule and avoid the influence of the basicity of POZ, the hydrogen at position 10 was substituted by methoxyethoxyethyl to give *N*-(methoxyethoxyethyl)-phenoxazine (MEEP). Derivatives of MEEP were synthesized by putting electron donating (methyl and methoxy) or withdrawing (bromo) groups at the *para* position to the nitrogen atom to obtain *N*-(methoxyethoxyethyl)-3,7-dimethoxy-phenoxazine (MeOMEEP), *N*-(methoxyethoxyethyl)-3, 7-dibromo-phenoxazine (BrMEEP), *N*-(methoxyethoxyethyl)-3-methyl-phenoxazine (MeMEEP), and *N*-(methoxyethoxyethyl)-3,7-dimethyl-phenoxazine (DMeMEEP).

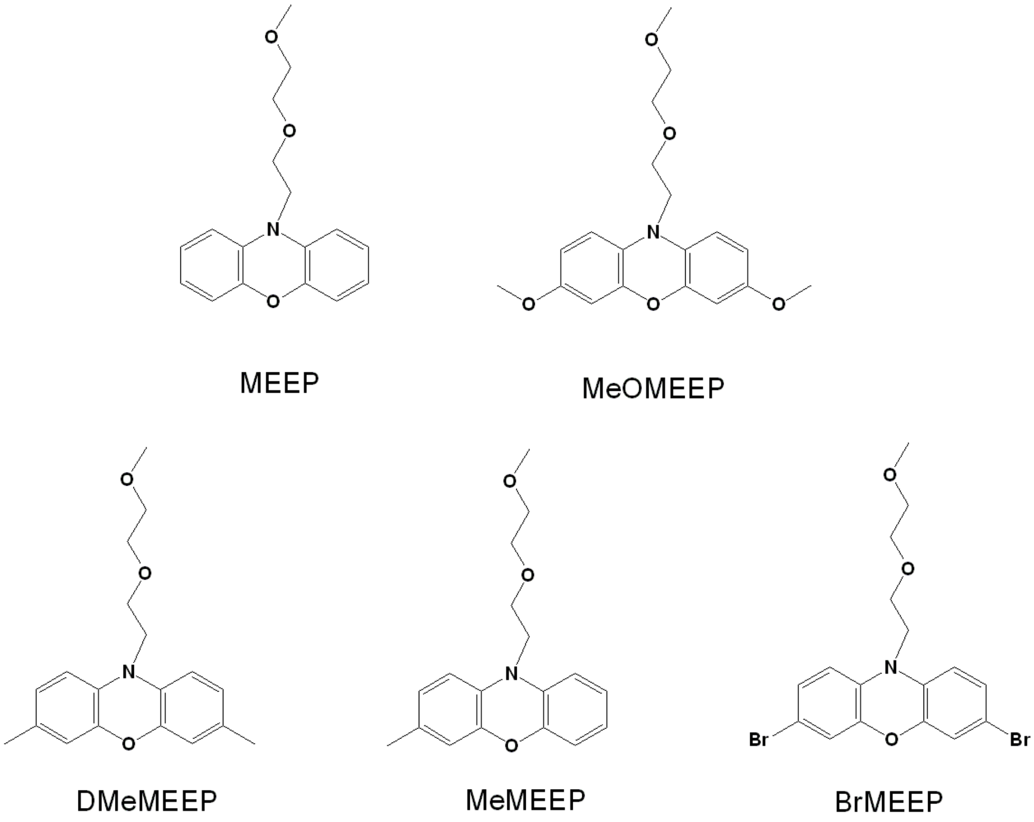

MEEP MeOMEEP

DMeMEEP MeMEEP BrMEEP

Figure 8.16 Structures of MEEP series compounds.

In previous studies, when PTZ derivatives were employed as the hole transporting material efficient recombination of photoinjected electrons in TiO_2 films with oxidized phenothiazine compounds was observed and the IPCE was reported to be less than 1%.[12] With the success in TEMPO based electrolytes, we wanted to study the POZ based electrolytes in a similar way to address some of the fundamental issues.

Figure 8.17 plots the cyclic voltammograms of a series of MEEP derivatives in the AcCN solution with 0.1 M TBATBF as the supporting electrolyte. The standard redox potential of MEEP/MEEP$^+$ was determined to be 0.26 versus Fc/Fc$^+$, similar to that of TEMPO/TEMPO$^+$. By the introduction of two electron-donating methoxy group at 3 and 7 positions, the HOMO energy was increased and the standard redox potential of MeOMEEP /MeOMEEP$^+$ was found to shift negatively to 0.04 V versus Fc/Fc$^+$. Similarly, introducing one or two methyl groups moved the standard redox potential of the molecule to 0.18 V and 0.13 V versus Fc/Fc$^+$, respectively. On the contrary, substitution of hydrogen by bromo groups at 3 and 7 positions decreased the HOMO energy and positively shifted the standard redox potential to 0.38 V versus Fc/Fc$^+$. Since the maximum photovoltage of the dye cell was determined by the difference between the quasi-Fermi level of TiO_2 and the Nernst potential of the electrolyte, the great tunability in the redox potential of the mediator provided us with a suitable system for photovoltaic studies.

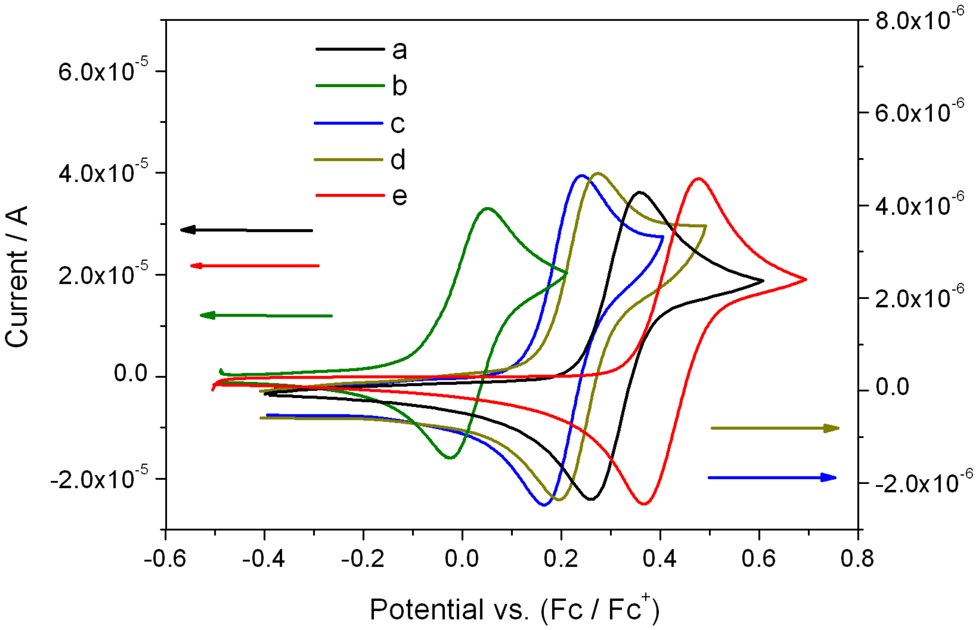

Figure 8.17 Typical cyclic voltammograms of a) 5 mM MEEP, b) 5 mM MeOMEEP, c) 0.6 mM DMeMEEP, d) 0.7 mM MeMEEP and e) 5.5 mM BrMEEP on Pt disc electrode in acetonitrile solution containing 0.1 M tetrabutylamonium tetraboronfluoride (TBATBF) as the supporting electrolyte. Scan rate: 0.1 V s^{-1}.

8.3.2 Photochemical studies of phenoxazine based electrolytes

The performance of the MEEP electrolytes were first evaluated with the cyanide dye Z-973 and a 4.9-µm-thick photoanode of 60-nm sized TiO_2 particles. Figure 8.18 shows the *I*-*V* curve of the devices with electrolytes of 0.2 M a) MEEP and b) MeOMEEP under the simulated AM 1.5 illumination at 10 mW cm^{-2}. The electrolytes contained 1.2 M LiTFSI, 0.5 M NBB and 10% mole percent of $NOBF_4$ as the dopant. Both devices showed a similar J_{sc} of 440 µA cm^{-2}, however, the device with MeOMEEP (trace b) had a much lower V_{oc}, 430 mV as opposed to 690 mV for that of the device with MEEP (trace a), in accordance with the difference in their standard redox potentials shown in Figure 8.17. This can be explained by the fact that the V_{oc} is determined by the difference of the quasi-Femi level in the TiO_2 and the redox potential of the electrolyte. By assuming a comparable quasi-Fermi level for both devices, a redox couple with a more positive potential would favor a higher photovoltage, as is the case presented here. The merit of using a redox couple with a high oxidization potential in this series of compound was also reflected in the conversion efficiency of the device with 1.9 % for trace a and 1.5 % percent for trace b at this light intensity, mainly due to the higher V_{oc} for the MEEP electrolyte. The IPCE of the devices peaked at 470 nm with a maximum of ~ 50 %.

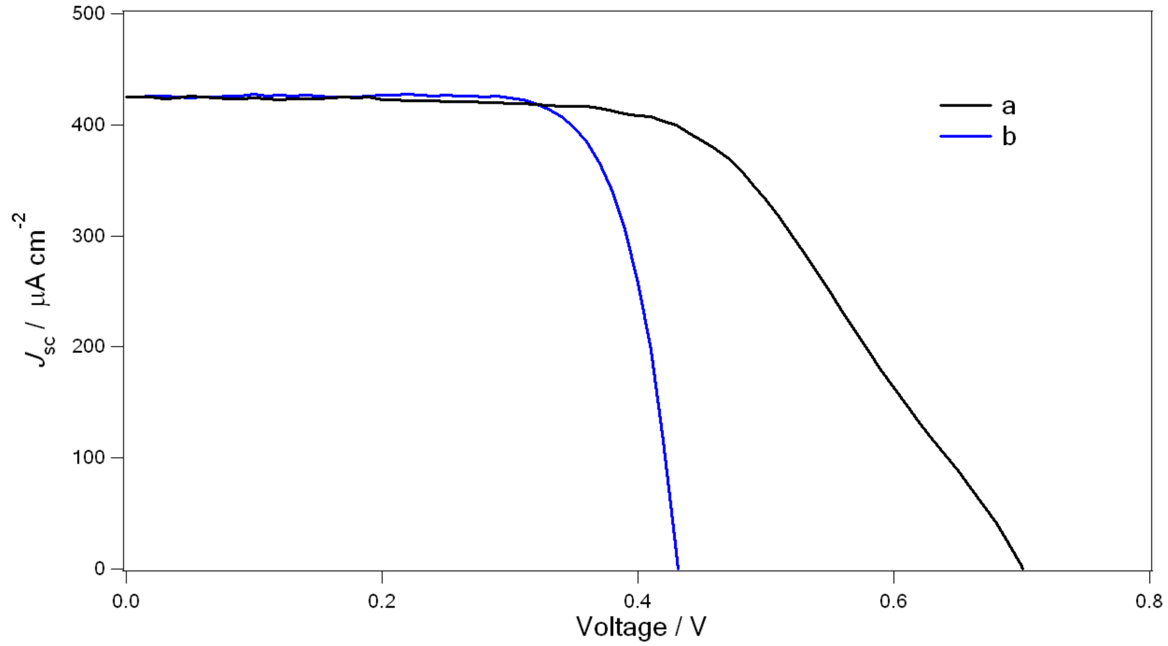

Figure 8.18 Current-voltage characteristics of a Z-973 sensitized device with electrolytes of 0.2 M a) MEEP and b)

MeOMEEP under the simulated AM 1.5 illumination at 10 mW cm^{-2}. The electrolytes contained 1.2 M LiTFSI, 0.5 M NBB and 10% mole percent doped by $NOBF_4$ as the dopant. The device was based on a 4.9-μm-thick photoanode made of 60-nm sized TiO_2 paste.

Table 8.2 summarizes the photovoltaic parameters of the devices with different POZ electrolytes under simulated AM 1.5 illumination at 100 mW cm^{-2}. It is interesting to note that the V_{oc} of the devices followed the same trend observed in the redox potentials, supporting the previous argument about the effect of redox potential on the photovoltage. As the light intensity increased, the *FF* became rather low, possibly related to the fast recombination and poor charge collection associated with POZ electrolytes, and led to a drop in the conversion efficiency to around 1 % for all the devices.

Table 8.2 Complete set of photovoltaic parameters for DSCs based on Z-973 sensitizer and a 4.9-μm-thick photoanode with 0.2 M different POZ electrolytes measured under simulated AM 1.5 full sunlight (100 mW cm^{-2}) irradiation. All electrolytes contained 1.2 M LiTFSI, 0.5 M NBB and 10% mole percent doped by $NOBF_4$ as the dopant.

Electrolytes	J_{sc} / mA cm^{-2}	V_{oc} / mV	*FF*	η / %
MeOMEEP	3.7	500	0.54	1.0
DMeMEEP	4.3	720	0.35	1.1
MeMEEP	4.1	750	0.42	1.3
MEEP	4.0	770	0.41	1.3

Following the same strategy to increase the light harvesting, D-149 dye was employed as the sensitizer of the device. The *I-V* curve of the D-149 sensitized device with 0.2 M MEEP measured at the same light intensity as that of Figure 8.18 is shown in Figure 8.19. The device showed a J_{sc} of 0.83 mA cm^{-2}, a V_{oc} of 680 mV and a conversion efficiency of 3.8 % at this light intensity. Compared to the device with the same electrolyte in Figure 8.18, the increase in η of the D-149 sensitized device mainly came from the larger photocurrent that was resulted from the higher light extinction by this organic dye. Yet the similar trend in *FF* decrease was also observed as the light intensity went up and η at the irradiance of 50 and 100 mW cm^{-2} dropped to 2.8 % and 2.0%, respectively.

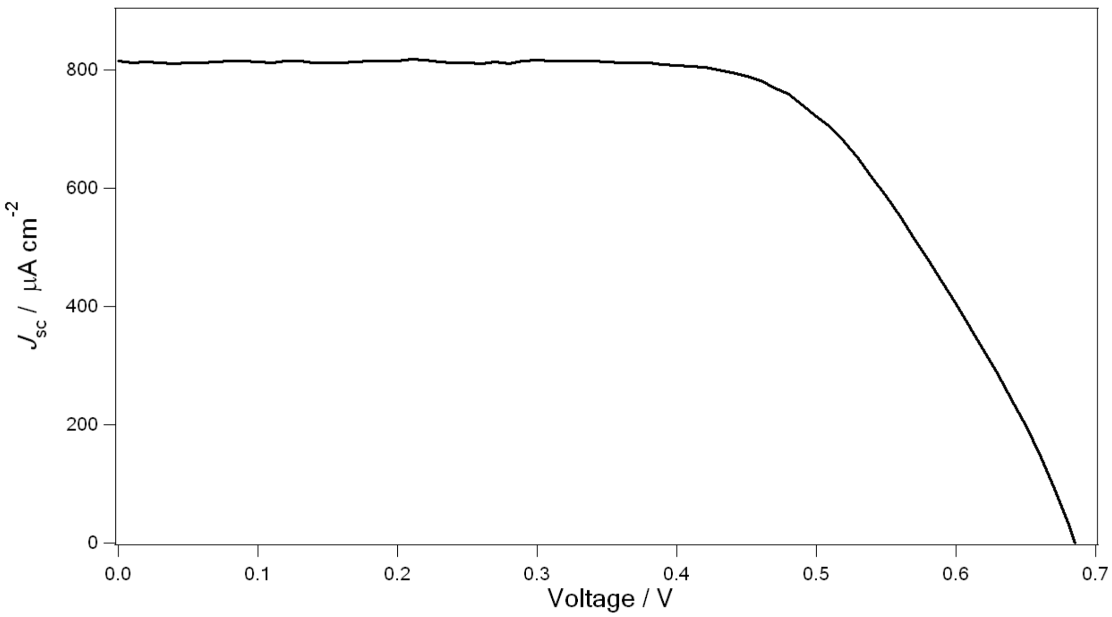

Figure 8.19 Current-voltage characteristics of a D-149 sensitized device with electrolytes of 0.2 M MEEP under the simulated AM 1.5 illumination at 10 mW cm^{-2}. The electrolytes contained 1.2 M LiTFSI, 0.5 M NBB and 10% mole percent doped by $NOBF_4$ as the dopant. The device was based on a 3.0-µm-thick photoanode made of 60-nm sized TiO_2 paste.

8.4 Electrolytes based on Tetrathiafulvalene (TTF)

8.4.1 Electrochemistry of TTF

TTF is an organosulfur compound that is widely used in molecular electronics. Its planarity and high symmetry favors the charge delocalization to give a stable radical cation upon the oxidation. Figure 8.20 displays a typical cyclic voltammogram of 2 mM AcCN solution of TTF. TTF underwent two oxidization processes to form TTF^+ and TTF^{2+} with standard redox potentials of -0.06 and 0.32 V versus Fc/Fc^+, respectively. To make the electrolyte used for photovoltaic studies in DSCs, a 10 mole percent of $NOBF_4$ was added to oxidize TTF. Although TTF^{2+} might be produced by the addition of nitrosonium, we yet considered the potential of the couple TTF/TTF^+ as the redox level of the electrolyte due to the large excess of TTF in the solution.

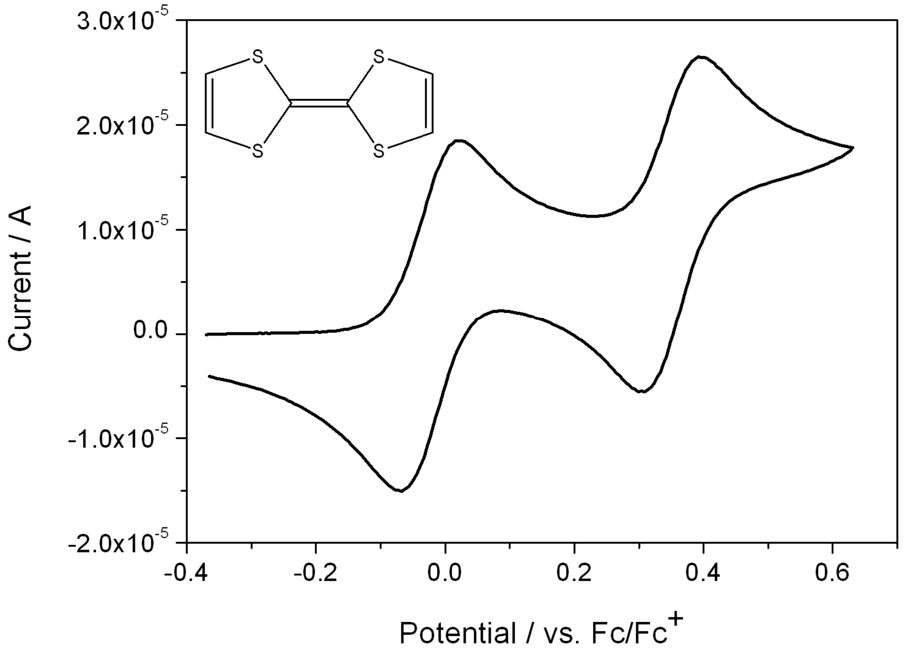

Figure 8.20 A typical cyclic voltammogram of a) 2 mM TTF on Pt disc electrode in acetonitrile solution containing 0.1 M tetrabutylamonium tetraboronfluoride (TBATBF) as the supporting electrolyte. Scan rate: 0.1 V s^{-1}.

The cyclic voltammogram of bis(4,5-dihydro naphtho[1,2-*d*])tetrathiafulvalene (BDHN-TTF) is shown in Figure 8.21. The conjugation of naphtho groups with TTF was found to slightly change the potential of the compound, leading to standard redox potentials of -0.08 and 0.26 V versus Fc/Fc$^+$ to form the BDHN-TTF cation and dication, respectively.

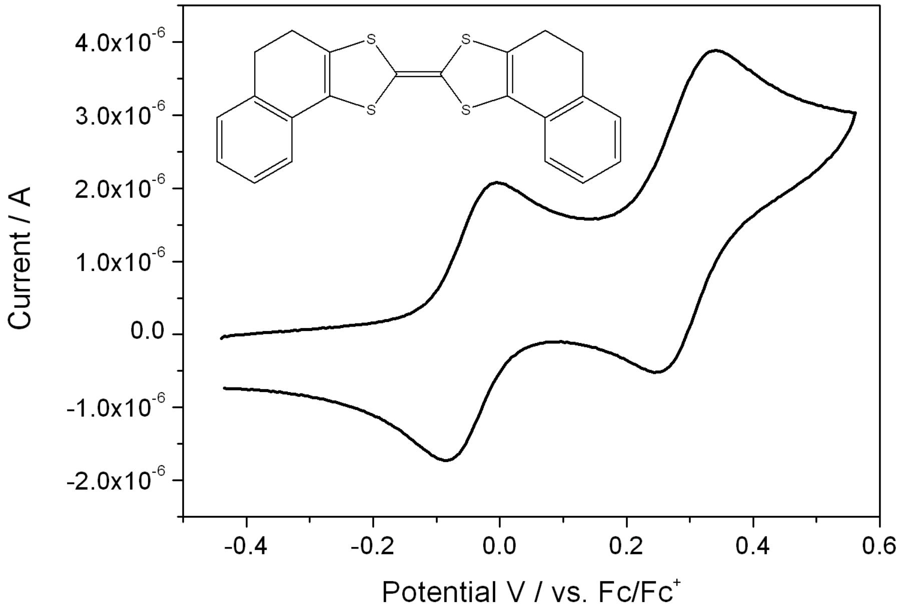

Figure 8.21 A typical cyclic voltammogram of a) 0.3 mM BDHN-TTF on Pt disc electrode in acetonitrile solution containing 0.1 M tetrabutylamonium tetraboronfluoride (TBATBF) as the supporting electrolyte. Scan rate: 0.1 V s^{-1}.

8.4.2 Photochemical studies of TTF based electrolytes

The photovoltaic performance of the TTF based electrolytes were evaluated in a similar way as we did for the TEMPO and PTZ electrolytes. Figure 8.22 shows the *I-V* characteristics of a device with K-51 sensitizer and 0.1 M TTF electrolyte a) in the dark and under simulated AM 1.5 illumination at b) 10 and c) 100 mW cm^{-2}. Under 1 sun, the device showed a J_{sc} of 6.0 mA cm^{-2}, a V_{oc} of 570 mV and a power conversion efficiency of 2.3%. Compared to the normal V_{oc} (~720 mV) of the K-51 sensitized device with iodine-based electrolytes,[11] the open-circuit photovoltage here was about 150 mV lower, despite the fact that the redox potential of TTF/TTF$^+$ was even a little higher than that of I^-/I_3^- (~ -0.15 V versus Fc/Fc$^+$). This phenomenon was contrary to previous cases where the application of mediators (TEMPO or PTZ) with more positive potentials than that of I^-/I_3^- led to a higher V_{oc} output. In the next section, we will see that this was due to the small electron density in the TiO_2 film, lowering the quasi-Fermi level of the TiO_2 and counterbalancing the shift in the Nernst potential of the redox.

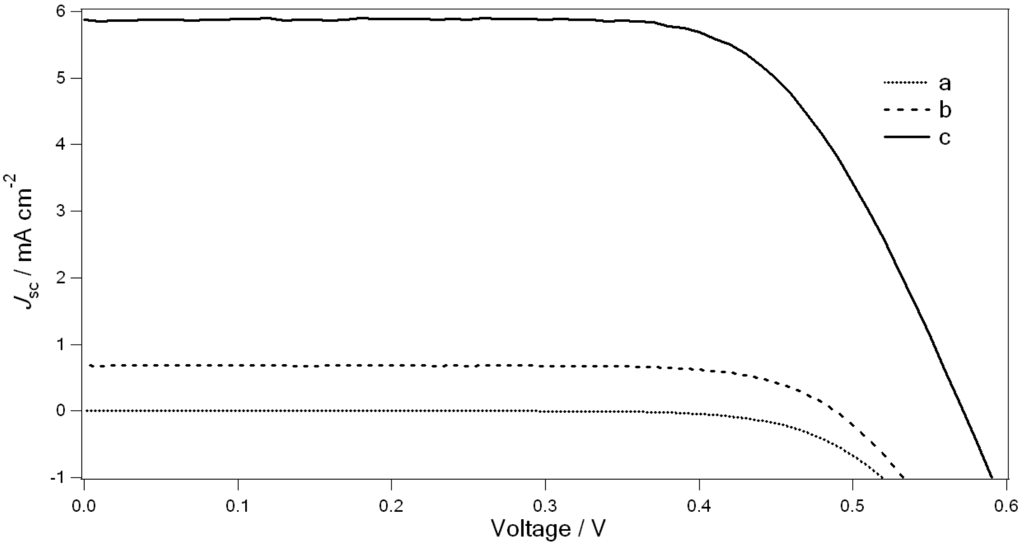

Figure 8.22 Current-voltage characteristics of a K-51 sensitized device a) in the dark and under simulated AM 1.5 illumination at b) 10 and c) 100 mWcm^{-2}. The device was based on a 5.8-µm-thick photoanode made of standard TiO_2 paste. The electrolyte contained 0.1 M TTF, 1.2 M LiTFSI and 0.5 M NBB in acetonitrile. $NOBF_4$ was added to

oxidize 10 mol percent of the TEMPO to $TEMPO^+$.

Due to the poor solubility of BDHN-TTF in AcCN, dichloromethane was used as the solvent. The device showed a J_{sc} of 4.2 mA cm^{-2}, a V_{oc} of 550 mV and a conversion efficiency of 1.5% at an irradiance power of 100 $mWcm^{-2}$. The *I-V* characteristic of the device is shown in Figure 8.23.

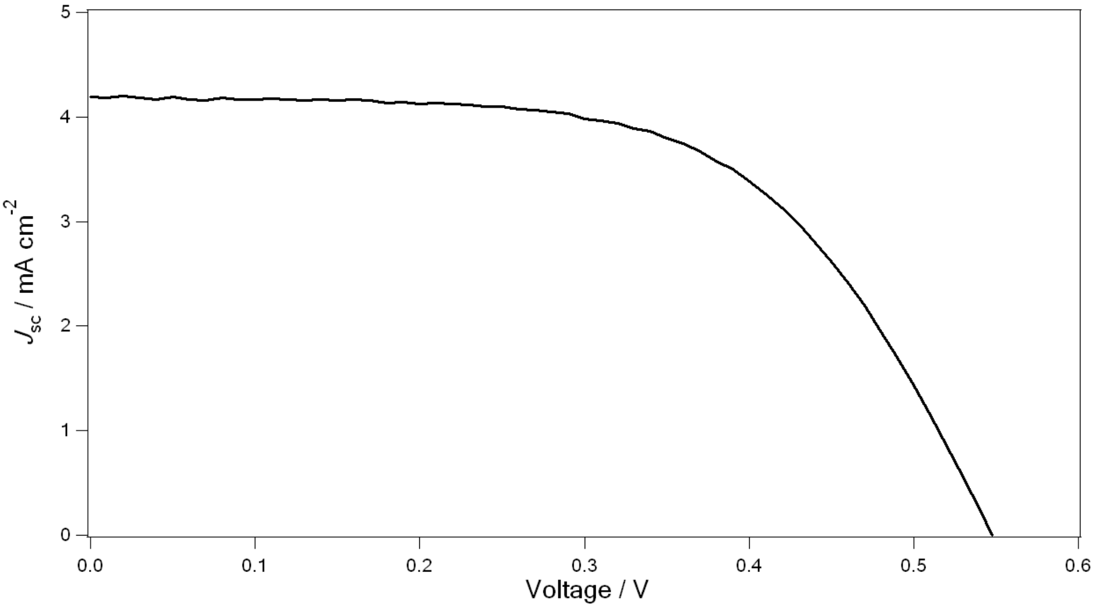

Figure 8.23 Current-voltage characteristics of a K-51 sensitized device under simulated AM 1.5 illumination at 100 $mWcm^{-2}$. The device was based on a 5.8-µm-thick photoanode made of standard TiO_2 paste. The electrolyte contained 0.1 M BDHN-TTF, 1.2 M LiTFSI and 0.5 M NBB in dichloromethane.

8.5 Factors limiting the conversion efficiency

In the previous sections, non-iodine redox couples have demonstrated their potential applicability as the mediator in DSCs and higher than 5% conversion efficiency at 1.0 sun AM 1.5G was achieved with TEMPO electrolytes. This was a remarkable improvement in alternative redox couples, yet still not comparable with the widely used I^-/I_3^- electrolytes that gave a conversion efficiency of ~10%. The difference mainly came from the smaller photocurrent (< 10 mA cm^{-2} for non-iodine electrolytes) than that of the “champion” cell with I^-/I_3^- electrolytes (15 to 20 mA cm^{-2} depending on the sensitizer). In this section, we want to tentatively rationalize the factors limiting the conversion efficiency of the alternative redox systems. Since all the couples investigated in this chapter were of a fast one-electron process, they were supposed to react readily with the dye cations (S^+) produced by the light-induced electron transfer from the sensitizer to TiO_2. As was shown in Section 8.2.3, the sensitizer D-149 was very fast regenerated by TEMPO and this rapid dye regeneration process ruled out any large photocurrent loss incurred by the insufficient recuperation of the dye ground state. Another possible factor limiting the photocurrent would be the fast recapture of photoinjected electrons in TiO_2 by the oxidized species of the redox, i.e. $TEMPO^+$, POZ^+ and TTF^+, which was also observed in other non-iodine electrolytes such as PTZ and Fc.[1][2][12] For this purpose, thin-layer electrochemical cells were fabricated to study the kinetics of electron transfer from TiO_2 to the oxidized species in the electrolyte. The cells were of an asymmetrical design, where an FTO with a blocking layer was used as working electrode and paired with a platinized FTO as the counter electrode. The dark currents of the two devices are compared in Figure 8.24. The electrolyte were a) 0.1 M PMII mixed with 0.01 M iodine, b) 0.1 M TEMPO 10% doped by $NOBF_4$ and c) 0.1 M MEEP 10% doped by $NOBF_4$ in AcCN. Due to the difference in the redox potentials between the three redox couples, a negative 310 mV was added to the scanning potential of the iodide cell so as to convert it to the potential scale of $TEMPO/TEMPO^+$ by calculation from the Nernst equation (Eq. 9.1). By coincidence, there was no need to make any corrections to the scanning potential measured with the device of MEEP electrolyte. It is apparent that trace a was much smaller than trace b and c at any given potential, indicating a much larger dark current for the device based on non-iodine electrolytes.

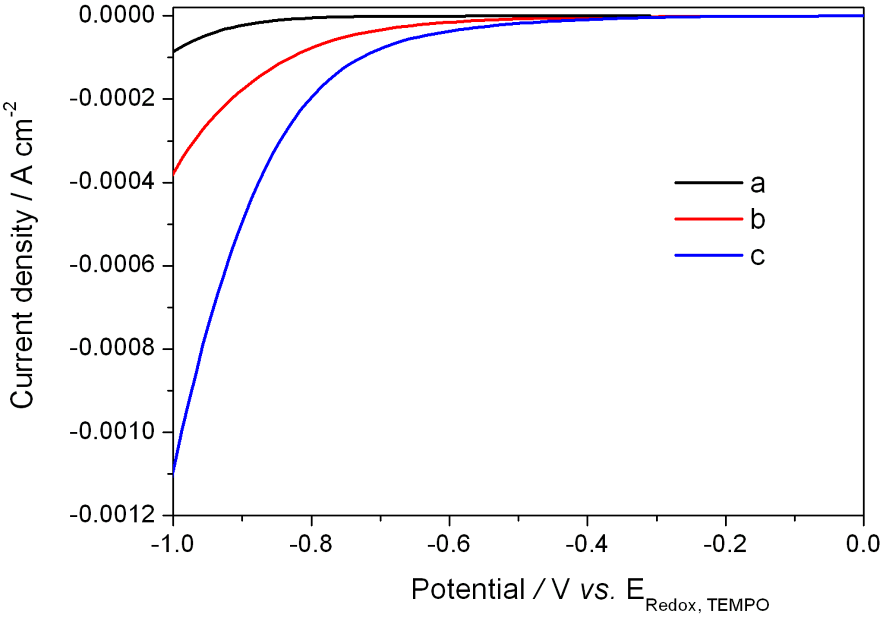

Figure 8.24 Cyclic voltammograms of thin-layer electrochemical cells with a) 0.1 M PMII, b) 0.1 M TEMPO and c) 0.1 M MEEP electrolytes. 10 mM iodine was added to a and 10 mol percent of $NOBF_4$ was added to b and c to produce the oxidized species.

The recombination kinetics of these electrolytes was studied in photovoltage transient experiments. Figure 8.25 shows the electron lifetime of the devices with electrolytes of a) 0.1 M PMII and b) 0.1 TEMPO and c) 0.2 M MEEP as a function of their quasi-Fermi level, which was varied by changing the intensity of the bias light. The Fermi level was expressed with respect to the redox potential of the TEMPO/TEMPO$^+$ couple. For electrolytes with TEMPO and MEEP, this difference corresponded to the measured V_{oc} values, while for the PMII electrolyte, 310 mV was added to the V_{oc} to account for the difference in the Nernst potentials of TEMPO and MEEP electrolytes. Note that for a given quasi-Fermi level, the electron lifetime in the iodide based device was much longer than that of TEMPO or MEEP containing devices.

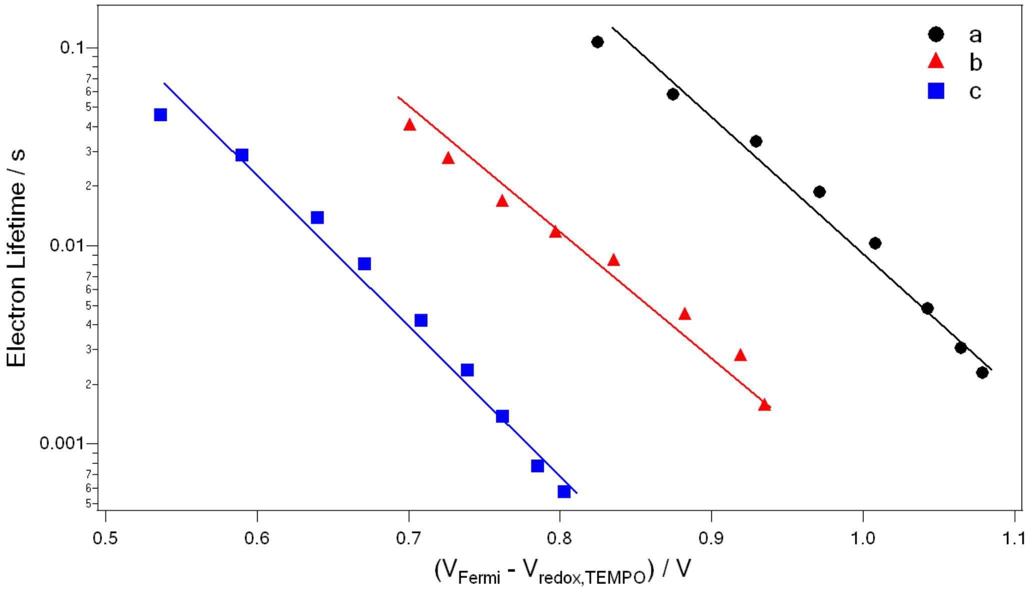

Figure 8.25 Electron lifetime of the devices with electrolytes of a) 0.1 M PMII and b) 0.1 TEMPO and c) 0.2 M MEEP at different electron quasi-Fermi levels of under varying external light bias. A 310 mV positive offset was added to the measured V_{oc} of the PMII electrolyte to adapt its value to the TEMPO/TEMPO$^+$ reference potential. The devices were based on a 3.0-µm-thick photoanode made of 60-nm sized TiO_2 paste. All electrolytes contained 10 mole percent of $NOBF_4$ as the dopant, 1.2 M LiTFSI and 0.5 M NBB in AcCN.

The presence of fast back reaction in these non-iodine couples were also reflected in the measurement of electron/electrolyte recombination rate constant at short-circuit (Section **2.6.2**). To obtain the recombination rate constant at short-circuit, the photovoltage decay was performed by putting the cell under 1.0 sun bias illumination and applying a bias current close to the J_{sc} of the cell at this light intensity.[13][14] In this condition, the apparent voltage was approximately equal to zero if the light intensity was kept constant. The cell was then biased in the vicinity of short-circuit where the back reaction rate constant should thus be much smaller than that measured under open-circuit at the same bias illumination. Figure 8.26 shows a typical photovoltage transient decay experiment performed under 1.0 sun illumination on a D-149 sensitized device with the iodide electrolyte a) at open-circuit and b) in the presence of the current bias. At open-circuit, the photovoltage transient decayed at a characteristic time of 2.7 ms, a normal value widely found in iodide cells with our setup. While in trace b, the decay time of the photovoltage increased to 30 ms, corresponding to the transient recombination lifetime at short circuit. Compared to a typical photocurrent decay lifetime (~1 ms) at short-circuit, the slower recombination kinetics ensured a high charge collection efficiency for iodide cells at 1.0 sun.

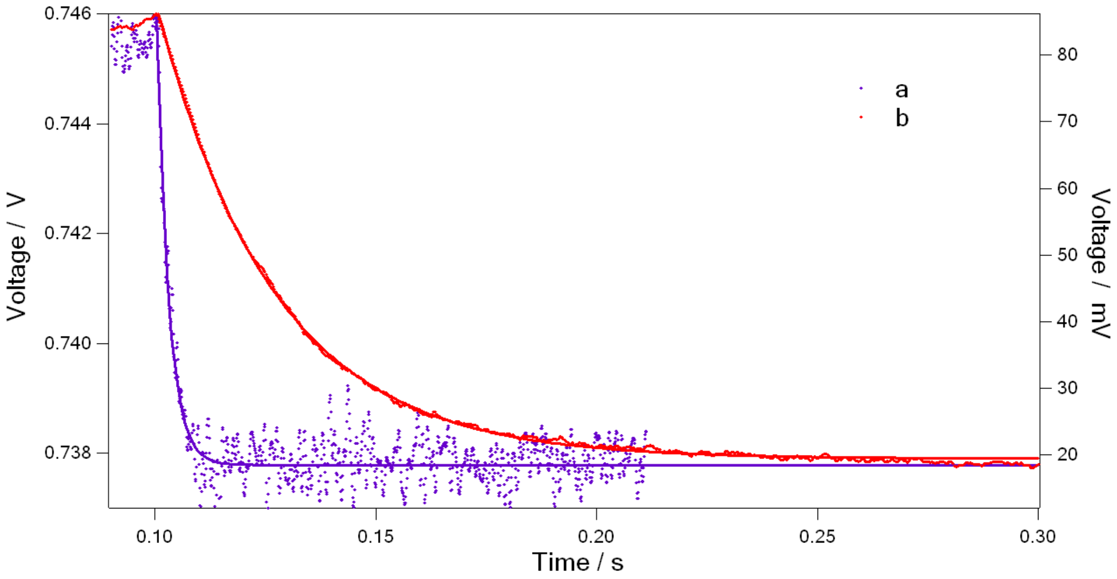

Figure 8.26 Photovoltage transient decays performed under 1.0 sun illumination a) at open-circuit and b) in the presence of the current bias of J_{sc}. The raw data are shown in dots and fitted by the full lines with an exponential decay model. The device was based on a D-149 sensitized, 3.0-µm-thick photoanode made of 60-nm sized TiO_2 paste. The electrolytes contained 0.1 M PMII, 0.01 M iodine, 0.1 M 1.2 M LiTFSI and 0.5 M NBB in AcCN.

The situation was a bit different when TEMPO electrolytes were used. Figure 8.27 plots the photovoltage transient decay experiment measured at the same conditions but with a D-149 sensitized device based on MEEP electrolyte. At open-circuit (trace a), the photovoltage transient decayed at a characteristic time of 2.5 ms, while the decay time of the photovoltage mildly increased to 6.9 ms under the current bias. The case was even worse when POZ electrolytes were used. Figure 8.28 shows the photovoltage transient decay experiment measured at the same conditions but with a D-149 sensitized device based on MEEP electrolyte. At open-circuit (trace a), the photovoltage transient decayed at a characteristic time of 430 μs, indicating a very fast recombination taking place in the cell. As opposed to the observation in the iodide device, the decay time of the photovoltage only slightly increased to 540 μs under the current bias. In comparison to the open-circuit condition, the lower quasi-Fermi level induced by the external current bias did not greatly mitigate the rapid recapture of the photoinjected electrons by MEEP$^+$ in the electrolyte, limiting the charge collection efficiency of the device at 1.0 sun. Unfortunately, we could not well resolve the photocurrent decay time of the same device at short-circuit due to the fast decay of the transient signal, however, a value of ~300 μs would be a good estimate. The comparable decay timescale of the photocurrent and phototransient at short-circuit implied a rather poor charge collection efficiency at 1.0 sun for the device based on POZ electrolytes.

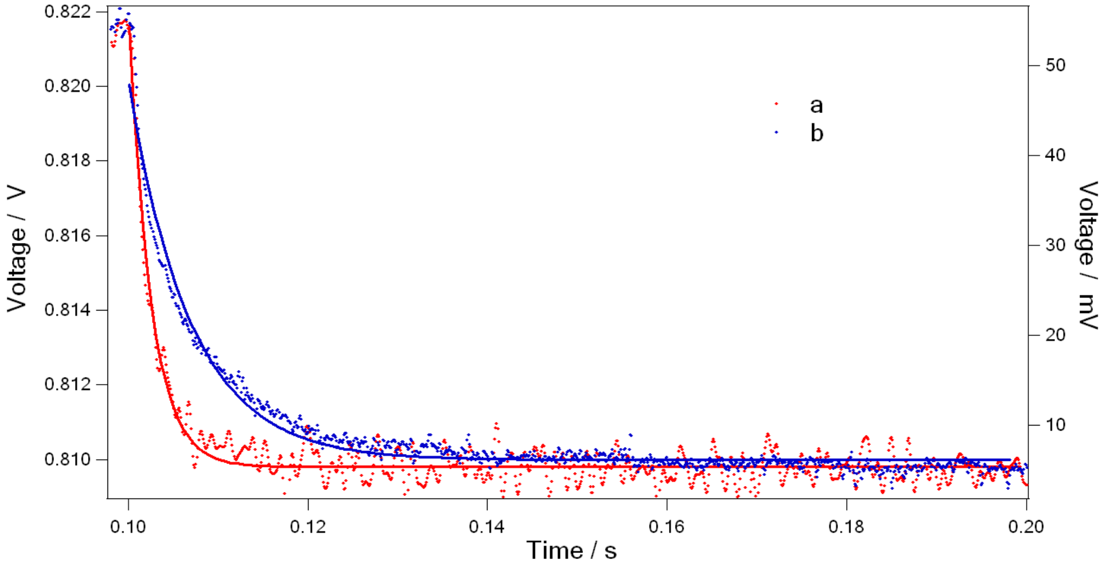

Figure 8.27 Photovoltage transient decays performed under 1.0 sun illumination a) at open-circuit and b) in the presence of the current bias of J_{sc}. The raw data are shown in dots and fitted by the full lines with an exponential

decay model. The device was based on a D-149 sensitized, 3.0-µm-thick photoanode made of 60-nm sized TiO_2 paste. The electrolytes contained 0.1 M TEMPO doped with 10 mole percent of $NOBF_4$, 0.1 M 1.2 M LiTFSI and 0.5 M NBB in AcCN.

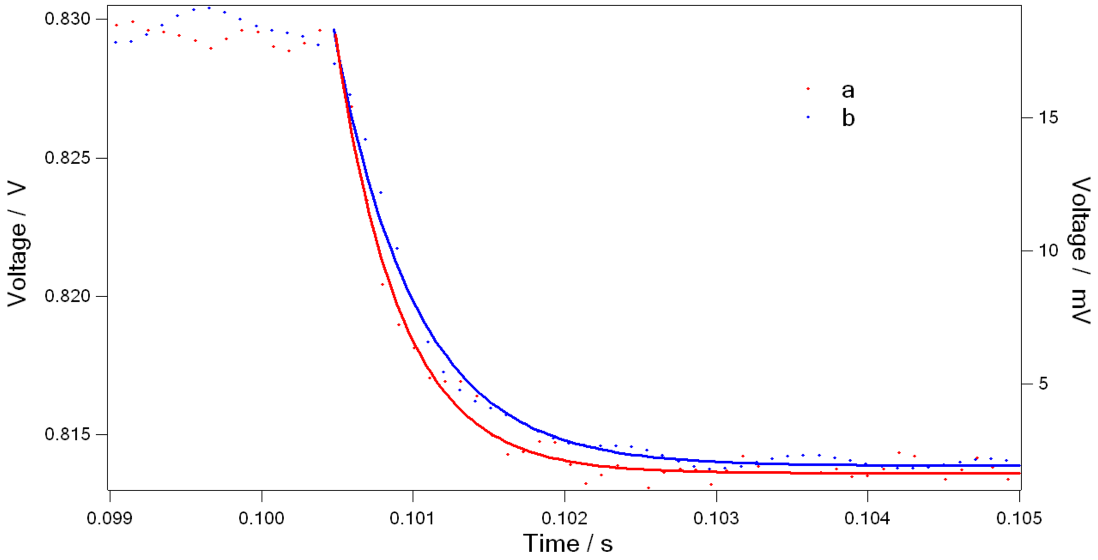

Figure 8.28 Photovoltage transient decays performed under 1.0 sun illumination a) at open-circuit and b) in the presence of the current bias of J_{sc}. The raw data are shown in dots and fitted by the full lines with an exponential decay model. The device was based on a D-149 sensitized, 3.0-µm-thick photoanode made of 60-nm sized TiO_2 paste. The electrolytes contained 0.2 M MEEP doped with 10 mole percent of $NOBF_4$, 0.1 M 1.2 M LiTFSI and 0.5 M NBB in AcCN.

The direct consequence of the rapid back reaction associated with the non-iodine electrolytes in this chapter was low carrier density in the TiO_2 film under normal operation. Figure 8.29 is the plot of recombination rate constant versus the charge density in the devices with a) 0.1 M iodide, b) 0.1 M TEMPO and c) 0.2 M MEEP electrolytes under different bias illuminations. The curve clearly shows the carrier density was much lower for the devices based TEMPO and MEEP electrolytes and at a certain carrier density, the recombination rate constant for TEMPO or MEEP based device was an order of magnitude higher than that of the iodide based device, in a good agreement with the previously observed trend in the electron lifetime of the corresponding devices as a function of the quasi-Fermi level in Figure 8.25. With the increasing light intensity, the devices having TEMPO and MEEP electrolytes were of a slower accumulation in carrier density but showed a more rapid increase in recombination rate constant as compared to that of the iodide device. The fast electron recapture taking place in the electrolytes with the alternative redox couples used in this chapter impaired the accumulation of electrons in the TiO_2, preventing the quasi-Femi level from reaching the same levels as for the iodide/triiodide based cells and thus reducing the increase in V_{oc} to a smaller value than that estimated from the simple shift in Nernst potentials. As shown in the application of some electrolytes, such as TTF and MeOMEEP, the V_{oc} of the device was more than 100 mV lower than that of the device based on iodide/triiodide electrolyte, though the redox potentials of TTF and MeOMEEP electrolyte were found to be more positive than the potential of the iodide electrolyte, proving that the advantageous difference in Nernst potential was negated by the fast back reaction and the large decrease in the quasi-Fermi level finally led to a drop in the photovoltage instead of an expected increase.

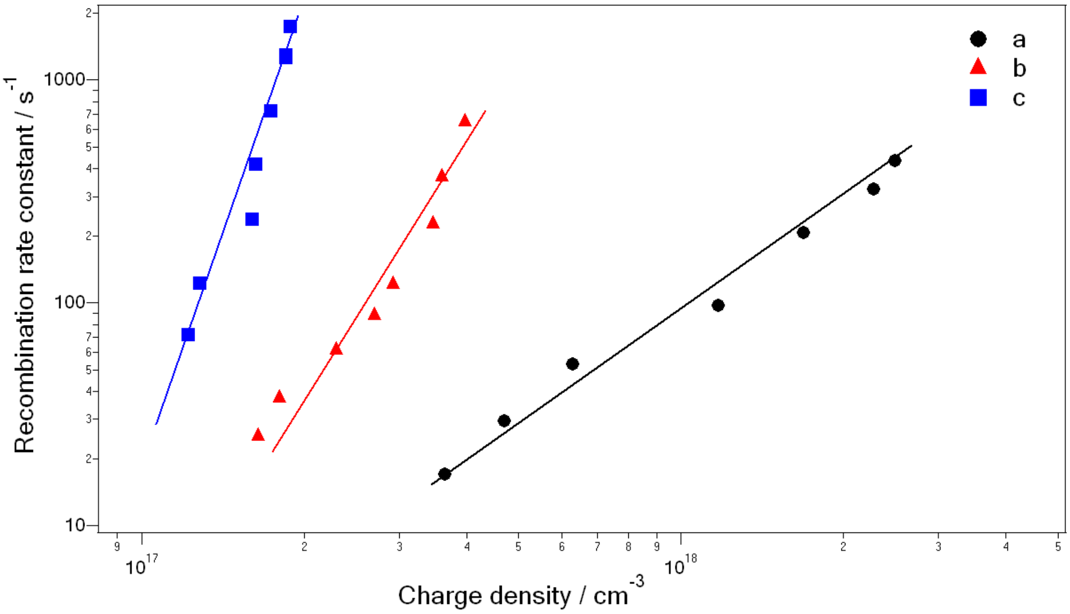

Figure 8.29 Recombination rate constant of the devices with electrolytes of a) 0.1 M PMII and b) 0.1 TEMPO and c) 0.2 M MEEP at different carrier densities under varying external light bias. The charge density was measured by the charge extraction method described in Section 7.1. The devices were based on a 3.0-µm-thick photoanode made of 60-nm sized TiO_2 paste. All electrolytes contained 10 mole percent of $NOBF_4$ as the dopant 1.2 M LiTFSI and 0.5 M NBB in AcCN.

8.6 Conclusions

In this chapter, the possibility of using fast, one-electron transfer redox couples as alternative electrolytes to the widely used I^- / I_3^- system has been evaluated by observing the photovoltaic performance of electrolyte based on TEMPO, POZ and TTF. Among these couples, TEMPO/$TEMPO^+$ showed the best conversion efficiency of more than 5 % under AM 1.5 illumination at 100 $mWcm^{-2}$, surpassing the previous record for electrolytes containing cobalt(II)/cobalt(III) redox couple. The redox potentials of these couples were determined to be 100 to 400 mV more positive than that of I^- / I_3^- couple, alleviating the potential mismatch between the Nernst potential of the dye cation and that of the redox mediator. Laser photolysis experiments demonstrated that the sensitizer was rapidly regenerated by TEMPO in the ns time domain though the driving force for this reaction was diminished by the replacement of the redox mediator. Due to the facile electron transfer kinetics associated with these redox couples, the recapture of the photoinjected electrons by the oxidized species in the electrolyte was found to be much faster than the iodine case, effectively reducing the carrier density and lowering the quasi-Fermi level in the TiO_2 film. As a result, the observed increase in V_{oc} of the devices with these electrolytes was lower than the expected values based on the shift in the Nernst potentials.

8.7 References to Chapter 8

[1]. Gregg, B. A.; Pichot, F.; Ferrere, S.; Fields, C. R. *J. Phys. Chem. B* **2001**, *105*, 1422.

[2]. Gregg, B. A. *Coord. Chem. Rev.* **2004**, *248*, 1215.

[3]. Nusbaumer, H.; Moser, J.-E.; Zakeeruddin, S. M.; Nazeeruddin, M. K.; Grätzel, M. *J. Phys. Chem. B* **2001**, *105*, 10461.

[4]. Nusbaumer, H.; Zakeeruddin, S. M.; Moser, J.-E.; Grätzel, M. *Chem. Eur.J.* **2003**, *9*, 3756.

[5]. Sapp, S. A.; Elliott, C. M.; Contado, C.; Caramori, S.; Bignozzi, C. A. *J. Am. Chem. Soc.* **2002**, *124*, 11215.

[6]. Cazzanti, S.; Caramori, S.; Argazzi, R.; Elliott, C.M.; Bignozzi, C.A. *J. Am. Chem. Soc.* **2006**, *128*, 9996.

[7]. Lebelev, O. L.; Kazarnovskii, S. N. *Zhur. Obshch. Khim.* **1960**, *30*, 1631.

[8]. Horiuchi, T.; Miura, H.; Sumioka, K.; Uchida, S. *J. Am. Chem. Soc.* **2004**, *126*, 12218.

[9]. Ito S.; Zakeeruddin, S. M.; Humphry-Baker, R.; Liska, P.; Charvet, R.; Comte, P.; Nazeeruddin, M. K.; Péchy, P.; Takata, M.; Miura, H.; Uchida, S.; Grätzel, M. *Adv. Mater.* **2006**, *18*, 1202.

[10]. Zhang, Z.; Chen, P.; Murakami, T. N.; Zakeeruddin, S. M.; Grätzel, M. *Adv. Funct. Mater.* **2008**, *18*, 341.

[11]. Kuang D. B.; Klein C.; Snaith H. J.; Moser J. E.; Humphry-Baker R.; Comte P.; Zakeeruddin S. M.; Grätzel, M. *Nano Lett.* **2006**, *6*, 769.

[12]. Argazzi, R.; Bignozzi, C. A.; Heimer, T. A.; Castellano, F. N.; Meyer, G. J. *J. Phys. Chem. B* **1997**, *101*, 2591.

[13]. O'Regan, B. C.; Lenzmann, F. *J. Phys. Chem. B* **2004**, *108*, 4342.

[14]. O'Regan, B. C.; Durrant, J. R.; Sommeling, P. M.; Bakker, N. J. *J. Phys. Chem. C* **2007**, *111*, 14001

9. The 2,2,6,6-Tetramethyl-1-piperidinyloxy, an Efficient, Iodine-free Redox Mediator for Dye-sensitized Solar Cells

Published in *Adv. Funct. Mater.* **2008**, *18*, 341-346.

*Zhipan Zhang, Peter Chen, Takurou N. Murakami, Shaik M. Zakeeruddin and Michael Grätzel**

*To whom the correspondence should be made

A promising redox system offering an alternative to the widely used iodide/triiodide couple based on the stable organic radical 2,2,6,6-tetramethyl-1-piperidinyloxy **(**TEMPO) has been employed in dye sensitized solar cells. The photovoltaic performance of this new redox couple has been evaluated by employing nanocrystalline TiO_2 films with different thickness. Judicious selections of a 5.0 µm photoanode made from TiO_2 mesoscopic particles and an organic sensitizer with a high molar extinction coefficient yield an overall solar to electric power conversion efficiency of 5.4 % under AM 1.5 illumination at 100 $mWcm^{-2}$, which is unprecedented for iodine-free mediator system.

9.1 Introduction

Dye-sensitized solar cells (DSCs) have been attracting increasing industrial and academic interests since their successful debut in 1991.[1] Unlike conventional p-n junction solar cells, a DSC employs a dye-sensitized nanocrystalline porous semiconductor metal oxide infiltrated by a hole transporting matrix or liquid electrolyte. Light absorption by the sensitizer (S) is followed by injection of an electron into the conduction band of the oxide. The dye is regenerated from the resulting oxidized state (S^+) by electron donation from a redox mediator present in the electrolyte. So far the I^- / I_3^- has almost exclusively been used as redox couple reaching a conversion efficiency of over 11 % in standard global AM 1.5 solar light under standard conditions.[2]

A drawback of the I^- / I_3^- system is the mismatch between its redox potential (0.4 V vs. NHE) and that of the sensitizer (ca. 1.0 V versus NHE) resulting in an excessive driving force of 0.6 eV for the dye regeneration process. Because the energy loss incurred during dye regeneration is one of the main factors limiting the performance of current dye sensitized solar cells, the search for alternative redox couples with a more positive redox potential than I^- / I_3^- is a current research topic of high priority. Reversible mediators such as ferrocene/ferrocenium yield a low photo-voltage and small photocurrents due to the rapid back reaction of injected electrons with the Fe(III) species.[3] Co(II) complexes show an impressive efficiency of 8% at low light intensity but their performance drops markedly under full sun illumination.[4] A combination of two mediators, operating in series to regenerate the dye and transport the positive charges to the counter electrode has recently produced interesting results.[5]However to date, the solar to electric power conversion efficiency achieved with all these systems in full AM 1.5 sun light still remains well below 5%. Stable organic radicals, such as 2,4,6-tri-*t*-butylphenoxyl, nitronyl nitroxide and 2,2,6,6-tetramethyl-1-piperidinyloxy (TEMPO) being certified as nontoxic agents are widely employed as antioxidants and light-stabilizers.[6a] Recently, these materials have also been examined from the perspective of electro-active or charge-storage components for organic radical based secondary batteries. [6b-6e] Here we introduce TEMPO as redox mediator, which allowed for the first time to exceed this performance benchmark.

9.2 Results and Discussion

The photovoltaic performance of the TEMPO-based redox system was assessed by testing it in dye sensitized solar cells (DSCs) fabricated with a high-extinction- coefficient indoline sensitizer, D-149.[7] Figure 1 presents the structure of D-149 and its absorption spectrum when it was anchored on TiO_2 film. With an extinction coefficient of 68,700 M^{-1} cm^{-1} at 526 nm, this dye was known to absorb intensely in the visible region and exhibit high performances with thin TiO_2 films.[8]

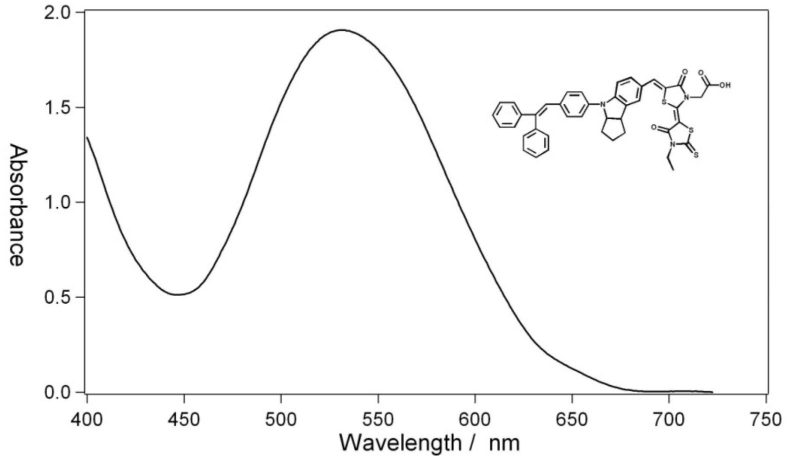

Figure 1. Structure of D-149 sensitizer and the absorption spectrum of D-149 sensitizer anchored on TiO2 films. The curve is measured with a 3-µm-thick layer of 20-nm-sized TiO_2 particles.

The photoanode was a screen-printed layer of a new paste synthesized in our lab by a published method.[9] Figure 2 shows the scanning electron microscope (SEM) images of the as-printed film. The film was homogeneous in the whole range and the average particle size was found to be around 50 nm from a larger magnification. The Brunauer-Emmett-Teller (BET) surface area of the paste was measured to be 31.9 m^2/g and the porosity of the film was determined to be 0.53.

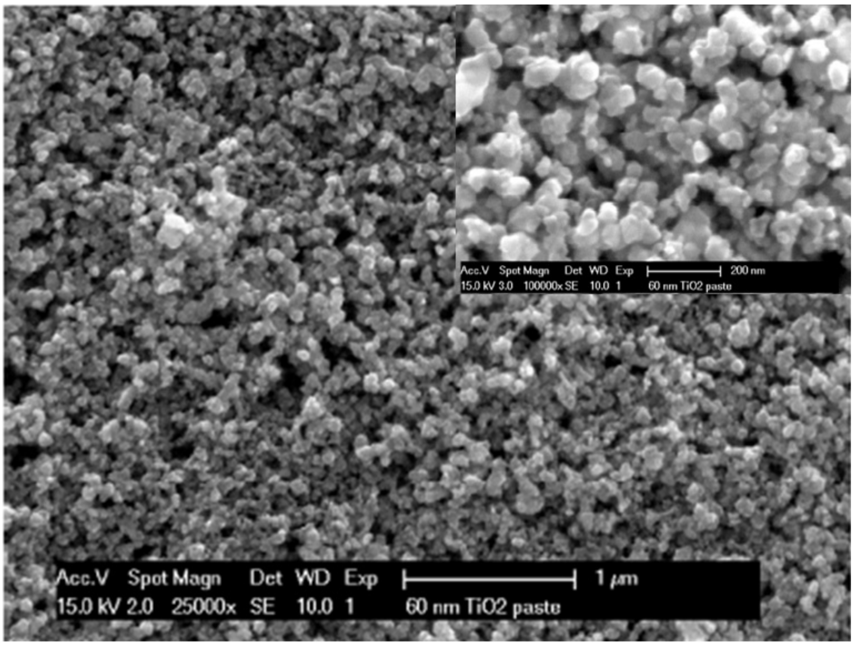

Figure 2. SEM images of a mesoscopic TiO_2 film at a lower and higher (insert) magnification. Scale bars are 1 µm and 200 nm, respectively. The film was screen printed from a homemade paste (see Experimental).

Figure 3 is a cyclic voltammetry (CV) of 2 mM TEMPO recorded at a scan rate of 10 mV s^{-1} in acetonitrile solution containing 0.1 M tetrabutylamonium tetraboronfluoride (TBATBF) as the supporting electrolyte. The voltammogram was typical for so-called quasi-reversible behavior with a peak separation of 80 mV, rather than the 59 mV expected for the reversible case.[10] The diffusion coefficient of TEMPO was measured to be 1.1×10^{-5} cm^2 s^{-1} by using a microelectrode, in agreement with previously measured values.[6d] The standard redox potential of TEMPO/TEMPO$^+$, was determined to be 0.26 V vs. ferrocene/ferrocium, i.e. about 0.80 V vs. NHE, which was 0.40 V higher than that of the I^-/I_3^- couple. The redox potential of D-149 sensitizer was 1.05 V vs. NHE and this was about 0.3 V more positive than the Nernst potential of TEMPO/TEMPO$^+$ electrolytes used in the present work (see later calculation with equation 1).

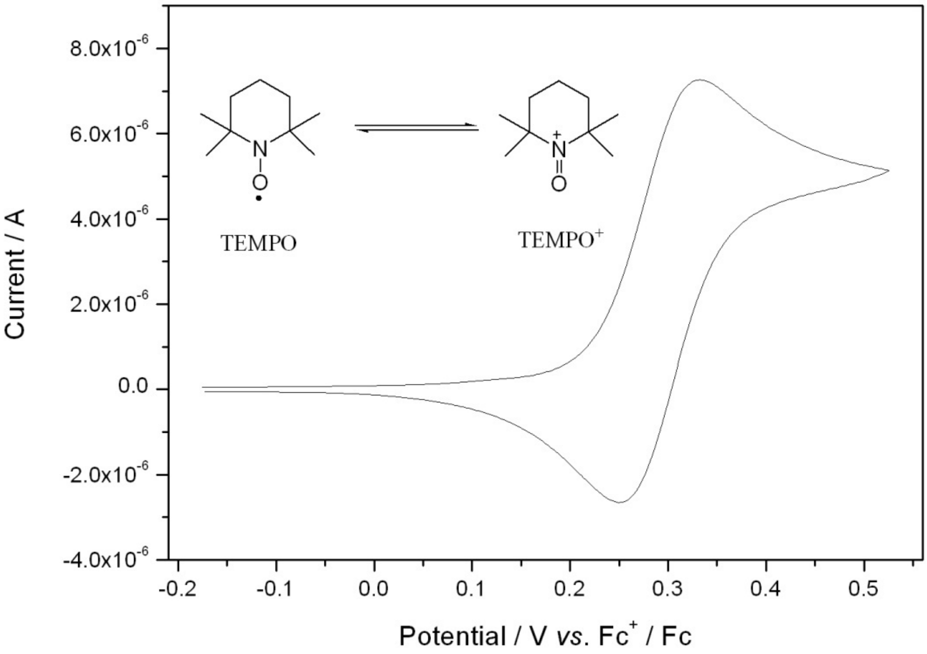

Figure 3 Cyclic voltammogram of 2 mM TEMPO on Pt disc electrode in acetonitrile solution containing 0.1 M TBATFB as the supporting electrolyte. Scan rate: 10 mV sec^{-1}.

To make a redox couple, $NOBF_4$ was added to oxidize 10 mol percent of the TEMPO to TEMPO$^+$.[4b] Figure 4a shows the UV-vis spectrum of 0.01 M TEMPO solution. The absorption of TEMPO was very weak in the visible region and peaked around 460 nm with a low molar extinction coefficient of 10. Doping TEMPO with 10 % $NOBF_4$ only slightly shifted the absorption spectrum (Figure 4b). Compared to the high absorption of the sensitizer in this region, the absorption of TEMPO/TEMPO$^+$ was negligible and avoided the loss incurred by light absorption of the electrolyte.

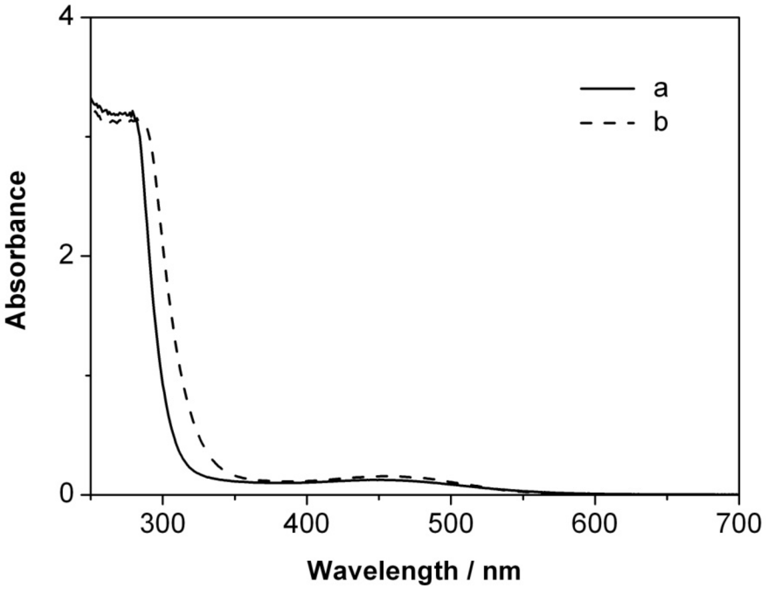

Figure 4. UV-visible spectra of acetonitrile solutions of 0.01 M TEMPO in the absence (a) and presence (b) of 10 mol percent dopant of $NOBF_4$.

Three electrolytes were employed in this work. Electrolyte A contained 1M TEMPO in acetonitrile and doped with 0.1 M $NOBF_4$. In electrolyte B, the concentration of TEMPO and $TEMPO^+$ was reduced 10 times. For comparison, the electrolyte coded C contained 0.1 M 1-methyl-3-propyl imidazolium iodide (PMII) and 0.01 M I_2, maintaining the same ratio of oxidized species to reduced species in electrolytes A and B. As is known to all, the actual redox potential of the redox couple is related to the standard potential by Nernst equation,

$$E = E_0 + \frac{0.059}{n} \lg \frac{[\mathrm{Ox}]}{[\mathrm{Red}]} \qquad \text{(Eq.9.1)}$$

where E_0 is the standard electrode potential, n is the number of electrons transferred in the half reaction, [Ox] and [Red] are the concentration of oxidized and reduced species, respectively. Note that n was 1 for $TEMPO/TEMPO^+$ system but 2 for I^- / I_3^- redox couple. According to Eq. 9.1, the actual redox potentials of electrolytes A and B were then calculated to be 0.74 V versus NHE, while that of electrolyte C was 0.43 V. Thus, using electrolytes A and B led to a 310 mV positive shift in redox potential when compared to the case of electrolyte C. Since the V_{oc} corresponds to the difference between the quasi-Fermi level of the electrons in the nanocrystalline TiO_2 electrode under illumination and the redox potential of the electrolyte, a higher V_{oc} should be expected with electrolytes A and B.

The thickness of the photoanode was first optimized by using mesoscopic TiO_2 films of 3.0, 5.0 and 8.0 µm in combination with electrolyte A. Table 1 summarizes the detailed photovoltaic parameters of these devices. The open-circuit voltage (V_{oc}) decreased with increasing film thickness, a phenomenon frequently observed in DSCs, mainly due to the increase in surface area that was in favor of dark current.[8] Meanwhile, the short circuit photocurrent density (J_{sc}) increased with film thickness, reaching a plateau of ~9 mA cm $^{-2}$ at 5.0 µm. Further increase in film thickness barely influenced J_{sc}. The overall light-to-power conversion efficiency (η) attained 5.4 % with a film thickness of 5.0 µm. To our knowledge, this is the highest power conversion efficiency reported in full sunlight for a DSC that does not employ I^- / I_3^- [4a,4b, 5] or the pseudo halide $SeCN^-/(SeCN)_3^-$ [11] as redox mediator. Figure 5a presents the photocurrent density-voltage characteristics of this device measured under various light intensity irradiations. The incident photon to current conversion efficiency (IPCE) of this device is shown in Figure 5b. The IPCE spectrum resembled the absorption spectrum of the dye anchored on TiO_2 mesoscopic films (Figure 1) exceeding 50% between 520 and 600 nm.

TABLE 1 Complete set of photovoltaic parameters for DSCs based on D-149 sensitizer and the electrolyte A with photoanodes of different thickness measured under AM 1.5 full sunlight (100 mW cm^{-2}) irradiation

Thickness (µm)	J_{sc} (mA cm^{-2})	V_{oc} (mV)	*FF*	η (%)
3.0	6.9	860	0.67	3.9
5.0	9.4	830	0.70	5.4
8.0	9.3	780	0.66	4.8

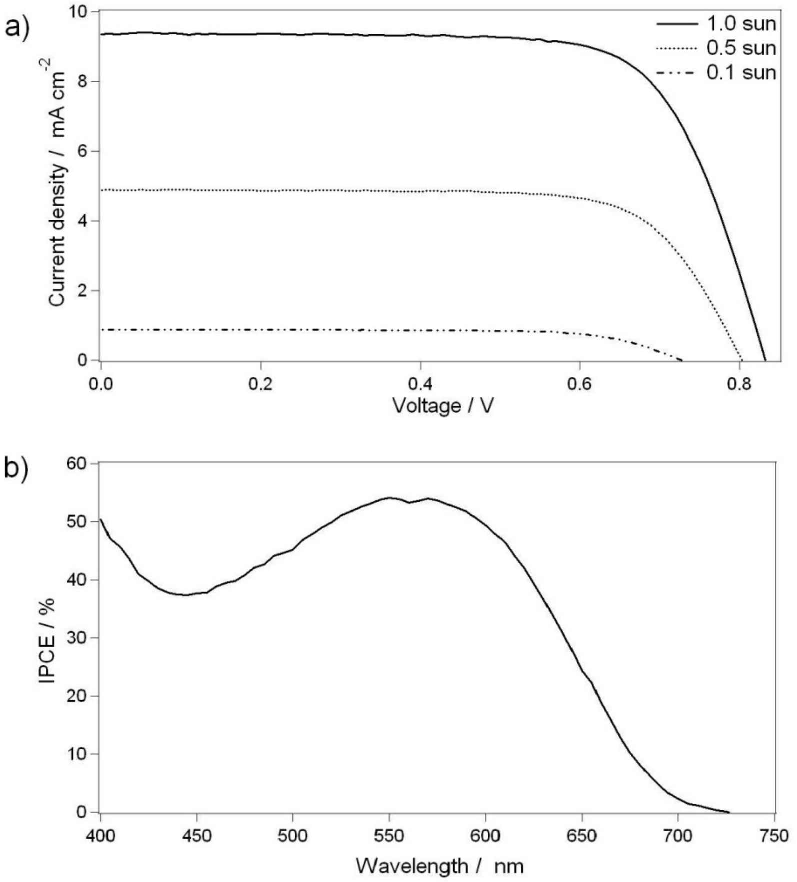

Figure 5. a) *J–V* characteristics of D-149 sensitized solar cell based on electrolyte A and a 5.0-μm-thick TiO2 mesoscopic film, measured at different light intensities. b) IPCE spectrum of the above device.

With the optimized film thickness of 5.0 μm, Figure 6a compares the current-voltage characteristics of devices fabricated with the electrolytes A and B in the dark. The dark current of the device with electrolyte B was much smaller than that of the device with electrolyte A, which could be explained by the 10 times less amount of oxidized species in the electrolyte. The current density-voltage curve of the device with electrolyte B under simulated AM 1.5 illumination at 100 mW cm^{-2} is plotted in Figure 6b. The drop in dark current with decreasing TEMPO^{+} concentration caused the open circuit voltage (V_{oc}) to increase from 830 mV for electrolyte A to 910 mV for electrolyte B, being a record V_{oc} value for a DSC based on a liquid organic electrolyte. The J_{sc} was 7.5 mA cm^{-2}for this device and the lower J_{sc} value was attributed to the incomplete interception of the recombination of electrons with sensitizer cation radicals at the 0.1 M TEMPO concentration. To compare this result, the most widely used ruthenium sensitizer, N-719, was used in combination of electrolyte B. The cell showed a short circuit density of 4.1 mA cm^{-2} and a conversion efficiency of 2.4%. The J_{sc} difference between D-149 and N-719 based devices were attributed to the fact that the molar extinction coefficient of D-149 sensitizer was much larger than that of N-719 sensitizer (13, 900 M^{-1} cm^{-1} at 541 nm) and the light absorption was thus higher for D-149 sensitized photoelectrodes.

We further tested an iodide electrolyte of a similar composition, namely electrolyte C, along with the same D-149 sensitized photoanode. The *J–V* curves of electrolyte C in the dark and under AM 1.5 illumination at 100 $mWcm^{-2}$ are included in Figure 6. The device showed a J_{sc} of 7.5 mA cm^{-2} by coincidence and V_{oc} of 720 mV, respectively. Comparison of the *J-V* characteristics of electrolytes B and C demonstrated that the TEMPO/$TEMPO^+$ couple produced a similar J_{sc} but a 190 mV higher V_{oc} than the 0.1 M iodide-based electrolyte, proving the concept of using this new mediator in increasing the V_{oc}. The J_{sc} of the device with electrolyte C seemed to be low when compared to our previous published value with D-149 sensitizer.[8] We emphasize that the high value in ref [8] was achieved with double layer photoanodes from 20-nm-sized particle and 400-nm-sized scattering particle pastes and the difference in current density could be explained by the weaker coloration of photoanodes made from 60-nm-sized particle paste. Nevertheless, the photoanodes used here gave a fair comparison of the V_{oc} difference between TEMPO/$TEMPO^+$ and I^- / I_3^- electrolytes at a similar J_{sc}, eliminating the effect of J_{sc} on V_{oc} that follows the diode equation.

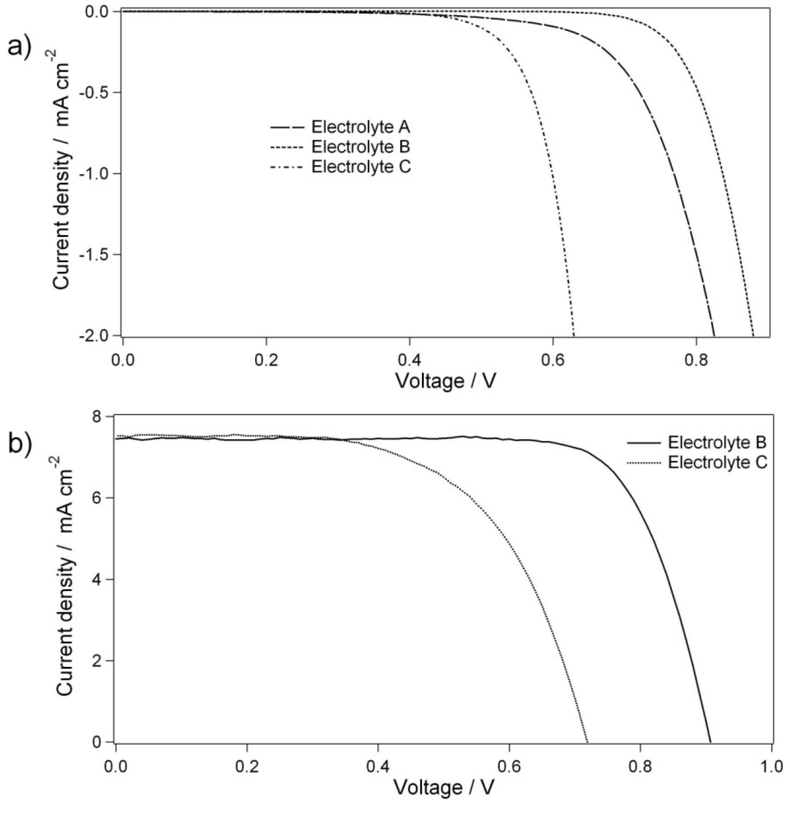

Figure 6. a) Dark current curves of D-149 sensitized solar cells devices are based on a 5-µm-thick TiO_2 nanocrystalline film with electrolytes A, B and C. b) *J–V* characteristics of the above devices with electrolyte B and C under simulated AM 1.5 illumination at 100 mW cm^{-2}.

As the V_{oc} is related to the difference between the quasi-Fermi level of the electrons in TiO_2 electrode under illumination and the redox potential of the electrolyte, a 310 mV positive shift the value of the latter should result in a corresponding increase in V_{oc} if the conduction band position and trap distribution of the oxide film remains fixed. However, the photovoltage increased only by 110 - 190 mV, depending on the concentration of $TEMPO^+$ in the electrolyte. Photovoltage transient decay experiments were used to rationalize this behavior. The principles of this technique and the experimental setup have been described previously.[12,13] Briefly, the solar cell, while being illuminated by a white bias at open circuit, was exposed to a short flash from a light emitting diode resulting in a small augmentation of the photovoltage during the pulse. The dynamics of the incremental increase and decrease of the V_{oc} due to this perturbation were monitored and can be used to extract the electron transport and recombination time. The V_{oc} decay closely followed an exponential law and the electron lifetime, τ, was derived from the semi-logarithmic plot. The electrons decay principally by recombining with the oxidized form of the mediator.

Figure 7 shows the lifetime of the electrons in the nanocrystalline TiO_2 film as a function of their quasi-Fermi level, which was varied by changing the intensity of the light bias. The Fermi level is expressed with respect to the redox potential of the $TEMPO/TEMPO^+$ couple. For electrolytes A and B, this difference corresponds to the measured V_{oc} values, while for electrolyte C, 310 mV was added to the V_{oc} to account for the difference in the Nernst potentials of electrolyte B and C. Compared to electrolyte A, electrolyte B has a longer electron lifetime and this can be explained by the lower $TEMPO^+$ concentration in electrolyte B. Note that at a given quasi-Fermi level, the electron lifetime in the iodide based device is much longer than that of TEMPO containing devices. It appears that the $TEMPO^+$ recaptures the electron from the conduction band of the nanocrystalline TiO_2 particles much faster than the triiodide ions. The faster electron recapture taking place in TEMPO based electrolyte prevents the electron concentration in the TiO_2, from reaching the same levels as for the iodide/triiodide based cells and thus reducing V_{oc} increase to a smaller value than the simple shift in Nernst potentials.

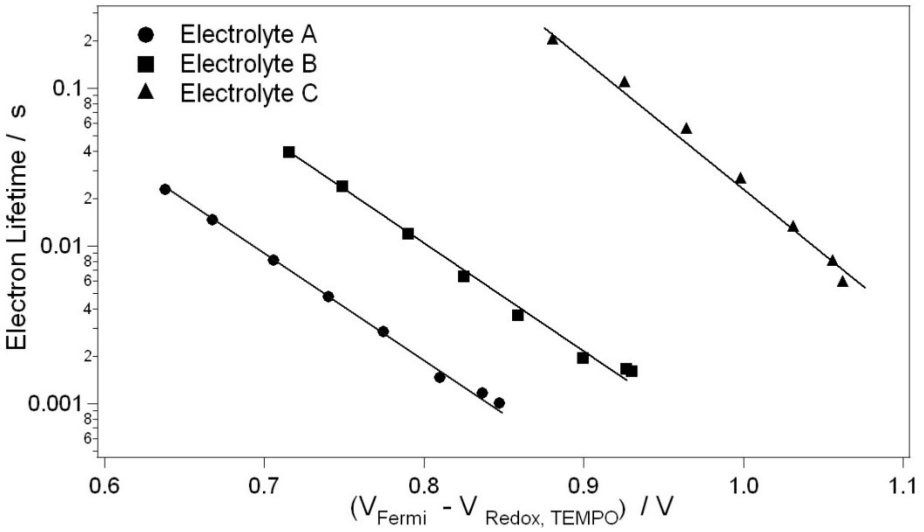

Figure 7. Electron lifetime of electrolytes A to C at different electron quasi-Fermi levels of under varying external light bias. A 310 mV positive offset was added to the measured V_{oc} of electrolyte C to adapt its value to the TEMPO/TEMPO$^+$ reference potential.

Although stability is not the main purpose of this work, the devices with electrolytes A and B were monitored upon a short period. The photovoltaic performance of the device with electrolytes A decreased rapidly, while the device with electrolytes B showed better stability. After a 24-hour aging at room temperature in the dark, the conversion efficiency at 0.1 sun kept the same, while that at 1.0 sun decayed fast, mainly due to a small decrease in J_{sc} but a large decrease in *FF*. It appears that the oxidized species, i.e. TEMPO$^+$, in the electrolyte was unstable and the decrease in TEMPO$^+$ concentration limited the diffusion current at high light intensity, reducing the *FF* of the device.

9.3 Conclusions

In summary, we have successfully demonstrated the concept of using TEMPO/TEMPO$^+$, a fast one electron redox couple, as an alternative to the widely used I^- / I_3^- system. Although a much faster recombination was observed when compared to I^- / I_3^- redox, the device showed an overall solar to electric power conversion efficiency of 5.4 % under AM 1.5 illumination at 100 mWcm^{-2}. Work is now underway to study derivatives of TEMPO, attempting to improve the performance and stability this redox system.

9.4 Experimental

All chemicals and solvents used in the present work were of puriss quality. Acetonitrile was obtained from Fluka and distilled before use. TEMPO and $NOBF_4$ were purchased from Fluka. *N*-Butylbenzimidazole (NBB) and lithium bis(trifluoromethanesulfonyl)imide were synthesized in our lab. The working electrode was prepared by first depositing a TiO_2 blocking underlayer on fluorine doped tin oxide glass (Nippon Sheet Glass, Solar, 4 mm thick) by spray pyrolysis[14] and subsequently coating a layer of TiO_2 paste. The coating of paste was repeated to get a desired thickness. The paste was prepared from 60-nm-sized particles (Showa Denko K.K.) with the method in ref [9]. The electrodes coated with the TiO_2 pastes were then gradually heated under an air flow at 325 °C for 5 min, at 375 °C for 5 min, at 450 °C for 15 min, and at 500 °C for 15 min. The TiO_2 films were treated again with $TiCl_4$ and sintered at 500 °C for 30 min. After cooling to 80 °C, the TiO_2 electrodes were immersed into a 0.3 mM solution of an organic sensitizer D-149 in acetonitrile/*tert*-butyl alcohol mixture (v/v,1:1). The counter electrode was also made of FTO glass onto which a nanocrystalline Pt catalyst was deposited. Electrolyte A contained 1M TEMPO, 1.2 M lithium bis(trifluoromethane sulfone imide) (LiTFSI) and 0.5 M N-butylbenzimidazole (NBB) in acetonitrile. $NOBF_4$ was added to oxidize 10 mol percent of the TEMPO to $TEMPO^+$.[4b] In electrolyte B, the concentration of TEMPO and $TEMPO^+$ was reduced 10 times. The electrolyte coded C contained 0.1 M propyl methylimidazolium iodide, 0.1 M I_2, 1.2 M LiTFSI and 0.5 M NBB in acetonitrile. The electrolyte was introduced through a hole in the counter electrode by vacuum filling after sealing the cell by a hot melt.

For photoelectrochemical measurements, a 450 W xenon light source (Oriel, USA) was used to give an irradiance of 100 mW cm^{-2} (the equivalent of one sun at AM 1.5) at the surface of the solar cell. The spectral output of the lamp was matched in the region of 350-750 nm with the aid of a Schott K113 Tempax sunlight filter (Präzisions Glas & Optik GmbH, Germany) so as to reduce the mismatch between the simulated and true solar spectra to less than 2%. Various incident light intensities were regulated with neutral wire mesh attenuators. The current voltage characteristics of the device under these conditions were obtained by applying an external potential bias to the device and measuring the generated photocurrent with a Keithley model 2400 digital source meter (Keithley, USA). UV-vis spectra were measured on a Cary 5 spectrophotometer.

Photovoltage transients were observed using an exciting pulse generated by a ring of red light emitting diodes (LEDs, Lumiled) controlled by a fast solid-state switch. Pulse widths of 200 ms were used. The pulse was incident on the photoanode side of the device and its intensity was controlled to keep the modulation of the voltage below 5 mV. An array of InGaN diodes (Lumiled) supplied the white bias light incident on the same side of the device. Usually, transients were measured at different light intensities ranging from 150 % to 0.1 % sun via tuning the voltage applied on the bias diodes.

Cyclic voltammetry measurements were performed on a computer-controlled Autolab P20 electrochemical workstation (Eco Chimie, Netherlands) in combination with a conventional three-electrode, one-compartment electrochemical cell. A Pt disc and an Ag disk were used as working and counter electrodes, respectively. The reference electrode was Ag/AgCl electrode, calibrated by measuring the redox potential of ferrocene dissolved in the solution and the redox potentials were converted to those versus a normal hydrogen electrode (NHE) reference scale by adding a constant of 0.55 V.

Acknowledgment. The Korean Institute of Science and Technology (KIST) supported this work through an Internal Project Grant. We thank the Korean principal investigator Dr. Nam-Gyu Park for helpful discussions. PC acknowledges the financial support of Taiwan Merit Scholarships (TMS-094-2A-026). We are also grateful to Dr. R. Humphry-Baker for experimental help and discussions, Mr. P. Comte for film preparation, Dr. N. Evans for the synthesis of NBB, Dr. S. Uchida for providing D-149 sensitizer and the CIME-EPFL for the SEM performance.

9.5 References

[1]. B. C. O'Regan, M. Grätzel, *Nature* **1991**, *353*, 737.

[2]. (a) M. K. Nazeeruddin, F. De Angelis , S. Fantacci , A. Selloni, G. Viscardi, P. Liska, S. Ito, T. Bessho, M. Grätzel, *J. Am. Chem. Soc.* **2005**, *127*, 16835. (b) M. Grätzel, *Chem. Lett.* **2005**, *34*, 8. (c) Y. Chiba, A. Islam, Y. Watanabe, R. Komiya, N. Koide, L. Han, *Japanese Journal of Appl. Phys., Part 2: Letters & Express Letters*, **2006**, *45*, 24.

[3]. (a) B. A., Gregg, F. Pichot, S. Ferrere, C. R. Fields, C. R. *J. Phys. Chem. B* **2001**, *105*, 1422. (b) B. A. Gregg, *Coord. Chem. Rev*. **2004**, *248*, 1215.

[4]. (a) H. Nusbaumer, J.-E. Moser, S. M. Zakeeruddin, M. K. Nazeeruddin, M. Grätzel, *J. Phys. Chem. B* **2001**, *105*, 10461. (b) H. Nusbaumer, S. M. Zakeeruddin, J.-E. Moser, M. Grätzel, *Chem. Eur.J.* **2003**, *9*, 3756. (c) S. A. Sapp, C. M. Elliott, C. Contado, S. Caramori, C. A. Bignozzi, *J. Am. Chem. Soc.* **2002**, *124*, 11215

[5]. (a) S. Cazzanti, S. Caramori, R. Argazzi, C. M. Elliott, C. A. Bignozzi, *J. Am. Chem. Soc.* **2006**, *128*, 9996.

[6]. (a) H. Nishide, T. Suga, *Electrochemical Society Interface*, **2005**, *14*, 32. (b) H. Nishide, S. Iwasa, Y. -J. Pu, T. Suga, K. Nakahara, M. Satoh, *Electrochim Acta*, **2004**, *50*, 827. (c) K. Nakahara, S. Iwasa, M. Satoh, Y. Morioka, J. Iriyama, M. Suguro, *Chem. Phys. Lett.*, **2002**, *359*, 351. (d) T. Suga, Y. -J. Pu, K. Oyaizu, H. Nishide, *Bull. Chem. Soc. Jpn*, **2004**, *77*, 2203. (e) L. M. Moshurchak, C. Buhrmester, R. L. Wang, J. R. Dahn, *Electrochim. Acta*, **2007**, *52*, 3779.

[7]. T. Horiuchi, H. Miura, K. Sumioka, S. Uchida, *J. Am. Chem. Soc.* **2004**, *126*, 12218.

[8]. S. Ito, S. M. Zakeeruddin, R. Humphry-Baker, P. Liska, R. Charvet, P. Comte, M. K. Nazeeruddin, P. Péchy, M. Takata, H. Miura, S. Uchida, M. Grätzel, *Adv. Mater.* **2006**, *18*, 1202.

[9]. S. Ito, P. Chen, P. Comte, M. K. Nazeeruddin, P. Liska, P. Péchy, M. Grätzel, *Prog. Photovolt: Res. Appl.* **2007**, *15*,603.

[10]. (a) A. J. Bard, L. R. Faulkner, *Electrochemical Methods: Fundamentals and Applications*, second ed., John Wiley and Sons Inc., New York, 2001. (b) P. J. Cameron, L. M. Peter, S. M. Zakeeruddin, M. Grätzel, *Coord. Chem. Rev.* **2004**, *248*, 1447.

[11]. P. Wang, S. M. Zakeeruddin, J. -E. Moser, R. Humphry-Baker, M. Grätzel, *J. Am. Chem. Soc.* **2004**, *126*, 7164.

[12]. (a) B. C. O'Regan, F. Lenzmann, *J. Phys. Chem. B* **2004**, *108*, 4342. (b) B. C. O'Regan, S. Scully, A. C. Mayer, E. Palomares, J. Durrant, *J. Phys. Chem. B* **2005**, *109*, 4616.

[13]. Z. Zhang, S. M. Zakeeruddin, B. C. O'Regan, R. Humphry-Baker, M. Grätzel, *J. Phys. Chem. B* **2005**, *109*, 21818.

[14]. L. Kavan, M. Grätzel, *Electrochim. Acta* **1995**, *40*, 643.

10. General Conclusions and Outlook

10.1 Conclusions

The objective of the current thesis was to optimize the interface between the nanocrystalline semiconducting metal oxide film and the redox electrolyte in order to enhance the photovoltage and performance of the dye-sensitized solar cells. It featured with the application of ω-guanidino acids as the coadsorbent with the ruthenium amphiphilic sensitizers. Meanwhile, fast, one electron-transfer couples were employed as the alternative redox mediators to the normal iodide/iodine system. The main conclusions of the work are as follows:

Electronic function of the TiO_2 light-scattering layer in dye-sensitizer solar cells was elucidated. The layer made a small contribution to dark current but produced a considerable photocurrent under illumination. A cell made purely with light-scattering material showed an impressive efficiency of 5% at AM 1.5 illumination and phototransient measurements showed that the *DOS* of light-scattering layer was about 50% that of TiO_2 transparent nanoparticle layer.

The coadsorption of K-19 sensitizer with 4-guanidinobutyric acid onto nanocrystalline TiO_2 films remarkably increased the photovoltage without suffering significant current penalty and thus enhancing the total power conversion efficiency. The device showed a long-term stability exhibiting approximately 8% power conversion efficiency under the dual stress of both thermal aging and light-soaking. FTIR results indicated that GBA firmly anchored on the surface during 60°C aging but underwent some desorption under 80°C aging.

A series of guanidinoalkyl acids was employed as coadsorbents with the Z-907 sensitizer and their effects on dye-sensitized solar cells were investigated. The addition of guanidino coadsorbents increased the open-circuit voltage of the DSCs and had no adverse effect on the photocurrent if a proper amount was used. Up to a 15 % increase in total power conversion efficiency was achieved by using 4-guanidinobutyric acid·HCl as the coadsorbent and a power conversion efficiency of 8.3 % under AM 1.5 illumination was reached. Phototransient measurements showed that the increase in open-circuit voltage for guanidinocarboxylic acids was a collective effect of suppression of surface recombination and negative band-edge movement. Guanidinopropyl phosphonic acid was found to remain on the surface of TiO_2 after the longtime aging process at 80°C when it was coadsorbed with the sensitizer.

Some carboxylic acids with a similar structure were studied as the coadsorbent to the Z-907 sensitizer and a large increase in the photovoltage was only observed with ω-guanidino molecules. A higher carrier density was measured in these devices and the recombination rate was slowed down at a fixed carrier density by the mixed layer of coadsorbent and the sensitizer.

Alternative redox couples of nitroxide radical, phenoxazine and tetrathiafulvalene were used as the non-iodine electrolytes to reduce the potential mismatch between the Nernst potential of the dye cation and that of the redox mediator. The devices based on $TEMPO/TEMPO^+$ showed an open-circuit photovoltage of over 900 mV and a conversion efficiency more than 5 % under AM 1.5 illumination at 100 $mWcm^{-2}$, being a new record for non-iodine electrolytes other than the selenide. Phenoxazine and tetrathiafulvalene electrolytes only showed intermediate photocurrents and conversion efficiencies, probably due to one or two orders of magnitude faster back reaction of the photoinjected electrons with the oxidized species in the electrolyte than that in the iodide case. The fast recombination was against the accumulation of the carrier and the building up of the quasi-Fermi level in the TiO_2 film. Thus, the observed increases in the open-circuit voltage of the devices based on these electrolytes were much lower than the expected values predicted by the simple shift in the redox potentials and in particular cases, even open-circuit voltages smaller than that of the iodide device were observed with some of the redox couples.

10.2 Outlook

Coadsorbents are known for years to have beneficial effects in DSCs. Chenodeoxycholic acid is probably the most widely used coadsorbent in the fabrication of “champion” cells. Small molecules of carboxylic and phosphonic acids were applied as the coadsorbent in this thesis. The photovoltage was found to increase without a big sacrifice in the photocurrent and the improvement in conversion efficiency was observed. Compared to the normally used coadsorbents such as chenodeoxycholic acid, guanidino-coadsorbents gave a higher photovoltage with Z-907 sensitizer, a widely used dye for stable systems. The current work provided a theoretical ground for the coadsorbent effect, which is believed to be helpful in the design of new coadsorbents for more efficient and stable DSC systems.

Meanwhile, the search for alternative redox mediators opened up a potential route to better understand the working principle and further improve the conversion efficiency of DSCs. By reducing the potential mismatch between the electrochemical potential of the dye cation and that of the electrolyte, V_{oc} of higher than 900 mV was achieved with TEMPO/TEMPO$^+$ electrolyte, up to 30% higher than I^-/I_3^- redox system. Unfortunately, a fast recombination was even measured at short-circuit when the device was subjected to AM 1.5 simulated illumination at 100 mW cm^{-2}. This fast back reaction tended to impair the carrier accumulation in the device and limited the photocurrent. One interesting question would be whether this fast reaction could be slowed down or not. If one could find a right couple with a similar Nernst potential but featured with less facile electron transfer kinetics, higher carrier densities would be found in the device under the same condition, a prerequisite for a good photocurrent for any DSCs. Meanwhile, the back reaction with the fast redox couples could be mitigated someway by surface treatment. The coadsorbent could be a good choice, however, it worked best with the amphiphilic ruthenium sensitizer, which only gave intermediate performance with these fast couples, owing to the complicated interaction between thiocyanate groups of the sensitizer and the oxidized species of the couples. On the other hand, though the organic D-149 sensitizer performed best with the above redox couples, the coadsorbent barely changed the efficiency of the device, probably due to the different anchoring ability and packing modes and between the organic sensitizer and the amphiphilic ruthenium ones. The surface core-shell coating was another option. There have been many publications with thin layers of oxide coating, such as Nb_2O_5, ZnO and In_2O_3 etc., claiming improvements in photocurrent and photovoltage. Nonetheless, these experiments strongly depended on the thickness of the coating layer, which was very hard to control and reproduce. We also conducted coatings with oxides of Nb, In, Mg in the TEMPO electrolyte system, but poor fill factors and lower photocurrents were normally found, a phenomenon attributed to the non-uniform coating and pore blocking. At this stage, if a reliable and general procedure for surface coating was formulated, the performance of the non-iodine redox couples could be comparable to the iodide device or even higher in an optimistic estimation.

Appendix I

Structures of the ruthenium sensitizers used in the thesis

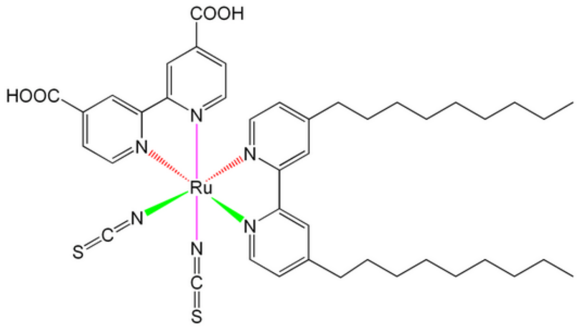

Z-907

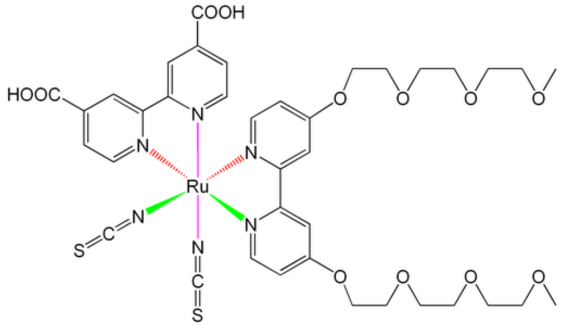

K-51

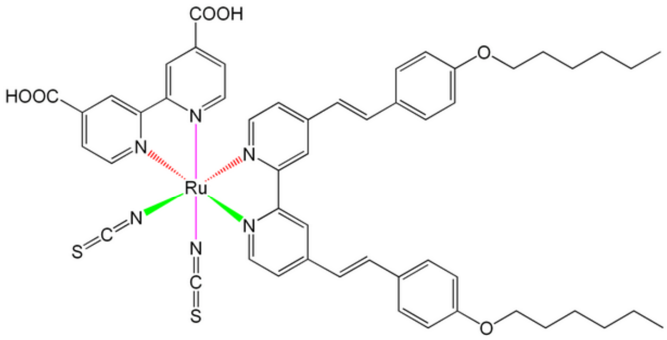

K-19

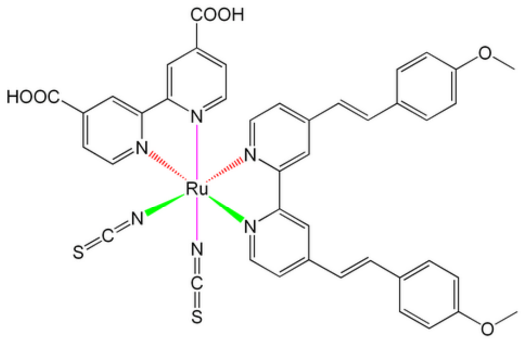

K-73

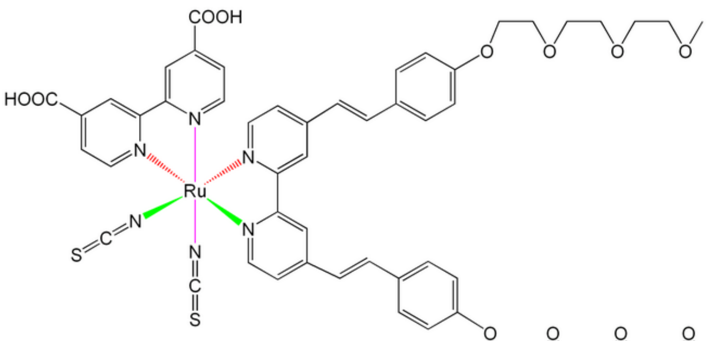

K-60

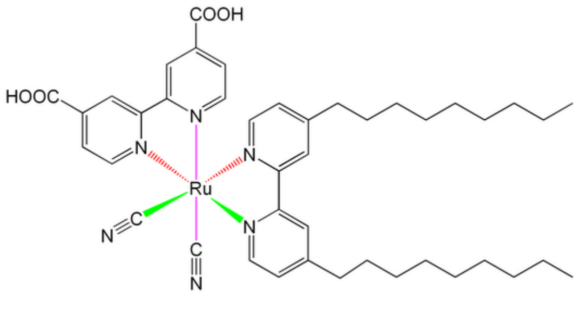

Z-973

Appendix II

Iodide electrolytes used in the thesis

Code	Description
Z-497	1 M PMII, 0.15 M I_2, 0.5 M NMB in MPN
Robust	0.8 M PMII, 0.15 M I_2, 0.5 M NMB in MPN
Z-610	0.5 M PMII, 0.15 M I_2, 0.5 M NMB in MPN
Z-611	2 M PMII, 0.15 M I_2, 0.5 M NMB in MPN
Z-612	2.5 M PMII, 0.15 M I_2, 0.5 M NMB in MPN
Z-647	1 M PMII, 0.15 M I_2, 0.5 M NBB in MPN
Z-770	1 M PMII, 0.1 M I_2, 1.2 M LiTFSI, 0.5 M NBB in AcCN
Z-770a	0.1 M PMII, 0.01 M I_2, 1.2 M LiTFSI, 0.5 M NBB in AcCN

Appendix III

Abbreviations

Shortened name	Full name
3TMMA	2-[2,2';5',2"]Terthiophen-5- ylmethylene-malonic acid
ABA	4-Aminobutyric acid
AcCN	Acetonitrile
APA	3-Aminopropionic phosphonic acid
Arg	Arginine
ATR-FTIR	Attenuated total reflectance Fourier transform infrared spectroscopy
BET	Brunauer-Emmett-Teller
BrMEEP	*N*- (Methoxyethoxyethyl)-3, 7-dibromo-phenoxazine
DMeMEEP	*N*-(Methoxyethoxyethyl)-3,7-dimethyl-phenoxazine
DOS	Density of states
DSC	Dye-sensitized solar cell
EIS	electrochemical impedance spectroscopy
EMITFSI	1-Methyl-3-ethylimidazolium bis (trifluoromethylsulfonyl) imide
ET	Electron transfer
FF	Fill factor
FTO	Fluorine-doped tin oxide
GAAHCl	2-Guannidinoactic acid hydrochloride
GBA	4-Guannidinobutyric acid
GBAHCl	4-Guannidinobutyric acid hydrochloride
GHAHCl	6-Guanidinohexanoic acid hydrochloride
GPA	Tetrabutylammonium 3-guanidinopropylphosphonate
HC	Hole conductor

IPCE	Incident photon-to-current conversion efficiency
ITO	Indium tin oxide
LHE	Light harvesting efficiency
LiTFSI	Lithium bis (trifluoromethyl) sulfonyl) imide
LSL	Light scattering layer
MEEP	*N*-(Methoxyethoxyethyl)-phenoxazine
MeMEEP	*N*-(Methoxyethoxyethyl)-3-methyl- phenoxazine
MeOMEEP	*N*-(Methoxyethoxyethyl)-3,7-dimethoxy-phenoxazine
MLCT	Metal-to-ligand charge transfer transitions
MPN	Methoxypropionitrile
NBB	N-butylbenzimidazole
NHE	Normal hydrogen electrode
NMB	N-methylbenzimidazole
PhA	Phthalic acid
PMII	1-Methyl-3-propylimidazolium iodide
POZ	Phenoxazine
RF	Roughness factor
SA	Salicylic acid
SEM	Scanning electron microscope
TBATBF	Tetrabutylammonium tetrafluoroborate
TCO	Transparent conducting oxide
TEMPO	2,2,6,6-Tetramethyl-1-piperidinyloxy
TNL	Transparent nanoparticle layer
TTF	Tetrathiafulvalene

Curriculum Vitae

Name: Zhipan Zhang Email: zhipan.zhang@epfl.ch

Educations

Oct. 2004 to date: Under supervision of Prof. Michael Grätzel, Laboratory of Photonics and Interfaces,

Swiss Federal Institute of Technology, Lausanne, Switzerland.

Sep 2002 to Jun 2004: M.S., Department of Chemistry, Tsinghua University, Beijing, China.

Sep 1998 to Jun 2002: B.S., Department of Chemistry, Nankai University, Tianjin, China.

Awards

Jun. 2004 Excellent Graduate of Tsinghua University

Feb. 2007 Chinese Government Award for Outstanding Self-financed Students Abroad.

Publications during PhD studies

1. Zhang, Z.; Zakeeruddin, S. M.; O'Regan, B. C.; Humphry-Baker, R.; Grätzel, M. **Influence of 4-Guanidinobutyric Acid as Coadsorbent in Reducing Recombination in Reducing Recombination in Dye-Sensitized Solar Cells** *J. Phys. Chem. B* **2005**, *109*, 21818.

2. Zhang, Z.; Evans, N.; Zakeeruddin, S. M.; Humphry-Baker, R.; Grätzel, M. **Effects of ω-Guanidinoalkyl Acids as Coadsorbents in Dye-Sensitized Solar Cells.** *J. Phys. Chem. C* **2007**, *111*, 398.

3. Zhang, Z.; Ito S.; O'Regan, B. et al. **Silica Coated and Insulated TiO_2 Microparticles as Light-Scattering Layer: Electronic Function of TiO_2 Light-Scattering Layer in Dye-Sensitized Solar Cells** *Z. Phys. Chem.* **2007**, *221*, 319.

4. Zhang, Z.; Chen, P.; Murakami, T.N. et al. **2,2,6,6-Tetramethyl-1-piperidinyloxy, an Efficient, Iodine-free Redox Mediator for Dye-sensitized Solar Cells.** *Adv. Funct. Mater.* **2008**, *18,* 341.

5. Wang, Q.; Zhang, Z.; Zakeeruddin, S. M.; Grätzel, M. **Formation of Shallow Transport Levels under Visible Light Illumination Enhancing the Performance of Dye-sensitized Solar Cell**. *J. Phys. Chem. C*. In press.

6. Kuang, D.; Klein, C.; Zhang, Z. et al. **Stable, High-Efficiency Ionic-Liquid-Based Mesoscopic Dye-Sensitized**

Solar Cells. *Small* **2007**, *3*, 2094.

Conferences

2007 NanoEurope 2007, **St. Gallen** (Switzerland); *poster presentation*

2,2,6,6-Tetramethyl-1-piperidinyloxy, a Novel, Iodine-free Redox Mediator for Dye-sensitized Solar Cells

2007 Material Research Society - Spring Meeting, **San Francisco** (USA); *oral presentation*

A Novel Efficient, Iodide-free Redox Mediator for Dye-sensitized Solar Cells

2006 Renewable energy, 2006, **Chiba** (Japan); *poster presentation*

Guanidinium Derivatives as Coadsorbents to Enhance Open-circuit Voltage in Dye-sensitized Solar Cells

Other Oral presentations

2008 National Renewable Energy Laboratory, Golden, CO.

Enhancing the Open-circuit Voltage of Dye-sensitized Solar Cells: Coadsorbents and Alternative Redox Couples

2006 Institute of Plasma Physics, Hefei, China

Characterization of Dye-sensitized Solar Cells (DSCs) by Transient and Electrochemical Impedance Methods

Acknowledgement

When I first began my writing on this thesis, I did not expect to have a long dedication to the acknowledgement. However, along with the building up of the file, I came to realize I owed a lot to all of my colleagues and collaborators. I would like to take this opportunity to express my sincere gratitudes to all, even some of them may never notice this by chance.

First of all, I really want to thank Professor Grätzel for leading me into the fascinating field of photochemical studies on the semiconductors. I was fortunate enough to write him an email a little more than three years ago and get the chance to conduct my research here. He has always been very kind and patient to me and I learned quite a lot from his amazing knowledge in semiconductors chemistry and physics. His perseverance and passion in energy research and alternative solutions to engery shortage guided me through all the difficulties I met in my PhD study and will light my path in my career life.

Many thanks to Dr. Robin A. Humphry-Baker and Dr. Shaik M. Zakeeruddin. Robin helped me with all the instrumental setups, which cost him lots of time to design and debug new programs for device physics measurements. I was well impresspled by his love in science and his perspective toward life, as well as his great help to spend his spare time correcting all the grammatical and spelling mistakes in this thesis to an acceptable level. Shaik aided me with his “second to none” expertise in inorganic syntheses and genourously provided me with his cherished sensitizers at all times. I really appreciate his extra efforts to make several fresh electrolytes everyday for a considerably long span of time and sincerely wish he would not need to do this again in the near future.

Many thanks to all of my compatriots, namely Dr. Daibin Kuang, Dr. Deyu Wang, Dr. Mingkui Wang Dr. Peng Wang and Dr. Qing Wang (in an alphabetic sequence) for helpful discussions and their help with my daily life. Also my gratitude to Dr. Nick Evans for his “made to measure” compounds, Dr. Henry Snaith and Dr Kay Cesar for their enthusiasm in research work, Mr. Pascal Comet, Mr. Takeru Bessho, Mr. Peter Chen, Dr. Seigo Ito and Dr. Takurou Murakami for film preparation and demonstration, Dr. Davide Di Censo and Mr. Gianluca Deghenghi for the Italian office atomosphere, Mrs Carole Grätzel for paper proof reading, Dr. Brian C. O’Regan for introducing me the

phototransient setup, Professor Jacque E. Moser and Mr. Joël Teuscher for the assistance in Laser experiments, Dr. Guido Rossenburg and Ms. Sophie Wenger for the help in TP, Dr. Yum Jun-ho, Dr. Lee Hyo Joong and Ms. Moon Soo-Jin for Korean customs, Dr. Md. Khaja Nazeeruddin and Dr. Peter Pètry for useful discussions and Dr. Kevin Sivula for a nice guide in UC Berkerley.

Special thanks to our secretaries Madam Gonthier for her patient help with all the administrative work and my starting time in Lausanne, and Madam Goudou for her kind assistance with my travels and her warm-hearted care of my wife. I would always remember all of your advices and try my best to better my life.

Finally, I should thank my parents for bringing me up, giving me all of their loves and having me educated. Last but not the least, my love to my wife, Hui, for her consideration and support in my studies.